An Experimental and Technoeconomic Study of Silicon Microwire Arrays for Fuel Production Using Solar Energy

Thesis by

Matthew Reed Shaner

In Partial Fulfillment of the Requirements for the

degree of

Doctor of Philosophy

CALIFORNIA INSTITUTE OF TECHNOLOGY

Pasadena, California

2016

(Defended November 23, 2015)

Acknowledgements

I vividly remember the morning I received my acceptance email to Caltech and wonder to this day why I was accepted into the Chemical Engineering Department, while most other top universities rejected me. For some reason I think this was meant to be because the more I learn about those other universities that rejected me the more I realize Caltech was the right choice no matter what. I feel so fortunate to have been a part of the incredibly smart, motivated, and open academic environment that is Caltech and will remember my time here for the rest of my life.

My first acknowledgements must go to my advisors Nate Lewis and Harry Atwater for supporting me scientifically, financially, and morally throughout my tenure at Caltech. I joined Nate's group just 3 months into my time at Caltech and quickly began working in the newly founded Joint Center for Artificial Photosynthesis (JCAP). Harry was the project leader for the JCAP group I joined, Membranes and Mesoscale, and thus became my second advisor.

Both Nate and Harry are absolutely brilliant, with knowledge and experience spanning fundamental scientific principles to successful start-up companies and beyond. Nate's attention to detail, Harry's perpetual positive attitude, and their combined compassion for and belief in me and hands-off approach empower and motivate me everyday to become the best scientist and person I can be. In addition to being such great scientists, both Nate and Harry are great, fun people outside of the lab. Nate's annual group windsurfing trip and frequent group parties at his house were always so enjoyable and provided unique bonding time with the group. Harry's biennial group retreat always involved afternoon activities from soccer matches to fun in the sun at the beach. Thank you for such a wonderful and enriching five years!

My adopted third advisor, Eric McFarland, a professor of Chemical Engineering at UCSB, provided me the opportunity to study with him at the University of Queensland in Brisbane, Australia, where he directed a Dow Chemical funded center, for five months during the later half of 2014. There I was able to pursue my interest in techno-economic analysis and cannot thank Eric enough for the mentorship throughout my time at UCSB and Caltech. While in Australia I chose to live in a van and did so for a month before Eric, his wife Wendy, their daughter Maddie, and their two dogs Rufus and Ellie politely encouraged me to live in the extra room in their home. I had so much fun with the whole McFarland family and cannot thank them enough for all that they did for me; it was so nice to be around familiar faces so far from home. Thank you also to Nirala Singh, Tom McConnaughy, Conor Young, Xiaoyu Wang, Daniel Klein-Marcuschamer, and Celestien Warner for a great office culture, showing me around Brisbane, and teaching me techno-economic analysis.

I also must thank my thesis committee members Rick Flagan, Mark Davis, and Sossina Haile. Sossina was a member of my candidacy committee prior to moving to Northwestern University. She provided great feedback and also taught me the important lesson that there is a limit to the number of slides one should present at candidacy. Rick stuck with me throughout my five years, allowed me the opportunity to TA his undergraduate Thermodyanmics class, and provided very insightful and challenging questions during this process. Mark was nice enough to replace Sossina on my thesis committee. I look back fondly on Mark's catalysis class first year and the connection we shared because we are both runners and share a love for the ocean.

Throughout my scientific endevors, Adam Nielander and Shane Ardo were and are my go to people. We spent so many hours learning semiconductor physics only to realize we understood less than we did before, which would lead to more reading and discussion of band-bending and the operational details of semiconductor diodes. We also had lots of fun outside the lab. I will never forget scalping tickets for the College National Championship Football game at the Rosebowl with Adam and Dan Torelli and the wild game that ensued.

The many summer softball championships we won with Adam at the helm, Shane covering the entire outfield singlehandedly, and the pure dedication of Rob Coridan's slides into nearly every base, and also the craziness that is Aaron and Wes Sattler, whom Adam introduced me to; someday I will get you both to eat a banana and go camping outside. Adam and Shane, I love you guys!

I had many in-lab mentors and collaborators that made my work possible and enjoyable. Emily Warren took me under her wing first year, as a senior lab member and Chem E. herself, and taught me how to grow Si microwire arrays, electrochemistry, and many other lab techniques crucial to my progress. Rob Coridan and Shane Ardo allowed me to ask endless questions and helped me so much with Si microwire arrays, depositing material on them, and basically anything else I published. Though not a mentor, Alex Pien was an undergraduate SURF student with me whose independence, willingness to ask questions, and great lab skills were so appreciated and enabled the work on tandem Si/TiO_2 devices to work at all. Nick Strandwitz, Dan Turner-Evans, Morgan Putnam, Mike Kelzenberg, Chris Chen, Hal Emmer, and Ron Grimm were all senior graduate students or Post-docs whom I am indebted to for mentorship inside and out of the lab. I look up to all of these people and only hope that I can be as good a mentor as you were to me.

Bruce Brunschwig is the director of the MMRC at the Beckman Institute and is an integral part of Nate's group. I cannot thank Bruce enough for the feedback he provided throughout my thesis work, his massive behind-the-scenes work to get JCAP up and running, and his jovial and positive attitude.

To the Lewis, Atwater, and JCAP groups, thank you so much for a wonderful five years. You are all brilliant and I am so fortunate to have been able to interact scientifically and as friends with all of you. Thank you for being safe in the lab, maintaining all of the equipment, and making lab such a positive and fun place to be.

None of my or anyone else's work would have been possible without the amazing support staff that is Barbara Miralles, Tiffany Kimoto, Jennifer Blankenship, and Kimberly Papadantonakis. It is and was always a joy to walk into their offiices; their big smiles and willingness to help support anything we ask for cannot be appreciated enough.

Being a part of JCAP was one of the best decisions I made at Caltech. I was one of the first students to join and with this came more responsibility and opportunity than I could ever have hoped for. The first two years of JCAP involved building the labs and ordering the equipment for these new labs. As a first year graduate student I was given the responsibility of ordering a SEM with a budget of $1 MM; I thought that was crazy, but it turned out to be so much fun and a hint at what was to come.

Through my work on Si microwire arrays, a central theme of JCAP, I was given the opportunity to present to all forms of JCAP review committees. Much of this is thanks to my advisors and also Joachim (Achim) Lewerenz, a JCAP Department head from the Helmholtz Center for Materials and Energy in Berlin, Germany, and Carl Koval, the JCAP Director from 2012-2014 and a professor at the University of Colorado, Boulder. I cannot thank Achim and Carl enough for their investment in me as a scientist through stimulating scientific conversations, opportunities to present my work to review committees, and the many enjoyable Friday evenings at JCAP NightCAP.

Xenia Amashukeli and Will Royea of JCAP management were another source of fantastic mentorship. Xenia and Will both provided generous amounts of their time to help prepare me and my presenations for what seemed like continual review committees. They worked tirelessly behind the scenes to maintain JCAP as a smooth running machine and cannot be thanked enough for this.

Two other JCAP members I must thank are Will West and Chris Karp. Will led the prototyping effort, which I participated in mostly out of interest, and Chris was a staff

scientist on the prototyping team. Will was an engineer among scientists and his passionate and disciplined approach provided me a view at how successful engineering projects are run in contrast to the more open and explorative academic approach. Chris held a similar passion for our work, but expressed it through comic relief and due criticism and tough questions. I will remember Chris for his down to earth personality, work-life balance, and big caring heart.

And last of the JCAP team is Josh Spurgeon. Josh was the first official hire of JCAP and was an integral part of the organization throughout his tenure. We spent a lot of time together from playing paintball with the Atwater group to traveling to JCAP conferences to continual discussions about the merits and practicality of different solar fuels technologies. Thank you Josh for being such a day to day mentor and making the lab such an enjoyable place to be.

During the later half of my time at JCAP, I was fortunate enough to receive a Resnick Institute for Sustainability Graduate Fellowship. Neil Fromer and Heidi Rusina have been nothing short of fantastic; their support throughout my last two years was unbelievable. They allowed my fellowship to support me while in Australia and I cannot thank Neil and Heidi enough for enabling such a wonderful scientific and personal adventure.

In my second year a quick succession of events led myself and my roommate and classmate, Matt Coggon, to become resident associates (RAs) in Dabney House. We were in this role from 2011-2014 and were responsible for the physical and mental health of ~70 students that lived in the house plus the 50+ house members that lived elsewhere. Along with Matt and I joining the RA program Chris Kempes, Suzanne Kern, Rachel Galimidi, and Harry Gristick also joined as RAs along with Taso Dimitriadis as the residential life coordinator (RLC) for our group of south houses. I cannot begin to explain how unique this group of people and experience was. The training and real life experiences of dealing with a students' mental health, group conflicts within the house, conflicts between the house and

undergraduate student life administration, and the crazy, wacky, and sometimes fun things Caltech undergraduates think up and actually try to enact made for a rich three years outside of the lab. I will never forget learning how to ride a unicycle from some of the students, nightly house dinner, and the tour of the steam tunnels, which was one of the last before access was officially denied. Nicholas Scheifer, Adam Jermyn, Jomya Lei, and Raymond Jimenez are some of the smartest, kindest, and most mature undergraduates I know; without their support and trust Matt and I would have been lost.

The comradarie of the south house RA crew and the RA group and support staff was amazing. Many long nights were spent in one of the south house RA apartments blowing off steam from the stress of grad school and the RA position. Taso is an amazing individual with the biggest heart and most talent in dealing with humans that I know. His constant monitoring of our wellbeing and help with any situation and at any time was unbelieveable.

I lived with Matt Coggon for four of my five years at Caltech. We shared the rough first year of Chem E. together and then moved on to being RAs and balancing that with work and all of our outdoor pursuits. We had so many good adventures, from running in six inches of snow in the San Gabriels in the winter of 2012 to painting the mural in our RA apartment to kayaking the Kern river and so many more.

To the others in the Chem E. class of 2010, Ricardo, Marilena, Carissa, Cat, Charlie, Vanessa, Zach, and Wendy, you are all awesome! We will always be bonded by the winter break that was quals and the many nights spent trying to make sense of Einstein notation let alone any physical intuition about the fluid mechanics problem at hand. Ricardo and I spent a memorable weekend exploring the Kelso sand dunes, the densest Joshua Tree forest in the U.S., and the symmetry of Cima Dome in Mojave National Preserve. So many fun nights were had at GSC events and other get togethers, most involving sending Cat into some sort of tizzy.

Kathy Bubash, the Chem E. graduate student, was so supportive throughout my time at Caltech. From making sure all my academic requirements were met to organizing the monthly department dinners to all the support with my candidacy and thesis, thank you!

When I wasn't doing science or RAing at Caltech, I was most likely outdoors surfing, rock climbing, mountain biking, or running. My first two years at Caltech were spent mountain biking and running in the mountains above Pasadena and Altadena and surfing at lower Trestles and Ventura point. In my third year I was introduced to rock climbing by Lauren Montemayor and the Caltech Alpine Club and added that to the quiver of activities. So many memorable trips were had during the last five years. To list a few, I went surfing in Mexico with my dad and his friends at least once a year, climbing on what seemed like every weekend for a while in Joshua Tree (and eating at Pie for the People!) and Tahquitz with Cody Finke, climbing/mountaineering up 14,000 ft peaks in the Sierra also with Cody, climbing (more!) at an unforgettable place called the Needles with Hayden Miller, surfing in Indonesia with my best friend Andrew, sailing in the British Virgin Islands also with Andrew, climbing with Moriel and Pica (her dog) at the Needles, Red Rocks and beyond, and many, many more. To Cody, Nafeesa, Stefan, Moriel, Grant, Hayden, Lauren, Hamik, Florent, Batiste, Danica and many more I am sure I have missed, thank you for keeping the stoke high!

Of course none of this would have been possible without the unwavering support of my family. Mom, you are a wonderful, caring mom with such a big heart; your care packages always brought such a big smile to my face and stomach. Dad, your discipline combined with all the support and positivity one could ask for as well as grounding in real world practicality will always stay with me; all those days working in the yard as kids were worth it. Sam, though we may have fought as kids I cannot express how impressed I am at the person you have become and thank you enough for all the support you have given me throughout graduate school. You are almost certainly going to be more successful than I and I can only hope to support you on your way. Andrew, our family's figuratively adopted

fifth member, you are my best friend and always will be. We have had so many awesome adventures and you are so supportive of every part of my life. I wouldn't be the person I am today without our friendship. I love you all unconditionally!

Matt Shaner
Pasadena, CA
November, 2015

Abstract

Direct solar energy conversion is one of few sustainable energy resources able to wholly satisfy global energy demand; however, utility scale adoption and reliance are currently limited by the lack of a cost effective energy storage technology. The production of fuel from sunlight (solar fuels) enables solar energy storage in chemical bonds, a volumetrically and gravimetrically dense form compatible with current infrastructure worldwide. Hydrogen production via water splitting is a first generation solar fuel targeted herein that is currently used for hydrocarbon up-grading and fertilizer production and could further be utilized in combustion cycles and/or fuel cells for electricity and heat production and transportation.

This thesis presents achievements that form the foundation for Si microwire array based solar water splitting devices beginning with a tandem junction device design using Si microwire arrays as the architectural motif and one of many active components. Si microwire arrays have potential advantages over two dimensional planar device architectures such as minimized resistance losses, lower semiconductor material usage, and embedment in a polymeric membrane enabling a flexible device.

Experimental fabrication and characterization of this tandem junction device design was realized in the form of a np^{+}-Si microwire array coated by either tungsten oxide (WO_3) or titanium dioxide (TiO_2) as the second tandem semiconductor. The Si/TiO_2 device

demonstrated the highest performance with an expected solar-to-hydrogen efficiency of 0.39%. To achieve these demonstrations new processing methods were needed and developed for formation of the np^+-Si microwire array homojunction and formation of a low resistance contact between the p^+-Si and second semiconductor using sputtered tin-doped indium oxide (ITO) and spray pyrolyzed fluorine-doped tin oxide (FTO).

Another achievement includes demonstration of the longest known (>2200 hours) photoanode stability for water oxidation using a np^+-Si microwire array coated with an in-house developed amorphous TiO_2 protection layer and $NiCrO_x$ electrocatalyst. Additionally, the Si microwire array architecture was used to enable decoupling of semiconductor light absorption and catalytic activity, two performance metrics that ideally are maximized simultaneously. However, all previous demonstrations have shown anti-correlation between these performance metrics because planar architectures are subject to a trade-off where adding electrocatalyst increases catalytic activity, but decreases semiconductor light absorption and vice versa.

Finally, a techno-economic analysis of solar water splitting production facilities was performed to assess economic competitiveness because this is the ultimate metric by which all energy production technologies are currently evaluated. This analysis suggests that a hydrogen production facility that is cosmetically similar to current solar panel installations with hydrogen collection from distributed tilted panels is unlikely to achieve

cost competitiveness with fossil fuel derived hydrogen due to the balance of systems costs alone. A cost of CO_2 greater than ~\$800 (ton CO_2)$^{-1}$ was estimated to be necessary for the least expensive base-case solar-to-hydrogen system to reach price parity with hydrogen derived from steam reforming of methane priced at \$3 (MM BTU)$^{-1}$ (\$1.39 (kg H_2)$^{-1}$). Direct CO_2 reduction systems were also explored and resulted in even larger challenges than hydrogen production. Accordingly, major facility wide breakthroughs are required to obtain viable economic costs for solar hydrogen production, but the barriers to achieve cost-competitiveness with existing large-scale thermochemical processes for CO_2 reduction are even greater.

Table of Contents

A Detailed Fabrication Processes for Si Microwire Devices 203

A Detailed Fabrication Processes for Si Microwire Devices 203

A.1 Chapter 3: Si/WO_3 Tandem Device Methods 203

A.2 Chapter 4: Si/TiO_2 Tandem Device Methods 211

A.3 Chapter 5: Si Photoanodic Protection Methods 219

List of Figures

List of Tables

List of Publications

Coridan, R. H., Shaner, M., Wiggenhorn, C., Brunschwig, B. S., & Lewis, N. S. (2013). Electrical and Photoelectrochemical Properties of WO_3/Si Tandem Photoelectrodes. *Journal of Physical Chemistry C*, *117*(14), 6949–6957. http://doi.org/10.1021/jp311947x

Shaner, M. R., Fountaine, K. T., & Lewerenz, H.-J. (2013). Current-voltage characteristics of coupled photodiode-electrocatalyst devices. *Applied Physics Letters*, *103*(14), 143905. http://doi.org/10.1063/1.4822179

Lichterman, M. F., Shaner, M. R., Handler, S. G., Brunschwig, B. S., Gray, H. B., Lewis, N. S., & Spurgeon, J. M. (2013). Enhanced Stability and Activity for Water Oxidation in Alkaline Media with Bismuth Vanadate Photoelectrodes Modified with a Cobalt Oxide Catalytic Layer Produced by Atomic Layer Deposition. *The Journal of Physical Chemistry Letters*, *4*(23), 4188–4191. http://doi.org/10.1021/jz4022415

Shaner, M. R., Fountaine, K. T., Ardo, S., Coridan, R. H., Atwater, H. A., & Lewis, N. S. (2014). Photoelectrochemistry of core–shell tandem junction n–p^+-Si/n-WO_3 microwire array photoelectrodes. *Energy & Environmental Science*, *7*(2), 779. http://doi.org/10.1039/c3ee43048k

Hu, S., Shaner, M. R., Beardslee, J. A., Lichterman, M., Brunschwig, B. S., & Lewis, N. S. (2014). Amorphous TiO_2 coatings stabilize Si, GaAs, and GaP photoanodes for efficient

water oxidation, *Science*. 344(6187), 1005–1009. http://doi.org/10.1126/science.1251428

Shaner, M. R., Hu, S., Sun, K., & Lewis, N. S. (2014). Stabilization of Si microwire arrays for solar-driven H_2O oxidation to O_2(g) in 1.0 M KOH(aq) using conformal coatings of amorphous TiO_2. *Energy & Environmental Science*, 8(1), 203–207. http://doi.org/10.1039/C4EE03012E

Nielander, A. C.*, Shaner, M. R.*, Papadantonakis, K. M., Francis, S. A., & Lewis, N. S. (2014). A taxonomy for solar fuels generators. *Energy & Environmental Science*, *8*(1), 16–25. http://doi.org/10.1039/C4EE02251C

Walczak, K., Chen, Y., Karp, C., Beeman, J. W., Shaner, M., Spurgeon, J., et al. (2015). Modeling, Simulation, and Fabrication of a Fully Integrated, Acid-stable, Scalable Solar-Driven Water-Splitting System. *ChemSusChem*, *8*(3), 544–551. http://doi.org/10.1002/cssc.201402896

Ager, J. W., Shaner, M. R., Walczak, K. A., Sharp, I. D., & Ardo, S. (2015). Experimental demonstrations of spontaneous, solar-driven photoelectrochemical water splitting. *Energy & Environmental Science*, 8(10), 2811–2824. http://doi.org/10.1039/C5EE00457H

Sun, K., McDowell, M. T., Nielander, A. C., Hu, S., Shaner, M. R., Yang, F., et al. (2015). Stable Solar-Driven Water Oxidation to O_2(g) by Ni-Oxide-Coated Silicon Photoanodes.

The Journal of Physical Chemistry Letters, *6*(4), 592–598. http://doi.org/10.1021/jz5026195

Shaner, M. R., McKone, J. R., Gray, H. B., & Lewis, N. S. (2015). Functional integration of Ni-Mo electrocatalysts with Si microwire array photocathodes to simultaneously achieve high fill factors and light-limited photocurrent densities for solar-driven hydrogen evolution. *Energy & Environmental Science*, 8(10), 2977-2984. http://doi.org/10.1039/C5EE01076D

Shaner, M. R., McDowell, M. T., Pien, A., Atwater, H. A., & Lewis, N. S. (2016). Si/TiO_2 Tandem-Junction Microwire Arrays for Unassisted Solar-Driven Water Splitting. *Journal of the Electrochemical Society*, 163(5), H261–H264. http://doi.org/10.1149/2.0141605jes

Shaner, M. R., Atwater, H. A., Lewis, N. S., & McFarland, E. W. (2016). A comparative technoeconomic analysis of renewable hydrogen production using solar energy. *Energy & Environmental Science*, Advance Article. http://doi.org/10.1039/C5EE02573G

1 Introduction

1.1 The Energy Landscape

The energy derived from fossil fuels has enabled the remarkable advancement of civilization over the past century and a half. Consider our current ability to feed, house, transport, and maintain the health of 7+ billion people as compared to less than 1 billion prior to fossil fuel adoption. The fundamental characteristics that make fossil fuels unique are their abundance and relatively large energy surplus, measured as the quantity of energy extracted versus the quantity of energy used to perform the extraction.[1] However, fossil fuels are finite in supply and a source of increased atmospheric carbon dioxide and any associated effects, as well as geopolitically destabilizing.[2-4] It is unknown when one or a combination of these effects will become unacceptable in the form of climactic events and/or social and political conflict, but their finite nature ensures that it will in the absence of other options. Accordingly, alternate energy sources are desired, but to provide the same opportunity for a high quality of life that fossil fuels have facilitated they must possess similar abundance and energy surplus characteristics

Direct conversion of solar irradiation into electricity or chemical fuels is one of two technically proven alternative primary energy sources (the other being controlled nuclear fission) that has the abundance to meet worldwide energy demand for thousands of years to come (debates are ongoing for the potential of wind power).[5,6] However, the spatial and temporal (seasonal, diurnal, intra-day weather affects, etc.) intermittencies of terrestrial solar irradiation, in general, do not match the spatial and temporal energy demands of prosperous societies. Thus, a method for

storing solar energy in a way that allows for on-demand use would enable higher solar energy contributions to total energy consumption. Conversion of sunlight into chemical fuels (solar fuels) addresses this issue by storing the photon energy in chemical bonds that can be used for on-demand energy production identical to the way in which fossil fuels are used today. To serve as a viable alternative to fossil fuels, solar fuel technology development must focus on generating an energy surplus comparable to fossil fuels.

1.2 Fundamentals of Solar Fuels

1.2.1 Photoelectrochemistry

Photoelectrochemistry is the conversion of electromagnetic radiation into chemical bonds or stable excited states and forms the foundation for the solar fuel devices described herein. This thesis is focused on a subset of photelectrochemical devices, namely photoelectrosynthetic devices that perform nonspontaneous ($\Delta G_{rxn} > 0$) reactions effectively storing the energy contained within the incident electromagnetic radiation in the form of chemical bonds.[7] For example, Equation 1.1 shows the water splitting reaction, which has a ΔG^0 = 237 kJ (mol H_2)$^{-1}$ and E^0 = -1.23 V and is the reaction pursued throughout this thesis.

$$H_2O \rightarrow H_2 + \frac{1}{2}O_2 \qquad 1.1$$

A photoelectrosynthetic device consists of a semiconductor or set of semiconductors that generate excited electron-hole pairs via photon absorption and separate the excited electron-hole pairs such that the electrons and holes can be collected at separate locations. These photoexcited and separated electrons and holes are transferred to their respective

electrocatalysts that perform the desired reduction and oxidation reactions. Ionic transport between the reduction and oxidation sites completes the electrochemical circuit shown schematically in Figure 1.1.

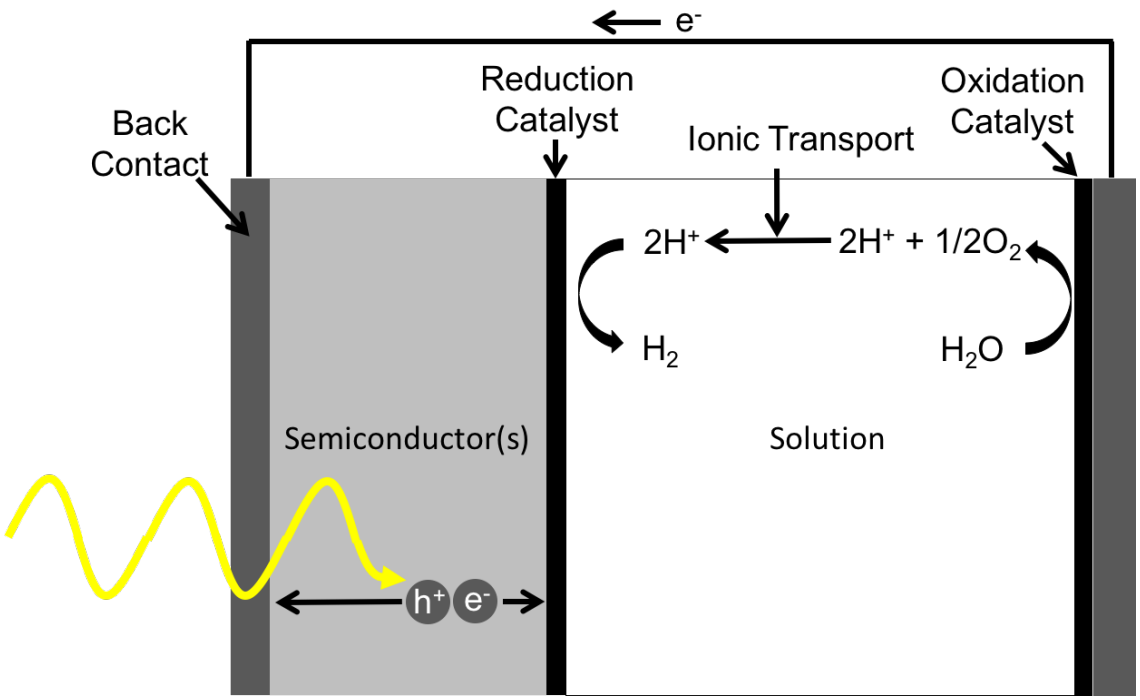

Figure 1.1: Photoelectrosynthetic device schematic A photoelectrosythetic device schematic shown performing the water splitting reaction. Each piece of this device is described in detail in the following sections.

1.2.2 Semiconductor Physics

A description of semiconductor physics relevant to this thesis is presented below. The reader is directed to more comprehensive texts for further specifics and information.[8-12]

The semiconductor component of a photoelectrosynthetic device is responsible for conversion of photons into electrical power. This occurs via generation of excess electron-hole pairs through

photon absorption, separation of the excess electron-hole pairs via an electrochemical potential gradient, and collection of the separated charge carriers at their respective contacts.

1.2.2.1 Generation

A semiconductor is defined as a material that has a conductivity between that of a conductor and an insulator. This property arises due to the presence of an energy bandwidth over which the density of electronic states is zero, known as a bandgap (Figure 1.2). The lower and higher energy bounds of the bandgap are known as the valence and conduction bands, respectively. Insulators also posses a bandgap, but differentiation arises from the size of the bandgap with insulators possessing larger bandgaps; the exact bandgap size at which the switch occurs is not rigorously defined.

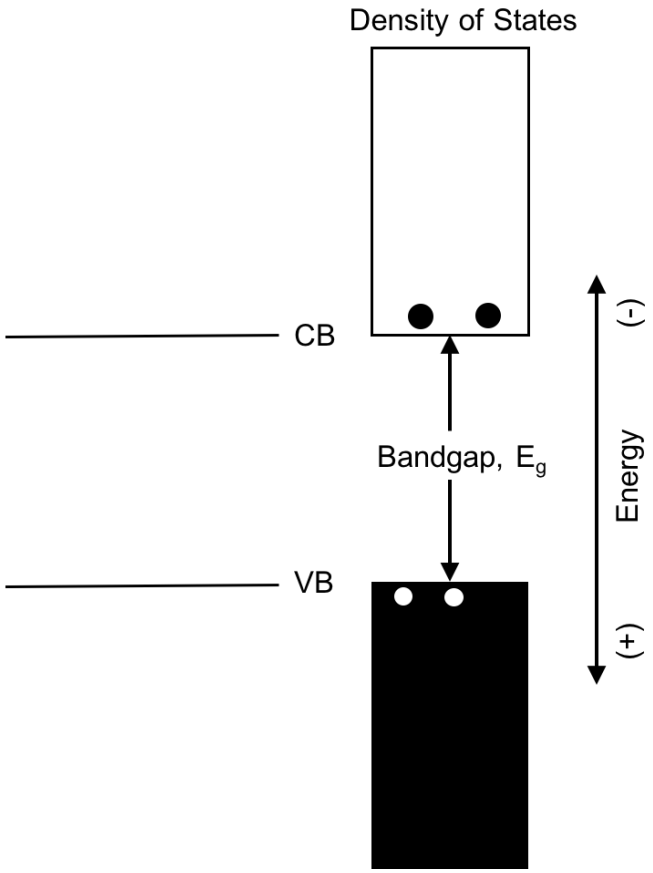

Figure 1.2: Semiconductor bandgap and density of states A simplified representation of a bandgap with the valence (VB) and conduction (CB) bands labeled and the density of states depicted on the right. E_g is the bandgap energy (eV). The valence band electronic states are almost completely filled with electrons (black fill) and relatively few holes (white circles) present due to thermal excitations. The conduction band electronic states are almost completely empty with relatively few electrons present due to thermal excitations.

Photons incident on a semiconductor that have an energy larger than the bandgap can result in absorption and consequent excitation of an electron from the valence band to the conduction band, leaving behind a hole (absence of an electron) in the valence band. This process is known as generation and creates excess electron-hole pairs (Figure 1.3). It is assumed that the excited electron and hole relax to the conduction and valence band edges immediately (thermalization) and thus any energy difference between the incident photon and bandgap is lost as heat.

Multiple semiconductor devices with differing bandgaps can be stacked on top of each other, forming a multi-junction device, where the bandgap of the devices decreases monotonically from the light incident side. In this way thermalization losses can be decreased because photons of higher energy are absorbed in semiconductors of larger bandgap (Figure 1.3b).

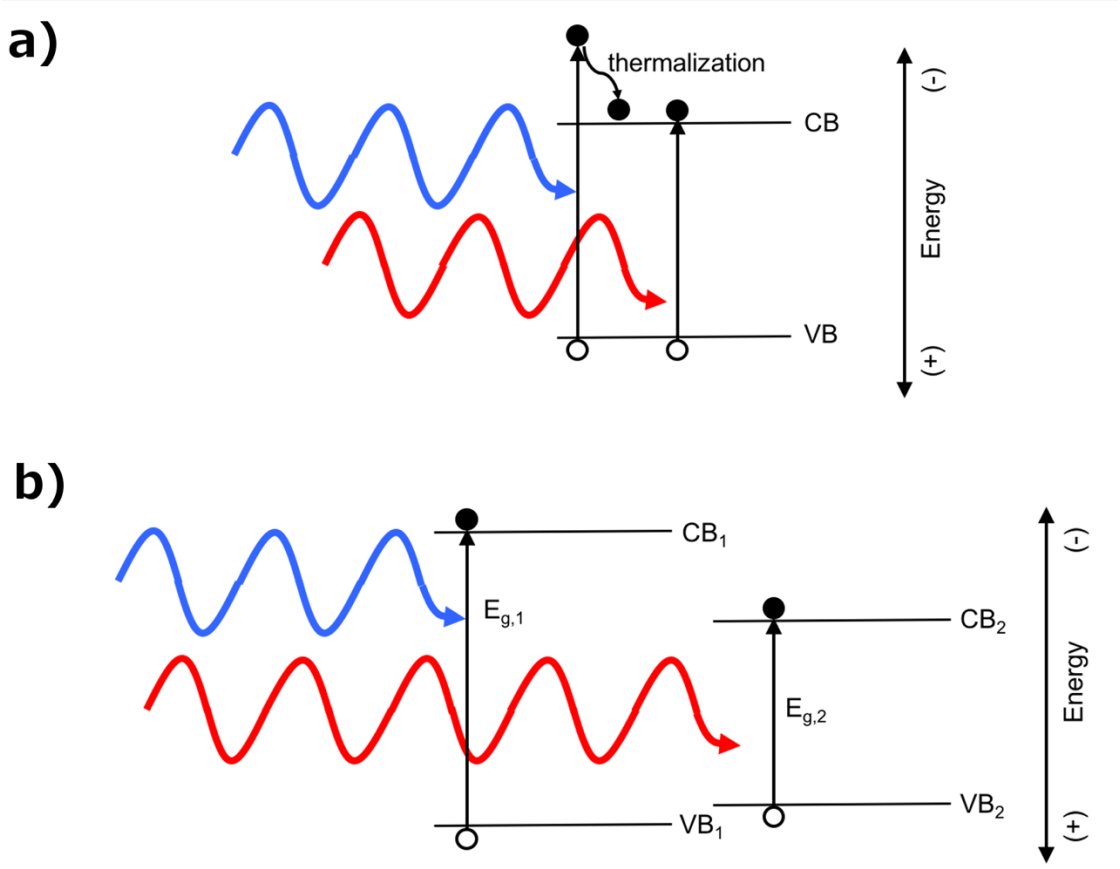

Figure 1.3: Multijunction concept a) A simplified representation of a bandgap with the valence (VB) and conduction (CB) bands labeled. The thermazliation process is demonstrated where two photons of differing energy create electron-hole pairs with the higher energy photons (blue) excited electron losing its excess energy as heat and relaxing to the conduction band minimum energy. b) A schematic demonstrating the multijunction concept where photons of differing energy are absorbed by semiconductors with different bandgap energies, E_g, such that thermalization losses are reduced.

1.2.2.2 Separation and Collection

To perform useful work these photoexcited, or excess, carriers must be collected at separate locations and electrochemical potentials. The rate at which the carriers are collected is proportional to the current, the potential difference between the collected carriers is the voltage, and the product of the two is the power (P = IV). An electrochemical potential gradient is required to effect carrier separation and is achieved through the presence of a junction and an excess carrier concentration from photon absorption.

A junction is formed by joining two materials of differing chemical potential and can be the same material with different levels and/or types of doping (homo-junction) or two different materials (hetero-junction). Here at least one material must be a semiconductor and the other can be a semiconductor, metal, or liquid with a redox potential (Figure 1.4a,b). The chemical potential of a pure and chemically pristine semiconductor at equilibrium (T > 0 K) lies within the bandgap, defines the concentration of electrons and holes in the conduction and valence bands, respectively, and can be altered by the presence of intrinsic or extrinsic (doping) defects. These defects result in either (i) the addition of electrons to the conduction band and simultaneous reduction of holes in the valence band (law of mass action), forming an n-type semiconductor, or (ii) the addition of holes to the valence band and simultaneous reduction of electrons in the conduction band forming a p-type semiconductor.

Equilibrium across this junction is represented by an equal electrochemical potential (aka Fermi level) everywhere (Figure 1.4a,b). The initial difference in chemical potential between the two

junction forming materials is exactly offset by formation of an electric field near the junction that has an equal and opposite electric potential. The electric field is formed by transfer of electrons from the material of higher chemical potential to the material of lower chemical potential leaving behind fixed positive charges in the material of higher chemical potential and forming fixed negative charges in the material of lower chemical potential. The ratio of potential drop in each material is related to the ratio of capacitances; the lower capacitance material, almost always the photoactive semiconductor, assumes the majority of the potential drop.

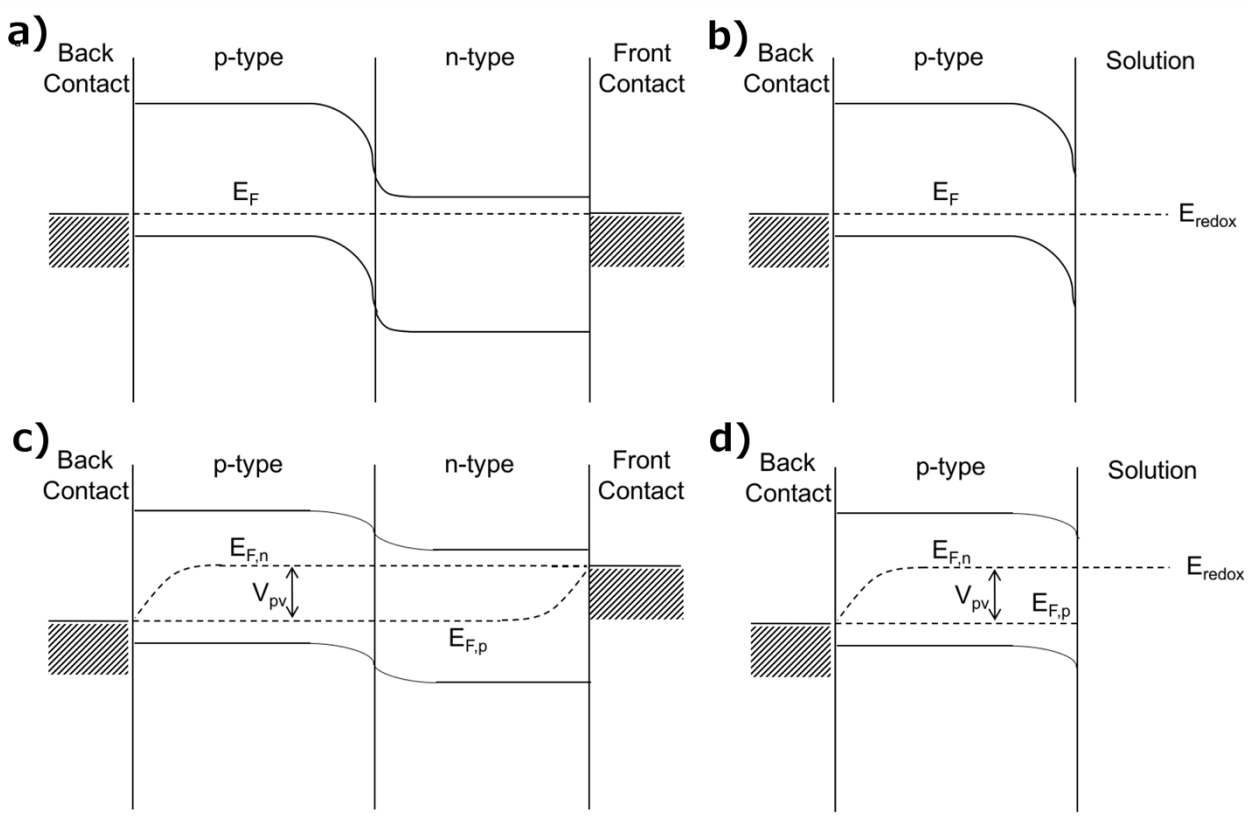

Figure 1.4: Semiconductor junction energetics a) A solid state semiconductor pn-junction at equilibrium. The electrochemical potential (E_F, Fermi level) is equal everywhere throughout the device. b) A semiconductor liquid junction at equilibrium where the semiconductor electrochemical potential is equal to the redox potential in solution. c) A solid state semiconductor pn-junction under illumination conditions where $E_{F,n}$ and $E_{F,p}$ represent the

electron and hole electrochemical potentials separately (quasi-Fermi levels). The potential difference between the two contacts determines the operating voltage. d) A semiconductor liquid junction under illumination where the electron quasi-Fermi level is level with the solution redox potential, assuming no electrocatalytic overpotential.

An excess carrier concentration perturbs the equilibrium electrochemical potential creating two separate electrochemical potentials (quasi-Fermi levels), one for electrons and one for holes (Figure 1.4c,d). This change in electrochemical potential is entirely due to a decrease in the initial chemical potential difference, prior to any carrier separation, because the excess electron-hole pairs formed act to overwhelm the equilibrium concentrations. In the limit of very high generation rates, known as high level injection, the concentrations of electrons and holes, and thus their respective chemical potentials, are identical everywhere assuming uniform generation rates. However, the electric potential remains constant and thus an electrochemical gradient is formed.

Given a constant photon flux, a steady-state concentration of excess electrons and holes is present such that the sum of the current collected due to the electrochemical potential gradient and current lost to recombination equals the absorbed photon flux (Figure 1.4c,d). A voltage can be applied across the device that affects the portion of successful carrier separation and collection (current) and deleterious recombination. This is a non-linear process described by the diode equation (Equation 1.2) with limiting cases for power production under illumination represented by the open circuit voltage (V_{oc}) where no current flows and the short circuit current density (J_{sc}) where no potential difference exists between the two contacts (Figure 1.5). Here *J* is the current density, j_{ph} is the light limited current density, j_0 is the exchange current density, q

is the charge of an electron, *V* is the voltage, n_d is the diode quality factor, k is the Boltzmann constant, and T is the temperature. The maximum efficiency the device can operate at is defined in Equation 1.3, where the denominator, 1000 W m^{-2}, is the standardized power input and the fill factor (FF) accounts for the ratio between the operating current density and voltage, and J_{sc} and V_{oc}.

$$J = j_{ph} - j_0\left(e^{-\frac{qV}{n_d kT}} - 1\right) \quad 1.2$$

$$\eta_{PV} = \frac{V_{oc}\, J_{sc}\, FF}{1000\,\frac{W}{m^2}} \quad 1.3$$

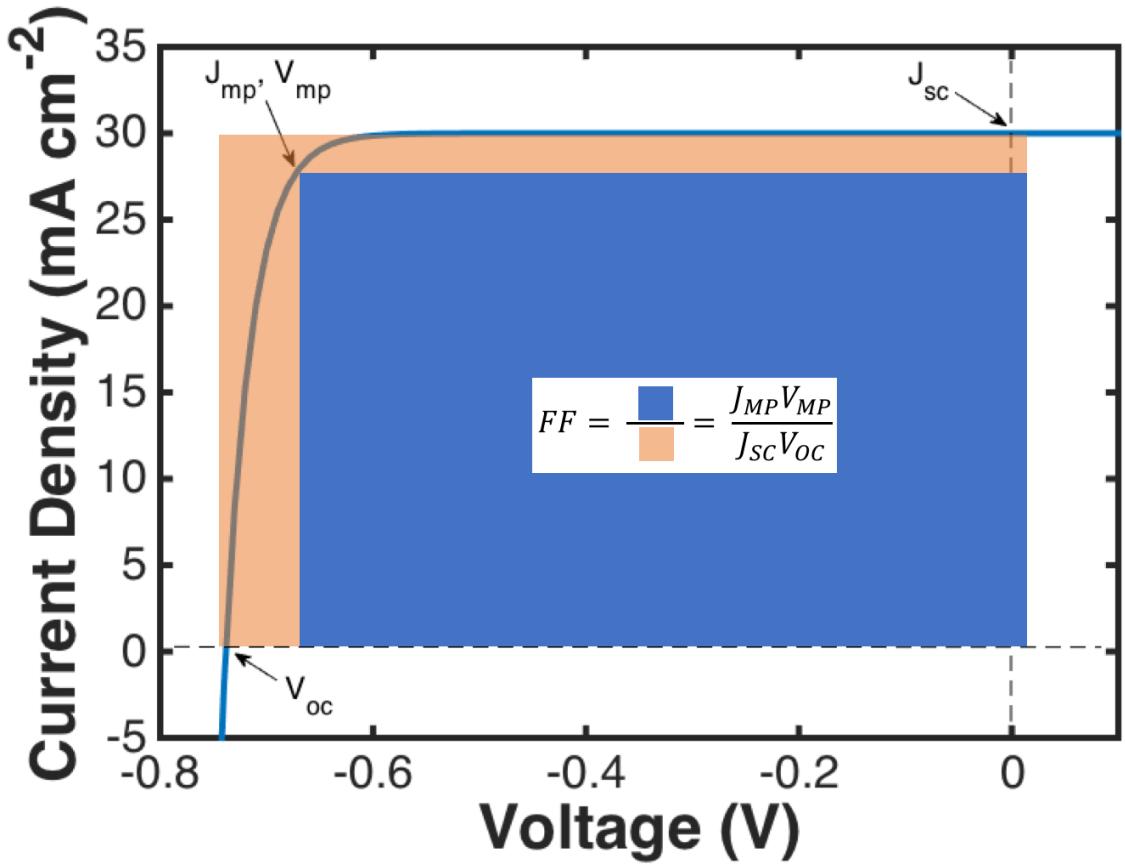

Figure 1.5: Illuminated semiconductor diode behavior Current density versus voltage behavior for a semiconductor diode under illumination as described by the diode equation (Equation 1.2)

with j_{ph} = 30 mA cm^{-2}, $j_0 = 10^{-11}$ mA cm^{-2} and n_d = 1. The V_{oc}, J_{sc} and FF are identified where the FF is the ratio of the areas of the two rectangles or the ratio between the product of the maximum power point current density (J_{MP}) and voltage (V_{MP}) and J_{SC} and V_{OC}.*Applications to Solar Fuels and Thermodynamic Limits*

The operating current and voltage of a photovoltaic device can be chosen at will over the entire devices current-voltage behavior. However, solar fuel device operation is fundamentally different, as the operating voltage is determined by the reaction thermodynamics and the extra voltage needed to drive the reaction at a given rate (overpotential). Thus the goal for solar fuel devices is to produce the maximum current density (J_{op}) possible given the reaction thermodynamics and overpotentials, as evidenced by the Equation 1.4, which defines the efficiency for a photoelectrosynthetic device performing the water splitting reaction.

$$\eta = \frac{(1.23\ V)\ J_{op}}{1000\ \frac{W}{m^2}} \qquad 1.4$$

Chemical biases in the form of operating partial pressure can be used to adjust the operating point, but the range over which the operating point can be modulated is limited. For example, using Equation 1.5 the thermodynamic potential required for water splitting can range from 1.23 V for 1 atm of H_2(g) and O_2(g) to 1.36 V for 10^3 atm of H_2(g) and O_2(g), assuming ideal behavior and no change in proton/hydroxide concentration between either reaction site. Here, E^0_{rxn} is the reaction standard potential, $a_{H_2}^{\upsilon_{H_2}}$ and $a_{O_2}^{\upsilon_{O_2}}$ are the hydrogen and oxygen activity coefficients, respectively, raised to the power of their respective stoichiometric coefficient, n is the number of electrons passed during the reaction, F is Faraday's constant, R is the gas constant, T is the temperature, and P is the pressure.

$$E_{total} = E^0_{rxn} + \frac{RT}{nF}\ln\left(a_{H_2}^{\upsilon_{H_2}} a_{O_2}^{\upsilon_{O_2}}\right) = E^0_{rxn} + \frac{RT}{nF}\ln\left(P_{H_2} P_{O_2}^{0.5}\right) \qquad 1.5$$

The thermodynamic limit and experimentally realized V_{oc} for a semiconductor junction is between 300-400 mV and 400-500 mV, respectively, less than the bandgap and results from entropy increase upon absorption of essentially point source photons from the sun and radiative emission of photons over all angles.[13] This upper bound on V_{oc} for a single semiconductor junction, the voltage requirements for the reaction of choice (water splitting, 1.23 V) and the solar spectrum together define the optimum number of semiconductor junctions and their bandgaps.

For a single semiconductor junction (single junction) device the bandgap must be >2.1 eV when accounting for realistic overpotentials. The thermodynamic efficiency limits for a single junction device are thus 17.4% and 30.7% (430 mV at the operating current density) with and without accounting for overpotentials, respectively. These values are low because of the high bandgap required and thus the inability to utilize a majority of the solar spectrum.[14]

Multi-junction devices, arranged electrically in series to produce higher voltages, have higher thermodynamic efficiency limits due to better utilization of the solar spectrum and voltage matching with the water splitting voltage requirements. Tandem junction devices split the voltage production requirement between two junctions with optimized bandgaps of ~1.1 eV and ~1.7 eV for water splitting given realistic assumptions on the overpotential needed. The thermodynamic efficiency limits for a tandem junction device are thus 24% and 43% with (430 mV at the operating current density) and without accounting for overpotentials, respectively.[15]

Triple and higher number junction devices utilize the solar spectrum better for each additional junction, but their thermodynamic efficiency limit for water splitting is lower than for tandem junction devices because the J_{sc} decreases at the expense of an increased V_{oc}, which is not needed. Accordingly, tandem junction devices posses the highest thermodynamic efficiency limit for solar water splitting and is evidenced by their world record efficiencies in experimental devices.[16,17] Note that this argument only holds for integrated photoelectrosynthetic devices; the thermodynamic efficiency limit does continue to increase with junction number for a system that consists of discrete photovoltaic and electrolysis devices separated by power electronics to optimize the operation of both devices independently.

1.2.3 Catalysis

A description of heterogeneous catalysis relevant to this thesis is presented below. The reader is directed to more comprehensive texts for further specifics and information.[18]

Catalysts are used to increase the power conversion efficiency of photoelectrosynthetic devices by decreasing the activation energy for a given reaction pathway. At equilibrium, a catalyst produces no net reaction but performs both the forward and reverse reactions at equal rates, known as the exchange current density ($j_{0,cat}$). In general, the higher the $j_{0,cat}$ the higher performance (activity) the catalyst will demonstrate. Under applied bias (voltage) one reaction direction proceeds at a higher rate the the other direction and thus net product is formed. This behavior is non-linear with respect to voltage and can be described by the Butler-Volmer

equation for a one electron process, Equation 1.6. Here α is the charge transfer coefficient with subscripts A for anodic and C for cathodic reactions, $j_{0,cat}$ is the catalyst exchange current density, n_e is the number of electrons transferred to produce one molecule of product, j is the current density (negative (positive) for a cathode (anode)), and η is the overpotential define as η ≡ V – E^0_{rxn}.

$$J = j_{0,cat}\left(e^{\frac{\alpha_A n_e F \eta}{RT}} - e^{-\frac{\alpha_C n_e F \eta}{RT}}\right) \quad 1.6$$

The overpotential is a measure of the catalyst efficiency for a given current density; the lower the overpotential the less excess voltage that the semiconductor needs to supply. In general, the catalyst material is different than but in electrical contact with the semiconductor device component.

Water splitting consists of two half reactions: the hydrogen evolution reaction (Equation 1.7) and oxygen evolution reaction (Equation 1.8). State-of-the-art catalysts for the hydrogen and oxygen evolution reactions have overpotentials of 40 mV (platinum) and 340 mV (iridium oxide in 1.0 M H_2SO_4 and NiMoFe in 1.0 M KOH), respectively, at 10 mA cm^{-2}, which is near the current density expected for devices limited by the solar photon flux.[19]

$$2H^+ + 2e^- \rightarrow H_2 \quad 1.7$$

$$H_2O \rightarrow \frac{1}{2}O_2 + 2H_2 + 2e^- \quad 1.8$$

1.2.4 Ionic Transport

Ion transport is the current carrying component in liquid systems as electrons are in solids. For water splitting in acidic media, protons are made during oxygen evolution and must be

transported to hydrogen evolution sites for reduction to hydrogen; in basic media hydroxide ions formed during hydrogen evolution must be transported to oxygen evolution sites.

At steady-state the transference number (the ratio of current carried by protons and hydroxide ions to total current) is by definition unity. Thus, as the proton or hydroxide ion concentration decreases the excess voltage required to support the same ionic transport rate (current) will increase due to solution resistance. Putting an upper limit on the acceptable voltage loss due to solution transport of 100 mV at 10 mA cm^{-2} dictates that the solution pH must be greater than 13 or less than 1.[20]

A common method of increasing the solution conductivity is by adding a supporting electrolyte. However, during initial, unsteady state operation the transference number of protons and hydroxide ions is not unity. Instead current is also carried by the supporting electrolyte ions, which leads to electrodialysis of the supporting electrolyte and a proton or hydroxide ion concentration gradient creating large internal solution resistances.[20,21] Nature has this same problem, but is able to use the potential created by the concentration gradients to perform useful functions in the dark; no such analog has been developed for solar fuel devices.

Solution agitation and turbulence can suppress some of the electrodialysis related resistances, but a boundary layer exists at each electrode that will still contain these concentration gradients. At solar flux current densities these potential losses do not allow extension of the pH operating range given above.[20]

1.2.5 Product Separation

Maintaining separation of oxygen and hydrogen is both a safety and overall plant efficiency concern. Explosive mixtures of hydrogen and oxygen span the range of 4% v/v H_2 in O_2 to 5% v/v O_2 in H_2 and are not welcomed by industry. Additionally, crossover of H_2 or O_2 can lead to losses in efficiency due to H_2 oxidation back to protons and O_2 reduction back to water (in acid) and the need for downstream separation units that require additional energy to operate.

To achieve sufficient H_2 and O_2 separation an ionically conductive, yet low gas permeability membrane, is needed.[20,22] The permeability required is a function of the partial pressure difference for each gas, the residence time of each gas in its headspace, and the gas production rate. Calculations have shown that, for a current density of 10 mA cm^{-2} and H_2 and O_2 partial pressures of 1 atm on either side of a membrane, decreasing the membrane gas permeability of current state-of-the-art proton exchange membranes (PEM), Nafion®, has diminishing returns as measured by the hydrogen collection efficiency; this suggests a 10x reduction in gas permeability relative to Nafion® is ideal.[22] Ionically conductive polymeric membranes, such as Nafion®, are the preferred materials that meet these requirements as evidenced by their use in commercial electrolysis and fuel cell devices. Nafion® is a proton exchange membrane (PEM) that finds heavy commercially use in PEM electrolysis and fuel cell devices, but is only applicable to acidic systems; systems in basic media require anion exchange membranes (AEM) which are produced at a smaller scale or are still under fundamental research as they generally lack the suite of ionic

conductivity, stability, mechanical processability, and low gas permeability that makes Nafion® successful.

1.2.6 Stability

Operational stability of all components is critical for any commercial product, especially one that is expected to perform for 20+ years. This requires merging stability requirements of electrolysis units which operate under oxidizing and reducing conditions with photovoltaics which are sealed from the atmosphere to remove oxygen and water contact.

1.2.7 Complete Photoelectrode Behavior

A photoelectrochemical device is a combination of all the individual phenomena described above, which can be difficult to separate and understand in a full device or single photoelectrode experiment. A mathematical description of a photoelectrode and its components can compliment such experiments by providing insight into the contribution of individual phenomena to the overall device performance and identification of the performance, limiting phenomena and ultimately predictive capabilities that can guide future experiments.

An analytical expression that describes the behavior of a photoelectrode containing a single junction semiconductor device coupled directly to an electrocatalyst can be obtained by combining the analytical expressions in Equations 1.2 and 1.6 that describe the semiconductor and electrocatalytic device components, respectively.[23] A series resistance is added to account for interfacial, material and solution resistances present in any photoelectrosynthetic device.[23]

The series connected nature of a photoelectrochemical devices electrochemical circuit (Figure 1.6a) indicates that the system voltage is a linear combination of the voltage generated by the semiconductor device, $V_{PV}(j)$, that used by the electrocatalyst, $\eta(j)$, and that used to overcome system series resistances, $V_{series}(j)$, as shown in Equation 1.9.

$$V(j) = V_{PV}(j) - \eta(j) - V_{series}(j) \qquad 1.9$$

Solving Equations 1.2 and 1.6 for voltage as a function of current density (j) for two sets of assumptions for the catalyst behavior and plugging them into Equation 1.9 results in Equations 1.10 and 1.11, which are in the form of a three-electrode-power-saved-relative-to-an-ideally-non-polarizable-dark-electrode measurement.[23,24]

$$V(j) = \pm\frac{n_d kT}{q}\ln\left(\pm\frac{j_L - j}{j_{0,PV}} + 1\right) + \frac{RT}{\alpha n_e F}\sinh^{-1}\left(\frac{j}{2j_{0,cat}}\right) + jR_s \qquad 1.10$$

$$V(j) = \pm\frac{n_d kT}{q}\ln\left(\pm\frac{j_L - j}{j_{0,PV}} + 1\right) - \frac{RT}{\alpha_C n_e F}\ln\left(-\frac{j}{j_{0,cat}}\right) + jR_s \qquad 1.11$$

Here $j_{0,PV}$ denotes the semiconductor device dark current density, j_L is the light-induced current (negative (positive) for a photocathode (photoanode)), n_d is the diode quality factor, α is the charge transfer coefficient with subscripts A for anodic and C for cathodic reactions, $j_{0,cat}$ is the catalyst exchange current density, n_e is the number of electrons transferred, j is the current density (negative (positive) for a cathode (anode)), and R_s is the total area-normalized series resistance. The Butler-Volmer equation (Equation 1.6) was solved for voltage assuming either equal charge transfer coefficients ($\alpha_A = \alpha_C = \alpha$), Equation 1.10, or Tafel behavior (reverse reaction rate is negligible as compared to the forward reaction rate), Equation 1.11. Figure 1.6b shows the normalized behavior for a stand-alone photovoltaic device (Equation 1.2) and the

photoelectrode device (Equation 1.10), demonstrating the affect of solution resistance and catalytic overpotential on the device performance as compared to a photovoltaic. Figure 1.6c demonstrates the analytical solution's (Equation 1.10) ability to reproduce the behavior of a high efficiency experimental photoelectrode.

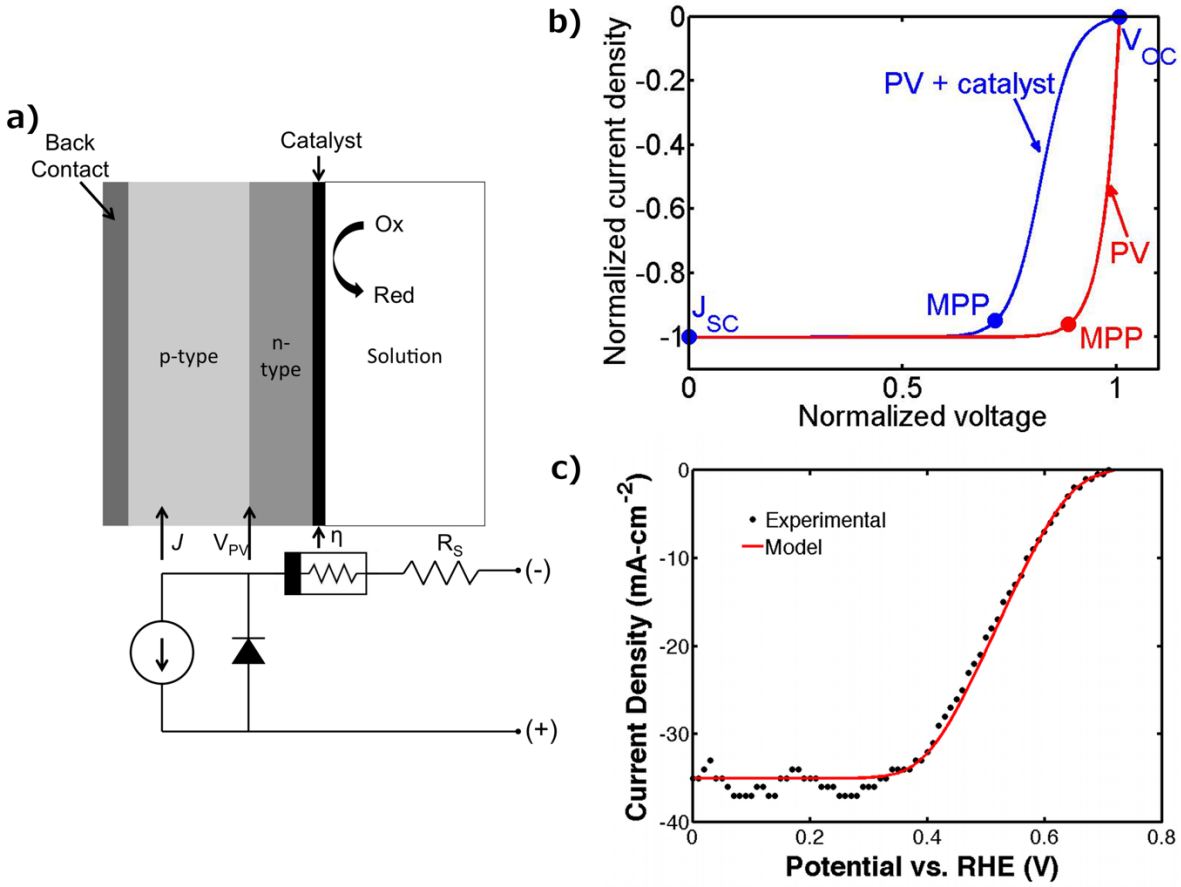

Figure 1.6: Analytically modeled photoelectrode behavior a) A general schematic and equivalent circuit diagram depicting the photoelectrode, electrocatalyst, and solution resistance components of the power saved measurement relative to an ideally non-polarizable dark electrode. b) Modeled normalized current density versus normalized voltage behavior of an isolated single junction semiconductor device and coupled semiconductor-electrocatalyst device. Equation 1.10 was used for the coupled device behavior, with j_L = 35 mA cm^{-2}, $j_{0,PV}$ = 5 x 10^{-11} mA cm^{-2}, $j_{0,cat}$ = 0.25 mA cm^{-2}, n_e = 2, n_d = 1, α = 0.5 and R_s = 0 Ω-cm^2. c) Experimental and modeled current density versus voltage behavior of hybrid InP/InO$_x$/Rh semiconductor-electrocatalyst

device. Note that the photocurrent variations of the half cell result from hydrogen evolution. Equation 1.10 was used to model the coupled device with j_L = 35 mA cm^{-2}, $j_{0,PV}$ = 3 x 10^{-11} mA cm^{-2}, $j_{0,cat}$ = 0.25 mA cm^{-2}, n_e = 2, n_d = 1 and α = 0.5. R_s was floated to find the best fit, which resulted in R_s = 0 Ω-cm^2.

1.3 Solar Fuels History

Solar fuels in their current form for the context of this thesis were first reported in 1972 and involved solar water splitting on a titanium dioxide (TiO_2) single crystal.[25] The concept consisted of a single junction semiconducting solid material that absorbed incident sunlight, converted the absorbed photons into excited charges, and collected these excited charges and used them to convert a reactant (water) into products (hydrogen and oxygen) that could be used as an energy storage mechanism for solar energy.

The past 43 years have seen a variety of different materials and approaches taken for solar fuels formation with the majority of work focusing on water splitting to form hydrogen and oxygen. Semiconductor and electrochemical engineering calculations were performed not long after the initial 1972 report to determine the theoretical and practical system configurations and efficiency limits.[14] These calculations have been revisited recently, although the conclusions remain identical to those published earlier and have been described above.[15]

Developing experimental devices that approach the maximum achievable efficiencies has proven challenging. Devices possessing two solid state junctions, identical to photovoltaic cells, have

record efficiencies of 18%, while systems with at least one solid-liquid junction have a record efficiency of 12.4%.[16,26] Stability and discovering a material with the proper wide bandgap for the tandem configuration were recognized in 1975 as the main challenges. Despite continued investigation these two issues remain as the fields major challenges.[27] Until the early 2000's many of the device reports focused on achieving ever higher efficiencies; however, a recent shift has occurred to lower efficiency materials with more potential for long term operational stability.[28-31] The reader is directed to a recent publication for a more detailed history of solar fuels.[32]

1.4 Scientific Gap

The majority of research performed on solar fuel devices has focused on a single semiconductor and catalyst combination for either the reduction or oxidation reaction to maintain experimental simplicity and analytic tractability. Accordingly, relatively few studies have investigated multijunction photoelectrodes and of those that have all have been planar architectures and nearly all have utilized semiconductor devices designed for the photovoltaic industry (tandem junction $Si/Al_{0.15}Ga_{0.85}As$[16], $GaAs/GaAsP_2$[33], $Ga_{0.35}In_{0.65}P/Ga_{0.83}In_{0.17}As$[34]; triple junction a-Si[33,35,36]). One noteworthy exception is a tandem junction $GaAs/GaAsP_2$ planar device that consisted of a GaAs homojunction and a $GaAsP_2$/liquid junction and holds the record solar water splitting efficiency for a device with at least one liquid junction at 12.4%.[26] However, this device was unstable for less than 24 hours of continuous operation due to photocorrosion of the $GaAsP_2$ semiconductor.

Consequently, a gap exists for exploring tandem junction devices designed specificially for the solar water splitting application and that incorporate the efficiency, stability and safety metrics needed to attract commercial interest. Further, non-planar tandem junction architectures did not exist prior to this thesis and possess possible technical and economic advantages over planar designs.

In addition, critical economic analyses of technically proven, yet economically unattractive solar fuel technologies are deficient. Such analyses can and should guide resource allocation and research milestones toward development of commercially attractive solar fuel generators.

1.5 Thesis Statement

Inline with the knowledge gaps mentioned above, I hypothesize that *a three dimensionally structured (silicon microwire array) tandem junction device, with the necessary catalyst and stabilization layers, can provide an optimized design and operate efficiently and be integrated into a system that can produce a solar fuel (hydrogen) safely, stably and at an economically competitive value.* Accordingly, this thesis focuses on the design of and experimental fabrication and characterization efforts toward a complete Si microwire array tandem junction device, experimental optimization efforts that leverage the Si microwire array architecture and focus on a subset of the phenomena present in a complete photoelectrosynthetic device, and a techno-economic analysis of solar water splitting technologies aimed at understanding the current landscape and progress required to achieve economic competitiveness.

2 Si Microwire Device Design and Fabrication

2.1 Si Microwire Background

Si microwire arrays have been studied for photovoltaic and photoelectrochemical applications due to their potential advantages over the planar designs that dominate these fields.[37-41] The Si microwire architecture effects orthogonalization of the light absorption and minority carrier collection directions, enabling lower material usage due to the architecturally enhanced light absorption[39,42], lower purity material requirements due to the short minority carrier collection lengths[43], minimized distance for ionic transport between the reduction and oxidation sites[41,44], and robustness against single Si microwire point failure due to the parallel nature of each individual microwire device, all as compared to planar designs.[17,31,43,45-47] Figure 2.1 schematically demonstrates orthogonalization of the light absorption and minority carrier collection directions where light is absorbed along the length of a microwire, identical to planar designs, while minority carriers are collected over the much shorter radial dimension.

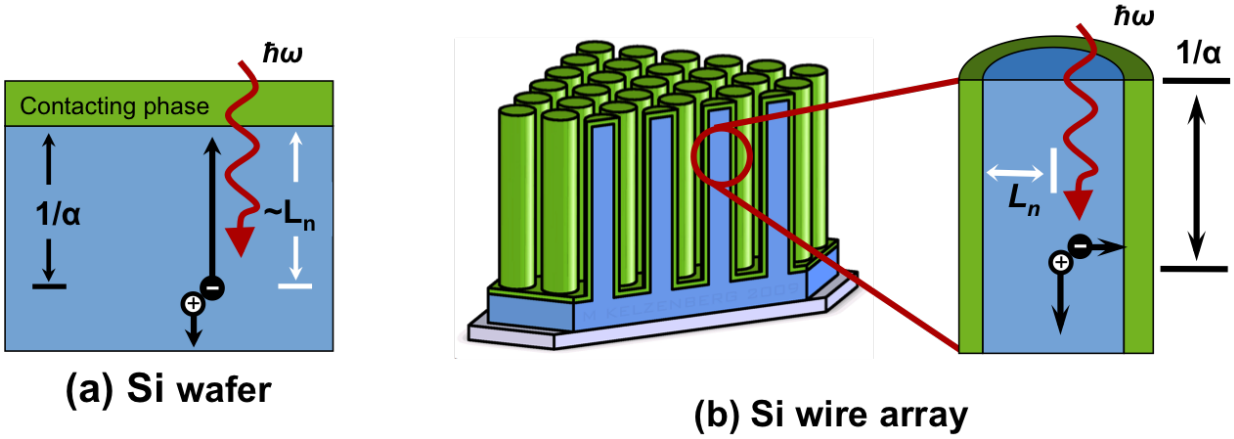

Figure 2.1: Si microwire array orthogonalization concept A schematic depicting the concept of directional orthogonalization of light absorption and minority carrier collection. a) An image

demonstrating the identical directionality of light absorption and minority carrier collection for a traditional planar device. This dictates that to collect minority carriers efficiently the absorption length (α is the absorption coefficient [1/length]) for a given photon energy ($\hbar\omega$) must be shorter than the minority carrier diffusion length (L_n). b) An image demonstration the orthogonal directionality of light absorption and minority carrier collection for a microwire device. Here the absorption direction remains along the vertical direction of the microwire, but the minority carrier collection direction is radial. This decoupling allows optimization of the length for absorption and minority carrier collection independently. (Image Credit: Michael Kelzenberg)

Photovoltaic demonstrations using Si microwire arrays have consisted of single pn^+-junction devices with champion array and single microwire efficiencies of 7.9% and 17%, respectively. [40,48] Near complete above bandgap light absorption has been achieved through introduction of scattering elements into the unoccupied space within the microwire array, thus leaving material, junction, and surface quality as the main factors that will affect performance.[39] Photoelectrochemical applications using Si microwire arrays have focused on the hydrogen evolution half reaction with single pn^+-junction devices coated with an electrocatalyst such as Pt. [37,49,50] Attempts to incorporate a second, wider bandgap material into Si microwire arrays to form a tandem junction structure have been challenging due to the complex nature of the exposed Si crystal facets on which a material must be grown and the choice of wide bandgap material (GaP, GaInP) which all require high quality epitaxial growth on the complex and non-traditional Si crystal faces present on the microwire sidewalls. [51-53] Additionally, these materials are unstable under oxidizing and/or reducing conditions at the pH values required for efficient operation.

2.2 Tandem Junction Si Microwire Design for Solar Water Splitting

Accordingly, an alternative design architecture for tandem Si microwire array devices was developed to allow incorporation of a wider variety of wide bandgap materials, some of which possess intrinsic stability under reducing or oxidizing conditions.[31] Figure 2.2a shows this core-shell design on the scale of a microwire array and Figure #b shows an individual microwire two-dimensional unit cell of the design. Each Si microwire is a complete device that consists of a np^+-Si homo-junction, conformally coated with a bilayer consisting of a transparent conductive oxide (TCO) to provide low resistance contact between the semiconductor devices and an n-type wide bandgap semiconductor that forms a semiconductor-liquid junction with solution (Figure 2.2b). Electrocatalysts, if necessary, are present at both the oxidation and reduction sites as dictated by the device polarity. A polymeric, gas impermeable, ionically conductive membrane lies between the individual microwires, providing mechanical support for the array. The np^+-Si homo-junction is of opposite polarity to the existing work on Si microwire array photovoltaics and photoelectrodes and thus required development of new fabrication procedures and subsequent characterization. The TCO layer is present to provide, in addition to a low contact resistance, a protection mechanism for the underlying Si homo-junction, which will oxidize in the presence of water and a robust layer upon which many of the currently studied metal oxide wide bandgap semiconductors can be deposited on without changing the underlying device.

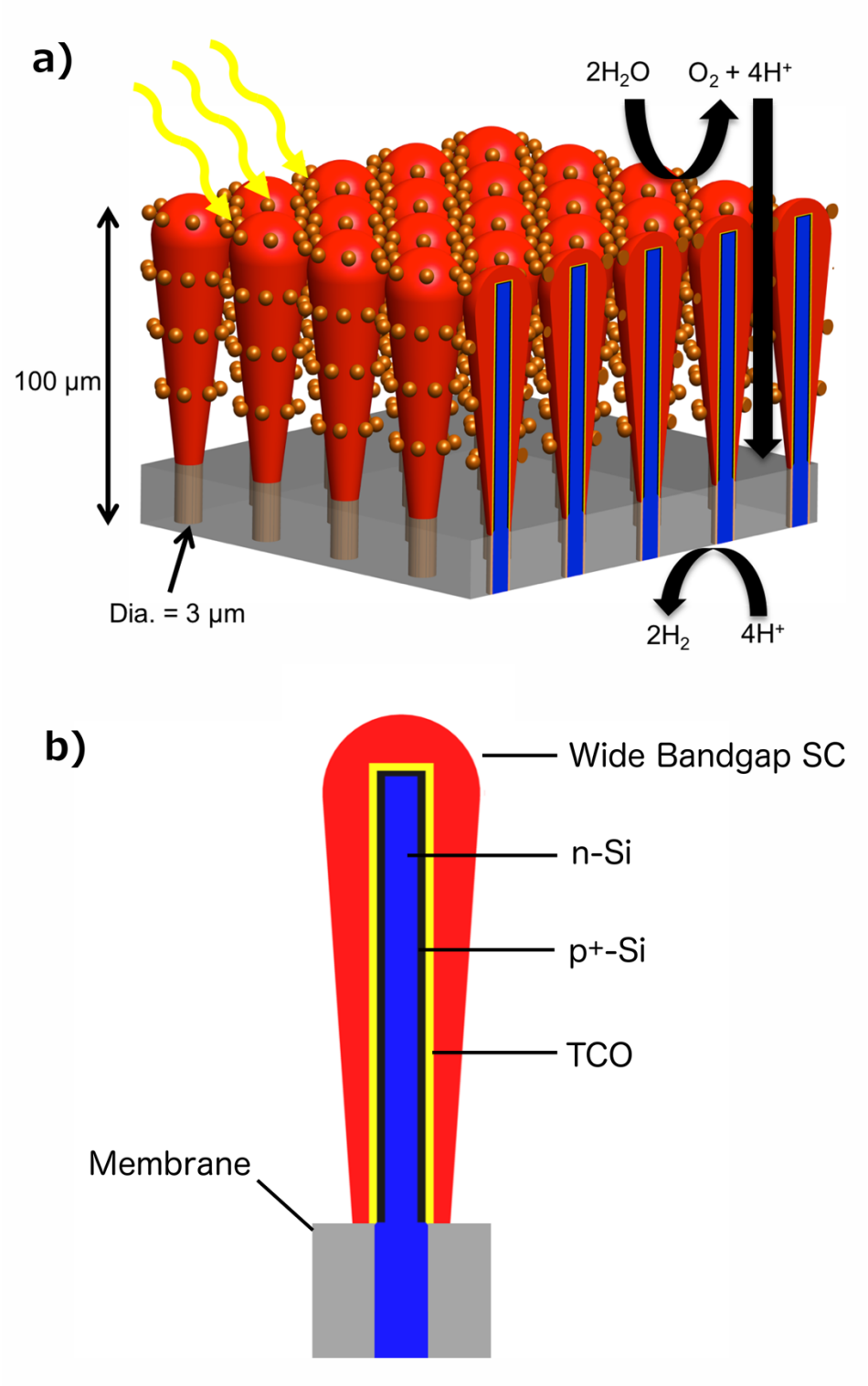

Figure 2.2: Tandem junction Si microwire array design a) A schematic of the tandem junction microwire array device with the dimensions, site of both water splitting half reactions, and ionic transport pathway indicated. Oxygen evolution catalysts are decorated on the surface of the

wide bandgap semiconductor. b) A two-dimensional single microwire cross-section with each layer labeled. The device is supported in a gas impermeable, ionically conductive membrane and consists of an np^+-Si homo-junction core covered by a transparent conductive oxide (TCO) and a wide bandgap semiconductor (SC).

Tin-doped indium oxide (ITO) and fluorine-doped tin oxide (FTO) were both investigated as the TCO material due to their compatibility with Si, high performance as TCOs, and relative stability under oxidizing conditions. The wide bandgap material choice began with many more candidates, but based on a combination of stability under oxidizing or reducing conditions and the maximum V_{oc} known for the material was narrowed down to WO_3 and TiO_2. The bandgaps of WO_3 and TiO_2 are 2.7 eV and 3.0 eV, respectively, which severely limit the maximum photocurrent density (< 5 mA cm^{-2}) and thus efficiency possible given the solar spectrum, but are the only materials that provide intrinsic stability under the operating conditions and thus were used for these proof of principle studies.

Figure 2.3a and Figure 2.3b depict the device electronic band structures in the absence and presence of illumination, respectively. Illumination (Figure 2.3b) results in splitting of the quasi-Fermi levels at both junctions, generating two voltage sources in series. Photoexcited majority-carrier electrons in the n-Si core are transported axially to the back contact through the degenerately doped substrate (n^+-Si) to perform the hydrogen-evolution reaction (HER) at an electrocatalyst site, while photoexcited minority-carrier holes are collected radially in the p^+-Si sheath. The holes in Si recombine with photoexcited majority-carrier electrons from the wide bandgap semiconductor at the TCO contact, while minority-carrier holes that are photoexcited

in the wide bandgap semiconductor are collected at the liquid interface and drive the oxidation of water or anolyte.[54]

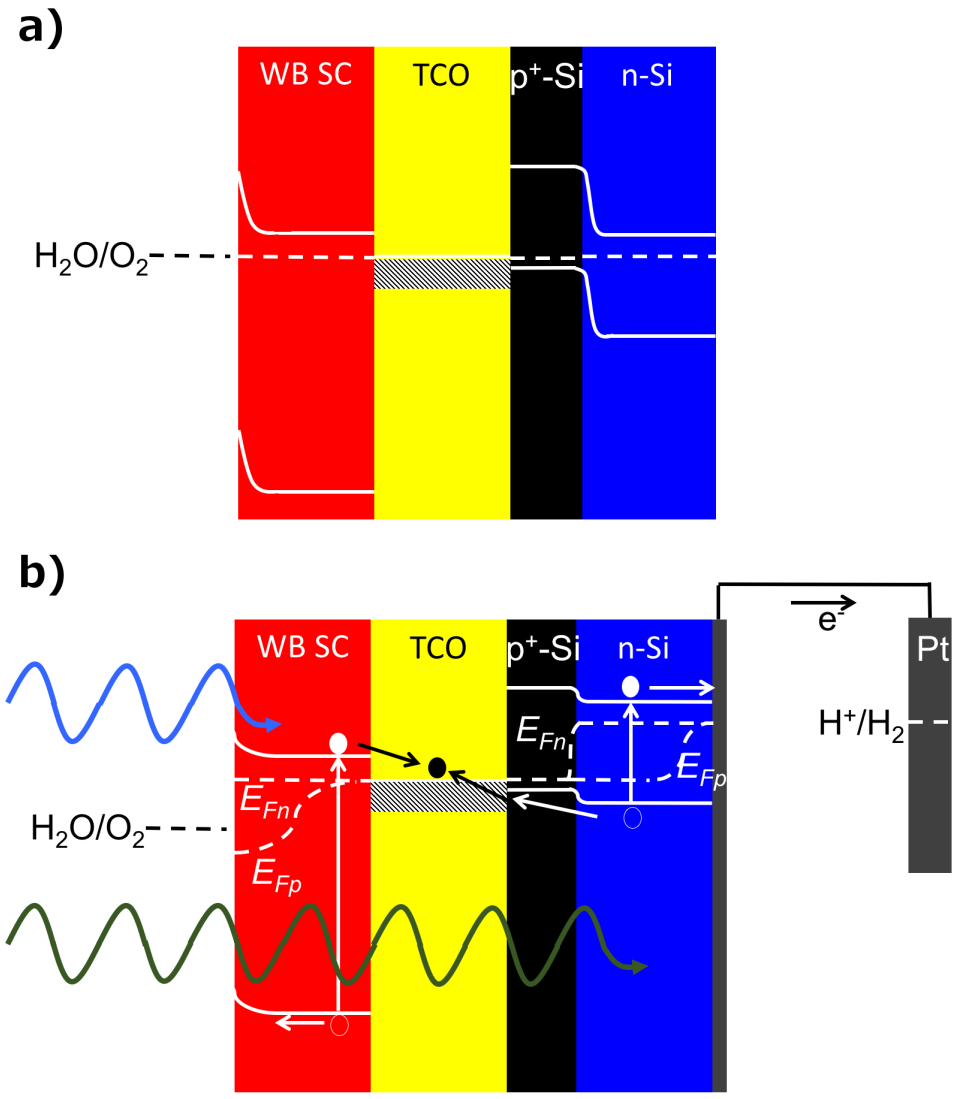

Figure 2.3: Equilibrium and operating tandem junction device electronic structure a) The electronic structure of the tandem junction device in the dark, at equilibrium, where the electrochemical potential is equal across the entire device and is defined by the oxygen evolution potential here. It is important to note that a complete device, with hydrogen and oxygen on opposite sides, is not at equilibrium as a non-zero ΔG exists. This is the reason for omitting the hydrogen evolution reaction in this picture. b) The electronic structure of the tandem junction

device under operation with illumination. The electrochemical potentials (quasi-Fermi levels) for electrons (E_{Fn}) and holes (E_{Fp}) are not equal in some parts of the device, which is responsible for the current and voltage production. An offset between the oxygen evolution potential and the E_{Fp} is needed to overcome the overpotential required to drive the reaction at rates comparable to the solar flux (10-20 mA cm^{-2}). Photoexcited electron-hole pair production and transport is shown to indicate the direction of current flow.

During the course of this work, a similar yet distinct device that performs unassisted water splitting was reported, which incorporates a p-n^+-Si nanowire junction connected to TiO_2 by the p-Si nanowire core (referred to as Si/TiO_2).[30] One major difference between the device design presented here (referred to as Si/WO_3) and the Si/TiO_2 design is the collection probability of excess charge carriers in Si. Excess minority carriers are collected radially throughout the Si wire for the Si/WO_3 design, maintaining collection lengths (< 2 μm) shorter than reported minority-carrier diffusion lengths (~10 μm).[48,55] Conversely, excess minority carriers are collected axially in the top half of the Si/TiO_2 design, requiring collection lengths much longer than the largest diffusion lengths measured in Si microwires (~10 μm).[48,55] Si nanowires also have excessive junction area that leads to high rates of carrier recombination relative to the use of Si microwires.[43] Optical absorption modelling of Si microwires indicates that a majority of the incident light is absorbed near the top of the wire, emphasizing the need for efficient minority-carrier collection in this region.[56] This difference is apparent as a V_{OC} difference between the Si/TiO_2 device (370 mV) and the Si/WO_3 device (480 mV). The Si/TiO_2 device utilized two masking steps to define the structure and a top-down fabrication process that began with a high-quality photo-active p-Si wafer, whereas fabrication of the Si/WO_3 device consisted of sequential

deposition of the active materials with a single masking step and featured a bottom-up fabrication process from a re-usable photo-inactive n^+-Si substrate.[57]

In addition to this tandem junction design, Si microwire arrays were also used to design and demonstrate a hydrogen evolution photoelectrode that decouples light absorption in the microwires and catalytic activity using a non-noble metal catalyst, which has traditionally limited planar designs (Chapter 6). Si microwire arrays were also used to extend a newly developed oxidatively protective coating to a three dimensional photoelectrode geometery (Chapter 5).

2.3 Device Fabrication

Below is a high level description of the fabrication process for the main device structures studied in this thesis. Complete fabrication details for all devices can be found in Appendix A.

2.3.1 Si Microwire Arrays

Figure 2.4 shows the Si microwire fabrication process used for all studies in this thesis. The process begins with a <111> Si wafer doped according to the experimental design and with 400-500 nm of a thermally grown SiO_2 (Figure 2.4a). 3 μm diameter holes in a 7 μm x 7 μm square lattice are formed in the SiO_2 layer using photolithographically defined mask and by etching through the SiO_2 using buffered hydrofluoric acid (BHF, aq.). 500 nm of copper (Cu) is then deposited and the photoresist is removed, lifting off the Cu on top of it, and leaving behind Cu in the 3 μm diameter holes only where it directly contacts the <111> Si growth wafer (Figure 2.4b).

Si microwires are then grown in a vapor-liquid-solid (VLS) chemical vapor deposition (CVD) process using the Cu as a catalyst to crack $SiCl_4$(g) such that Si becomes dissolved in the Cu. When the Cu becomes supersaturated with Si, the Si deposits epitaxially on the underlying <111> Si, thereby growing a vertically aligned microwire (Figure 2.4c).

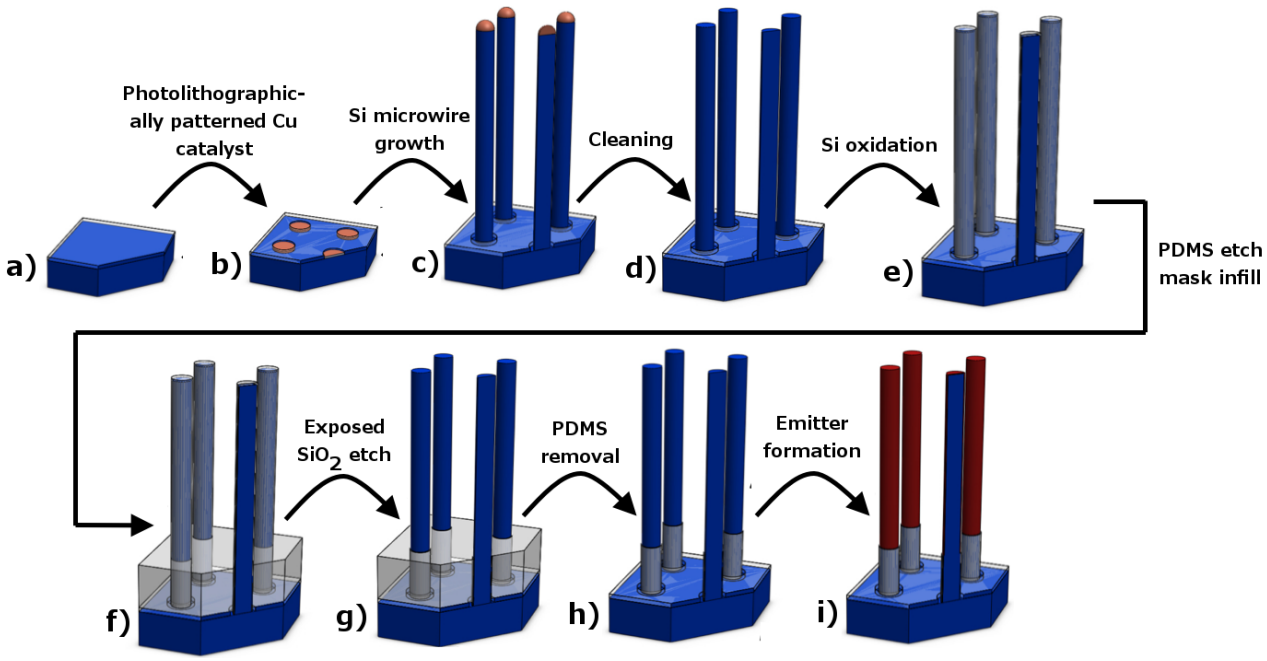

Figure 2.4: Si microwire fabrication process a) A Si wafer with 400-500 nm of thermally grown SiO_2. b) Photolithographically patterned Cu growth catalysts in the SiO_2 layer. c) A Si microwire array as grown. d) RCA I (organics) and II (metals) cleaned Si microwire array. e) ~100 nm growth of thermal SiO_2. f) PDMS infilled (10 µm) Si microwire array to mask the SiO_2 near the microwire bases. g) HF etched Si microwire array where the exposed SiO_2 has been removed. h) Post PDMS removal with the masked SiO_2 visible. i) A homo-junction Si microwire array with an emitter of the opposite doping type as the core.

Following the growth of a Si microwire array, further processing is required to make an efficient homo-junction. This begins by removing metals and organics on or near the surface using RCA II and I etches, respectively (Figure 2.4d). Next a ~100 nm thick dry thermal oxide is grown that is used to provide electronic isolation between the growth wafer and emitter (Figure 2.4e). For all

devices, except those in Chapter 6, a 10-15 μm layer of polymethyldisiloxane (PDMS) is deposited at the base of the microwire array to mask this region of SiO_2 (Figure 2.4f). The exposed SiO_2 is removed by BHF (Figure 2.4g) and followed by removal of the PDMS layer (Figure 2.4h). This forms a "boot" of SiO_2 at the base of the microwire. A ~100 nm thick emitter of high doping density and opposition doping type than the Si microwire core is formed via solid state diffusion and is the source of the homo-junction (Figure 2.4i). For devices used in Chapter 6 the SiO_2 layer on the Si microwire and that between the microwires is removed using BHF, leaving bare Si everywhere. An emitter is then formed everywhere on the device.

2.3.2 Further Device Processing Specific Experimental Designs

Following formation of Si microwire array homo-junction devices, additional and specific processing was required to fabricate functioning devices for each set of experiments. For tandem junction devices (Chapters 3 and 4) a Si microwire array that consisted of a moderately doped n-type core and heavily doped p-type emitter (np^+-Si) was conformally coated with a transparent conductive oxide (TCO) to provide low resistance electrical contact between the Si homo-junction and the wide bandgap semiconductor (outermost layer) while remaining as transparent as possible to photons above Si's bandgap. A photoactive wide bandgap semiconductor layer was then deposited conformally on the np^+-Si/TCO structure to form a semiconductor-liquid junction with solution (the devices second junction). For oxidatively stable and electrocatalytically active np^+-Si microwire array devices (Chapter 5) a layer of amorphous TiO_2 was conformally deposited on the np^+-Si microwire array followed by a nickel-chromium oxide ($NiCrO_x$), which only coated near the microwire tops. Finally, for pn^+-Si microwire array hydrogen evolution devices (Chapter

6) a nanoparticulate bilayer of nickel-molybdenum (Ni-Mo) electrocatalyst covered TiO_2 was deposited by centrifugation to form an optoelectronically optimized photoelectrode architecture.

3 Photoelectrochemistry of Core–Shell Tandem Junction n-p^+-Si/n-WO_3 Microwire Array Photoelectrodes

3.1 Introduction and Motivation

Si microwire array photocathodes have been shown to generate photovoltages in excess of 500 mV in acidic aqueous environments, and provide a preferred geometry, relative to planar structures, for devices that effect the unassisted generation of fuels from sunlight.[37,38,41] Microwire arrays benefit from orthogonalization of the directions of light absorption and minority-carrier collection,[17,43,45-47] as well as from light-trapping effects,[39,42] an increased surface area for catalyst loading per unit of geometric area,[49,58] a small solution resistance as compared to planar designs,[41,44] a reduced material usage through reusable substrates,[57] and from the ability to embed the microwires into ion exchange membranes that exhibit little permeability to H_2 and O_2,[59] thereby producing flexible devices that persistently separate the products of the water-splitting reaction. However, the voltage generated from single-junction Si microwire arrays is much lower than the 1.23 V required for solar-driven water splitting, so a wider band gap partner light absorber must be introduced electrically in tandem (Si/partner tandem device) to generate useful current at voltages that exceed the thermodynamically required values for fuel production. Accordingly, tandem-junction devices offer the highest theoretical[14] and experimentally realized[17] efficiencies for solar-driven water splitting through additive voltages across two photoabsorbers that effectively utilize multiple regions of the solar spectrum. Tandem device structures are also simpler to fabricate and operate effectively under a greater

variety of insolation conditions than more complex 3- or 4-junction devices. Additionally, when kinetic overpotentials are considered in detail, water-splitting devices will most likely require a tandem architecture to achieve appreciable current densities, i.e., 10 mA-cm^{-2}, thereby further motivating the use of tandem structures in such applications.

In addition to band gap considerations for a Si/partner tandem system, achieving the desired electronic behaviour at the interface between Si and its tandem partner presents a significant challenge for production of an integrated solar fuels generation device. The materials must be mutually compatible and generally must operate in a batch reactor that contains a single, concentrated (1.0M) [41,60] aqueous electrolyte. Such materials considerations are important to the performance of a functioning device that consists of microwires embedded in a gas impermeable, ion-exchange membrane, because both semiconductors need to be simultaneously in contact with the electrolyte to produce a full solar-driven water-splitting device. Tandem junction water-splitting devices using nanoscopic or microscopic materials have focused on a single-junction n–n hetero-junction design in series with a liquid second junction. [61,62] In contrast, the highest efficiency water-splitting devices[16,17] consist of planar tandem homo-junction photovoltaic cells that are physically isolated from the solution and are electrically connected to the catalysts in contact with solution. The materials currently used in high-efficiency planar tandem devices are not stable in concentrated aqueous electrolyte environments. Nevertheless, the concept of buried p-n homo-junctions is a promising route to increase the efficiency of solar-driven water-splitting devices relative to systems that utilize n-n hetero-junctions.[30,37,61-63] To realize the advantages of replacing the n-n hetero-junction with a

p-n homo-junction, ohmic behaviour at the Si/tandem partner interface is required. This ohmic behaviour can be achieved in at least two ways: (i) the Si tandem partner must have proper band alignment (type III, broken gap) such that upon direct contact, ohmic behaviour is produced or (ii) a discrete intermediate third material must be introduced that facilitates ohmic behaviour between the Si and the tandem partner light absorbers.

TiO_2, WO_3, $BiVO_4$, and Fe_2O_3 are stable in concentrated aqueous electrolytes and form suitable tandem partners for Si. However, Si is stable only in acidic aqueous environments, limiting the presently available partner materials that are stable under such conditions to only TiO_2 and WO_3. WO_3 is the preferred material because of its smaller band gap ($E_g \approx 2.6$ eV) and significant photocurrent response to visible-light illumination.[64] The electronic behaviour of the Si/WO_3 interface has recently been shown to be non-ohmic, but addition of an intermediate tin-doped indium oxide (ITO) layer has been shown to provide low resistance, ohmic behaviour between p-type, or p^+-type, Si and WO_3.[65] Thus, a Si/WO_3 microwire device with an intermediate ITO layer presents an opportunity to demonstrate an unassisted integrated solar-driven water-splitting device that exploits of the advantages of the microwire-array architecture.

We describe herein a tandem core-shell photoelectrochemical device that consists of a periodic array of buried homo-junction n-p^+-Si microwires that have been sequentially coated with a radial sheath of ITO and WO_3. When immersed in air-saturated 1.0 M H_2SO_4, the dual radial-junction microwire structure enables efficient carrier collection from both the Si and WO_3 light absorbers, despite short minority-carrier diffusion lengths, i.e., ~10 μm in Si[48] and ~1 μm in WO_3. A

necessary feature of this tandem architecture is the incorporation of the ITO layer between the Si and WO_3 light-absorbing materials. This ohmic contact layer ensures facile, low-resistance carrier transport between the Si and WO_3 and relaxes the requirements for proper band alignment between the p+-Si emitter and the WO_3. Transparent conductive oxides, such as FTO or ITO, are commonly used as back contacts to metal oxides; thus this design is expected to be robust towards implementation of newly discovered materials, because the ITO layer will be amenable to many different Si tandem partner absorbers.

3.2 Device Fabrication

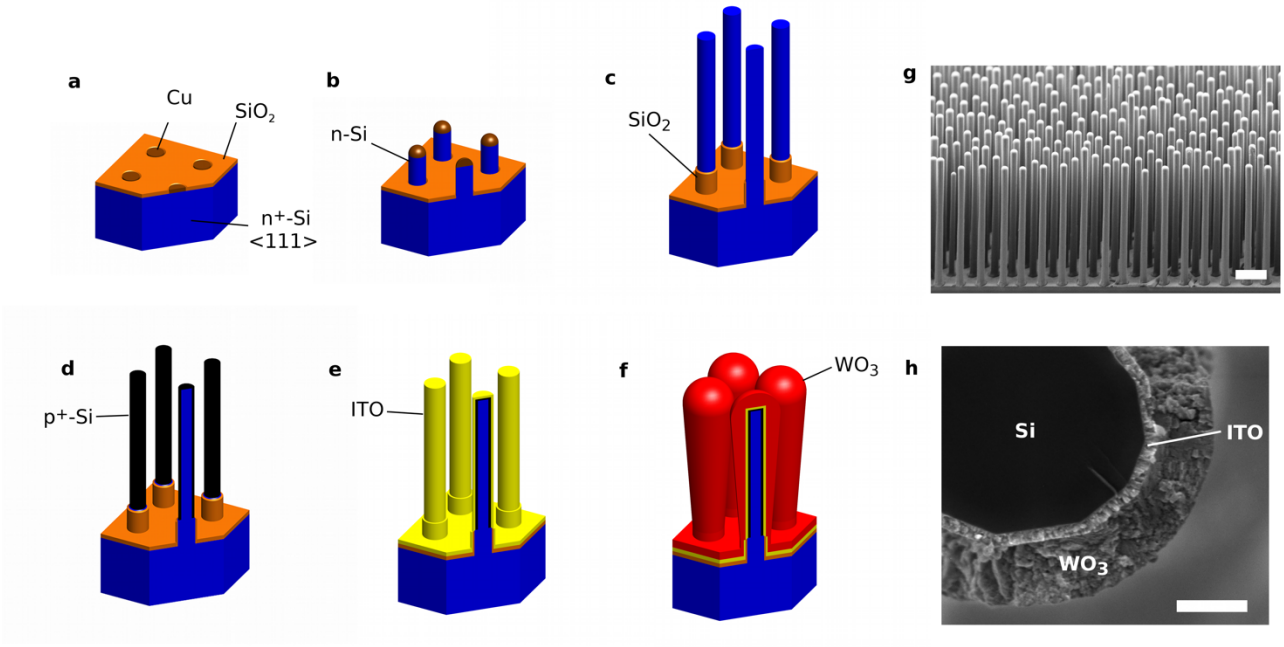

Figure 3.1: Si/WO_3 tandem junction microwire array fabrication and SEM images a) Photolithographically patterned n+-Si <111> wafer with a SiO_2 mask layer and Cu catalyst in the desired growth pattern. b) VLS Cu-catalyzed growth of n-type Si microwires on n^+-Si substrate followed by a metal etch (RCA 2). c) SiO_2 diffusion barrier (boot) formation via SiO_2 growth, PDMS infill, HF etch, and PDMS removal. d) p^+-Si emitter drive-in from BCl_3 precursor at 950°C for 30min

in a CVD furnace. d) Conformal DC sputter coating of ITO. f) Conformal n-WO_3 electrodeposition and annealing at 400 °C for 2h. g) Fully assembled tandem junction device array SEM (scale bar = 10 µm). h) Cross-sectional SEM of a fully assembled tandem junction single wire demonstrating the layered structure of the device (scale bar = 500 nm).

Figure 3.1a-f depicts the process used to fabricate on-wafer devices used herein and is described in detail in Chapter 2 and Appendix A. Figure 3.1g displays an image of a completed device wire array, while Figure 3.1f shows a cross-section of a single wire demonstrating the layered device structure. The Si microwires were 40-70 µm in length, had a diameter of ~ 2 µm and had doping densities on the order of 10^{17} cm^{-3}. Secondary-ion mass spectrometry data from planar samples indicated that the p^+-Si emitter thickness was ~ 200 nm. The sequential, conformal layers of ITO and WO_3 were ~100 nm and ~400 nm, respectively.

3.3 Photoelectrochemical and Optoelectronic Modeling Results

3.3.1 np^+-Si Microwire Non-Aqueous PEC

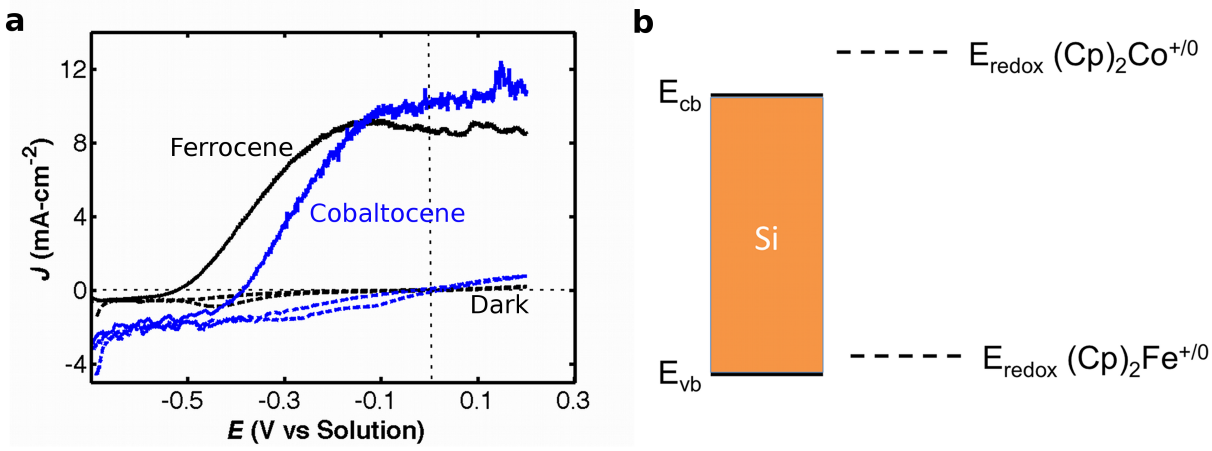

Figure 3.2: Non-aqueous PEC characterization of Si/WO_3 device a) Non-aqueous PEC (forward scan, scan rate = 20 mV-s^{-1}) results using ferrocene$^{+/0}$ (black) and cobaltocene$^{+/0}$ (blue) as redox

couples to probe the np^+-Si buried junction performance in microwires arrays. The dark scans are dashed lines and light scans are shown as solid lines. b) Redox potentials of cobaltocene ($(Cp)_2Co^{+/0}$) and ferrocene ($(Cp)_2Fe^{+/0}$) with respect to the potentials of the conduction band edge and the valence band edge of Si.

The performance of individual buried junction np^+-Si microwire array devices was investigated through non-aqueous photoelectrochemical (PEC) measurements in contact with a series of one-electron, outer-sphere redox couples (Figure 3.2). The cobaltocene$^{+/0}$ ($CoCp_2^{+/0}$) and ferrocene$^{+/0}$ ($FeCp_2^{+/0}$) redox species were used to determine the quality of the buried junction, by probing the n- and p-type character at the Si–liquid interface. Figure 3.2b displays the redox potentials of $CoCp_2^{+/0}$ and $FeCp_2^{+/0}$ with respect to the potentials of the Si conduction and valence bands. The p^+-Si radial sheath is expected theoretically, and was observed experimentally, to form an ohmic contact to $FeCp_2^{+/0}$ and to form a tunnel junction to $CoCp_2^{+/0}$. For a fully buried junction, similar performance should therefore be observed in contact with both of these redox systems. However exposed n-Si forms is expected theoretically and is observed experimentally to form an electrical short (i.e., an ohmic contact) to $CoCp_2^{+/0}$ and a rectifying contact to $FeCp_2^{+/0}$.

In contact with $FeCp_2^{+/0}$ under 100 mW-cm^{-2} of simulated Air Mass 1.5G illumination, the n-p^+-Si microwire array devices exhibited an open-circuit potential of E_{oc} = -0.5 V versus solution, and a short-circuit current density of J_{sc} = 8.7 mA-cm^{-2}, with a fill factor of 0.44 (Figure 3.2a). Similar performance was observed for microwire structures in contact with $CoCp_2^{+/0}$, and the comparable photodiode performance characteristic indicates that the performance is due to the buried n-p^+-Si junction.

The 0.1 V decrease in E_{oc} observed for the $CoCp_2^{+/0}$ contact compared to the $FeCp_2^{+/0}$ contact is consistent with the presence of exposed n-Si near the SiO_2/Si boundary (boot), creating an electrical short to solution.[49] This is important to note; however, it has been shown that the n-Si/ITO interface produces a barrier rather than an electrical short like n-Si/$CoCp_2^{+/0}$.[65] Thus, the np^+-Si-microwire part of the ultimate tandem structure is expected to contribute an open-circuit voltage of V_{oc} = 0.5 V and is not expected to limit the current of the tandem device, because the maximum possible J_{sc} from WO_3 is ~5 mA-cm^{-2}.[66]

3.3.2 Single (WO_3) and Tandem (Si/WO_3) Junction PEC

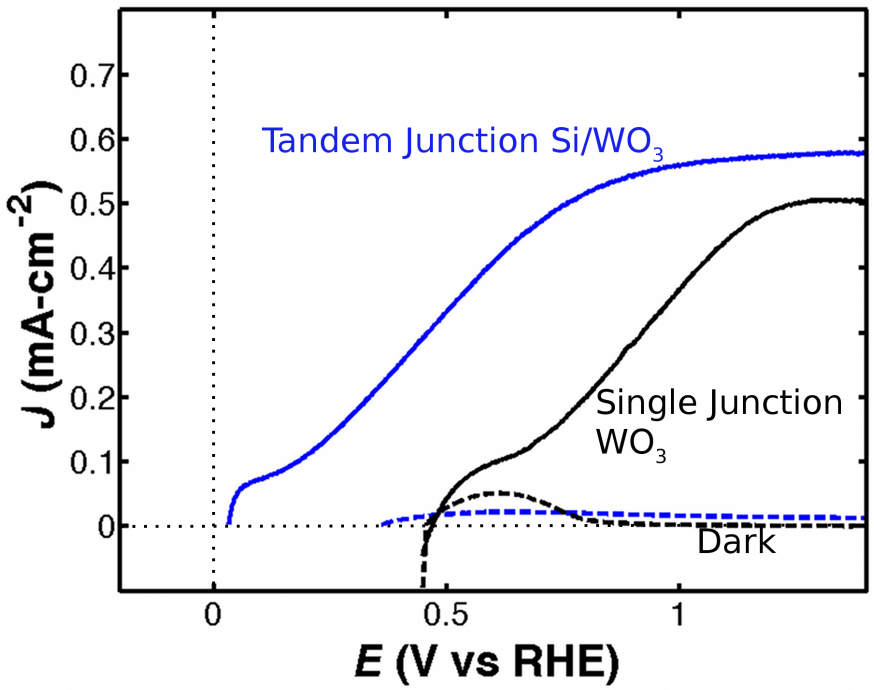

Figure 3.3: Si/WO_3 PEC water splitting performance under simulated 1 Sun illumination Three-electrode PEC (forward scan, scan rate = 20 mV-s^{-1}) performance for single (black) and tandem (blue) junction microwire devices in contact with 1.0 M H_2SO_4(aq). The single junction microwire device consisted of WO_3 supported on p-Si microwires that had been coated with ITO. Here the

p-Si/ITO contact is ohmic so the only rectifying junction is at the WO_3/liquid junction. These data demonstrate the presence of an additive voltage from each junction, with 0.73 V and 0.5 V produced by the WO_3/liquid and n-p^+-Si buried junctions, respectively. The E_{oc} for the single junction device was defined as the point at which the dark current, due to capacitive charging, and the illuminated current separated. The E_{oc} for the tandem junction device was defined as the point at which no current was flowing because no positive dark current existed in this region.

Figure 3.3 shows the photoelectrochemical (PEC) behaviour of single junction (p-Si/ITO/n-WO_3/1.0 M H_2SO_4) and tandem junction (n-Si/p^+-Si/ITO/n-WO_3/1.0 M H_2SO_4) microwire array devices under simulated one Sun illumination conditions. The p-Si/ITO and p^+-Si/ITO contacts have been shown to produce ohmic behaviour allowing isolation of the n-WO_3/1.0M H_2SO_4 liquid junction performance in the single junction case and efficient use of the buried n-p^+-Si junction in the tandem junction case.[65] The single- and tandem-junction microwire devices exhibited J = 0.50 mA-cm^{-2} and J = 0.58 mA-cm^{-2}, respectively, at $E^{o\prime}(O_2/H_2O)$. The first peak in photocurrent density is a dark redox process that results in the photochromism of WO_3, whereupon reverse scans the WO_3 film is reduced through proton intercalation, and is subsequently oxidized on the forward scan. The second peak is associated with photocurrent that results in actual solution redox reactions. The slightly lower current density exhibited by the single junction is consistent with decreased absorption due to the use of shorter microwire arrays.

The open-circuit potentials were E_{oc} = -0.73 V vs. $E^{o\prime}(O_2/H_2O)$ and E_{oc} = -1.21 V vs. $E^{o\prime}(O_2/H_2O)$ for the single- and tandem-junction devices, respectively. The E_{oc} for the WO_3/liquid contact is in accord with expectations for WO_3 photoanodes operating under these conditions.[19] The 0.48 V shift in E_{oc} of the tandem junction device relative to the single junction device is therefore

attributable to the presence of the np^+-Si buried junction in the tandem device (Figure 3.2). This voltage shift demonstrates that the buried np^+-Si junction increases the voltage generated by Si as compared to n-Si/n-type metal-oxide heterojunction devices.[61,62]

3.3.3 Load-line Analysis

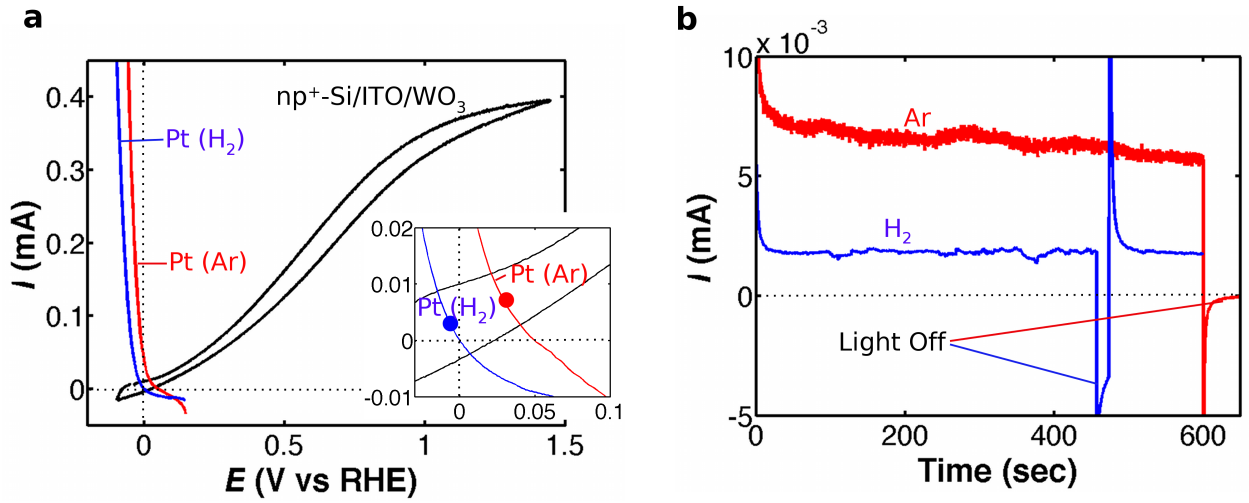

Figure 3.4: Si/WO_3 PEC water splitting performance and stability under simulated 11 Suns illumination a) *J–E* curves and load-line analysis of the tandem junction ($n\text{-}p^+$-Si/ITO/WO_3) microwire device at 12 suns (AM1.5D) plotted against the dark HER curves (mirrored about the abscissa) using a Pt disc electrode in an Ar(g)- or H_2(g)-saturated solution. These measurements were conducted in a two-electrode cell with 1 M H_2SO_4 in both compartments separated by a Nafion membrane to maintain product separation. The Pt disc HER curves include solution and membrane resistances because the reference electrode (SCE) was placed in the opposite cell at the same location used for the tandem microwire array device. The inset is a zoomed in view around the operational points, which are indicated by the red (Ar) and blue (H_2) circles. b) Two-electrode measurements at 0 V applied bias between the tandem junction device (concentrated illumination) and Pt disc electrode in either Ar(g)- or H_2(g)-saturated solution. Turning the light off, as indicated, demonstrated that the positive current was photoinduced.

Under modest optical concentration (12 Suns, AM.15D), tandem junction microwire-array devices exhibited E_{oc} = -1.27 V vs $E^{0'}(O_2/H_2O)$, which exceeds the 1.23 V potential difference necessary for unassisted water splitting under standard-state conditions (Figure 3.4a). The operating current for this device under modest optical concentration can be predicted using a load-line analysis.[67] Figure 3.4a shows the *I-E* behaviour of an illuminated tandem microwire device, along with the *I-E* behaviour, mirrored about the abscissa, of a Pt disc electrode of similar projected area, in contact with either a saturated Ar (g) or H_2(g) solution at 1 atm. In a Ar(g)-saturated solution, the onset potential for the HER was shifted positive compared to that observed in a H_2(g)-saturated solution, in accordance with Le Chatelier's principle. These data were obtained using a two-compartment cell with a Nafion membrane separating the anode and cathode compartments. The *I-E* behaviour of the Pt disc includes the solution and membrane resistances of the electrochemical cell, because the reference electrode was placed in the opposite (anode) compartment. This type of measurement provides a robust prediction of the unassisted operating current that should be obtained between an illuminated Si/WO_3 microwire array device and a Pt button electrode in the same geometry and physical location. The anolyte was not purged with O_2 because the primary oxidation product from WO_3 under these conditions has been shown to be peroxydisulfate.[21]

Figure 3.4b displays the chronoamperometric response from a two-electrode experiment at 0 V applied bias between an illuminated tandem junction WO_3/Si microwire array device and a Pt disc electrode. The devices produced solar-to-hydrogen energy conversion efficiencies of 0.0068% (6.5×10^{-3} mA, 0.060 mA-cm^{-2}) and 0.0019% (1.9×10^{-3} mA, 0.017 mA-cm^{-2}) when the Pt

disc was in contact with Ar(g)- and H_2(g)-saturated solutions, respectively, which agree with the predicted operating points from the load-line analysis (dots at intersection points in Figure 3.4 insets). The peroxydisulfate/sulfate redox system has a formal reduction potential that is ~ 0.75 V positive of $E^{o'}(O_2/H_2O)$, indicating that the tandem core-shell microwire device generated ~ 1.8 V of photopotential under these conditions. Device photostability was demonstrated for over 10 min by the H_2(g)-purged device. Thus, the decrease in current for the Ar(g)-purged device is attributable to an increasing H_2 concentration in solution from the HER at the Pt disc electrode. Additionally, the chopped-light response demonstrated that the observed current was photo-induced. The negative current observed in the dark for the H_2(g)-purged device is consistent with O_2 (g) and H_2(g) recombination to form water, similar to fuel cell operation. This behaviour demonstrates that the operating voltage of the device can be tuned by changing the partial pressures of the photoelectrochemical reaction products, i.e., by changing the chemical load across the device, which can be calculated using the Nernst equation.

3.3.4 Product Analysis

Product analysis was performed separately on the oxidation and reduction products in 1.0 M H_2SO_4. As reported previously, electrolyte buffer species are oxidized preferentially at the WO_3/liquid interface, relative to the oxidation of water.[54] Thus, in contact with H_2SO_4(aq), sulfate (SO_4^{2-}) is preferentially oxidized to peroxydisulfate ($S_2O_8^{2-}$), which was confirmed as an oxidative product by UV-vis spectroscopy as published previously.[54] Although direct oxygen evolution was not realized due to WO_3's poor O_2 evolution kinetics, peroxydisulfate has been shown to stoichiometrically evolve O_2 using Ag^+ as a catalyst.[54]

At the Pt disc cathode, H_2(g) production was detected by mass spectrometry of the reaction products when the operational current density was passed at the Pt disc electrode. Due to the small amount of H_2(g) produced, direct quantification of the faradaic efficiency was not performed; however, no other products are expected due to the use of trace metal grade H_2SO_4.

3.3.5 1D Optoelectronic Model

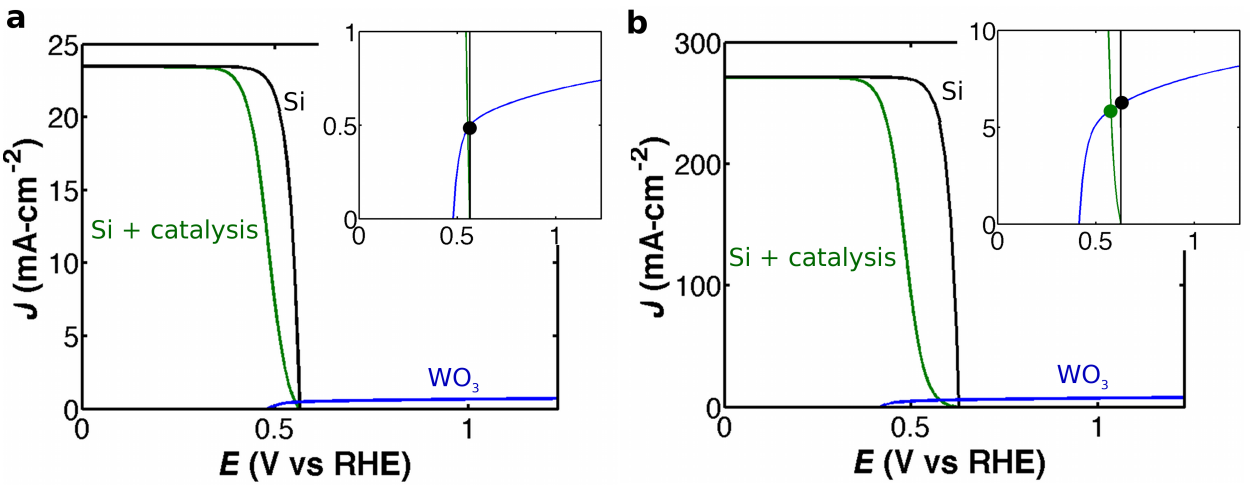

Figure 3.5: Modeled PEC behavior of Si/WO_3 device Modeled *J–E* curves and load-line analysis for unconcentrated (a) and concentrated (b) illumination conditions that match the experimental photon fluxes at 1 and 12 Suns (AM 1.5D). The Si homo-junction is shown with (green) and without (black) inclusion of realistic hydrogen evolution catalytic overpotentials. Butler–Volmer kinetics with $\alpha = 1$ and $j_0 = 10^{-3}$ A-cm^{-2} was used to calculate the catalytic overpotentials in the absence of mass transport limitations. The insets show the operating point for unconcentrated illumination (black dot) and for concentrated illumination, with (green dot) and without (black dot) overpotential due to HER catalysis included. The rate of catalysis is not expected to affect the WO_3 *J-E* behaviour due to the large band gap of WO_3 and proximity of $E^{o'}(O_2/H_2O)$ to the potential of the conduction band of WO_3.

Figure 3.5 shows *J–E* behaviour and simulated load-line analyses of the one-dimensional device architecture in the bulk recombination limit under both unconcentrated (1 Sun) and concentrated illumination to match the experimental photon flux. Here, the Si homojunction performance is shown in the absence of mass-transport limitations, with and without the incorporation of catalytic overpotentials (η) associated with the HER, which is present in any actual water splitting device. The maximum predicted operating points from this analysis are 0.5 mA-cm^{-2} (Figure 3.5a inset) and 5.7 mA-cm^{-2} (Figure 3.5b inset) for unconcentrated (one Sun) and concentrated illumination, respectively. This corresponds to an E_{oc} = -1.29 V vs. $E^{0'}(O_2/H_2O)$ for unconcentrated illumination and E_{oc} = -1.44 V vs. $E^{0'}(O_2/H_2O)$ for concentrated illumination. The modelled *J-E* behaviour for a Pt electrode performing the HER under 1 atm of H_2 included the electrocatalytic behavior only and excluded any mass-transport resistances.

3.3.6 2D Microwire Optical Modeling

Table 3.1: Modeled PEC current density values for differing WO_3 thicknesses Dependence of the light limited photocurrent density (J_{ph}) on the WO_3 coating thickness for light above the WO_3 band gap in: (i) all photoactive material in the core-shell tandem structure (Si + WO_3), (ii) WO_3 and (iii) WO_3 on the microwire sidewalls only (WO_3 on Microwire). J_{ph} is calculated assuming unity IQE.

WO_3 Thickness (nm)	Geometric Filling Fraction (%)	Si + WO_3 J_{ph} <476nm (mA-cm^{-2})	WO_3 J_{ph} (mA-cm^{-2})	WO_3 on Microwire J_{ph} (mA-cm^{-2})
300	11.7	3.34	0.56	0.41
500	15.4	3.43	0.7	0.54
700	19.6	3.47	0.8	0.65
1000	26.9	3.53	0.89	0.79
1500	41.7	3.52	1.08	1.07

Table 3.1 shows the light-limited photocurrent densities (J_{ph}) that were calculated assuming unity internal quantum efficiency (IQE) for the tandem structure for varying WO_3 coating thicknesses: (i) the entire device (Si and WO_3), (ii) only WO_3, and (iii) WO_3 coating the microwire sidewalls only.

3.4 Discussion

3.4.1 Tandem Junction Performance

The E_{oc} = -1.27 V vs $E^{o'}(O_2/H_2O)$ exhibited by the tandem junction np^+-Si/ITO/n-WO_3 microwire array device indicates that the structure provides enough voltage to drive unassisted solar-driven water splitting under standard-state conditions and 12 Suns illumination (AM1.5D). Additionally, $H_2(g)$ was detected as a reduction product confirming unassisted hydrogen production. To realize a complete, direct water-splitting device, an oxygen-evolution catalyst coupled to the WO_3 surface would be required. Two-electrode operation with a Pt HER electrode demonstrated stable operation of the device as well as validation of the operating point determined by the load-line analysis. This demonstration therefore provides a proof-of-concept for the development of core-shell high-aspect ratio tandem junction devices for fuel formation directly from sunlight. Such a device could be embedded in a gas impermeable, ion-selective membrane[59] and removed from a reusable substrate[57] to form a free-standing device. This architecture minimizes the distance ions must travel to complete the fuel-forming circuit, thus minimizing the potential drop due to solution resistance effects.

3.4.2 1D Optoelectronic Modeling

The performance of the tandem junction n-p^+-Si/ITO/n-WO_3 device described herein is fundamentally limited in two ways by WO_3: (i) its wide band gap (~2.6 eV) limits the maximum current density to ~5 mA-cm^{-2} under AM1.5G illumination conditions; and (ii) the barrier height between WO_3 and $E^{o\prime}(O_2/H_2O)$ limits the E_{oc} to less than half of the band gap. Given these two limitations, a one-dimensional optoelectronic model for the tandem structure was developed to investigate the maximum performance that could be expected from the Si/WO_3 device and can be compared to the experimental results.

The modeled E_{oc} values are 80 mV and 170 mV larger, respectively, than the experimentally observed E_{oc} values, which can be ascribed to an increased junction area (~9x) in the experiment as compared to the planar model. These open circuit potential differences manifest themselves as large differences between the modeled and experimental two-electrode operating points due to the proximity of the modeled operating point to the maximum power point in the WO_3 *J-E* behaviour; any unaccounted for resistances and/or open circuit potential losses between model and experiment, such as junction area, will therefore cause a precipitous decrease in the experimental operating current density. This is observed in both experimental illumination conditions where under one Sun illumination the E_{oc} is less than 1.23 V such that the device cannot perform unassisted water splitting at standard conditions. Under concentrated illumination the experimental E_{oc} exceeds 1.23 V, but is lower than the modeled value and explains the cause for the difference in operating points.

3.4.3 2D Optical Modeling

As shown in Figure 2.2a, b, WO_3 forms a conformal coating on the Si microwires and the planar, degenerate Si base, all of which can result in photocurrent. To investigate the photocurrent contribution from WO_3 on the microwire sidewalls relative to that from WO_3 on the planar, degenerate Si base, two-dimensional finite-difference time domain (FDTD) electromagnetic modelling was performed. Table 3.1 demonstrates that for thin WO_3 coatings (300nm), only 17% (0.56 mA-cm^{-2}) of the above band gap light absorbed by the device is absorbed in WO3. The WO_3 absorption fraction increases to 31% (1.08 mA-cm^{-2}) for thicker WO_3 coatings (1.5 μm). The carrier generation rate spatial profiles demonstrate that the majority of the WO_3 absorption is within the top 10 μm of the device, with many photons whose energies are larger than the energy of the WO_3 band gap transmitted through the WO_3 to the underlying Si, where absorption is not useful due to the current limiting absorption in the WO_3. This behaviour implies that an alternative WO_3 geometry is desired to enhance the WO_3 absorption. However, a device geometry designed to increase the WO_3 absorption should optimally accommodate the ~1 μm minority carrier diffusion length of WO3, implying the beneficial use of WO_3 layers <1 μm thick.

For 300 nm thick WO_3 coatings, 73% of the total WO_3 optical absorption occurred in WO_3 on the sidewalls of the Si microwires. This absorption fraction increased to 99% for 1.5 μm thick WO_3 coatings; the 500nm thick WO_3 coatings used experimentally are projected at ~76%. This substantial fraction of absorption along the sidewalls versus at the bottom of the device architecture indicates that similar performance is expected for on-wafer microwires compared to free-standing microwire array devices that have been removed from the growth wafer, which

will be a crucial step for integration of this tandem device into a fully functional solar fuels generator. Additionally, scattering particles could be introduced to redirect more light toward the microwire sidewalls for enhanced WO_3 absorption.[37,39]

3.4.4 Toward Higher Efficiency Devices

Integration of new photoanode materials in place of WO_3 has the potential to increase the performance of the tandem device by producing more negative E_{oc} values as well as much larger values of the current density at E = $E^{o\prime}(O_2/H_2O)$. To produce a more negative value of E_{oc}, the potential of the conduction band of the anode material must be more negative than the potential of the conduction band of WO_3, i.e., closer to the vacuum, thereby increasing the barrier height at the semiconductor/liquid junction. Recent studies of mixed-metal oxides have demonstrated photoanode materials with smaller electron affinities than WO_3.[28,68,69] The production of increased current density at $E = E^{o\prime}(O_2/H_2O)$ will require lowering the recombination rates by improving the material quality and passivating surface states, as well as discovering narrower band gap materials that are stable under oxidizing conditions. Additionally the anodes must be stable under conditions where the cathode and membrane materials are stable, and under conditions where the membrane exhibits high transference numbers for protons, to allow for effective, passive neutralization of the pH gradient between the sites of water oxidation and water reduction while maintaining product separation for intrinsically safe operation of the system under varying levels of illumination.

3.5 Conclusions

A Si/WO_3 integrated tandem junction device capable of unassisted solar-driven water- splitting has been developed and used to demonstrate unassisted hydrogen evolution under moderate light concentration. This system provides proof-of-principle for the design. The approach is attractive because it provides materials flexibility for the Si tandem partner absorber, an optimized electrochemical geometry, embedment in a flexible, gas impermeable, ion exchange membrane, and enhanced absorption and carrier collection properties relative to planar designs. The Si/WO_3 described herein demonstrated additive voltages across the tandem device resulting in an E_{oc} = -1.21 V vs $E^{o\prime}(O_2/H_2O)$ Modest optical concentration (12 Suns) produced a shift in E_{oc} to potentials negative of $E^{o\prime}(O_2/H_2O)$ indicating that the device could split water in an unassisted fashion. Two-electrode measurements performed with no applied bias between the photoanode and a Pt disc cathode resulted in hydrogen production at current densities of 0.060 mA-cm^{-2} and 0.017 mA-cm^{-2} when the catholyte was saturated with Ar(g) and H_2(g), respectively. These operating points agreed well with the values that were predicted from the load-line analysis based on separate measurements of the performance of the cathodic and photoanodic electrodes. The low energy conversion efficiencies result from a highly non-optimal band gap and photovoltage of the WO_3/liquid contact, and much higher efficiencies could be obtained if an alternative suitable photoanode system were identified that was also stable under conditions where the remainder of the system was stable.

4 Si/TiO_2 Tandem-Junction Microwire Arrays for Unassisted Solar-Driven Water Splitting

4.1 Introduction and Motivation

Arrays of semiconducting nanowires or microwires provide an interesting morphology for solar fuels generation, due to a minimized ionic transport length between the anode and cathode, the arrangement of individual and complete device units in parallel to provide protection against catastrophic failure in the event that a single device unit fails, reduced materials purity and usage requirements due to orthogonalized directions of light absorption and minority-carrier collection, the ability to decouple optical absorption and catalytic activity of metallic electrocatalysts through strategic placement of the catalyst in the internal volume of the array, and a high internal surface area for facile functional support of earth-abundant electrocatalysts.[31,41,43] Single-junction Si microwires cannot provide sufficient voltage to perform unassisted solar-driven water splitting (1.23 V at STP), and hence tandem core-shell structures or dual microwire array structures are being explored. Theoretical calculations indicate that tandem-junction devices can produce high efficiencies for integrated solar-driven water splitting, and hence both planar and non-planar tandem-junction systems have been designed and fabricated.[14-17,30,62]

Typical demonstration tandem-junction devices have been fabricated using either a homojunction or heterojunction on a Si microwire core. The core is surrounded by a wide band gap absorber that forms the second junction, which is generally a semiconductor-liquid junction.

Si micro- and nano- wire tandem-junction devices have, however, exhibited low operating current densities for water splitting, due to the need for large open-circuit voltages (V_{oc}) to overcome the thermodynamic and kinetic requirements for sustained H_2(g) and O_2(g) production under standard-state conditions.[30,62] WO_3 is attractive for a demonstration system because it is acid-stable, as is Si and Nafion, enabling the construction of a fully functional membrane-embedded device for operation in locally acidic conditions.

In such structures, the open circuit potential (E_{oc}) of the WO_3/liquid contact ultimately limits the water-splitting performance of microwire Si/WO_3 core-shell tandem devices.[31] Si/WO_3 devices fabricated previously also included a tin-doped indium oxide (ITO) layer to provide efficient charge transfer between the Si and WO_3, but the ITO layer was unstable under operating conditions and thus limited the ultimate device stability.[31]

Larger E_{oc} values have been obtained from nanowire Si/TiO_2 core-shell structures than from microwire Si/WO_3 structures because the wide band gap TiO_2 produces a relatively large photovoltage for the device as a whole. In such structures, relatively low E_{oc} values were, however, observed from the radial Si junction,[30] limiting the observed solar-to-hydrogen (STH) efficiency, $\eta_{STH,}$ of devices reported to date. We describe herein the fabrication and properties of a device in which the WO_3 has been replaced by TiO_2, to generate a larger E_{oc}, and in which the ITO has been replaced by fluorine-doped tin oxide (FTO), to improve the long-term stability of the demonstration device. In conjunction with the high band gap of TiO_2, the presence of a high-quality np^+-Si homojunction is expected to result in a larger complete device E_{oc} that should

enable higher operating current densities and thus produce improved STH efficiencies in a demonstration-type of device.

4.2 Fabrication Methods

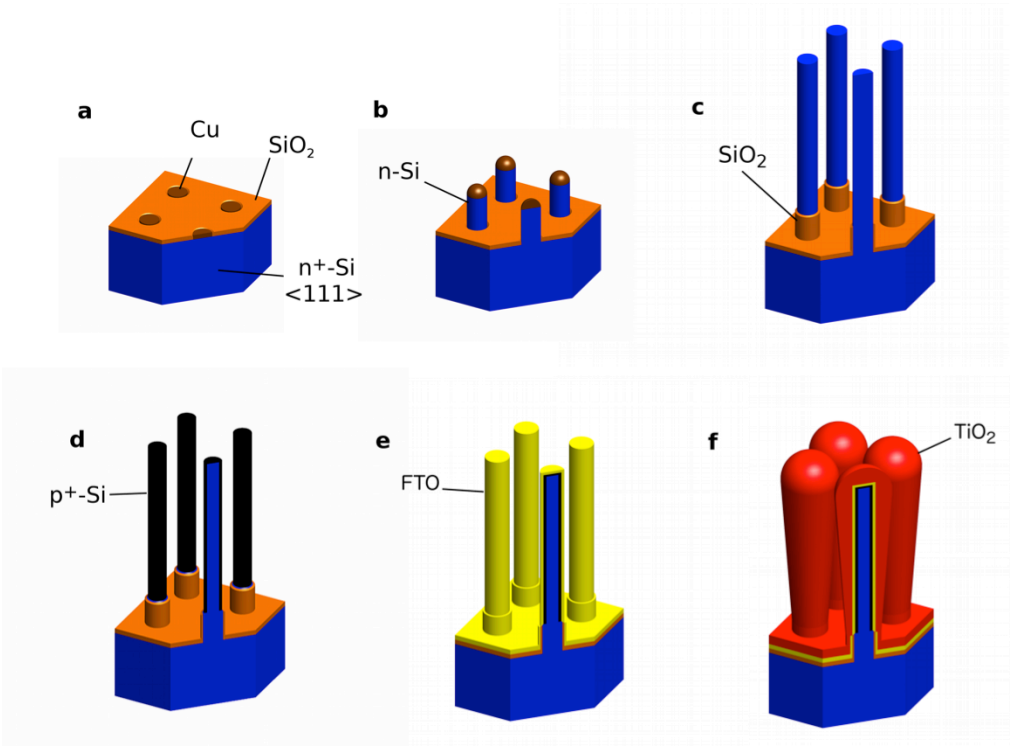

Figure 4.1: Si/TiO_2 tandem junction device fabrication process a) 3 µm diameter circular Cu growth catalysts photolithographically patterned in a 7 µm x 7 µm matrix in a 500 nm thick SiO_2 layer on an n^+-Si (111)-oriented wafer. b) n-Si microwire array growth at 1000 °C in a flowing gas consisting of $SiCl_4$ and PH_3 in H_2. c) Metal and organic cleaned Si microwire array that has a SiO_2 diffusion barrier around each wire's base, formed by a dry oxidation of the entire wire array followed by a polymetyldisiloxane mask infill and subsequent etch in HF(aq) to remove the exposed SiO_2. d) p^+-Si emitter formation by gas phase doping with BCl_3. e) Conformal deposition of FTO by spray pyrolysis at 500° C in air. f) TiO_2 deposition by an aqueous hydrothermal process followed by a 30 min anneal at 450 °C in air.

np^+-Si/FTO/TiO_2 devices were fabricated through formation of a radial np^+-Si microwire homojunction, followed by sequential deposition of conformal FTO and TiO_2 layers (see the Appendix A for complete details). Si microwires were first grown on a photolithographically patterned wafer in which 3 μm diameter circular Cu catalysts were deposited in a 7 μm x 7 μm square pattern, with a SiO_2 mask layer on the remainder of the Si surface (Figure 4.1a). The Si microwires were grown using a vapor-liquid-solid (VLS) chemical-vapor deposition (CVD) process in which $SiCl_4$ at 1000 ˚C in H_2(g) was the Si source, and PH_3(g) was the n-type dopant source (Figure 4.1b). The Si microwire arrays were then cleaned using RCA I and II processes to remove organics and metals, respectively, including the remaining Cu catalyst. A SiO_2 diffusion barrier was formed at the microwire bases by producing a SiO_2 layer using a dry oxidation, masking the bottom of the microwire array with polydimethylsilicon (PDMS), etching the exposed SiO_2 in HF(aq), and then removing the PDMS layer (Figure 4.1c). Radial p^+-Si emitters were formed through gas-phase diffusional doping using BCl_3 at 950˚C in H_2(g) (Figure 4.1d). A conformal FTO layer was then deposited on a Si microwire array via spray pyrolysis of 0.015 M ammonium fluoride and 0.49 M butyltin trichloride in an ethanol/water solution (Figure 4.1e), while the sample was placed on a hotplate and maintained at 500 ˚C. Finally, a conformal nano-structured TiO_2 layer was deposited at 150 ˚C for 6 h on the FTO in a hydrothermal process that used an aqueous solution of 0.05 M titanium n-butoxide and 6 M HCl.[70] Subsequent annealing of the array at 450 ˚C for 30 min resulted in the formation of a nano-structured, conformal rutile TiO_2 (Figure 4.1f) coating. Figure 4.2 shows scanning-electron micrograph (SEM) images of the structures obtained after the process steps depicted schematically in Figure 4.1d-f.

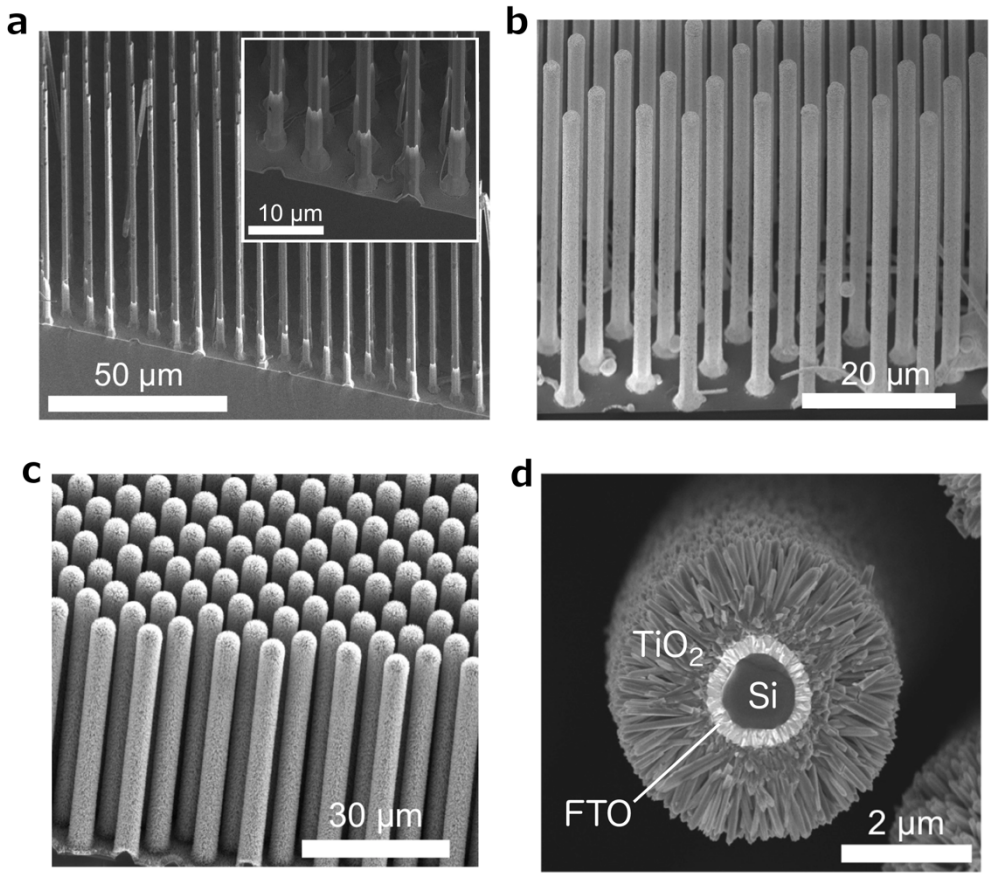

Figure 4.2: SEM images throughout Si/TiO_2 device fabrication process Scanning-electron microscopy (SEM) images showing samples at various stages in the fabrication process. a) A radial junction np^+-Si microwire array (Figure 4.1d). Inset shows a zoomed-in image of the SiO_2 diffusion barrier at the bases of the microwires. b) FTO-coated np^+-Si microwire array (Figure 4.1e). c) TiO_2-coated np^+-Si/FTO microwire array (Figure 4.1f). d) Cross section of a single np^+-Si/FTO/TiO_2 microwire with each layer labeled.

4.3 Photoelectrochemical Performance

In contact with a non-aqueous ferrocenium/ferrocene redox couple, the np^+-Si microwire arrays demonstrated similar performance to arrays reported previously, exhibiting V_{oc} = 0.483 V, a short-circuit current density (J_{sc}) of 13 mA cm^{-2}, and a fill factor (*ff*) of 0.48, resulting in an ideal

regenerative cell efficiency, η, of 3.0%.[31,71] Contact resistance measurements between p^+-Si and FTO performed on planar substrates using the circular transmission line measurement technique (see Supplementary Information for complete details)[72] yielded a specific contact resistance value of 16.6 ± 9.3 Ω cm^2. This resistance corresponds to a ~3 mV voltage loss due to the p^+-Si/FTO contact, assuming light-limited current densities of ~ 2 mA cm^{-2} for rutile TiO_2 under Air Mass (AM) 1.5G illumination conditions and the ~10x surface area increase of Si microwires relative to the area of an analogous planar device. At geometric current densities of ~ 10 mA cm^{-2}, the voltage losses due to this contact resistance will be ~16 mV and ~160 mV for the Si microwire and planar architectures, respectively. Therefore the contact resistance of the p^+-Si/FTO interface is sufficiently low as to allow use of Si microwire arrays under 1 Sun illumination conditions. However, further contact development is required for planar architectures because a 160 mV contact resistance would significantly affect the overall device performance.

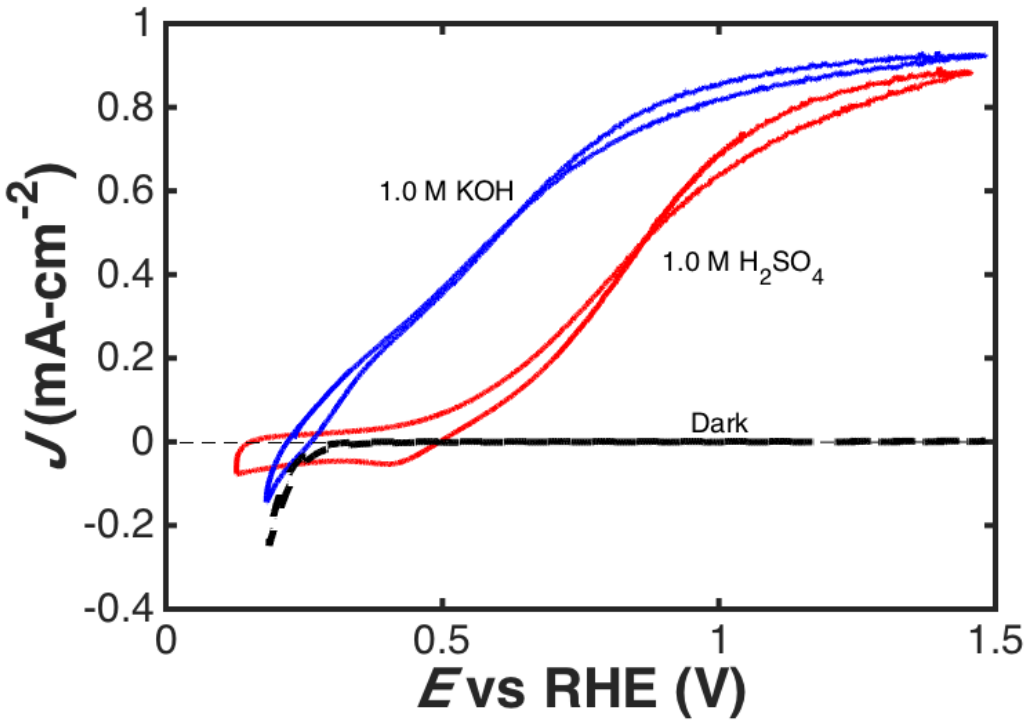

Figure 4.3: PEC behavior of Si/TiO_2 device in acid and base Current density versus potential behavior of p^+-Si/FTO/TiO_2 microwire array photoelectrodes under dark (1.0 M KOH) and simulated 1 Sun conditions in 1.0 M KOH(aq) and in 1.0 M H_2SO_4(aq). This behavior demonstrates the superior photoanode performance in 1.0 M KOH, consistent with higher catalytic activity for oxygen evolution on the TiO_2 surface in alkaline media relative to under acidic conditions.

Figure 4.3 shows the current density versus potential (*J-E*) behavior of p^+-Si/FTO/TiO_2 microwire arrays in 1.0 M H_2SO_4(aq) and 1.0 M KOH(aq), respectively, in a three-electrode electrochemical cell configuration. In 1.0 M KOH, p^+-Si/FTO/TiO_2 microwire arrays, in which the p^+-Si microwires acted as a physical scaffold that facilitated evaluation of the performance of the TiO_2 in the microwire geometry, exhibited an open-circuit potential, E_{oc} = -1.0 V vs $E^{0\prime}(OH^-/O_2)$, a current density at $E^{0\prime}(OH^-/O_2)$ = 0.89 mA cm^{-2}, and *ff* = 0.39, for a solar-to-oxygen ideal regenerative cell efficiency of η_{IRC} = 0.35% (Figure 4.4). In contrast, complete np^+-Si/FTO/TiO_2 core-shell microwire

array devices exhibited voltage addition across the series-connected np^+-Si and TiO_2-liquid junctions, with E_{oc} = -1.41 ± 0.11 V vs $E^{0\prime}(OH^-/O_2)$, as expected for this tandem junction. The devices exhibited J = 0.62 ± 0.20 mA cm^{-2} at $E = E^{0\prime}(OH^-/O_2)$ ff = 0.52 ± 0.04, and η_{IRC} = 0.47 ± 0.18% over the 9 photoelectrodes tested. Figure 4.4 presents the behavior for one of the best performing devices tested, which exhibited E_{oc} = -1.50 V vs $E^{0\prime}(OH^-/O_2)$, J = 0.78 mA cm^{-2} at $E = E^{0\prime}(OH^-/O_2)$, ff = 0.51, and η_{IRC} = 0.60%. Due to the low current densities, this device is expected to operate near 0 V vs the reversible hydrogen electrode (RHE) for unassisted water splitting, and thus ought to exhibit J = 0.32 mA cm^{-2} and η_{STH} = 0.39% in a two-electrode full cell configuration.

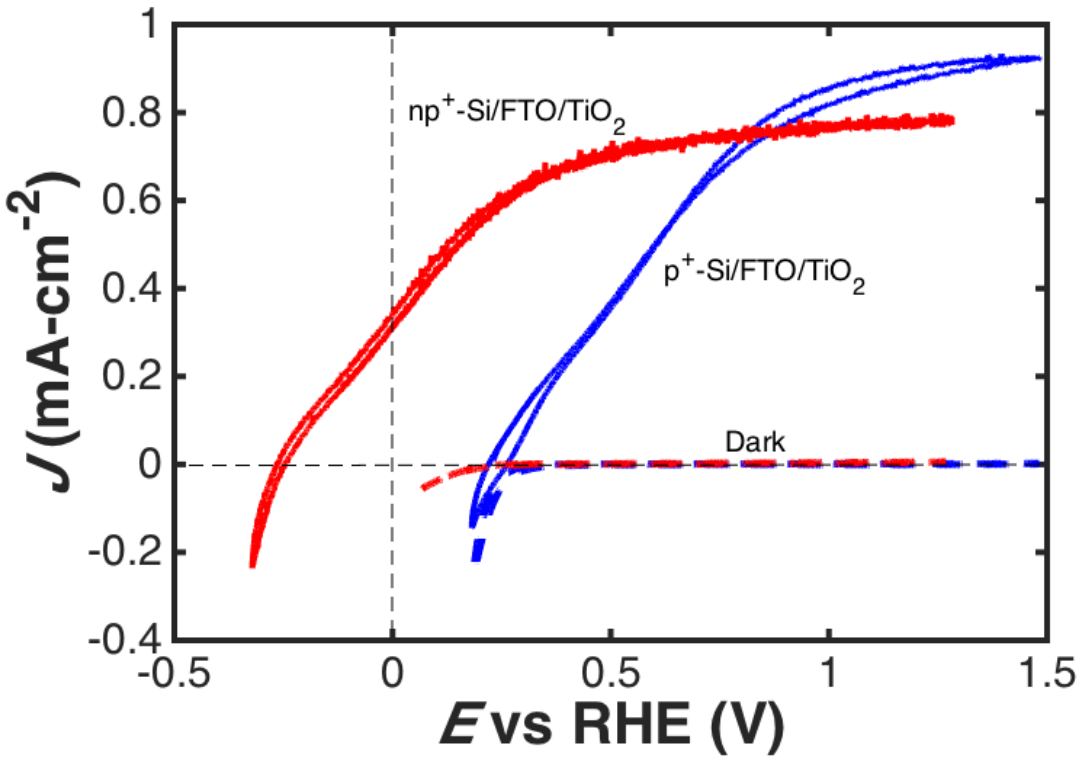

Figure 4.4: Tandem and single junction Si/TiO_2 device performance under simulated 1 Sun illumination Current density versus potential behavior of p^+-Si/FTO/TiO_2 and np^+-Si/FTO/TiO_2 microwire array photoelectrodes in the dark and under simulated 1 Sun conditions. This demonstrates the additive voltage of the tandem junction device and its high E_{OC}, -1.5 V vs $E^{0\prime}(OH^-$

/O_2), allowing for a relatively high current density of 0.32 mA cm^{-2} at E = -1.23 V vs $E^{0'}(OH^-/O_2)$ (0 V vs RHE).

The efficiency of complete core-shell np^+-Si/FTO/TiO_2 microwire-based devices was higher in 1.0 M KOH(aq) than in 1.0 M H_2SO_4(aq), consistent with the reduced catalytic activity of TiO_2 for the oxygen-evolution reaction in acidic media relative to the catalytic activity under alkaline conditions. In contact with 1.0 M H_2SO_4(aq), addition of an IrO_2 electrocatalyst to the TiO_2 surface only slightly enhanced the fill factor, in accord with prior work.[30]

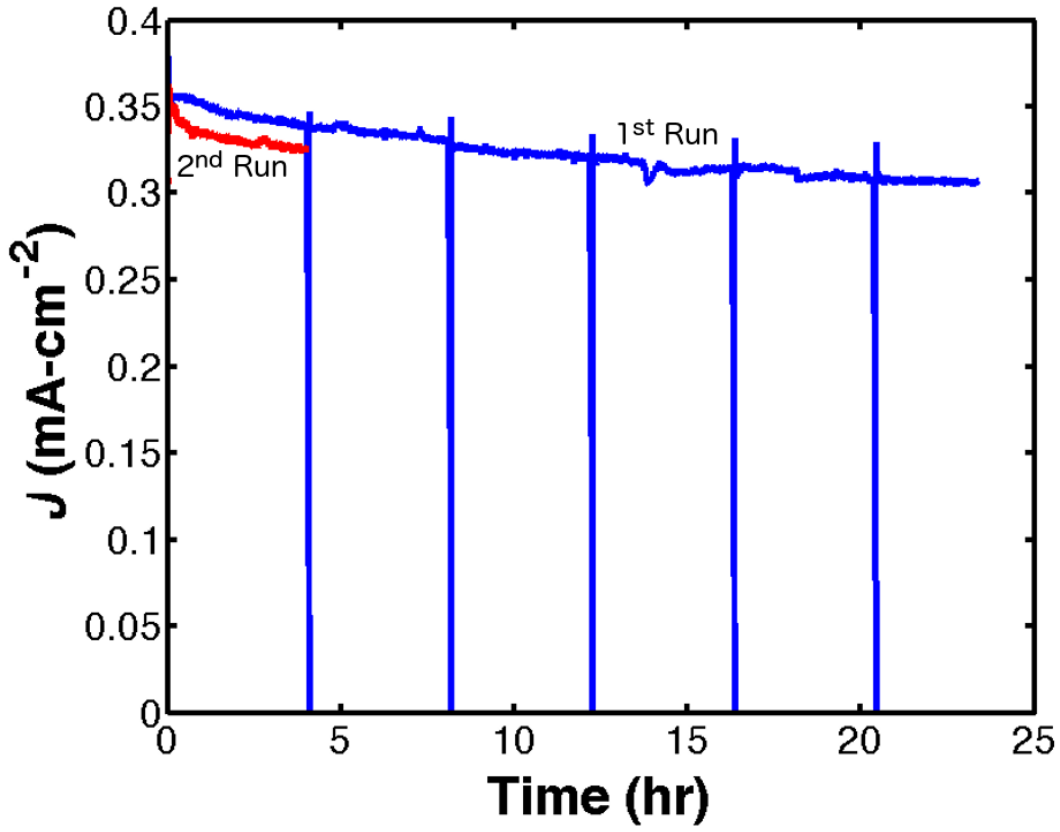

Figure 4.5: 24 hour PEC stability of Si/TiO_2 device Current density versus time behavior of np^+-Si/FTO/TiO_2 microwire array photoelectrodes under simulated 1 Sun conditions and held potentiostatically at 0 V vs RHE. The first run lasted 24 h and was followed by 1 h without

illumination at open circuit, in addition to a subsequent 4 hour run under simulated 1 Sun conditions while being held potentiostatically at E = -1.23 V vs $E^{0\prime}(OH^-/O_2)$ **(**0 V vs RHE**)**.

Under 1 Sun of simulated sunlight, the current density decreased by ~15% from its initial value during 24 h of continuous operation under potential control at 0 V vs RHE (Figure 4.5). However, when the illumination was discontinued for 1 h and then reestablished, the electrode returned to near its initial performance and subsequently exhibited a similar, albeit slightly lower, current density vs time behavior as that observed in the initial stability measurement. Cyclic voltammograms taken throughout the stability measurement demonstrate a decreased current density near E_{oc} as the measurement progressed. However, at more positive potentials the current density was essentially constant vs time, suggesting that a potential dependent mechanism affects the current density at the most negative potentials. Two possible physical mechanisms consistent with a long time constant and potential dependent behavior include a surface reaction at the TiO_2/liquid interface that interferes with catalysis and/or carrier separation and activation of trap states within the TiO_2 layer.

4.4 Discussion and Conclusions

Although the results herein demonstrate an improvement in open-circuit voltage and stability for microwire array devices when used to effect unassisted solar-driven water splitting relative to the behavior of np^+-Si microwire/WO_3 devices, the band gap of the TiO_2 severely limits the current density achievable under 1 Sun illumination conditions. Accordingly, maintaining the high E_{oc} from the wide-band gap material while narrowing the band gap of the top absorber layer

is crucial to obtain further significant efficiency improvements, as has been demonstrated in many planar designs.[16,17] To date, incorporation of lower band gap, high quality materials has been challenging on Si microwire arrays and other similar semiconductor architectures.[51,52]

The combination of material stability and sufficient voltage production has limited and continues to limit microwire and similar three dimensionally structured water splitting device efficiencies. Furthermore, the operational conditions under which the highest performance is achieved further limit options for free-standing device fabrication, such as membrane compatibility. For example, the TiO_2 used herein limits operation to aqueous alkaline conditions, which requires an anion exchange membrane to provide ionic conductivity and gas separation capabilities. However, anion exchange membranes remain at the fundamental research level and are not generally designed to be recast in Si microwire arrays while also providing suitable mechanical support when removed from the growth substrate. To-date, attempts to incorporate anion exchange membranes into these devices and thereby obtain a free-standing device failed due to the inability of the membrane casting process to infiltrate the Si microwire array and/or membrane brittleness thwarting attempts to remove the arrays intact from the substrate.

The tandem-junction np^+-Si/FTO/TiO_2 microwire device reported herein demonstrates an efficiency and stability improvement over previously reported devices. This improvement was achieved by combining two high output-voltage junctions with complementary absorption regimes that simultaneously provide intrinsic stability under the designated operational conditions. Incorporation of an intermediate FTO layer provided a sufficiently low resistance

contact between the p^+-Si and TiO_2. Further efforts to develop compatible anion exchange membranes or to improve the performance in acidic media should provide additional improvements that are necessary for application of free-standing devices in scalable solar-driven water-splitting systems.

5 Stabilization of Si Microwire Arrays for Solar-Driven H_2O Oxidation to $O_2(g)$ in 1.0 M KOH(aq) using Conformal Coatings of Amorphous TiO_2

5.1 Motivation

Technologically important, small band-gap semiconductors such as Si are highly attractive materials for use as photoanodes to oxidize water, but are unstable to corrosion and/or passivation under anodic conditions in aqueous electrolytes.[73] Single crystalline n-Si, n-GaAs, n-GaP, n-CdTe, and n-$BiVO_4$ photoanodes have all recently demonstrated enhanced stability (4-100+ hours) under continuous operation for water oxidation to $O_2(g)$ in aqueous alkaline electrolytes, with 100% Faradaic efficiency, by use of electrically conductive, optically transparent, 10-100 nm thick protective films of amorphous TiO_2 deposited by atomic-layer deposition (ALD).[74-77] Arrays of semiconductor microwires or nanowires provide an especially attractive system architecture for the direct production of fuels from sunlight, because such a structure provides a minimal path for ionic conduction, high optical absorption, [78-82] a high surface-area support for electrocatalyst loading[49], and other distinctive, advantageous operational features.[41] The application of conformal protective films to such highly anisotropic structures by use of sputtering or evaporation is expected to be difficult, whereas the self-limiting ALD surface condensation reaction technique is a conformal coating process. Accordingly, we describe herein the use of ALD-deposited amorphous TiO_2 films to enable the continuous

oxidation of water to O_2(g) by Si microwire array photoanodes for > 2200 h in 1.0 M KOH(aq) under simulated 1 Sun illumination conditions.

5.2 Fabrication Methods

To fabricate the structures of interest, arrays of n-type and np^+-radial junction Si microwires were coated with ALD-grown TiO_2,[77] followed by deposition of a nickel-chromium oxide oxygen-evolution catalyst using magnetron-sputtering (see the Appendix A for full experimental details). Figure 5.1a shows a schematic of the process, and Figure 5.1b and c show scanning-electron micrographs (SEM) of the Si microwire arrays before and after deposition of the TiO_2 protective coating (2000 ALD cycles, ~94 nm) and the $NiCrO_x$ catalyst layer (20 min sputtering, ~40 nm planar equivalent), respectively. Figure 5.1d shows a cross-section near the base of a single fully processed (np^+-Si/TiO_2/$NiCrO_x$) microwire within an array, demonstrating that the fabrication produced the desired structure as well as a conformal layer of TiO_2 having a relatively uniform thickness along the height of the wire. A detailed inspection of an individual Si microwire indicated that the $NiCrO_x$ deposited at the top and base of each Si microwire, due to the relatively line-of-site deposition profile of the magnetron sputtering process. Only the regions of the $NiCrO_x$ catalyst on the surfaces of the wires are expected to be electrocatalytically active, due to the electrically insulating SiO_2 on the sample substrate.

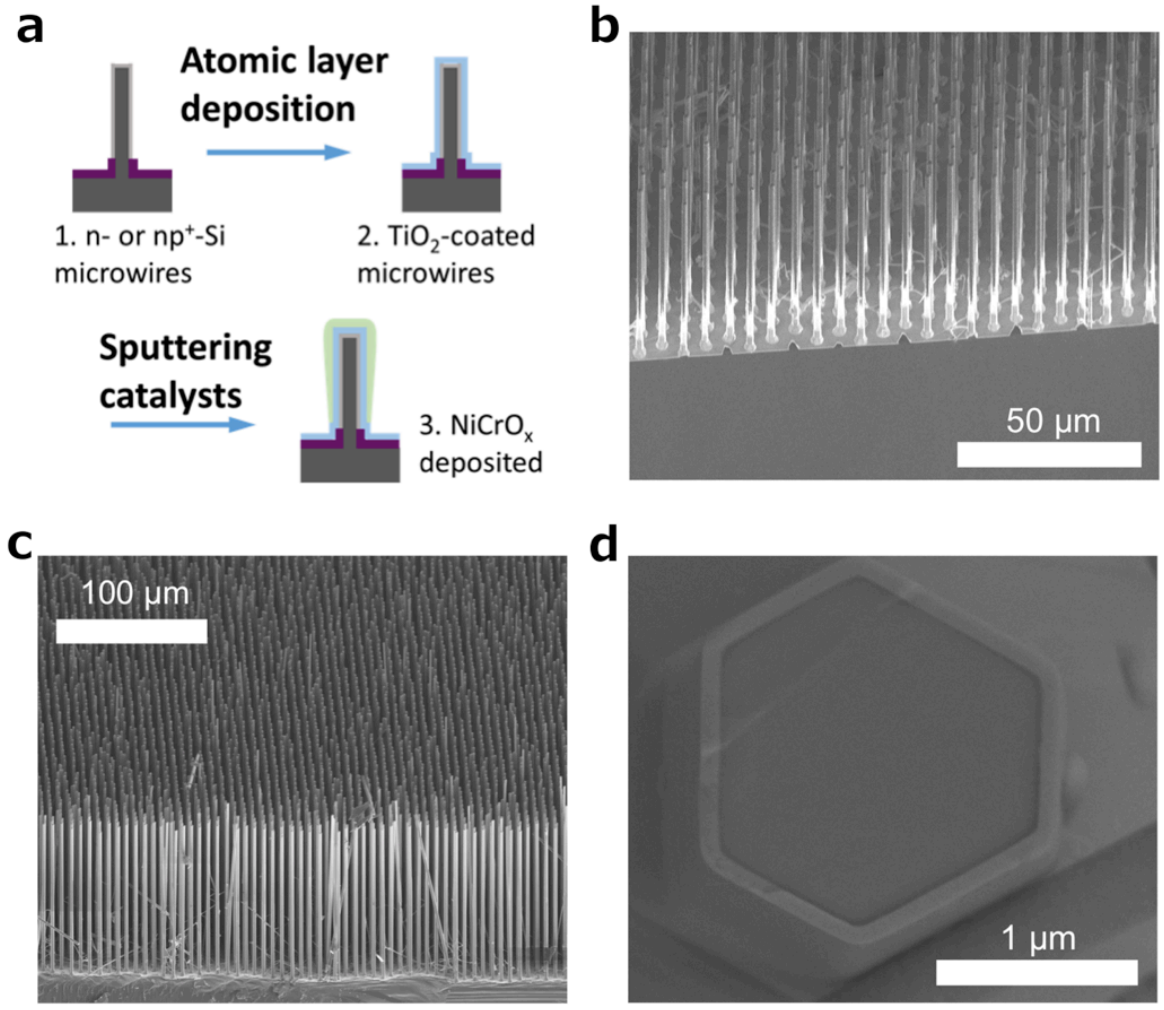

Figure 5.1: Fabrication process and corresponding SEM images of a TiO_2 protected Si microwire array photoanode a) Schematic of a structure that consists of an np^+-Si microwire-array conformally coated with a protective, transparent, and hole-conducting TiO_2 layer, with the TiO_2 layer subsequently coated with a $NiCrO_x$ oxygen-evolution catalyst. b) Scanning-electron micrograph (SEM) images of an np^+-Si microwire-array prior to further processing. c) SEM image of a fully processed microwire array. d) SEM cross-section near the base of a single microwire, showing the conformality of the TiO_2 coating with a thickness of 94 nm.

5.3 Aqueous Photoelectrochemical Behavior

Figure 5.2 shows the current density vs potential (*J-E*) behavior of an np^+-Si/TiO_2/$NiCrO_x$ microwire-array photoelectrode in contact with (a) 1.0 M KOH(aq) (pH = 13.6) and (b) 0.50 M K_2SO_4-0.050 M $K_3Fe(CN)_6$-0.35 M $K_4Fe(CN)_6$(aq) in the presence and absence, respectively, of 100 mW cm^{-2} of simulated Air Mass (AM) 1.5 illumination. Figure 5.2a also depicts the *J-E* behavior of a p^+-Si/TiO_2/$NiCrO_x$ microwire-array electrode in the absence of illumination, to allow for a comparison of the onset potentials for the oxygen-evolution reaction between the illuminated photoanode and a degenerately doped unilluminated p^+-Si anode. The one-electron, outer-sphere, reversible $Fe(CN)_6^{3-/4-}$ redox couple was used to measure the intrinsic energy-conversion properties of the microwire-array photoanodes. Under 100 mW cm^{-2} of simulated Air Mass (AM) 1.5G illumination, the np^+-Si/TiO_2/$NiCrO_x$ microwire-array produced an open-circuit potential (E_{oc}) of -0.62 V vs. the formal potential for water oxidation, $E^{0'}$ (O_2/OH^-), and a light-limited photocurrent density (J_{ph}) of 7.1 mA cm^{-2} in 1.0 M KOH(aq), and produced E_{oc} = -0.44 V vs. the Nernstian potential of the solution ($E(Fe(CN)_6^{3-/4-})$) and J_{ph} = 7.3 mA-cm^{-2} in contact with $Fe(CN)^{3-/4-}$(aq). A diode quality factor of 1.9-2.2 was measured in contact with $Fe(CN)^{3-/4-}$(aq) from the *J-E* data obtained as a function of illumination intensity.[78,83] The intrinsic photoelectrode behavior observed for the np^+-Si/TiO_2/$NiCrO_x$ photoanode in contact with the one-electron, reversible, $Fe(CN)_6^{3-/4-}$ redox system (Figure 5.2b) demonstrated an energy conversion efficiency of 1.8% with a fill factor of 0.54.

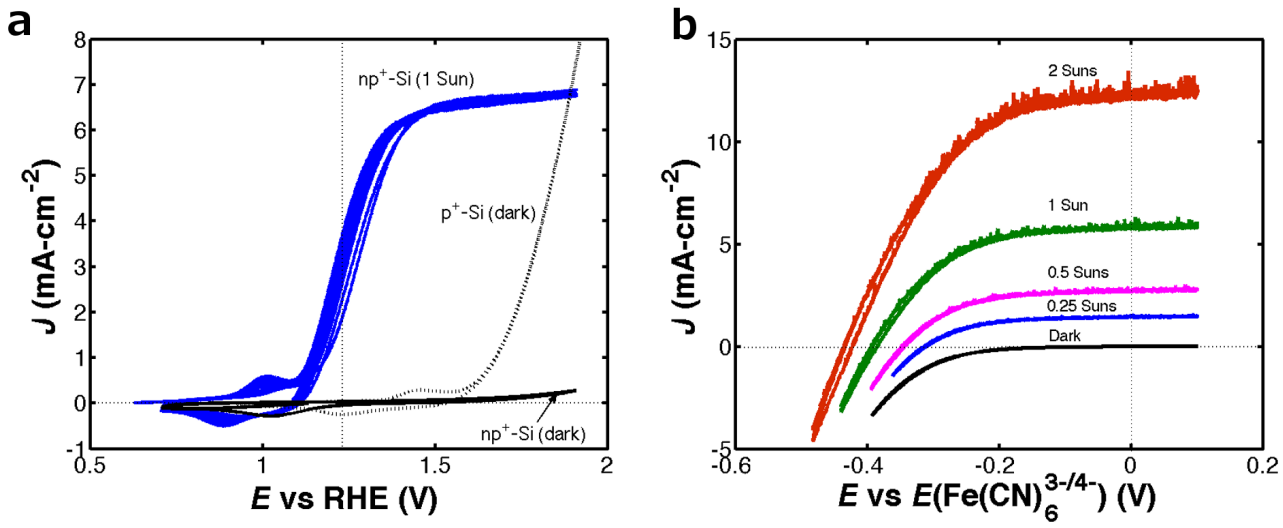

Figure 5.2: PEC behavior of an n-Si/a-TiO_2 microwire array photoelectrode in contact with 1.0 M KOH and $Fe(CN)_6^{3-/4-}$(aq) Current density versus potential performance of np^+-Si/TiO_2/$NiCrO_x$ microwire-array photoelectrodes in contact with a) 1.0 M KOH(aq) and b) $Fe(CN)_6^{3-/4-}$(aq). a) The solid blue curve is under 1-Sun simulated illumination, the solid black curve is under no illumination (dark), and the dashed black curve is the performance of a p^+-Si/TiO_2/$NiCrO_x$ microwire-array electrode. b) The illumination intensity was adjusted using a series of 0.3 optical density neutral-density filters, with the illumination intensity labelled on the plot.

For comparison, Figure 5.3 shows the *J-E* behavior in the presence and absence of illumination, respectively, of n-Si/TiO_2/$NiCrO_x$ microwire-array photoelectrodes in (a) 1.0 M KOH and (b) an aqueous $Fe(CN)_6^{3-/4-}$ solution. In contact with 1.0 M KOH(aq), these samples exhibited E_{oc} = 0.49 V vs. $E^{0'}$ (O_2/OH^-) and J_{ph} = 3.7 mA-cm^{-2} (Figure 5.3a), whereas in contact with $Fe(CN)_6^{3-/4-}$(aq) the n-Si/TiO_2/$NiCrO_x$ microwire-arrays exhibited E_{oc} = 0.18 V vs. $E(Fe(CN)_6^{3-/4-})$ and J_{ph} = 3.1 mA-cm^{-2}. The intrinsic photoelectrode behavior observed for the n-Si/TiO_2/$NiCrO_x$ photoanode in contact with the $Fe(CN)_6^{3-/4-}$ redox system (Figure 5.3b) demonstrated an energy conversion efficiency of 0.3% with a fill factor of 0.51. When measured under nominally identical conditions, all six of the microwire-array photoelectrodes studied herein showed mutually similar photovoltages, but

exhibited variable photocurrent densities with a spread of ~5 mA-cm^{-2}, consistent with a variation in wire height at various locations on the wafer from which the electrodes were fabricated.[84,85] The addition of scattering particles can significantly increase J_{ph} by increasing the illumination path length through the photoactive Si microwire array.[39]

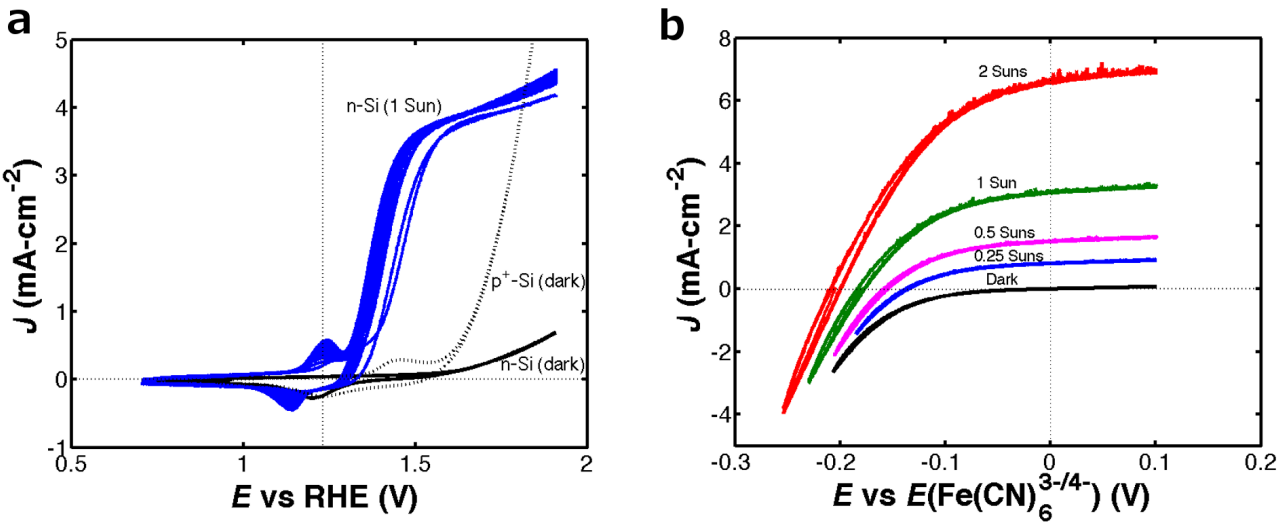

Figure 5.3: PEC behavior of an np$^+$-Si/a-TiO$_2$ microwire array photoelectrode in contact with 1.0 M KOH and Fe(CN)$_6^{3-/4-}$(aq) Current density versus potential data for n-Si/TiO$_2$/NiCrO$_x$ microwire-array photoelectrodes in contact with a) 1.0 M KOH(aq) and b) Fe(CN)$_6^{3-/4-}$(aq). a) The solid blue curve is under 1 Sun simulated illumination, the solid black curve is in the absence of illumination (dark), and the dashed black curve is the performance of a p$^+$-Si/TiO$_2$/NiCrO$_x$ microwire-array electrode. b) The illumination intensity was adjusted using a series of 0.3 optical density neutral-density filters, with the resulting illumination intensity labeled on the plot.

Figure 5.4a shows the external quantum yield (Φ_{ext}) for np$^+$-Si/TiO$_2$/NiCrO$_x$ and n-Si/TiO$_2$/NiCrO$_x$ microwire-array photoelectrodes in contact with 1.0 M KOH(aq). The observed behavior was similar to that obtained previously for microwire-array photocathodes and photovoltaics at normal incidence.[39] The Φ_{ext} exhibited a similar dependence on wavelength for both the np$^+$-Si and the n-Si microwire-arrays, consistent with behavior dominated by absorption and charge-

carrier collection in a microwire array. Integration of the wavelength-dependent spectral response data of protected np^+-Si and n-Si microwire-arrays with respect to the AM 1.5G solar spectrum yielded calculated photocurrent densities of 7.9 mA-cm^{-2} and 2.9 mA-cm^{-2}, respectively, in excellent agreement with the J_{ph} values measured from the *J-E* behavior.

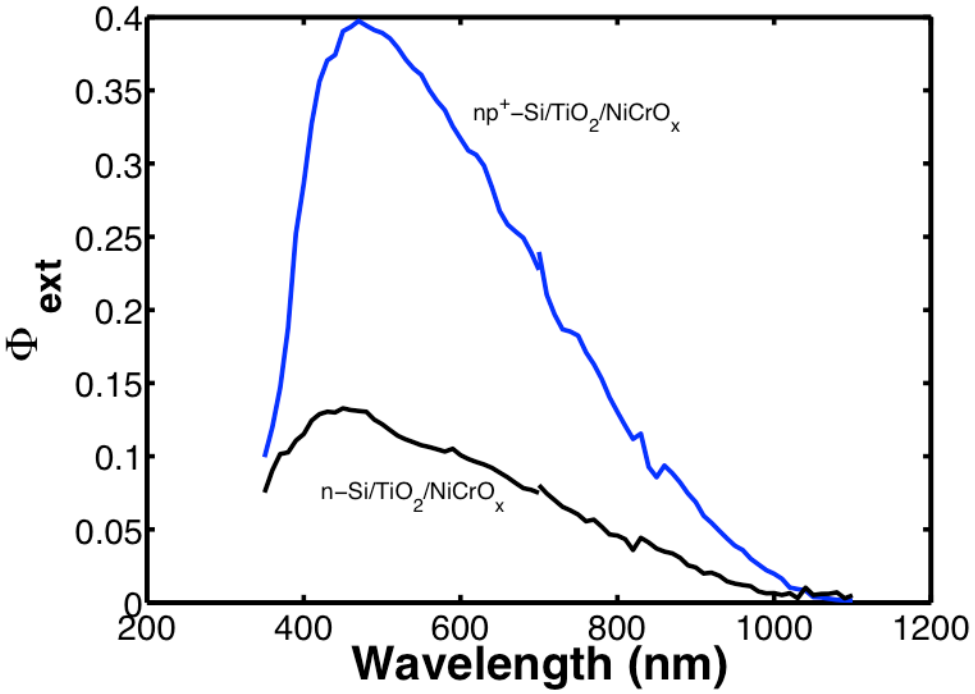

Figure 5.4: External quantum yield of n-Si and np^+-Si microwire array photoelectrodes in 1.0 M KOH External quantum yield (Φ_{ext}) versus wavelength plot of representative protected n-Si and np^+-Si microwire-array photoelectrodes in contact with 1.0 M KOH(aq).

Figure 5.5a shows the time dependence of the photocurrent density of an np^+-Si microwire-array under potentiostatic control at 0.36 V vs. $E^{0'}$ (O_2/OH^-) (0.70 V vs. a Hg/HgO reference electrode). Figure 5.5b shows the *J-E* data at 10 h intervals throughout the stability test, showing no significant change in J_{ph}, E_{oc} or fill factor during the stability evaluation. As shown in Figure 5.5c, a comparison between the amount of O_2(g) expected based on Coulomb's law and the amount

of O_2(g) detected using a calibrated fluorescent O_2(g) probe indicated ~100% Faradaic efficiency for oxygen evolution. Assuming four electrons per Si atom dissolved, the total number of coulombs of charged passed during the stability test, 6000 C, exceeded by a factor of 20 the 300 C of charge that would have been required to dissolve the entire Si microwire array. Furthermore, assuming that 10 nm of oxide formation would result in complete passivation of the electrode, the amount of charge passed establishes a lower limit of 9×10^4 on the branching ratio for water oxidation to O_2(g) relative to oxidation of the Si.

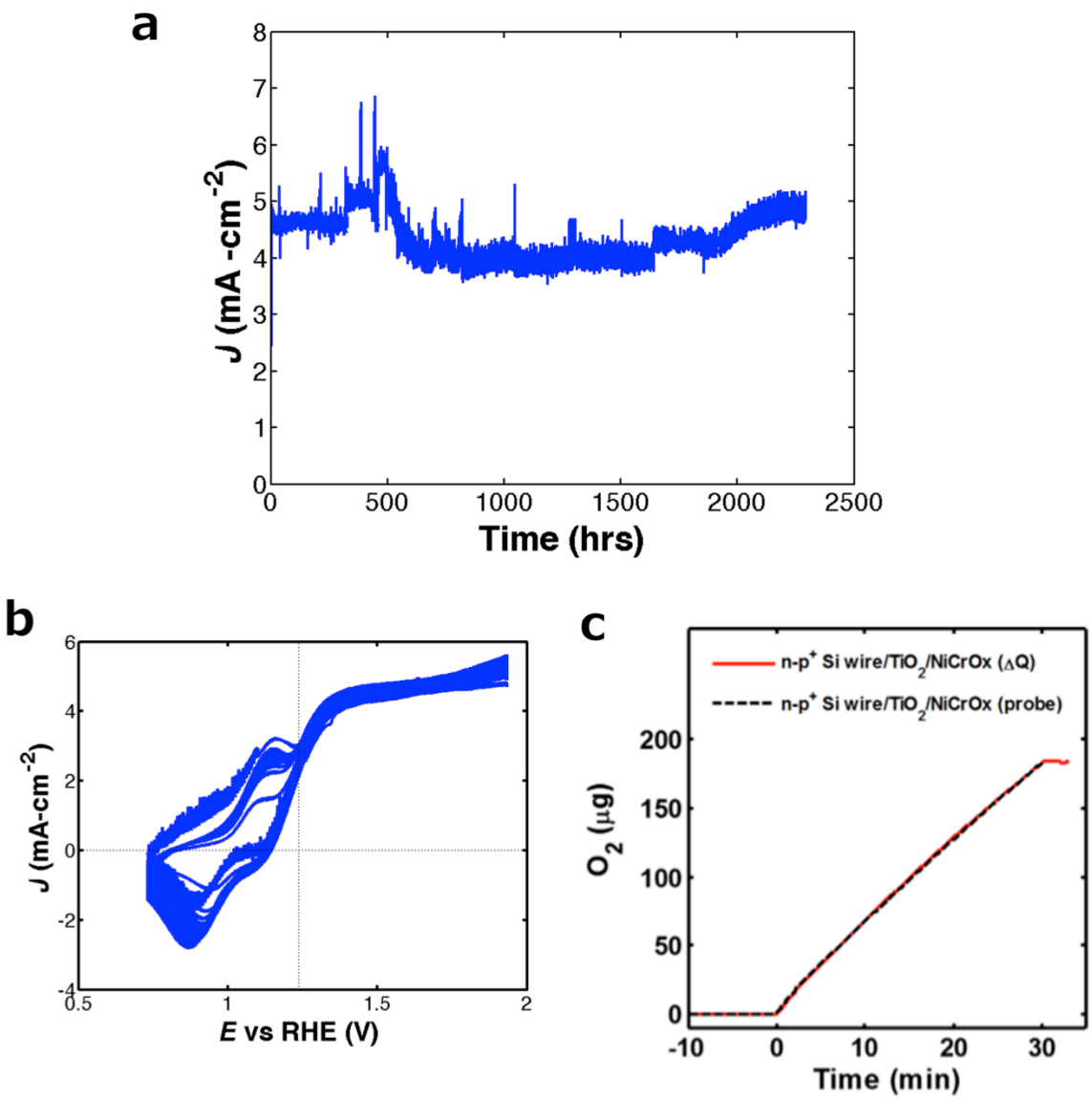

Figure 5.5: >2200 hour stability and oxygen evolution faradaic efficiency of np$^+$-Si/a-TiO$_2$ microwire array photoelectrode a) Current density versus time for an n-p$^+$-Si/TiO$_2$/NiCrO$_x$ microwire-array photoelectrode under 1 Sun simulated illumination in 1.0 M KOH(aq) under potential control at 0.36 V vs $E^{0'}$ (OH^-/O_2). b) Current density versus potential behavior of cyclic voltammograms taken at 10 h intervals throughout the duration of the stability test. c) Oxygen production as a function of time in 1.0 M KOH(aq) while under potential control at 0.36 V vs $E^{0'}$ (OH^-/O_2). The Faradaic efficiency for oxygen evolution, ~100%, was determined by comparing the observed oxygen produced relative to the amount expected based on the total current passed in conjunction with the use of Faraday's law.

5.4 Discussion and Conclusions

Accounting for the ~20% capacity factor of sunlight, the 2200 h of continuous operation contained the same amount of charge as would be passed during > 1 year of outdoor operation. Because lower current densities away from peak illumination times would likely increase the stability, this projected > 1 year stability plausibly represents a lower limit on the actual stability of the NiO_x-coated Si photoanodes under operational conditions. A detailed failure analysis study and validated accelerated testing protocols, additionally incorporating possible effects of temperature cycling and extended periods of no photocurrent current due to day/night cycling, would clearly be required to establish the ultimate limit on the stability of the photoanodes described herein. The high internal surface area of a highly anisotropic structure such as a microwire array produces a correspondingly low current density at the areas exposed to the electrolyte. This low current density is expected to beneficially reduce the rate of light-intensity-dependent photocorrosion or photopassivation processes, because the photon flux per projected geometric area provided by sunlight produces minority- carrier currents that are distributed over a large internal surface area of the solid/liquid contact in the internal volume of a microwire-array. Consistently, the microwire arrays exhibited a greater degree of stability than crystalline Si electrodes protected by amorphous TiO_2 films and operated at 30 mA cm^{-2}, which exhibited a small but significant decay in photocurrent after 24 h of continuous operation in the same electrolyte.[77] Incorporation of the np^+-Si/TiO_2/$NiCrO_x$ photoanode into a complete water splitting device operating at 10% solar-to-hydrogen efficiency would require a photocathode capable of producing >10 mA-cm^{-2} at 1.5 V and addition of scattering particles to increase the absorption and current density in the Si microwires.[39] For efficient operation, such a

photocathode, operating near its Shockley-Quiesser limit, would need to have a band-gap of ~2.0 eV with either a buried junction or proper band positioning relative to the hydrogen evolution potential. The observations reported herein therefore illustrate an additional advantage of the amorphous TiO_2-based protection strategy in that the deposition method, ALD, is especially well suited to be compatible with a wide range of high-efficiency materials while also being compatible with a broad range of morphologies associated with highly anisotropic structures of the light absorber.

6 Functional Integration of Ni-Mo Electrocatalysts with Si Microwire Array Photocathodes to Simultaneously Achieve High Fill Factors and Light-Limited Photocurrent Densities for Solar-Driven Hydrogen Evolution

6.1 Introduction

Photon management is an important attribute of photoelectrodes used for solar-driven water-splitting, especially for device architectures that incorporate optically opaque electrocatalyst coatings on the surface of a light absorbing material.[49,86-88] Specifically, the fill factor (*ff*) is generally negatively correlated with the light-limited photocurrent density (J_{ph}), because increases in catalyst loading increase the *ff*, but also produce larger parasitic optical absorption losses and thus decrease the value of J_{ph} (Figure 6.1).[49] Such behavior is especially apparent for earth-abundant electrocatalysts for the hydrogen-evolution reaction (HER), which are generally optically opaque and require large mass loadings (≥ 1 mg cm^{-2}) to achieve the requisite catalytic activity.[89-91] Similar issues can also preclude optimal functional incorporation of currently available electrocatalysts for the oxygen-evolution reaction (OER) into integrated photoanode structures for the solar-driven oxidation of H_2O to $O_2(g)$.[39,92]

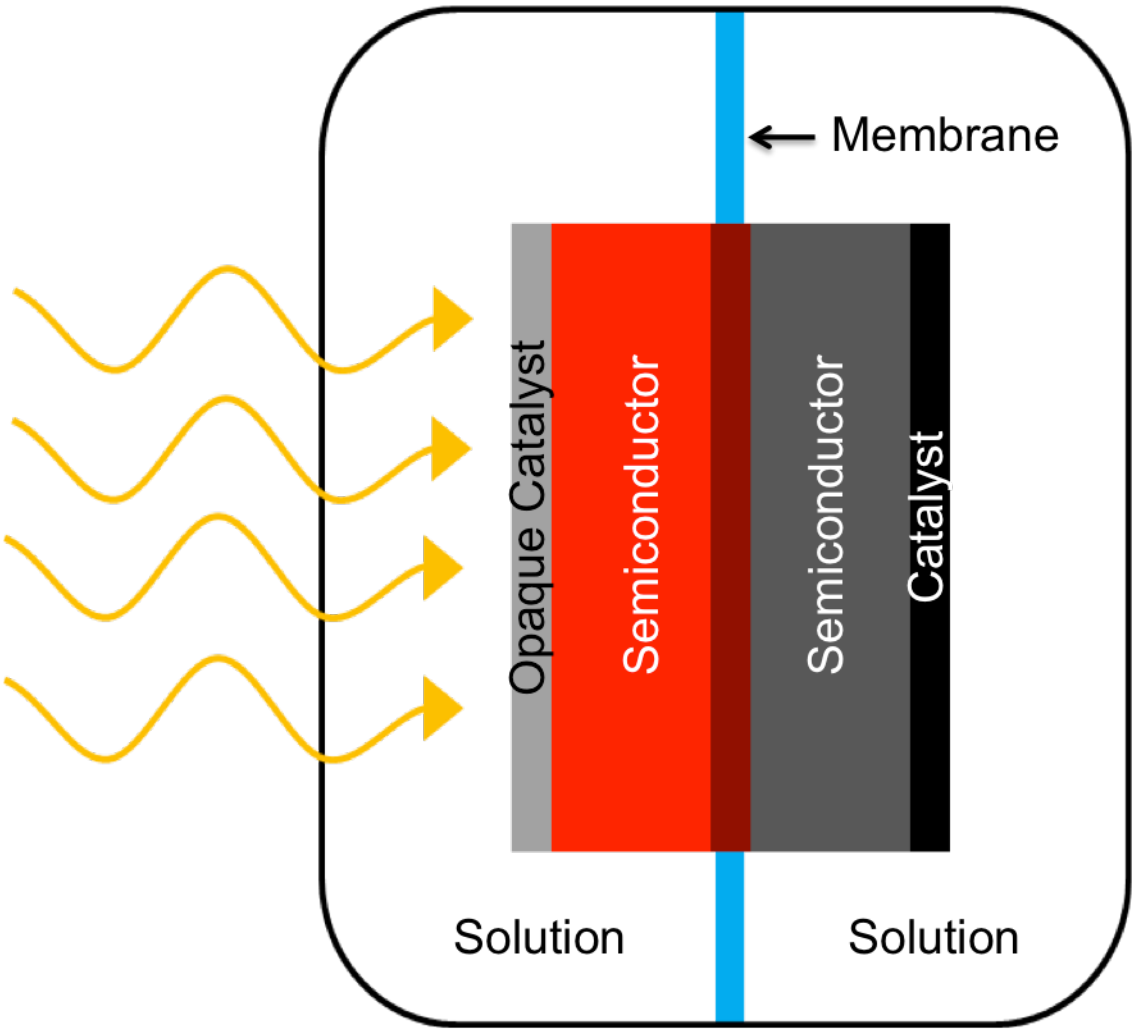

Figure 6.1: Generic planar water splitting device demonstrating deletrious catalyst light absorption a) Schematic of a water-splitting device incorporating two planar light absorbers in a tandem configuration, two electrocatalysts, and a single tunnel junction to allow serial addition of the photovoltages produced by each semiconducting light-absorber unit. The opaque catalyst on the light-incident surface (left side) is the source of the trade-off between the fill factor (*ff*) and the light-limited current density (J_{ph}).

For planar photoelectrode architectures, various options to mitigate this deleterious tradeoff between catalytic activity and optical transparency have been developed. For discrete photovoltaic (PV)-biased electrolysis systems[7,49,86-88], the PV device can be connected electrically

to discrete, catalytic electrodes that do not physically obscure incoming light from the PV cell, with the interfacial reactions being performed by majority carriers.[16,49] Alternatively, in photoelectrode structures composed of a single photoabsorber, a transparent back contact can be used in conjunction with "backside" illumination so that the catalyst layer is not in the optical path of the semiconductor.[28,89-91] For integrated photoelectrodes in which the interfacial reactions can be performed by photogenerated minority carriers (as well as by majority carriers, for structures that contain a buried junction[7,39,92]), the thickness of the electrocatalyst film can be adjusted to obtain an optimum compromise between the optical density and activity of the electrocatalyst film. This type of optimization favors the use of an extremely thin (< 5 nm) catalytic layer, at the expense of catalytic activity.[92] In certain instances, nanostructuring can produce optically transparent, highly active films of noble metal electrocatalysts.[88] Yet another method involves optimization of the spatial location and areal coverage of islands of an active, but optically absorbing electrocatalyst film, by use of a photolithographic or shadow mask.[93] This approach is analogous to the use of grid-line top contacts in photovoltaics.

Absorbers that are structured in three dimensions, such as Si microwire arrays[43,46,94,95], provide an alternative, general approach to ameliorating the negative correlation between the *ff* and J_{ph}. In such systems, a relatively high loading of catalyst can be positioned at the base of a high-aspect-ratio microwire array, leaving exposed a large proportion of the array (Figure 6.2). For example, earth-abundant metal catalysts such as Ni–Mo[89], Ni or Co phosphide[90,91], or Mo chalcogenides[96] with mass loadings on the order of 1 mg cm^{-2} (i.e., several μm thick) exhibit comparable geometric HER activity to a planar > 10 nm thick Pt film. By comparison, the depth

over which light can be completely absorbed in a sparse silicon microwire array with appropriate scattering elements is on the order of 100 μm. The relatively low proportional volume occupied by high catalyst mass loadings can therefore enable high overall catalytic activity while preserving optical accessibility to the majority of the light-absorber material.

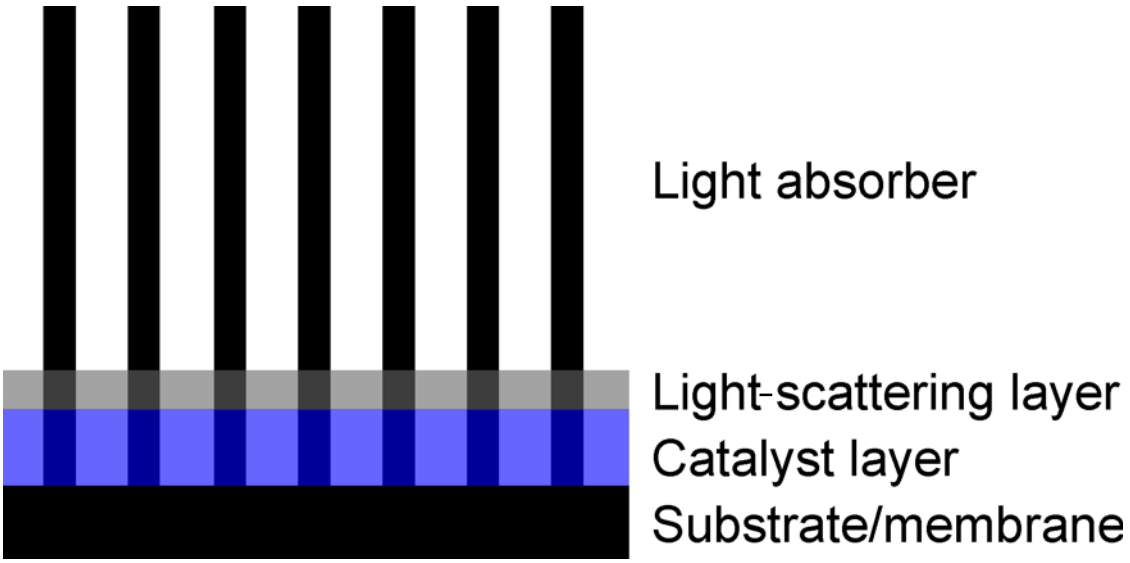

Figure 6.2: Si microwire-catalyst design to decouple light absorption and catalytic activity Schematic depiction of the membrane-electrode assembly (MEA)-type hydrogen-evolving photocathode based on arrays of Si microwires embedded in a membrane or supported on a substrate, with a layer of a non-noble catalyst deposited at the base of the array and covered by a light-scattering layer.

A recent study has shown that a CoP HER electrocatalyst could be deposited at the base of a Si microwire array, yielding activity toward photoelectrochemical hydrogen evolution comparable to that of a control sample that instead used Pt as the HER electrocatalyst.[97] Si microwire arrays, however, do not absorb a large proportion of incoming, normally incident photons on the "first

pass" of such photons through the structure of the device.[39] As a result, significant parasitic optical absorption occurs in such devices even with the catalyst film deposited exclusively at the base of the array. An improved device structure, which we denote as the "MEA" architecture, resembles a fuel cell or an electrolyzer membrane-electrode assembly (MEA) (Figure 6.2). Such a structure is characterized by a Si microwire array on the order of 100 μm in height with a 5–10 μm thick porous catalyst layer consisting of an earth-abundant electrocatalyst, such as Ni–Mo, Mo sulfide, or a transition-metal phosphide, in addition to a 1–3 μm thick porous light-scattering layer, such as particulate TiO_2 or another high-dielectric scattering material. The catalyst layer is analogous to the one found in a conventional MEA, whereas the light-scattering layer serves as an optical scattering element as well as a gas-diffusion layer. The microwires act as current collectors by absorbing solar photons and producing sufficient electrochemical potential to effect the HER.

In this approach, if the catalyst and scattering layers are both sufficiently porous, reactant species (e.g., water or H^+) can diffuse through and hydrogen gas can diffuse out of the internal volume of the device. However, when incident on the scattering layer, photons will be reflected laterally and will therefore pass multiple times through the Si microwires. An analogous light-scattering design was proposed and validated for Si microwire photovoltaics, and high light-limited photocurrent densities (> 15 mA cm^{-2} at 100 mW cm^{-2} of Air Mass (AM) 1.5G simulated illumination intensity) were indeed obtained in that system.[39,40] In principle, the MEA approach allows for simultaneous maximization of the catalytic activity and optical absorption in the semiconducting material, even when a relatively large mass loading of electrocatalyst is required.

In this work, we have modeled and validated the MEA design using Si microwire-array photocathodes to drive the HER in conjunction with a Ni–Mo nanopowder catalyst and a TiO_2 light-scattering layer. All experimental details can be found in Appendix A.

6.2 Photoelectrochemical and Optoelectronic Modeling Results

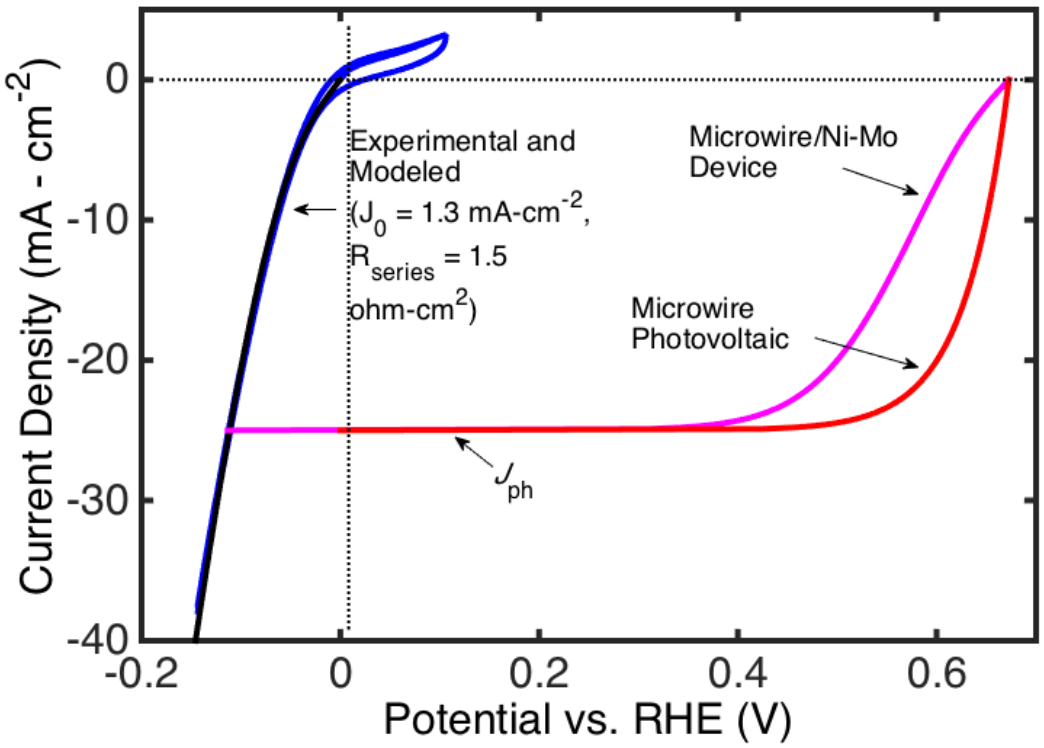

Figure 6.3: Modeled behavior of Si microwire MEA design Current-density versus potential (*J*-*E*) behavior obtained from the modeling of an n^+p-Si microwire-array membrane-electrode assembly (MEA, magenta curve) and for a stand-alone n^+p-Si microwire-array photovoltaic device wired to a discrete, purely catalytic electrode (red curve). Ni-Mo was used as the hydrogen-evolution catalyst in both cases, and the dark catalytic activity of the catalyst was modeled according to experimental observations (blue curve).

Figure 6.3 shows the modeling results for a photocathode consisting of an n^+p-Si microwire array in conjunction with a Ni–Mo nanopowder catalyst covered by a porous TiO_2 light-scattering overlayer. To provide a first-order approximation to the maximum expected device performance for such a structure, the modeling treated the integrated photoelectrode as a zero-dimensional, series-connected n^+p-Si junction coupled to a catalyst layer and to a resistive circuit element. The increased dark-current junction area (γ in Equation A.4.2), and the series resistance required to transport electrons down the length of the microwire through the n^+-Si emitter to the catalyst, were considered explicitly. The light-limited current density was obtained through two-dimensional full-wave electromagnetic simulations of a Si microwire array architecture.[87,88] The modeling indicated that utilization of a stand-alone n^+p-Si microwire array PV device having a solar energy-conversion efficiency of 12.9% could, in principle, yield a maximum ideal regenerative cell efficiency (η_{IRC})[98] of 11.2% based on the hydrogen-evolution half-reaction being performed at such a photocathode. This value is essentially the same as the value that would be obtained by wiring the respective photovoltaic device to a discrete, catalytic electrode obtained by using a high mass-loading of the Ni–Mo HER catalyst on an inert conducting substrate.

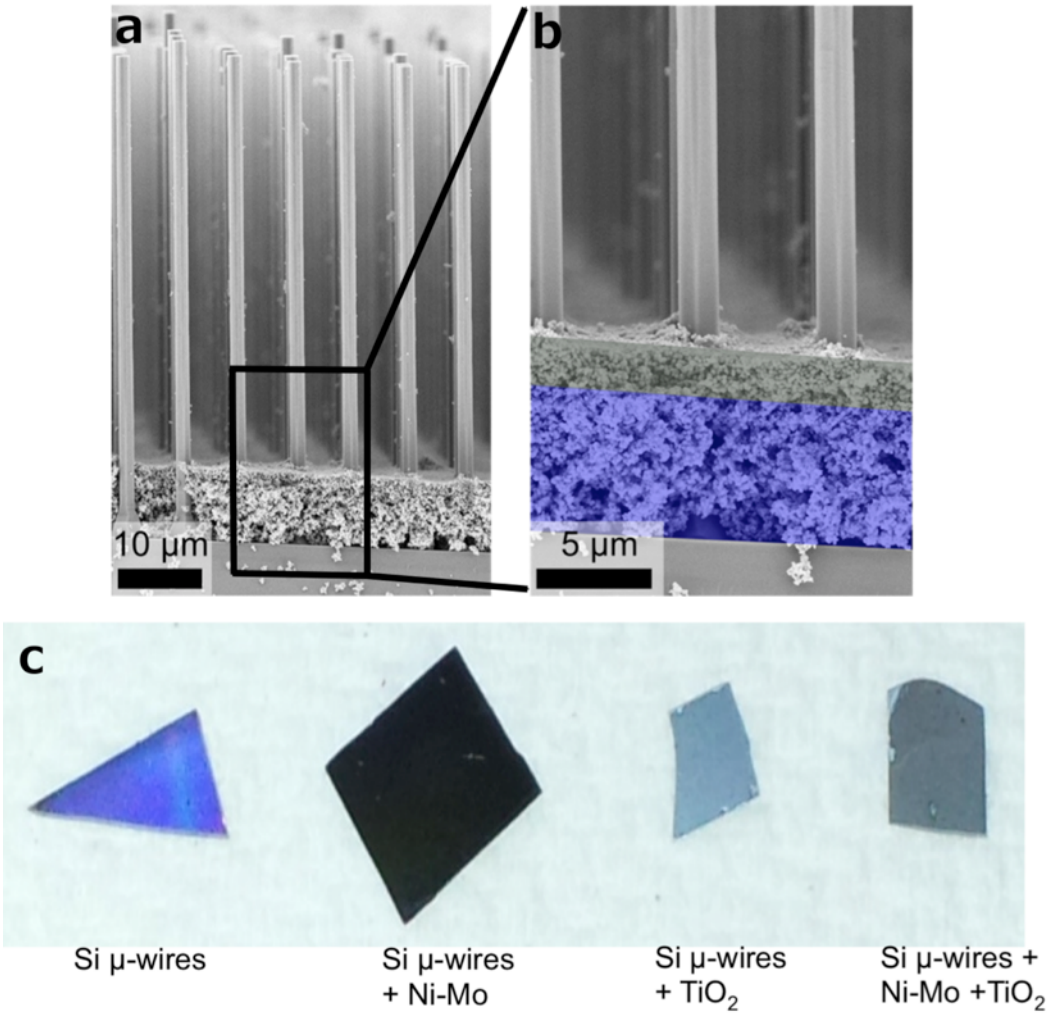

Figure 6.4: SEM images of Si microwire MEA device and optical images of Si microwire MEA variations a) Scanning-electron micrographs of a silicon microwire array onto which a layer of Ni–Mo nanopowder and a layer of TiO_2 light-scattering particles have been deposited sequentially. b) Detail of the boxed area in a, highlighted to delineate the Ni-Mo nanopowder layer beneath the layer of TiO_2 particles. c) Optical image of four microwire arrays with different nanoparticulate depositions within the array.

Figure 6.4a,b shows a scanning-electron micrograph of a Si microwire array coated at the base by a layer of Ni–Mo nanopowder, with the Si and Ni–Mo bound together by a small quantity of poly-tetrafluoroethylene (PTFE). The structure also contained an overlayer of TiO_2 nanoparticles bound together with a Nafion ionomer, in accord with the full device structure depicted

schematically in Figure 6.2.[99] Figure 6.4b has been highlighted to delineate the layers of Ni–Mo and TiO_2, respectively, and clearly demonstrates the successful fabrication of the desired MEA photocathode structure. Figure 6.4c shows an optical image of four microwire samples. A bare Si microwire array was iridescent and reflective, similar to the starting wafer prior to microwire growth, because of the highly ordered, sparse microwire array. However, the addition of a Ni-Mo catalyst layer altered the appearance to a matte black, due to the optical absorption in both the microwires and the Ni-Mo electrocatalyst. Deposition of a nanoparticulate TiO_2 layer directly onto the base of the Si microwire array, or over a Ni–Mo film, yielded a gray photoelectrode, consistent with scattering of a large proportion of the incoming light into the vertically oriented Si microwires. The sample that contained an underlying Ni-Mo layer was slightly darker, due to imperfect Ni-Mo deposition leaving some residual optically absorbing catalyst on the sidewalls of the microwires.

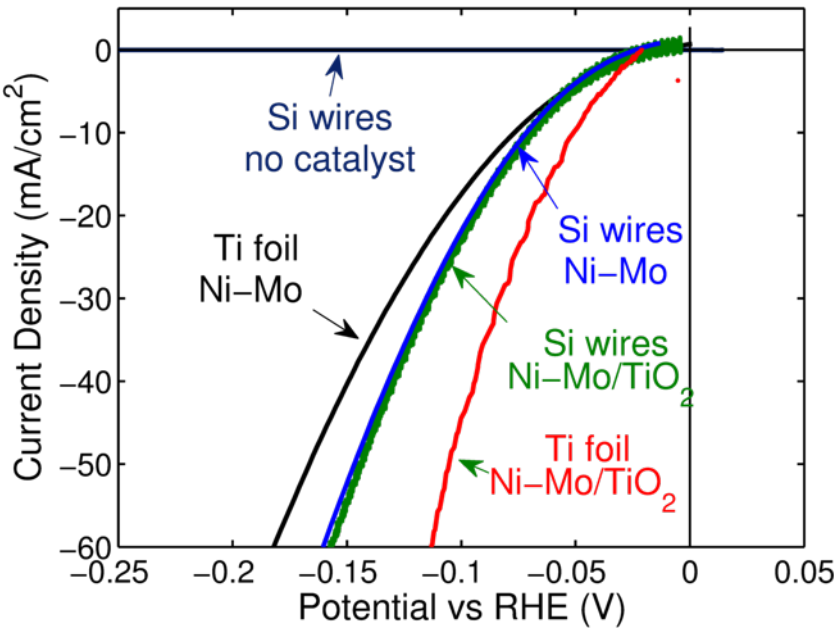

Figure 6.5: Dark catalytic performance of Ni-Mo electrocatalyst in Si microwire MEA configurations Dark *J-E* behavior for electrodes with the noted compositions. The Si microwire

samples were degenerately doped p-type and were metallized with Ag to minimize the interfacial contact resistance. All of the samples were evaluated in 1.0 M H_2SO_4(aq), and Ni–Mo samples had mass loadings of ~1 mg cm^{-2}, except for the Ti foil Ni–Mo/TiO_2 sample, which had a mass loading of ~3 mg cm^{-2}.

Figure 6.5 shows the *J-E* behavior for dark HER electrocatalysis by Ni–Mo nanopowders deposited on planar Ti substrates, as well as for Ni-Mo nanopowders deposited at the bases of degenerately doped p-type Si microwire arrays (p^+-Si MWs), with and without overlayers of TiO_2 particles, respectively. Before catalyst deposition, the Si microwire arrays were metallized with Ag and annealed to minimize any effects of interfacial contact resistance with the catalyst materials. As indicated in Figure 6.5, the dark catalytic HER performance of the Ni–Mo films on the Si microwires matched, or slightly exceeded, that exhibited by the same loading of pure Ni–Mo nanopowder on planar Ti electrodes.

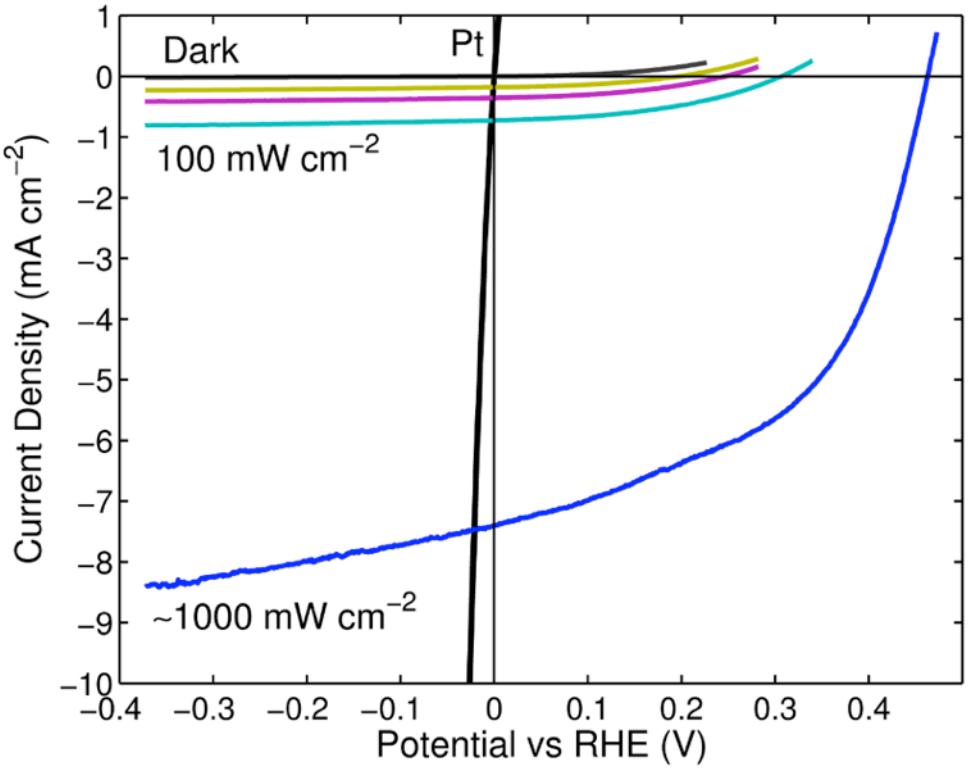

Figure 6.6: PEC performance of pn^+-Si/Ni-Mo microwire photocathode under a variety of illumination intensities Current-density versus potential (*J-E*) behavior of a planar n^+p-Si/Ni–Mo/TiO_2 photocathode in contact with 0.5 M H_2SO_4(aq) over a range of illumination intensities from dark to ~10 Suns, with the light having an AM 1.5G simulated spectral distribution. A polished Pt button control electrode is shown for reference.

Figure 6.6 depicts the *J-E* behavior observed for illuminated planar Si n^+p-junction photoelectrodes coated with a Ni–Mo/TiO_2 MEA composite film. For Ni-Mo catalyst mass loadings on the order of 1 mg cm^{-2}, the catalyst and scattering film produced nearly complete blocking of the incident light. For example, with the MEA layers present, the planar n^+p-Si device produced $|J_{ph}| < 1$ mA cm^{-2}, as compared to $|J_{ph}| > 25$ mA cm^{-2} for low loadings of Pt on planar n^+p-Si photocathodes.[37] Increasing the light intensity to ~10 Suns resulted in $J_{ph} \approx -7.5$ mA cm^{-2}, accompanied by a rapid onset of cathodic photocurrent, attesting to the high activity of the Ni–Mo catalyst. Similar results were obtained for Ni–Mo films alone on planar Si substrates, attesting to the extremely high optical opacity of a μm-thick, nanostructured, metallic Ni-Mo catalyst film.

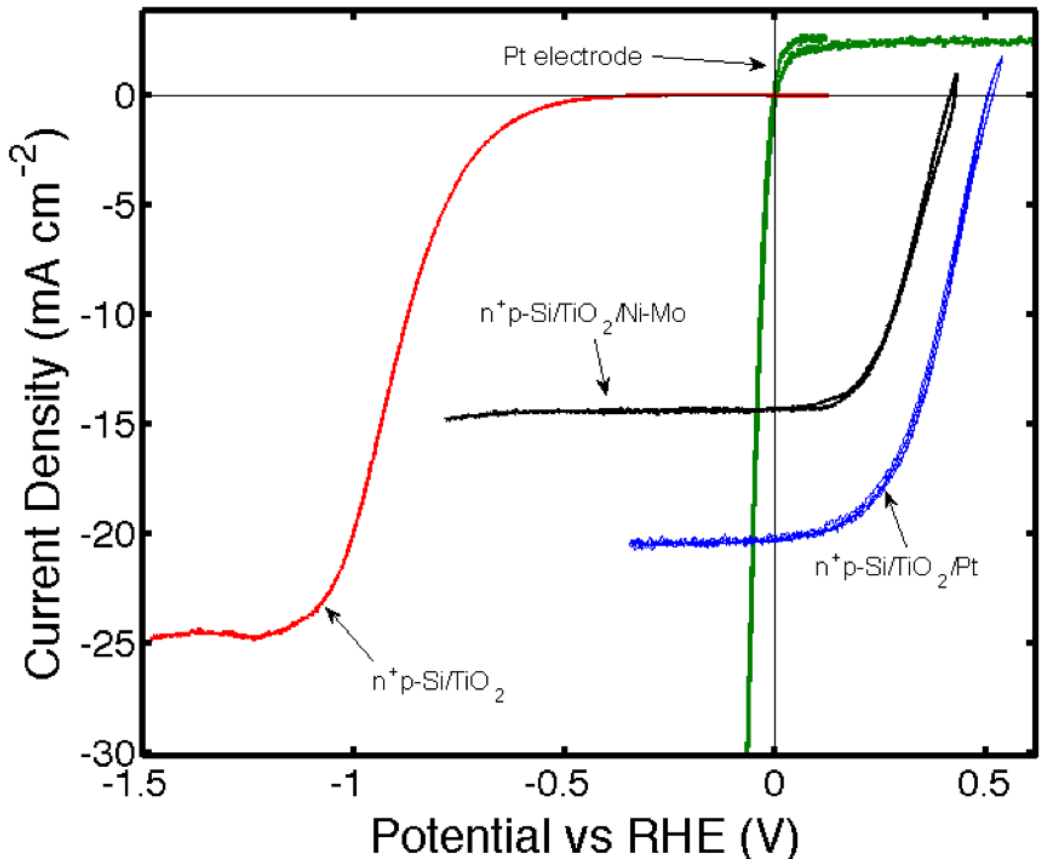

Figure 6.7: Behavior of the best-performing Si microwire array MEA photocathodes of each type Current-density versus potential (*J-E*) behavior of the best-performing Si microwire-array devices prepared in this work, as well as for control samples involving Si microwires without the catalyst (n^+p-Si/TiO_2) and instead utilizing only a Pt electrode in the dark.

Figure 6.7 presents the *J-E* behavior of the best-performing Si n^+p-junction microwire array devices prepared in this work that also contained electrocatalyst and/or scattering composites. To investigate the maximum light-limited current density generated solely by the n^+p-Si microwires, a TiO_2 scattering layer was introduced at the base of such a microwire array to remove any influence from the growth substrate and to increase the length of the optical path through the microwires. Without a catalyst, the light-limited current densities for such a structure approached 25 mA cm^{-2}, in agreement with two-dimensional full-wave modeling

simulations. However, illuminated Si microwire arrays without an electrocatalyst exhibited negligible photocurrent density at potentials positive of 0 V vs RHE. In contrast to the behavior without a catalyst, deposition of 2 mg-cm^{-2} of Ni–Mo at the base of the microwire array produced similar J_{ph} values and fill factors to those observed when Pt was electrolessly deposited on the microwire sidewalls (Figure 6.7).

Table 6.1: Figures of merit for the best-performing Si microwire devices of each type

Device	V_{oc} (mV)	J_{sc} (mA cm^{-2})	*ff*	η_{IRC} (%)
TiO_2 layer	n/a	25	0	0
TiO_2/Pt	510	20.2	0.49	5
TiO_2/Ni–Mo	420	14.3	0.48	2.9

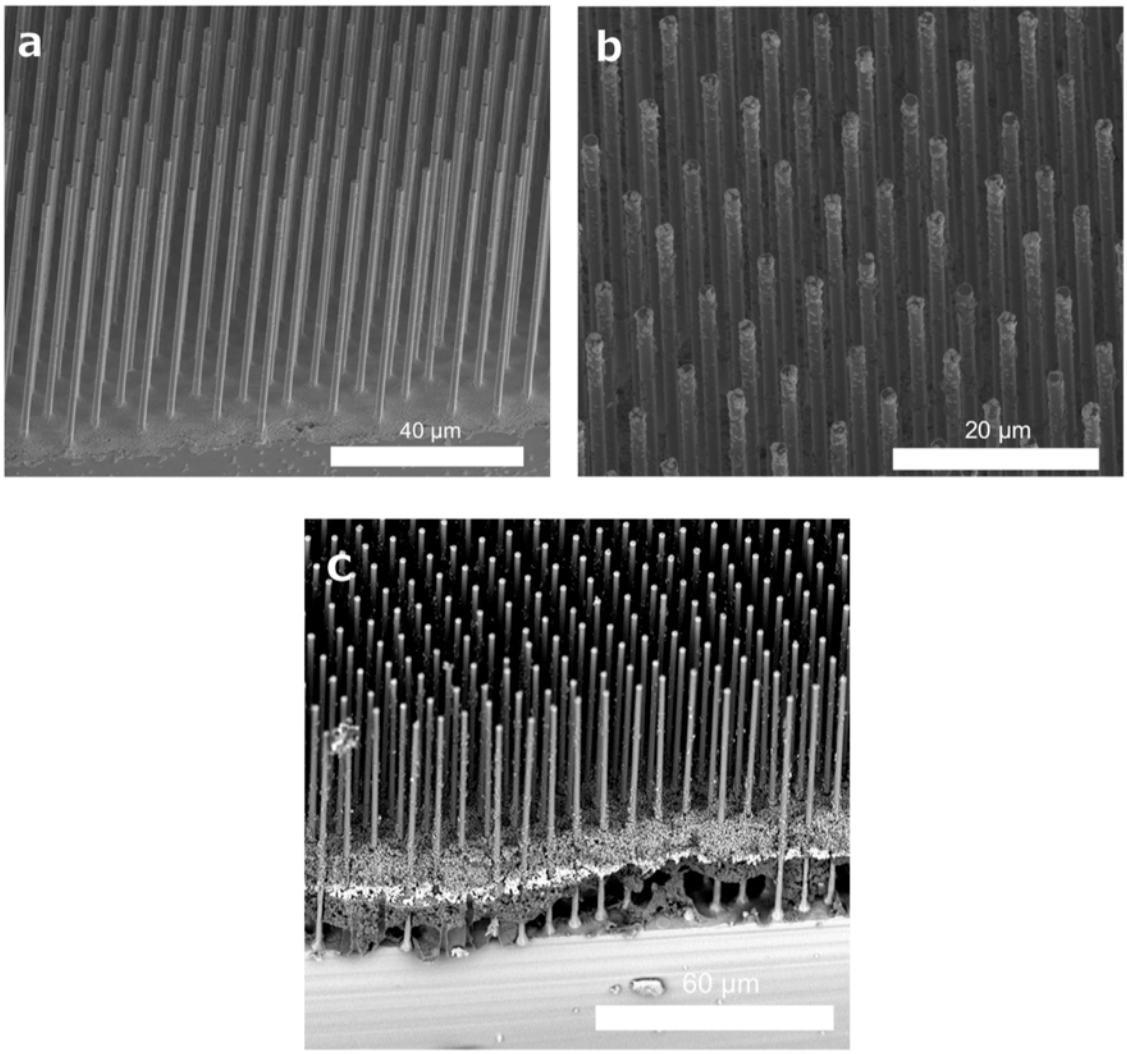

Figure 6.8: SEM images of the best-performing devices prepared in this work a) Microwire array with a TiO_2 scattering layer only; b) Microwire array with a TiO_2 scattering layer as well as with electrolessly deposited Pt catalyst at the tops of the microwires; c) Ni–Mo/TiO_2/Si microwire array full MEA device.

Table 6.1 presents the compiled results for photoelectrodes of each type, and Figure 6.8 presents SEM images each type of device. The best-performing MEA-type device incorporating the Ni–Mo HER catalyst exhibited V_{oc} = 0.42 V, J_{sc} = -14.3 mA cm^{-2}, and a fill factor, *ff* = 0.48, resulting in η_{IRC} = 2.9%, without any corrections for solution or mass-transport losses. This efficiency value exceeds previous values of η_{IRC} = 2.2% produced by electrodeposition of Ni–Mo onto Si n^+p-

junction microwires.[16,49] For comparison, a device with a TiO_2 scattering layer and a Pt catalyst electrolessly deposited on the sidewalls of the microwires produced V_{oc} = 0.51 V, J_{sc} = -20.2 mA cm^{-2}, and *ff* = 0.49, resulting in η_{IRC} = 5.0%. Performance statistics are given in Table S1 for MEA-type device electrodes along with n^+p-Si/Pt planar electrodes.

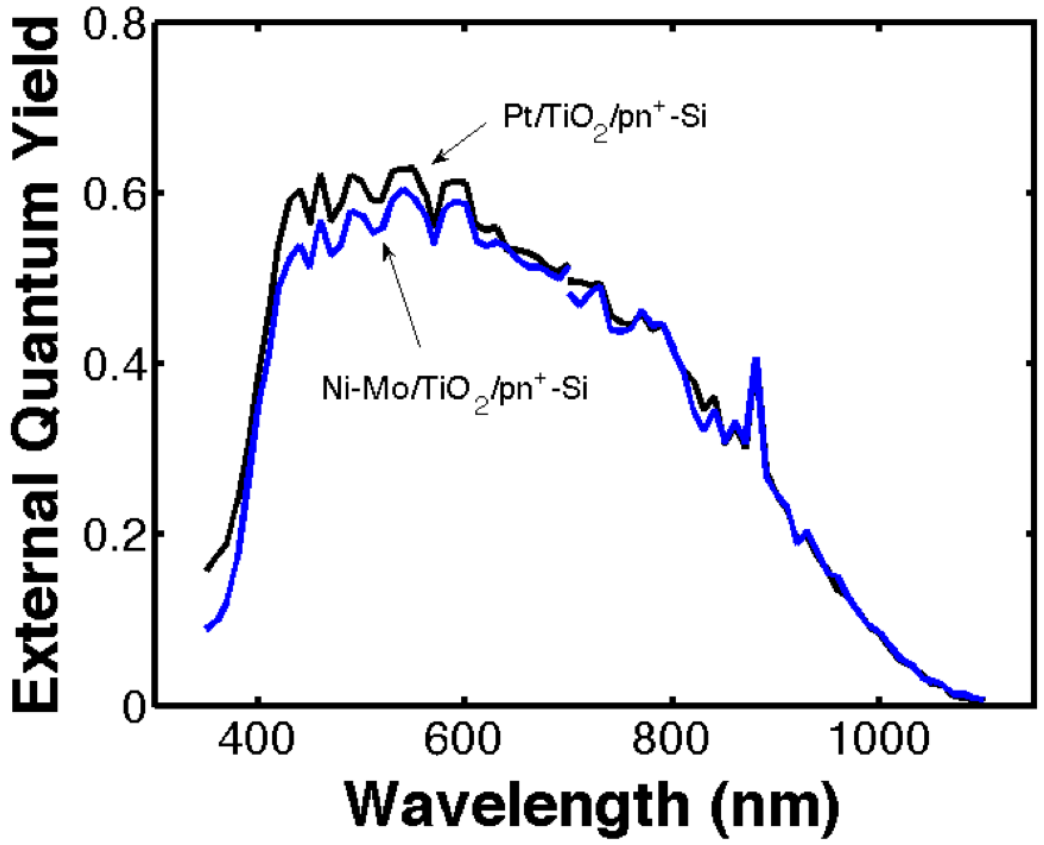

Figure 6.9: Spectral response behavior of best-performing Si microwire array MEA type devices Spectral response data for the best-performing n^+p-Si microwire-array photocathode loaded with Ni–Mo and TiO_2 scattering particles (blue curve) and for the best-performing n^+p-Si microwire-array photocathode loaded with Pt and TiO_2 scattering particles (black curve). Integration of each data set with the AM 1.5G spectrum binned at the same intervals (50 nm) resulted in light-limited photocurrent densities of 15.8 and 17.5 mA cm^{-2} for the Ni–Mo and Pt samples, respectively. The slightly lower integrated current density than the J_{sc} measured for the Pt sample could be due to

morphological changes in the Pt between the *J-E* and spectral response measurements (>1 month).

Figure 6.9 shows the spectral response data for the best-performing Ni–Mo/TiO_2 and Pt/TiO_2 devices. Integration of the spectral response data with the AM 1.5G spectrum produced light-limited photocurrent densities of 15.8 and 17.5 mA cm^{-2} for the Ni-Mo/TiO_2 and Pt/TiO_2 devices, respectively. These values reflect the trend observed in the *J-E* behavior of each device (c.f.Figure 6.7). Consistent with previous reports[37,92], the maximum external quantum yield for the Pt-deposited sample was ~0.6 at ~540 nm, with a monotonic decrease at longer wavelengths.

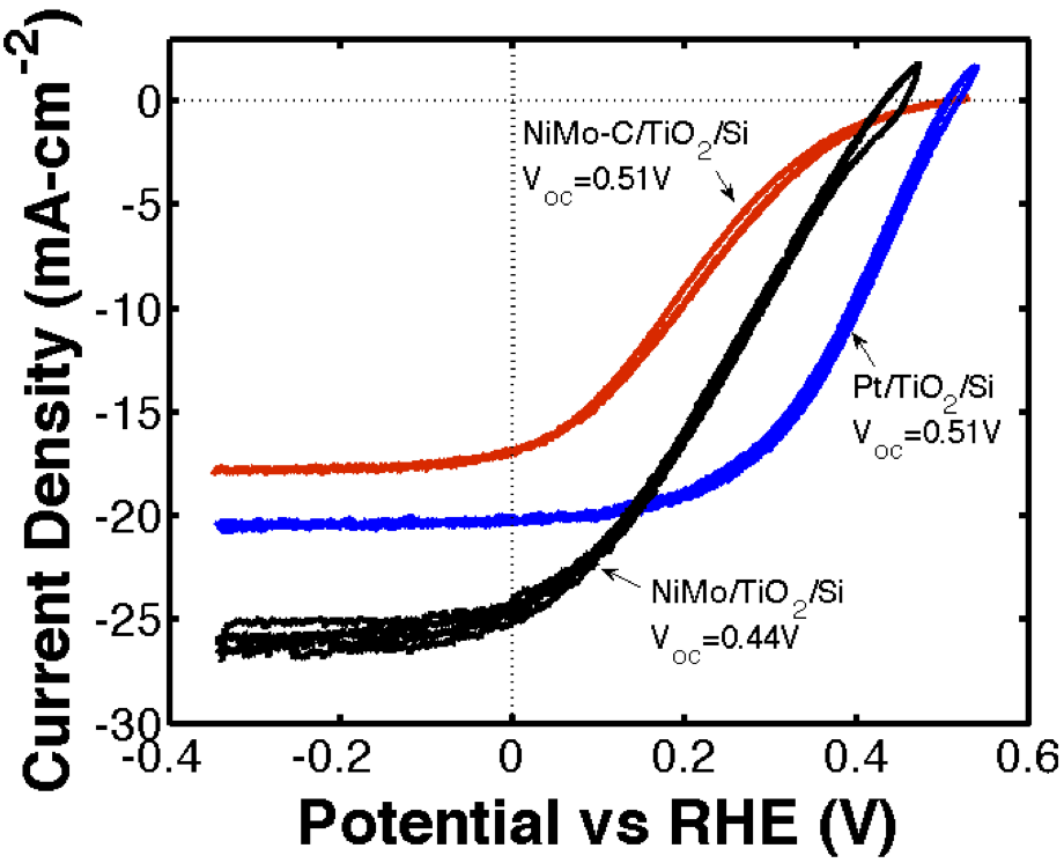

Figure 6.10: Hydrogen evolution behavior of Si microwire array MEA devices to understand voltage loss with Ni-Mo Current-density versus potential (*J-E*) behavior for three samples in 1.0

M H_2SO_4(aq), demonstrating the decrease in open-circuit voltage (V_{oc}) consistently observed in the Ni–Mo containing samples as compared to in samples that were coated with Pt. A V_{oc} similar to that exhibited by the Pt-coated Si microwire arrays was observed upon introduction of a carbon-supported Ni-Mo catalyst that did not require annealing to activate the Ni-Mo after deposition.

Diminished photovoltages were generally observed for Si/Ni–Mo MEA devices that had been treated under reducing atmosphere at moderate temperatures (450 °C), relative to Pt-coated samples that had not been annealed. To address this disparity, a modified Ni–Mo nanopowder synthesis was developed involving reduction of the Ni–Mo oxide intermediate powder in the presence of carbon black. This carbon-containing catalyst (Ni–Mo/C) did not require an annealing step after deposition onto Si substrates. Figure 6.10 compares the *J–E* behavior for n^+p-Si microwire-array photocathodes loaded with the standard Ni–Mo and Ni–Mo/C catalysts, with the latter samples not annealed after deposition of the catalyst layer. These data demonstrate a recovery of the V_{oc} upon removal of the catalyst-activation annealing step.

6.3 Discussion and Future Directions

6.3.1 Model

The modeling indicated the performance advantages provided, in principle, by the MEA architecture relative to many other designs for integrated photoelectrodes that contain earth-abundant electrocatalysts. Specifically, the modeling predicts that η_{IRC} >10% is possible (Figure 6.3), with the main contribution to higher η_{IRC} being provided by the decoupling of the optical

absorption and catalytic activity of the electrocatalyst, allowing for simultaneous achievement of high *ff* and J_{ph} values. These predicted efficiencies rival the best-performing previously reported devices for hydrogen-evolving photocathodes that involve noble-metal catalysts.[28,100]

6.3.1.1 Performance of Ni–Mo Nanopowder Electrocatalysts

Realization of the predicted high η_{IRC} values requires fabrication of high-performance individual components, along with synergistic integration to form full MEA device architectures. One crucial component is the hydrogen-evolution catalyst. Ni-Mo nanopowders have exhibited high activity using a Ni–Mo nanopowder catalyst on planar Ti substrates (Figure 6.5), yielding overpotentials of -80 mV to produce current densities of -10 mA cm^{-2} for H_2(g) production in 1.0 M H_2SO_4.[43,46,89,94,95] As shown in Figure 6.5, this performance was matched in the MEA structure with Ni–Mo/TiO_2 layers at the base of the metallized Si microwire array. Furthermore, the catalytic activity observed for Ni–Mo even when deposited at the base of a Si microwire array indicated that mass transport of reactants and products was not significantly attenuated by the presence of the microwires or by the porous TiO_2 scattering layer.[44] The data also illustrate that Ni–Mo/TiO_2 MEA composite electrodes can be characterized in strongly acidic solutions, due to the high activity and relatively stable initial performance of Ni–Mo nanopowders under such conditions.[89] We note, however, that Ni–Mo nanopowders produced in this way do not exhibit indefinite stability under acidic conditions.

6.3.2 Photoelectrode results

The other main components of the MEA photocathode are the absorber and photovoltage-producing junction, both of which are provided by the n^+p Si microwire array. The observed η_{IRC} = 5% from photoelectrodes formed using thin Pt electrocatalyst layers indicated the formation of high-quality homojunctions in the Si microwires, with high accompanying optical absorption in the material (Figure 6.7). This combined behavior thus produced similar performance to the best-performing microwire-array photocathodes that have been reported previously.[37,90,91] Integration of the Ni–Mo and TiO_2 layers to form the complete MEA device depicted in Figure 6.2 resulted in a η_{IRC} = 2.9% for the best-performing Si microwire photocathodes in conjunction with earth-abundant electrocatalysts that were prepared in this work. This level of performance was obtained by maintaining high catalytic activity and high open-circuit voltages, in conjunction with J_{ph} values 50% larger than those obtained for devices having catalysts deposited on the sidewalls of the microwires.[49,96] Additionally, these devices far outperformed planar devices having similar catalyst loadings, demonstrating the merits of decoupling the catalytic activity with respect to the light-limited current density.

6.3.3 Potential for Improved Device Performance

A comparison between the best-performing device prepared in this work, η_{IRC} = 2.9%, and the predictions of the modeling indicates significant potential for improvement by optimization of the microwire device architecture. The observed V_{oc} and J_{ph} values were markedly lower than those predicted by the idealized, series-connected equivalent-circuit representation of the individual components. Specifically, the best-performing n^+p-Si microwire-array photoelectrodes

investigated herein exhibited V_{oc} values between 450 and 550 mV at light intensities sufficient to produce light-limited photocurrent densities of 5–25 mA cm^{-2}. A statistical analysis on nine MEA-type electrodes indicated a lower average V_{oc} value, of 330 mV, for MEA devices that incorporated the Ni–Mo catalyst. These values contrast with the V_{oc} = 600 mV value used in the modeling of the optimal device performance. Significant contributors to the difference include limitations with the Si microwire synthesis and resulting device fidelity. Additionally, the Si-based Ni–Mo/TiO_2 MEA devices suffered from adventitious deposition of catalyst and scattering particles on the microwire sidewalls consistent with physisoprtion and/or chemisorption forces that are stronger than the centrifugal force imparted throughout the flocculation process. Deposition of either nanopowder material on the microwire sidewalls acts to reduce the light-limited photocurrent density, as discussed further in the Supporting Information. Each of these performance issues can presumably be addressed with improved attention to growth and processing procedures for Si microwire arrays, providing a credible path to η_{IRC} > 10% for MEA photocathodes.

To illustrate the possibility of improving further the performance of the MEA devices, the origin of the low observed V_{oc} values for devices that incorporated the Ni–Mo catalyst was investigated. Metal incorporation via solid-state reactivity and subsequent diffusion into the Si absorber during the catalyst-activation annealing step likely degrades the minority-carrier lifetime of the Si. Mo concentrations of $<10^{12}$ cm^{-3} can significantly decrease the minority-carrier lifetimes in p-Si.[39,101] Although these low impurity concentrations are difficult to detect analytically, decreases in V_{oc} were observed for Si microwire n^+p-junction samples that contained Ni–Mo particles and were

subsequently annealed at 450 °C, as compared to samples from the same substrate that were instead coated with Pt at room temperature (Figure 6.10). The observed difference in V_{oc} is therefore consistent with a decrease in charge-carrier lifetime due to the presence of impurities in the Si. To remedy this deficiency, carbon-supported Ni–Mo catalysts (Ni–Mo/C) were synthesized without an annealing step following the deposition of the catalyst into the microwire array. Figure 6.10 demonstrates a recovery of the V_{oc} when Ni–Mo/C catalyst was used without a post-deposition annealing step; however, significant sidewall deposition, due to a reduced efficiency of centrifugal flocculation, precluded these samples from also obtaining exhibiting high J_{ph} values. Further efforts to improve the device fidelity, as well as to optimize the MEA-layer deposition conditions, are warranted to achieve further improvements in the performance of such photocathodes.

Optimization of the Ni-Mo and TiO_2 layer thicknesses could also provide improved performance. Increasing the thickness of the Ni-Mo layer is expected to improve the catalytic activity, but assuming that the TiO_2 thickness remains constant, the reflectivity of the device would increase due to the increase in the height of the Si microwires that protrude from the Ni-Mo/TiO_2 layers. Similarly, an increase in the TiO_2 layer thickness is expected to increase the light scattering until the layer becomes optically dense, at which point the light scattering properties are expected to remain relatively constant. However, in an analogous fashion to the effect of increasing the thickness of the Ni-Mo layer, an increase in the thickness of the TiO_2 is expected to increase the device reflectivity by decreasing the Si microwire height that is available for light absorption.

6.3.4 Device Stability

Direct stability measurements were not performed because these Ni-Mo nanopowder electrocatalyts are known to degrade rapidly after ~7 h of operation in acidic conditions consistent with the known chemical instabilities of the individual elements.[89] The device stability is not expected to be limited by Si or TiO_2, as both materials are chemically stable under the operating conditions. SEM images taken after photoelectrochemical testing confirm that the sample construct remained intact throughout PEC testing, suggesting that the Ni-Mo electrocatalyst under the test conditions will provide the ultimate stability limit for this particular device. Accordingly, mutual compatibility of all components is ultimately desired and thus incorporation of hydrogen-evolution electrocatalysts with long-term stability in acid media should result in improved overall device longevity. The device architecture described herein can accommodate high mass loadings to allow for the use of electrocatalysts that have a relatively low intrinsic catalytic activity, thereby expanding the range of electrocatalyst activity as a trade-off for stability, if needed.

6.4 Conclusions

We have designed, fabricated, and experimentally verified a broadly applicable photoelectrode architecture that circumvents the trade-off between catalytic activity (*ff*) and optical absorption in the overlayer. This trade-off would otherwise significantly reduce the light-limited photocurrent density (J_{ph}) and, unless mitigated, would preclude efficient solar-driven water splitting. The architecture consists of a high aspect-ratio three-dimensional semiconductor structure (e.g., Si microwires) with a particulate catalyst layer covered by a high-dielectric

particulate layer that scatters light back into the semiconductor structure. Modeling of the design suggests that η_{IRC} > 10% is possible with earth-abundant electrocatalysts that have a relatively low per-atom activity. The best-performing Si homojunction microwire-array photocathodes investigated herein with ~1–2 mg cm^{-2} of a Ni–Mo nanoparticulate catalyst layer, covered by a TiO_2 nanoparticulate light scattering layer, demonstrated a η_{IRC} = 2.9%. Replacing the Ni–Mo nanoparticulate layer with electrolessly deposited Pt on the microwire sidewalls resulted in η_{IRC} = 5%, similar to that of the best-performing previously published Si microwire device.[37] The modeling indicated that still higher η_{IRC} values can be obtained by optimization of the microwire growth and doping process, in conjunction with optimization of the deposition procedures used for the catalyst and optical scattering layers.

7 A Comparative Techno-Economic Analysis of Renewable Hydrogen Production Using Solar Energy

7.1 Motivation

Electrolysis using solar energy as a potential commercial source of hydrogen from water has been pursued for over four decades.[1] Solar-driven water electrolysis has been practiced in two basic system configurations: (1) photoelectrochemical (PEC) water splitting, which consists of a single, fully integrated unit that absorbs sunlight and produces hydrogen and oxygen, and (2) photovoltaic electrolysis (PV-E), which consists of independent photovoltaic modules that drive separate electrolyzer units. To have significant impact on the worldwide supply of energy, these technological solutions must necessarily be competitive within the economic realities of the marketplace. Rigorous economic competitive analyses, applied to these proof-of-concept research and development technologies, can provide critical guidance on their further resource allocation, priorities, and trajectory. Accordingly, we describe a technoeconomic evaluation of renewable and carbon-free hydrogen production by solar-driven water splitting. In so doing we build on existing literature by adding (i) an updated technoeconomic evaluation of photoelectrochemical systems based on recent engineering designs and prototypes, (ii) a complete plant design evaluation and direct comparison of photoelectrochemical and photovoltaic-electrolysis technologies, (iii) a comparison of solar hydrogen production technoeconomics to other low-carbon technological options, and (iv) an extension of the solar hydrogen technoeconomic analysis to solar-driven CO_2 reduction systems.

The systems analyzed herein include two integrated PEC designs, as well as grid electrolysis with proton-exchange membrane electrolyzers and two PV-E designs using discrete photovoltaic modules and electrolyzer units. Current and predicted hydrogen production prices from steam reforming of natural gas (SMR) are reported as a benchmark. The capital and operating expenses for each system have been estimated based on technical design specifications and allowed calculation of an estimated plant-gate levelized cost of hydrogen such that the net present value is zero at the end of the plant life.

Prior to broader comparisons, an initial comparison between solar hydrogen production methods has been performed to determine the least expensive technology and to suggest future research needs. Integrated photoelectrochemical hydrogen production and discrete photovoltaic electrolysis hydrogen production constitute functionally identical systems and hence can be compared directly on a cost-basis. The trade-offs involving construction of a single integrated unit that has potentially fewer components and directly produces hydrogen, relative to the increased operational flexibility of the discrete photovoltaic electrolysis configuration, will therefore ultimately determine the most economic technology that provides this specific quality and quantity of energy.

Subsequently, the most economic solar hydrogen source is compared to steam reforming (SR) of relatively low-cost fossil hydrocarbons, the dominant current source of molecular hydrogen. The costs of production of hydrogen by SR are well known at ~ \$1.39 kg^{-1} or \$0.042 kWh^{-1} (\$3 (MM

BTU natural gas)$^{-1}$), which is less than current US average electricity prices.[2] In the absence of a price applied to CO_2 production, or other policy-driven mandates such as a renewable fuels standard, all hydrogen production technologies will compete in the marketplace directly against fossil fuels for energy production and storage. Because photovoltaic electricity production currently is more expensive in most locations than levelized electricity prices of \$0.07 kWh^{-1}, the more complicated task of solar hydrogen production by stand-alone or grid assisted PV-electrolysis is not expected to be economically favored relative to fossil-fuel-derived energy or hydrogen. Given the length of energy system transitions being generally 40-60 years or more[3], under this scenario, fossil fuels are thus expected to continue to dominate over any solar hydrogen system throughout at least the first half of this century.

However, solar hydrogen technologies constitute a carbon-neutral source of energy production and storage, and thus provide a differentiated quality of energy that may eventually be valued in the marketplace. Therefore we have also compared the cost of solar hydrogen to other carbon neutral or low carbon sources of hydrogen that could play a role in a carbon-constrained energy market. Nuclear fission-based grid electrolysis and biomass reforming are two of the main alternative technical approaches, though biomass-derived energy is potentially limited in scale due to land area constraints. Another potential low-carbon technology option is fossil-fuel-derived grid electrolysis in conjunction with carbon capture and storage (CCS).

We have also compared the cost of solar hydrogen to other approaches that can provide similar functionality as a part of a low-carbon energy system. Carbon-neutral energy production and

storage technologies, such as electricity derived from either nuclear fission or solar electricity, in conjunction with battery storage, pumped hydroelectricity, or compressed air-based energy storage, provide alternative technological options relative to the use of solar hydrogen in the grid storage and, in some cases, the transportation sectors. These technologies mainly compete with the electrolysis unit, and all of the approaches will have different operational efficiencies as well as mutually different capital and operating expenses. Many of these existing technologies have a first-to-market advantage, while PEC-derived hydrogen remains at a fundamental research level.

7.1.1 Solar Hydrogen Technologies

In each of the PEC and PV-E system configurations, solar photons are absorbed in semiconducting materials that have at least one junction that converts photogenerated electron/hole pairs into incipient electrical energy. The photogenerated electrons and holes are collected asymmetrically at the two electrodes and are transferred to electrocatalysts or electrocatalytic sites to perform the respective hydrogen- and oxygen-evolution reactions. The ions that are generated at one electrode surface must be transported through a membrane and/or electrolyte to complete the electrochemical circuit, and must react to form the complementary product without an explosion hazard being present. The products are collected separately, or alternatively must be separated subsequent to collection and then processed for final use.

Numerous types of photoelectrochemical cells have been demonstrated at the laboratory scale, with solar-to-hydrogen (STH) efficiencies as high as 12.4% for a cell possessing at least one semiconductor-liquid junction[4] and 18% for a cell constructed from semiconductors that only

contain buried semiconductor junctions.[5-7] Many small-scale demonstrations of photovoltaic-based electrolysis systems, and models optimizing their behavior, have been described, with differing levels of complexity of the connection between the photovoltaic modules and electrolyzers leading to differing operational flexibility and ultimately to different system efficiencies.[8-10] In general, the efficiency of a PV-E system is the product of the individual efficiencies of the photovoltaic module, the power electronics, and the electrolyzer unit.

The current costs of photovoltaic installations and components are well known, with national- and state-level monitoring of the total installed costs for residential, commercial, and utility-scale photovoltaic systems performed extensively throughout the United States and parts of Europe.[11,12] Commercial electrolyzer costs, including proton-exchange membrane (PEM) and alkaline electrolyzers, are also known, with published values verified by system manufacturers.[13]

Many configurations are possible for a photovoltaic electrolysis system, each having different systems economics. One of two configurations analyzed herein consists of a photovoltaic array interfaced directly to a PEM electrolyzer. The electrolyzer units have been sized to accept all, or most, of the maximum instantaneous power produced by the photovoltaic array. This design results in a capacity factor for the electrolyzer equal to that of the photovoltaic array (~20%). The second configuration analyzed includes a grid connection to supplement the electrical power supplied by the photovoltaic array, such that the electrolyzers are able to operate at their maximum capacity factor (97%), with the photovoltaics being sized such that their maximum instantaneous power matches the capacity of the electrolyzers. Another system not investigated

herein, but that could provide an economic opportunity, is a H_2 and electricity co-generation system that consists of an overcapacity of the photovoltaic component as compared to the electrolysis component, similar to current photovoltaic installations that are limited by the capacity of the inverter.[11] This type of configuration would yield a slight increase in the capacity factor of the electrolyzer, as is demonstrated by recent photovoltaic installations[11], and could generate added revenue from sale of the excess electricity during times of peak solar flux.

The key active components of PEC-based systems are currently the subject of intense research and development. Many potential configurations exist, including non-concentrating and concentrating planar semiconductor designs (Type 3 & 4, respectively),[14] as well as slurry systems that utilize particulate semiconductors suspended in a solution to absorb light and effect hydrogen and oxygen evolution (Type 1 & 2).[14,15] The Type 3 & 4 technologies can, and have, made use of existing knowledge from the photovoltaic industry, and are thus further in development than Type 1 & 2 technologies. Accordingly, the costs of PEC systems are less well understood as compared to PV-E systems, because no commercial PEC systems have been constructed and operated to date. To obtain reasonable estimates and guide research, technoeconomic analyses have been performed for these Type 1-4 system configurations and technology options.[14,15] The predicted levelized cost of hydrogen (LCH) is lowest for the less-developed Type 1 & 2 systems,[14] albeit with far more unknowns and thus more associated technological as well as market risk, relative to the Type 3 & 4 technologies. We update and build on these analyses herein by focusing on recent PEC system engineering designs, broadening the

scope of comparison to discrete PV-E systems and other technological options, and extending the analyses to CO_2 reduction concepts.

7.2 Assumptions and Analytical Methods

7.2.1 Capital Cost Analysis

Table 7.1 lists that base-case design specification and financial parameters that were used to evaluate the capital costs for each 3.65 kiloton per year (10,000 kg/day, 13.8 MW of H_2, 5.1 MW_e given current MW-scale storage and fuel cell efficiencies) system. All capital costs and results were inflation adjusted to 2014 dollars.[111]

Table 7.1: Operating and Financial Parameters Used for All Systems Analyzed

Parameter	Value
Hydrogen production rate[111]	10,000 kg/day
Plant Lifetime[110]	20 years
Hydrogen plant gate pressure[110]	450 psi
Solar capacity factor (2008-2013 average)[113]	0.204
Discount rate (r)	12%
Inflation rate[111]	1.9%
$ Basis year	2014

7.2.2 Systems

Figure 7.1 displays schematically the five types of systems that were evaluated herein. The first two systems are photoelectrochemical in nature, with the first consisting of a louvered design having slats of a semiconductor and catalyst oriented towards the sun and slats of a membrane

oriented perpendicular to the sun, all held within a chassis that allows light penetration while holding the aqueous electrolyte[17]. This system is similar to the Type 3 system that was the subject of a previous technoeconomic analysis.[14] The second PEC system considered herein is similar to the first, but includes 10x optical concentration and pressurized gas production of 10 atm from the PEC module. This system is similar to a Type 4 system that has been evaluated previously. In both PEC systems, H_2 gas is collected via polyvinylchloride (PVC) piping that has been sized to balance pipe usage against pumping losses.[14]

The next two systems considered herein consist of photovoltaic modules connected through DC power electronics to discrete electrolysis units. One system, referred to as PV-E, relies solely on solar energy for hydrogen production. In this system, the electrolyzers are connected to the photovoltaics with or without a DC-DC converter, and are sized to match the maximum output of the photovoltaics. The second system, referred to as GSPV-E, includes a grid connection and sized the electrolysis units based on their maximum capacity factor such that grid electricity supplements the photovoltaic electricity whenever the photovoltaic modules are not operating at their maximum capacity.

The last system, grid electrolysis, which served as a benchmark by which to measure the above four systems, is the predominant currently practiced technique for hydrogen production from electricity.

A final general scenario is mapped out over a range of capital expenses and STH full plant efficiency values, to demonstrate their relationship to the LCH, as well as to describe the performance and economic values that must be met for solar hydrogen to be economically competitive with existing and developing technologies.

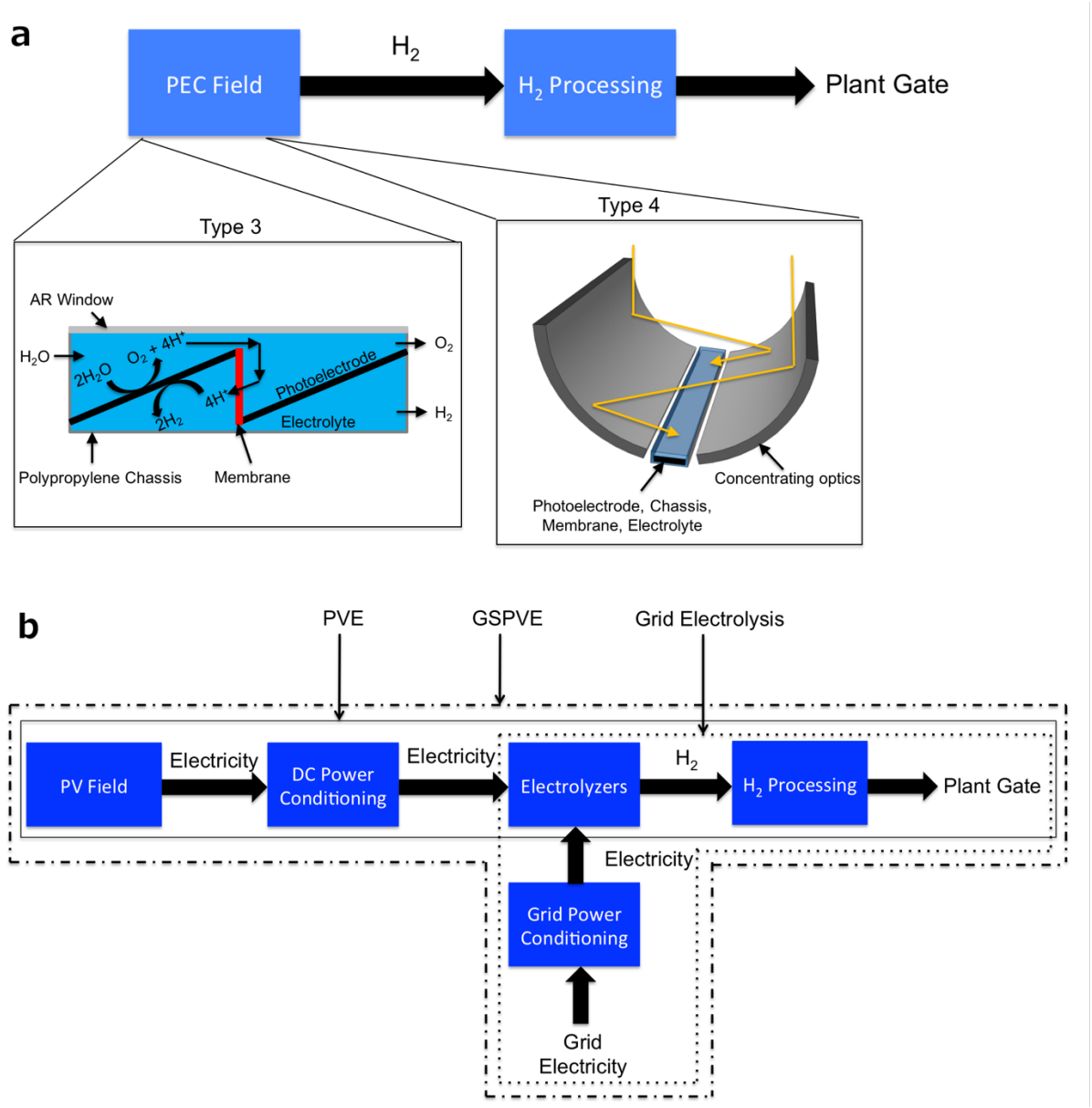

Figure 7.1: Hydrogen production facility schematics for all designs analyzed and active component architectures a) Block diagram depicting the power flow through a PEC plant. The

cell specifics for the Type 3 and 4 systems are shown in the insets. b) Block diagram of the power flow through photovoltaic electrolysis (PV-E), grid assisted photovoltaic electrolysis (GSPV-E), and grid electrolysis plants.

7.2.3 Techno-economic Assumptions

All economic assumptions are based on values taken from the U.S. market. In general, material and equipment capital expenses are transferrable globally, but installation labor and other soft balance of system costs such as customer acquisition and permitting can be more location dependent. Weighted average capital costs for utility scale photovoltaic installations in 2013-2014 were ~\$2.3 W_p^{-1} in the U.S. with only Europe and China having lower costs at ~\$1.9 W_p^{-1} and ~\$1.6 W_p^{-1}, respectively.[18] Such differences are likely due to soft balance of systems cost differences as is the case for residential systems, but the magnitude of the differences is significantly smaller for utility-scale installation.[19] These capital cost differences for utility-scale systems are roughly offset by the higher capacity factors in the U.S., suggesting that the conclusions discussed herein remain valid irrespective of the location dependent cost differences and are representative of the state-of-the-art costs globally.[18]

7.2.3.1 Photovoltaic Electrolysis (PV-E) System

Table 7.2: PV-E system technical parameters and capital and operating expenses.

System Specific Technical Parameters	
STH Efficiency	9.76%
Electrolyzer Efficiency	61%
Electrolyzer and PV Capacity Factor	0.204
Photovoltaic Efficiency	16%
Photovoltaic Area	7.5×10^5 m^2
Number of PEM stacks (500 kg day^{-1} $stack^{-1}$)	99
Capital Expenses	
Component	*2014 \$ m_S^{-2}*
Electrolyzer Stacks[110]	65
Photovoltaic Modules[115]	96
Wiring[116,117]	16
Other Electrolyzer Hard BoS[110]	61
Panel Mounting Materials[116,117]	29
PV Installation Labor[116,117]	29
Electrolyzer Installation Labor[110]	19
Other PV Soft BoS[116,117]	56

Table 7.2 shows the system specific technical parameters and capital expenses for the PV-E system. Values for non-subsidized, single crystalline Si photovoltaic module costs are taken from very recent wholesale prices; these costs include the cells along with the encapsulation and electronics necessary for operation and stability for 20+ years.[20] Wiring, panel mounting material,

and other hardware balance-of-system (BoS) costs are taken from very recent utility-scale photovoltaic installation costs.[22] A direct connection was assumed between the photovoltaic modules and electrolyzers, because the efficiency loss due to non-optimal operation is similar to the efficiency losses incurred with a DC-DC converter which can provide optimal operation at all times but incurs additional costs for the converter unit.[23,24] The assumed electrolyzer unit costs are identical to those assumed for the grid electrolysis system evaluated below.[13] Photovoltaic installation labor and other soft BoS costs are taken from very recent utility-scale PV installation costs.[21,22]

The base-case system STH efficiency was assumed to be 9.76%, which is the product of the photovoltaic module efficiency of 16% and the electrolyzer plant efficiency of 61%.[13,21,22] Replacement expenses for the electrolyzer were assumed to be identical to that of the grid electrolysis system, whereas the photovoltaics were assumed to last the lifetime of the plant. [13]

7.2.3.2 Grid Supplemented Photovoltaic Electrolysis (GSPV-E) System

Table 7.3: Grid-assisted PV-E system technical parameters and capital and operating expenses.

System Specific Technical Parameters	
STH Efficiency	9.76%
Electrolyzer Efficiency	61%
Electrolyzer Capacity Factor	0.97
Photovoltaic Efficiency	16%
Photovoltaic Area	1.8×10^5 m^2
Number of PEM stacks (500 kg day^{-1} $stack^{-1}$)	21
Capital Expenses	
Component	*2014 $ m_S^{-2}*
Electrolyzer Stack[110]	64
Photovoltaic Modules[115]	96
Wiring[116,117]	16
DC-DC Converter	51
AC-DC Rectifier[110]	30
Other Electrolyzer Hard BoS[110]	61
Panel Mounting Materials[116,117]	29
Photovoltaic Installation Labor[116,117]	29
Electrolyzer Installation Labor[110]	19
Other Soft BoS[116,117]	56
Operating and Maintenance Expenses	
Electricity[118]	\$0.07 kWh^{-1}

Table 7.3 shows the assumed GSPV-E system specific technical parameters, capital expenses, and electricity price. All costs are identical to the PV-E system, except that grid electricity operating costs and the capital costs of an AC-DC rectifier and DC-DC converter are included for proper electrical control.[13,26] The electrolysis units were sized based on their maximum capacity factor (0.97), and the photovoltaics were sized such that their maximum instantaneous power output

(at 1000 W m^{-2}) matched the electrolysis capacity (1.8 x 10^5 m^2). The electrolyzer stack cost per solar collection area is the same as for the PV-E system because both systems are sized to match the electrolyzer to the maximum instantaneous power output of the photovoltaic array. Thus, the area of solar collection determines the number of electrolyzers or vice versa, and the electrolyzer cost per photovoltaic area remains constant for the PV-E and GSPV-E systems, aside from the slightly sub-unity electrolyzer capacity factor for the GSPV-E system. This set of assumptions resulted in 21% of the hydrogen produced by the solar energy input and 79% of the hydrogen resulting from the input of grid power. The replacement expenses for the electrolyzer were assumed to be identical to those assumed for the grid electrolysis system, and the photovoltaics were assumed to last the lifetime of the plant. Implicit in the electricity price is the cost of the existing transmission and distribution system; if, however, new transmission and distribution is required for such a GSPV-E system due to remote siting of the solar electricity installation, the electricity price could be significantly higher than the base-case assumption.

7.2.3.3 Type 3 PEC System

Table 7.4: Type 3 PEC system technical parameters and capital and operating expenses.

System Specific Technical Parameters	
STH efficiency	9.76%
PEC Area	7.6 x 10^5 m^2
Capital Expenses	
Component	*2014 $ m_S^{-2}*
Window (AR coated glass)[120]	5
Chassis (Polypropylene)[121]	33
Semiconductors (c-Si, 16% S-E) [115,122]	48
Catalyst (Pt, IrO_x)[119]	8
Membrane (Nafion, 5 mil)[123]	50
PEC Cell Assembly Labor[110]	10
Compressors (2 stage)[111]	16
Water Condenser[111]	0.3
Heat Exchangers[111]	0.4
Piping (PVC)[111]	3.4
Control Systems[111]	5.4
Panel Mounting Materials[116,117]	29
Installation Labor[116,117]	29
Other BOS[116,117]	56

Table 7.4 shows the assumed Type 3 PEC system specific technical parameters, capital expenses, and electricity price. The semiconductor component cost was assumed to be identical to the current Si photovoltaic cell cost ($0.38 W_p^{-1}) and is distinct from the photovoltaic module cost for the PV-E and GSPV-E systems (

Table 7.2 and Table 7.3) because these costs only encompass the photoelectrode semiconductor material and fabrication costs and do not include the module material and assembly costs. Costs for junction formation and front contact metallization, which compose approximately 20%, or \$0.08 W_p^{-1}, of the cell cost, were excluded because PEC systems can utilize semiconductor-liquid junctions.[20,29] This assumes that a tandem and/or triple-junction stacked structure can be fabricated at costs equivalent to Si cell fabrication today, with a solar-to-electric efficiency equivalent to 16% and with current and voltage characteristics optimized for the electrolysis current and voltage load characteristics. Because this assumption has yet to be realized commercially, three high-photovoltage (>650 mV) Si photovoltaic cells could be arranged side-by-side and wired electrically in series, to produce the necessary voltage while still achieving the efficiency metrics assumed; multiple architectures for such a device have been outlined and/or demonstrated previously. Figure 7.2 depicts one possible architecture with no major cost differences expected between different side-by-side system designs.[31,32] The semiconductor cell cost would increase by \$13 m^{-2} (to \$61 m^{-2}) relative to the Si cell cost of \$48 m^{-2} (\$0.3 W_p^{-1}) as specified in Table 7.4 to include junction formation and front contact metallization costs; the overall PV efficiency would remain identical being equivalent to that of an individual cell. The major cost differentiator between these two architectural options, stacked tandem or triple-junction cell versus side-by-side, is the semiconductor cell costs; all other components are expected to be identical. Thus, at present the side-by-side design is expected to be the lowest cost option commercially and the challenge for stacked cells is to outcompete single junction Si cells.

Including the PEC chassis material, PEC module labor and AR coated glass window would result in a component similar to a PV module with costs (not including membrane or catalyst costs) of \$96 m^{-2}, identical to the PV module areal cost. Thus, any capital cost differences between the Type 3 and PV-E systems will be due to balance of system costs or any material differences for the electrolysis portion of the system.

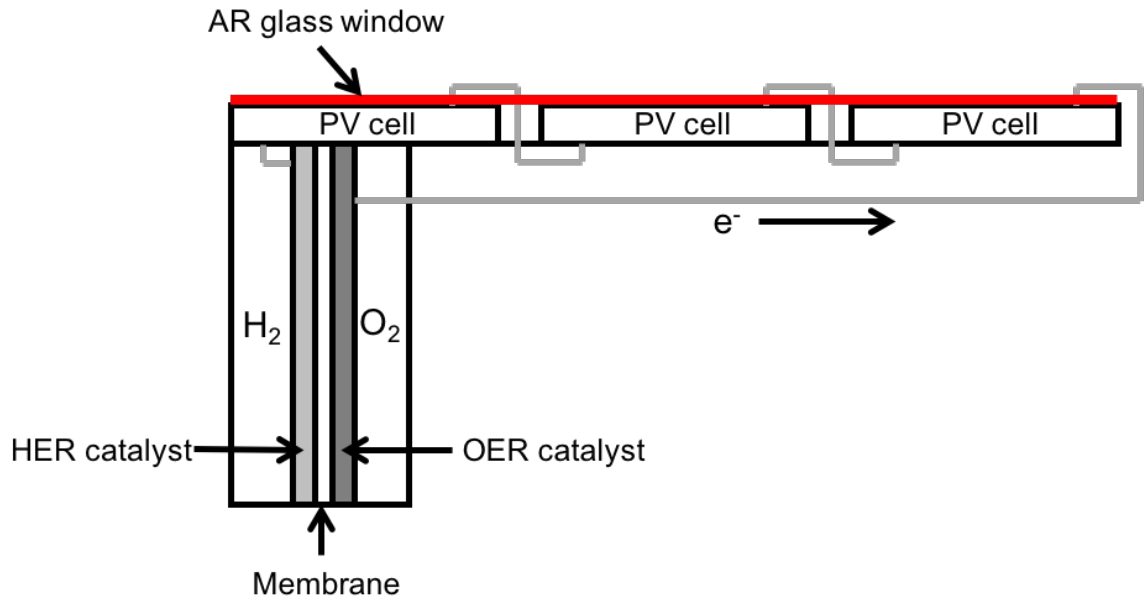

Figure 7.2: Side-by-side Si PV-MEA PEC architecture One possible architecture (not to scale) for a series connected side-by-side triple junction Si PV cell structure directly integrated into the chassis of an electrolysis unit designed for the Si device output. Such a structure would be a single unit that could be installed like a traditional PV panel, identical to the base case Type 3 design, with gas collection as opposed to electrical connections.

This near-term demonstration system serves as a baseline for comparison with photoelectrochemical approaches on a technoeconomic basis. Platinum (Pt) and iridium oxide (IrO_x) catalysts were assumed a worst-case cost scenario because of the high spot prices for both

materials. The \$8 m_S^{-2} cost of the catalyst for a specified solar collection area (m_S^2) is assumed to be identical to that of the PV-E system because state-of-the-art PEM electrolyzer catalyst loadings, ~1 mg cm^{-2} of Pt (466 nm thick) and ~2 mg cm^{-2} of IrO_2 (1.7 μm thick)[33] for 1-10 A cm^{-2} operating current density, correspond to similar total catalyst mass loadings as state-of-the-art photoelectrochemical catalyst loadings, 1-10 μg cm^{-2} (0.5 – 5 nm thick) of Pt and 2 – 20 μg cm^{-2} of IrO_2 (1.7- 17 nm thick) for 10 mA cm^{-2} of operating current density in a PEC system.[26]

A Nafion PEM was assumed to serve as the ionically conductive, gas impermeable membrane, with costs of \$2000 kg^{-1} estimated based on current production volume prices for a 5 mil (127 μm) thick membrane.[30] Based on the photoelectrochemical cell design, the membrane area required is 10% of the solar collection area.[34] A polypropylene chassis having a 1 cm thickness and an area equal to the PEC area was assumed, with a raw material price of \$1.5/kg.[28] The chassis was assumed to be manufactured via injection molding, where the raw materials cost is approximately 43% of the total manufactured chassis cost.[35] The window was assumed to be made from high quality, anti-reflective glass used by the photovoltaic industry that is compatible with acidic media.[27] Replacing the back of the polypropylene chassis with glass would decrease the materials cost of the PEC module. However, the cost differential is relatively small as compared to the total capital cost, and increases in handling related costs due to the different mechanical properties of glass versus polypropylene could nullify the material cost differential. If, however, a measurable difference in the base-case capital costs assumed herein exists, the impact of these differences on the LCH can be assessed using the analysis summarized below (in Figure 7.10). These cell materials were assumed to be resistant to degradation by sunlight over

the lifetime of the device, and any mechanical issues related to thermal mismatches between materials were assumed to be solved for the quoted costs of the base case. The photoelectrochemical module assembly labor was assumed to be equal to the electrolyzer assembly cost on a $ W^{-1} basis because both systems entail assembly of the chassis and active components (membrane electrode assembly for an electrolyzer and membrane and photoelectrode(s) for a PEC device).[13] This is a reasonable estimate given publicly available data, but is likely an optimistic lower bound because the PEC system areal power density (W m^{-2}) is roughly two orders of magnitude lower than the electrolyzers, requiring significantly larger areas of PEC components to be assembled and/or seamless integration of the materials to allow for fabrication integrally and/or with minimal labor.

The water delivery and gas collection, processing, and control system costs were taken from previous work[14], but the compressors were assumed to provide a higher compression ratio of ~5.5:1 versus 4.5:1 in the reference case evaluated previously. Polyvinyl chloride (PVC) piping was assumed in the base case due to the sufficiently low hydrogen permeability and embrittlement of PVC at the modest hydrogen collection pressures present in both PEC systems.[26,36] These assumptions result in gas processing and water delivery unit costs ($ m_s^{-2}) that are roughly half the cost of the units used to perform the same tasks in the PV-E design. Confidence is higher on the PV-E hard BoS costs due to the commercial maturity of each of the individual systems, while the PEC system costs have only undergone a high-level engineering design because no known systems have received design certifications and permitting nor been constructed.[14] Thus the potential for significant changes to the PEC system hard BoS costs exists,

with the values assumed herein likely representing an optimistic cost scenario. The panel mounting materials, installation labor, and other soft balance of systems (BoS) costs were taken directly from utility-scale photovoltaic panel installations on a $ m_S^{-2} basis.[21,22] The installation was assumed to be sited in areas that historically on a decade-scale have little chance of experiencing a hard freeze, specifically in plant hardiness zones 8 and above (i.e., where citrus trees are planted and thrive); consequently, additional costs associated with heating to avoid any liquid water from freezing were not included.[37]

The active components (semiconductors, catalyst, membrane) were assumed to be replaced every 7 years, based on expected component lifetimes from the electrolyzer industry, though no complete PEC cell that performs unassisted water splitting has yet been demonstrated to be stable for more than one week.[13,17] The installation cost for replacement components were taken to be 15% of the component cost. All other components were assumed to need no replacement over the system lifetime. An annual operating and maintenance cost of 3.2% of the installed capital was taken from the PEM electrolyzer industry.[13] All of the other components (DI water production, initial charge of acid or base, etc.) were not considered independently because previous studies have found these costs to be insignificant relative to the other capital and operating cost contributions.[14,15]

The plant efficiency was assumed to be identical to that of the PV-E system, 9.76%. This efficiency is consistent with a photovoltaic component efficiency of 16%, an electrolysis and electrochemical cell efficiency of 70% (1.75 V), and a gas collection and processing efficiency of

87%. A maximum practical PEC efficiency of 25% was estimated using the product of the maximum predicted efficiency of the PEC cell (28.7%, radiative recombination-limited photovoltaics and state-of-the-art catalysts)[38] and a gas collection and processing efficiency of 87%.

7.2.3.4 Type 4 System

Table 7.5: Type 4 PEC system technical parameters and capital and operating expenses.

System Specific Technical Parameters	
STH efficiency	20%
Capacity Factor	0.186
PEC Area	3.7×10^5 m^2
Capital Expenses	
Component	*2014 $ m_S^{-2}*
Window (AR coated glass)[120]	0.5
Chassis (Polypropylene) [121,125]	6.6
Semiconductors (InGaP/GaAs)[128]	175
Catalyst (Pt, IrO_x)[119]	8
Membrane (Nafion, 5 mil)[123]	5
Tracker Hardware[129]	44.8
Concentrators (Parabolic)[130]	48
Compressor (1 stage)[111]	14.5
Water Condenser[111]	0.2
Heat Exchanger[111]	0.4
Piping (PVC)[111]	1.6
Control Systems[111]	8.9
Panel Mounting Materials[116,117]	29
Installation Labor[116,117]	29
Other BOS[116,117]	59

Table 7.5 lists the system specific technical parameters and capital expenses assumed for the Type 4 base-case system design. A medium-range predicted cost for a high-efficiency tandem-junction photovoltaic cell was assumed at \$5.8 W_p^{-1}, commensurate with state-of-the-art III-V photovoltaic fabrication methods at present.[39] Pt and IrO_x catalysts were taken to be the same for the same solar collection areal cost as the Type 3 system; this assumption is consistent with

a situation in which a 10x increase in the catalyst thickness offsets the 10x decrease in the area of the semiconductor. The Type 4 chassis was assumed to be twice as thick (2 cm) as that in the Type 3 system, to withstand the higher hydrogen pressure assumed in the Type 4 system.[14] Two-dimensional parabolic trough concentrators were assumed for the concentrating optics.[41] Additional costs for tracking hardware were taken from the difference between utility-scale fixed and single-axis tracking capital costs, \$0.28 W_p^{-1} or \$44.8 m_S^{-2}, for 16% efficiency modules.[40]

In this Type 4 base-case system, the assumed electrochemical compression to 10 atm reduces the required downstream compression to a single stage, with a single heat exchanger, relative to the two-stage compressor assumed in the base-case Type 3 system. Increased controls are needed in the base-case Type 4 system to handle the collection of pressurized gas from the PEC panels.[14] All of the other component capital costs are identical to those for the Type 3 system, but the cost per unit of PEC area is different from the Type 3 base-case system due to the increased efficiency and thus decreased PEC area in the Type 4 base-case system. The components replaced and replacement period (7 years) and installation expense for the Type 4 base-case system are assumed to be identical to those assumed for the base-case Type 3 system.

The capacity factor for the Type 4 base-case system is lower than that assumed for the other systems, because it is assumed that the concentrators cannot collect diffuse sunlight (see supplementary information for calculation). The plant efficiency was assumed to be 20%, consistent with component efficiencies of 33% for the photovoltaic, 68% (1.8 V) for electrolysis and the electrochemical cell, and 90% for the gas collection and processing.

7.2.3.5 Grid Electrolysis System

Table 7.6 shows the specific technical parameters, capital expenses, and electricity prices assumed for the grid electrolysis benchmark system, as based on a recent technoeconomic analysis of PEM electrolyzers.[13] The only change between the two analyses is associated with the electricity price, which was taken herein to be the current average industrial retail price in the U.S. and includes generation, transmission, and distribution costs.[25] The number of electrolyzer stacks is a function of the system capacity factor and individual stack capacity. Replacement of major components every 7 years was assumed to be 15% of the installed capital expense.[13]

Table 7.6: PEM electrolysis system technical parameters and capital and operating expenses.

System Specific Technical Parameters	
Plant Efficiency	61%
Capacity Factor	0.97
Number of PEM stacks (500 kg day^{-1} stack^{-1})	21
Capital Expenses	
Component	*2014 $ W^{-1}*
Electrolyzer Stacks[110]	0.4
Balance of Systems[110]	0.57
Installation (12% of un-installed capital) [110]	0.12
Contingency Factor (15% of un-installed capital) [110]	0.15
Site Preparation (18% of un-installed capital) [110]	0.18
Operating and Maintenance Expenses	
Electricity[118]	\$0.07 kWh^{-1}

7.2.4 Net Present Value (NPV) Analysis

A standard discounted cash flow was applied to each technology and sensitivity case over the assumed plant lifetime. The capital expenditure was assumed to occur over a one-year construction period. All of the operating expenses and product revenues depend on the LCH and were discounted to the year of construction (Equations 7.1 and 7.2). Replacement costs were included as operating expenses every 7th year. A pre-tax environment was assumed and thus depreciation was not applied to any capital assets. The LCH was calculated by adjusting its value such that the net present value of the capital and operating expenses and product revenue summed to zero (Equation 7.3).

$$Operating\ Cost\ PV = \sum_{i=1:n}^{n} \frac{OC_i}{(1+r)^i} \qquad 7.1$$

$$Product\ Revenue\ PV\ (LCH) = \sum_{i=1:n}^{n} \frac{PR_i(LCH)}{(1+r)^i} \quad 7.2$$

$$NPV = 0 \quad 7.3$$
$$= Product\ Revenue\ PV\ (LCH) - Operating\ Cost\ PV - Capital\ Expense$$

7.3 Analysis Results

7.3.1 PV-E System

A combination of discrete photovoltaic and electrolyzer units is an important benchmark comparison to photoelectrochemical systems. PV and electrolyzer systems are commercial items with known costs. This combination can provide the highest solar-to-chemical conversion efficiency because each unit can be independently operated and optimized. Accordingly, the system efficiency is limited by the product of the independent photovoltaic and electrolyzer thermodynamic efficiency limits rather than the coupled PEC system thermodynamic efficiency limit.[38,42]

Given the base-case capital and operating expenses, and the technical parameter assumptions, the LCH and total capital expense values for the base-case PV-E system were found to be \$12.1 kg^{-1} and \$260 MM (\$371 m_S^{-2}), respectively. Figure 7.3 displays the impact of the two most sensitive parameters, plant efficiency and active component capital expense per area of solar collection, m_S^{-2}, on the LCH of the base-case PV-E system. This analysis thus indicates that improving the plant efficiency has the largest impact on the LCH. Improved system efficiency

could in principle be achieved through technological improvements in both the photovoltaic and electrolyzer units. For example, achieving the current photovoltaic cell record-efficiency, 46%[43], with all other parameters and capital expenses identical to the base-case system, results in LCH values of \$9.4 kg^{-1} for the PV-E system. Decreases in the capital cost of the photovoltaic and/or electrolyzer units lead to diminishing returns because the hard and soft BoS costs remain, and constitute the dominant costs of an installed system.

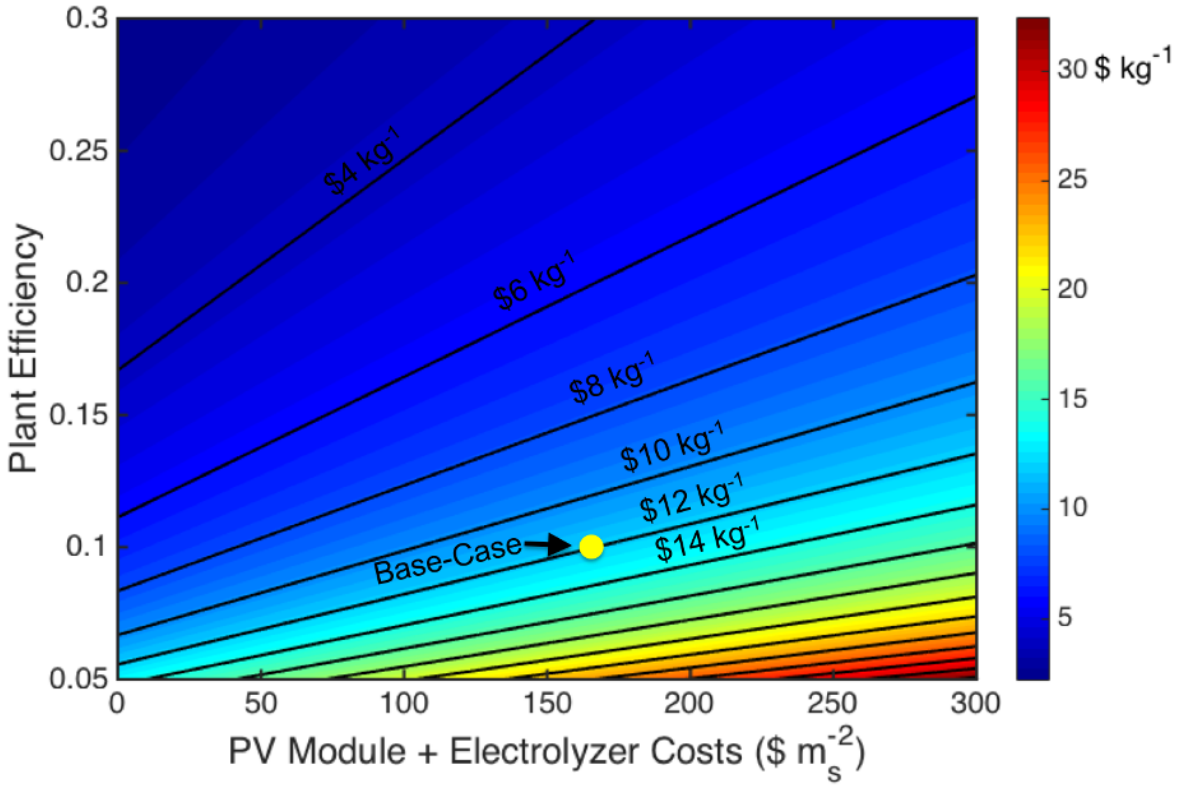

Figure 7.3: LCH contour plot of plant efficiency versus PV module and electrolyzer costs for the PV-E system A contour plot of the LCH (\$ kg^{-1}) for the PV-E system as a function of the plant efficiency and active component (PV modules and electrolyzers) areal capital expense normalized by the required solar collection area (\$ m_S^{-2}). The base-case result is indicated by the yellow circle. Contours are labeled at \$2 kg^{-1} intervals.

For a broader perspective, Figure 7.4 illustrates the impact that the PV and electrolyzer subsystem costs have on the levelized cost of hydrogen. As an example, assume that PV systems can achieve levelized cost of electricity (LCOE) value of \$0.02 kWh^{-1}, which would require a capital cost of ~\$0.5 W_p^{-1} (assuming a 25 year lifetime, 10% discount rate, and 30% capacity factor). Figure 7.4 demonstrates that at a PV subsystem cost of \$0.5 W_p^{-1}, a free electrolyzer would produce a levelized cost of hydrogen of \$2.50 kg^{-1}. This situation reflects the cost per joule of electricity at \$0.02 kWh^{-1}, converted directly into a cost per joule of H_2, in conjunction with an electricity-to-H_2 system conversion efficiency of 61%, with no cost for the conversion unit. To obtain a cost of \$3 kg^{-1} of H_2 with a PV capital cost of \$0.5 W_p^{-1}, the electrolyzer capital cost must be <\$0.1 W^{-1}, an order of magnitude lower than current capital cost values. The development of a truly disruptive electrolysis technology is required to attain these costs, because electrolysis and the closely related chlor-alkali process have been practiced at scale for over a century. The current global chlor-alkali production of 60 million metric tons per year consumes ~ 150 TWh of electricity annually, which is similar to the current worldwide annual solar electricity production of ~280 TWh (178 GW installed, 18% capacity factor). These large reductions in capital costs are required due to the low capacity factor of solar electricity as well as the modest electrolysis efficiency.

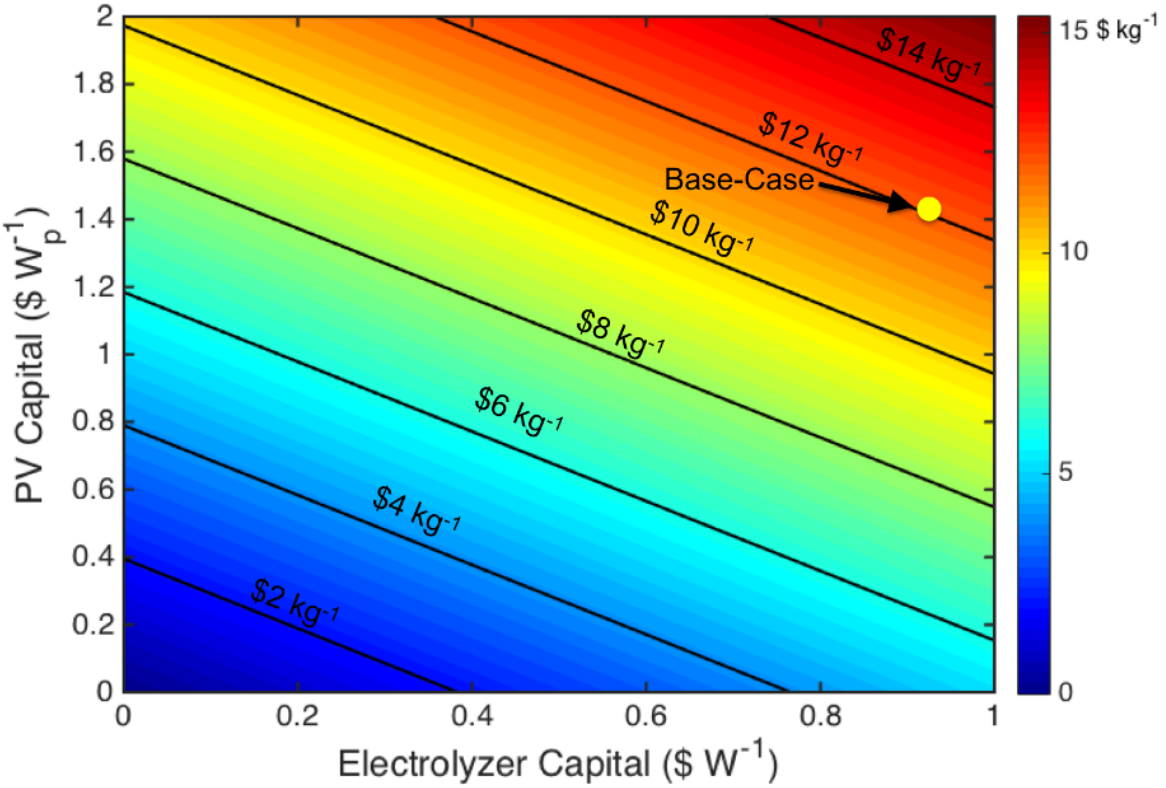

Figure 7.4: LCH contour plot of PV capital expense versus electrolyzer capital expense for the PV-E system A contour plot of the LCH ($ kg^{-1}) for the PV-E system as a function of the PV and electrolyzer subsystem capital expenses in $ W^{-1}. The base-case result is indicated by the yellow circle. Contours are labeled at $2 kg^{-1} intervals.

An alternative scenario could include a combination of photovoltaics and wind turbines to increase the capacity factor of the electrolyzers while maintaining 100% carbon free electricity. If electricity prices as low as $0.03 kWh^{-1} and an electrolyzer capacity factor of 75% could be achieved (to estimate an optimistic projected situation for large-scale PV and wind electricity combined, with no storage, as the sole electricity generation sources, and assuming negligible costs for any needed new transmission lines), the resultant LCH value is $3.8 kg^{-1} assuming all other base-case values are constant. To reach $3 kg^{-1} or $2 kg^{-1} would require electrolyzer capital cost reductions of 60% (to $0.6 W^{-1}) or 80% (to $0.16 W^{-1}), respectively. If, alternatively, the

electrolyzer is free and the capacity factor remains at 75%, the electricity price required to achieve LCH values of \$3 kg^{-1} and \$2 kg^{-1} is \$0.055 kWh^{-1} or \$0.037 kWh^{-1}, respectively.

7.3.2 GSPV-E System

Capacity factors are critical to any commercial operation and are a fundamental limitation of terrestrial solar energy systems. Increases in the electrolyzer capacity factor can be obtained during non-peak solar hours and at night by supplementing the PV electricity with grid electricity. The GSPV-E system thus constitutes a hybrid of grid electrolysis and photovoltaic electrolysis systems, with ~75% of the hydrogen produced by power supplied by grid electricity.

The LCH and total capital expense values for the GSPV-E system are \$6.1 kg^{-1} and \$66 MM (\$441 m_S^{-2}), respectively. Figure 7.5 displays the impact of the two most sensitive parameters, the photovoltaic efficiency and the electricity price, on the LCH of the GSPV-E system. This analysis suggests that at high photovoltaic efficiencies (> ~25%) the electricity price has the largest impact on the LCH because the photovoltaic areal requirement, and thus capital cost, decreases with increasing efficiency. However, the photovoltaic efficiency becomes more impactful at values < ~25%, because of the increase in photovoltaic areal requirements. Achieving the current record-efficiency photovoltaic cells (46%[43]) within this device, assuming base-case capital expenses, results in LCH values of \$5.6 kg^{-1} for the GSPV-E system. Such high module efficiency values have not yet been demonstrated and will require multi-junction architectures that can achieve cost metrics similar to Si on a \$ W^{-1} basis.

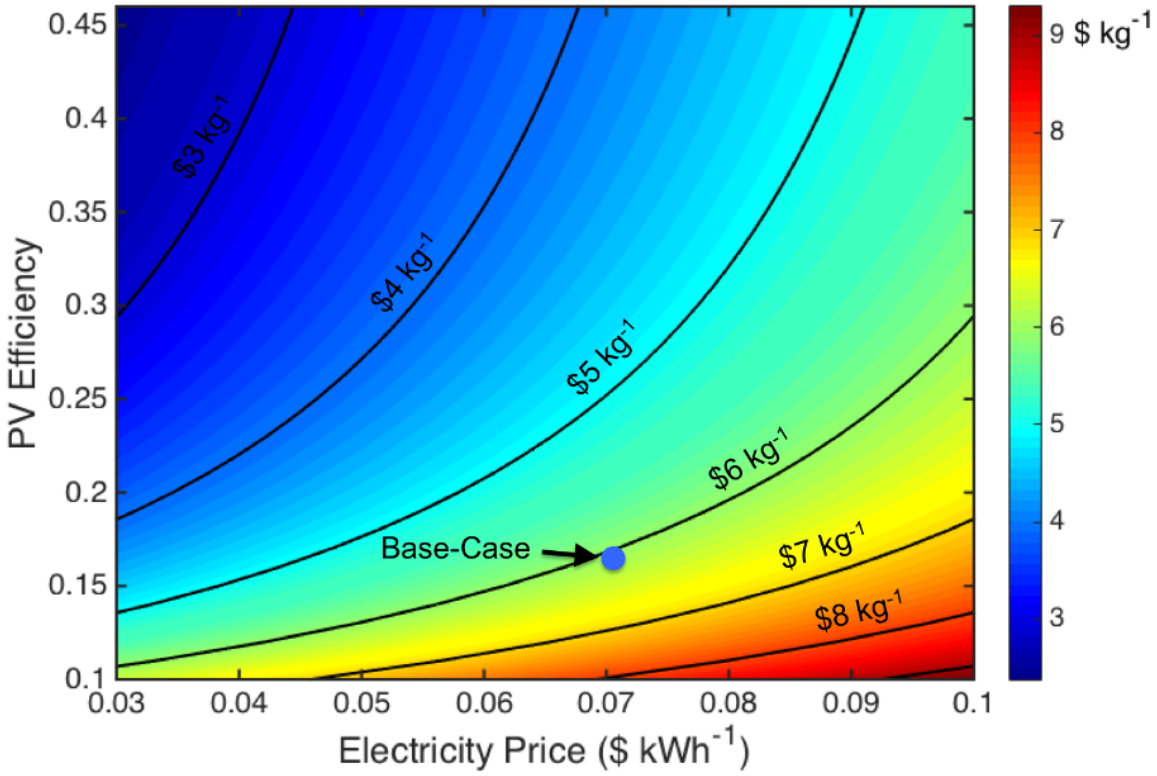

Figure 7.5: LCH contour plot of PV efficiency versus electricity price for the GSPV-E system A contour plot of the LCH ($ kg^{-1}) for the GSPV-E system as a function of the photovoltaic efficiency and electricity price ($ kWh^{-1}). The base-case result is indicated by the blue circle. Contours are labeled at $1 kg^{-1} intervals.

7.3.3 Grid Electrolysis

Grid electrolysis using alkaline or proton-exchange membrane electrolyzers are mature, commercial technologies that are used herein as a benchmark. Prior studies have investigated the detailed costs of each component of a PEM electrolysis system and are used herein.[13] However, the total capital cost of PEM and alkaline electrolysis facilities are similar, such that all conclusions based on the PEM systems apply approximately to alkaline systems as well. Supported by these previous studies, a high-level analysis was performed and resulted in a base-

case LCH and capital cost for grid electrolysis of \$5.5 kg^{-1} and \$34 MM, respectively. Operating expenses, in the form of the cost of electricity, constituted the largest component of and sensitivity to the LCH, as has been shown previously.[13]

7.3.4 Type 3 PEC System

The Type 3 base-case LCH and capital cost values are \$11.4 kg^{-1} and \$205 MM (\$293 m_S^{-2}), respectively, which are lower than the LCH for the comparable base-case PV-E systems. Relative to the base case, the PV-E system must exhibit an efficiency increase to 11.5%, or a decrease in the capital expense to \$245 MM (\$351 m_S^{-2}), to overcome this difference and reach cost parity with the base-case Type 3 PEC system.

Figure 7.6 demonstrates the impact of the two most sensitive parameters, plant efficiency and active component capital expenses, on the Type 3 system LCH value. Similar to the PV-E system, the efficiency has the largest impact on the LCH value, while decreases in the active component capital expenses have diminishing returns due to the continuing presence, and dominance, of the hard and soft BoS costs. Achieving a maximum practical plant efficiency of 25% at the base-case capital cost would result in a \$5.1 kg^{-1} H_2 LCH, while maintaining the base-case efficiency and reducing the photovoltaic stack, membrane and catalyst component costs to \$0 m_S^{-2}, a non-practical value, would result in a ~ \$6.1 kg^{-1} H_2 LCH. Improvements in the efficiency of Type 3 systems can be achieved by focusing on the most optimal tandem junction band-gap pairs[38,42], optimizing the semiconductor material growth quality and electronic properties[44,45] and improving the oxygen-evolution reaction efficiency through catalyst development. These

advances must be achieved with cost effective materials and fabrication techniques to justify any resulting increase in efficiency relative to the assumed base-case system characteristics.

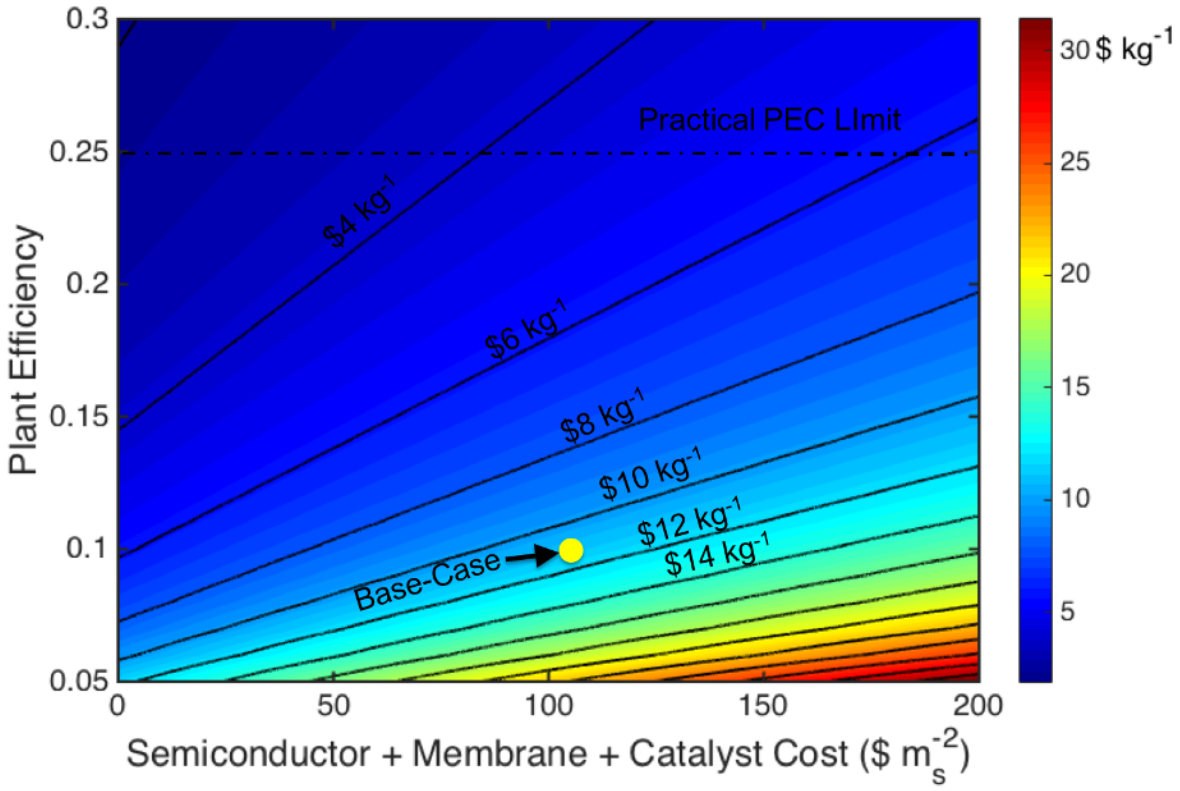

Figure 7.6: LCH contour plot of plant efficiency versus semiconductor, membrane, and catalyst cost for the Type 3 PEC system A contour plot of the LCH ($ kg^{-1}) for the Type 3 PEC system as a function of the plant efficiency and active component (semiconductor, membrane and catalyst) capital expense normalized by the required solar collection area ($ m_S^{-2}). The base-case result is indicated by the yellow circle. Contours are labeled at \$2 kg^{-1} intervals and the practical efficiency limit for PEC systems is indicated assuming direct electrical connection between the semiconductor and catalyst components without additional power electronics.

The Type 3 bill of materials (Table 7.4) indicates that the capital costs of the electrocatalysts constitute a minor contribution to the active material costs, and moreover, to the total capital cost of the Type 3 base-case system. Furthermore, the base-case catalyst costs assumed use of

the most expensive catalysts, platinum and iridium oxide; use of any other catalyst would only decrease the catalyst capital cost contribution. These findings are consistent with, and reinforce, a recently performed analysis that focused only on the active components of a generic PEC system. That study found that, for an optimized system, the catalyst capital costs of even the most expensive catalysts are insignificant compared to the capital costs of the semiconductors.[134] This conclusion is also consistent with commercial PEM electrolyzer cost breakdowns, which indicate that the catalysts constitute < 7% of the total capital cost of the system.[119]

7.3.5 Type 4 PEC System

The Type 4 base-case LCH and capital cost values were \$9.2 kg^{-1} and \$160 MM (\$428 m_S^{-2}), respectively, and are also lower than the LCH of the base-case PV-E system. The PV-E system must exhibit an efficiency of > 16%, or must have a decrease in capital expense to \$175 MM (\$251 m_S^{-2}), to overcome this difference and reach cost parity with the base-case Type 4 PEC system.

Figure 7.7 demonstrates the impact of the two most sensitive parameters, plant efficiency and active component capital expenses, on the base-case Type 4 system LCH value. In contrast to the base-case PV-E and Type 3 PEC systems, the active component cost has the largest impact on the LCH value of the base-case Type 4 PEC system, mainly because of the current high cost and level of uncertainty in the component cost of the III-V high-efficiency photovoltaic materials. Achieving a maximum practical plant efficiency of 25% at the base-case capital cost would result in a LCH of ~ \$7.4 kg^{-1} H_2. In contrast, maintaining the base-case efficiency and reducing the

capital cost to \$283 m_S^{-2}, consistent with lowering photovoltaic component cost to \$30 m_S^{-2} or \$0.1 W_p^{-1} at 30% photovoltaic efficiency, would result in a LCH of \$5.2 kg^{-1} H_2.

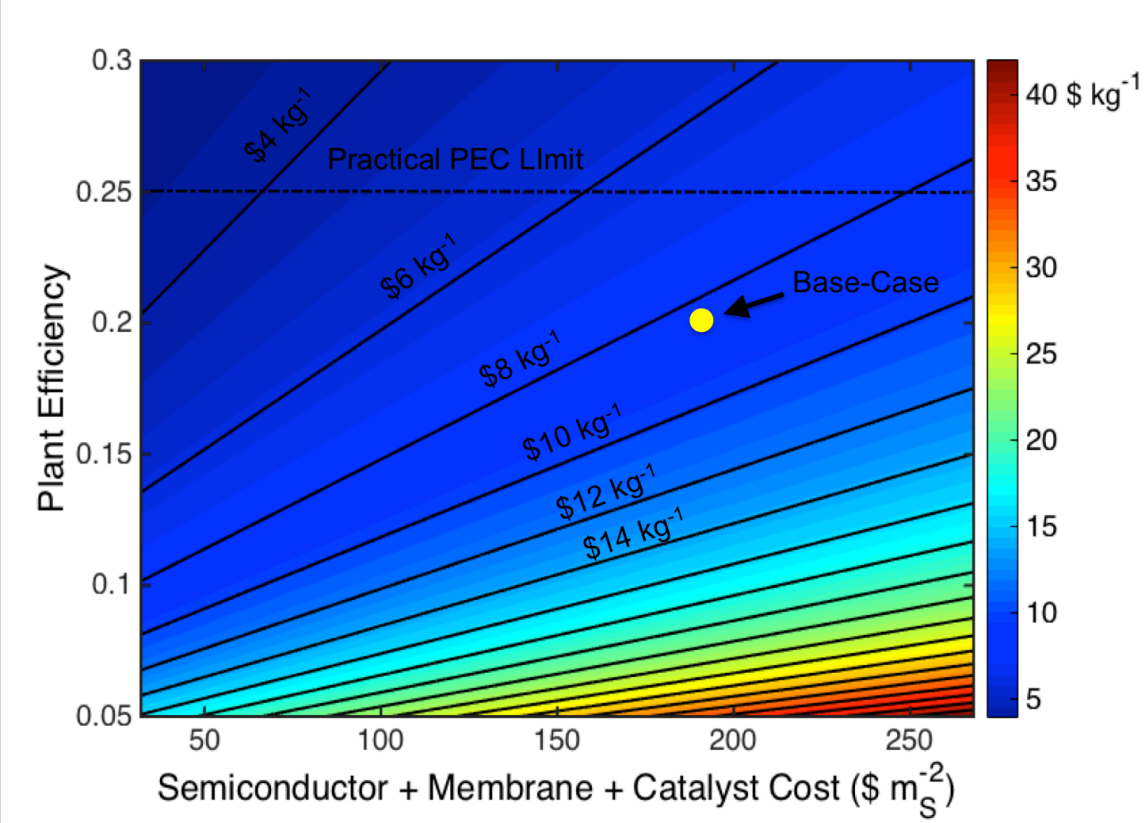

Figure 7.7: LCH contour plot of plant efficiency versus semiconductor, membrane, and catalyst cost for the Type 4 PEC system A contour plot of the LCH (\$ kg^{-1}) for the Type 4 PEC system as a function of the plant efficiency and active component (semiconductor, membrane and catalyst) capital expense normalized by the required solar collection area (\$ m_S^{-2}). The base-case result is indicated by the yellow circle. Contours are labeled at \$2 kg^{-1} intervals and the practical efficiency limit for PEC systems is indicated assuming direct electrical connection between the semiconductor and catalyst components without additional power electronics.

7.3.6 Type 3 PEC vs PV-E System Comparison

To support deployment at scale, PEC systems must be cost-advantaged relative to PV-E systems, because both systems provide identical functionality and energy quality. To understand the source of this difference in LCH, the capital expenses for each system were separated into active

module, hard BoS, and soft BoS capital expenses, according to the technical and economic assumptions associated with each base-case scenario. We note, however, that the PEC system technical hurdles of simultaneous stability, efficiency, and operational safety that have challenged the field for 40+ years were assumed to be satisfied simultaneously in a single large area system.

Given these assumptions, Table 7.7 presents the discretized capital expenses for the PEC and PV-E systems, respectively. The difference in active component and soft BoS expenses between each system is relatively small, especially given the uncertainty in PEC active component expenses due to an absence of any commercial experience. The hard BoS costs demonstrate the largest difference with the PEC system estimated to be ~2x lower than those of the PV-E system.

This difference is due to different modes of energy transmission within the PEC and PV-E plants as well as the fact that the PV-E system has two sets of hard BoS expenses, one for the photovoltaic and one for the electrolyzer units, while the PEC system has one set of hard BoS costs for its sole, integrated unit. In the PV-E system, electricity is the major energy carrier being transported from the photovoltaic modules to the electrolyzers (Figure 7.1). However, in the PEC system, hydrogen is the energy carrier being transported from the modules to the gas processing systems and to the plant gate (Figure 7.1). This difference indicates that transportation of hydrogen gas at low pressure, and subsequent compression of the H_2, is less expensive per joule of energy transmitted than transportation and conditioning of relatively low power electricity. This result is consistent with capital expenses for high power transmission lines, in which

electricity transmission expenses are ~$1 MM (GW-mile)$^{-1}$ [47,48] as compared to hydrogen pipeline expenses of ~$0.1MM (GW-mile)$^{-1}$.[49,50] The LCH difference between both systems is relatively small, < $1 (kg H_2)$^{-1}$, and thus only a slight advantage lies with PEC systems.

Table 7.7: PEC versus PV-E capital expense comparison for systems without light concentration in $ m_S^{-2} of solar collection area

PEC (ηSTH = 10%)		PV-E (ηSTH = 10%)	
Active Components			
Membrane	50 $ m_S^{-2}	Electrolyzer Stack	65 $ m_S^{-2}
Catalyst	8	Photovoltaic Module	96
Semiconductor	48		
Chassis	38		
Assembly Labor	10		
Subtotal	***154***	***Subtotal***	***161***
Hard BoS			
Gas Processing	20 $ m_S^{-2}	Wiring	16 $ m_S^{-2}
Control Systems	6	Other Electrolyzer Hard BoS	61
Panel Mounting Materials	29	Panel Mounting Materials	29
Subtotal	***55***	***Subtotal***	***151***
Soft BoS			
Install Labor	29 $ m_S^{-2}	PV Install Labor	29 $ m_S^{-2}
Other Soft BoS	56	Electrolyzer Install	19
		Other Soft BoS	56
Subtotal	***85***	***Subtotal***	***104***

7.4 Summary, Comparative Analysis Beyond Solar Fuels and Extenstion to CO_2 Reduction Systems

7.4.1 Summary of LCH and Sensitivity Results

Figure 7.8 presents the base-case estimated LCH values for all systems analyzed herein. The LCH sensitivity to either system or photovoltaic efficiency, whichever is most appropriate, is also presented in Figure 7.8, because efficiency has the greatest impact on LCH, by virtue of the areal dependencies of most of the component costs.

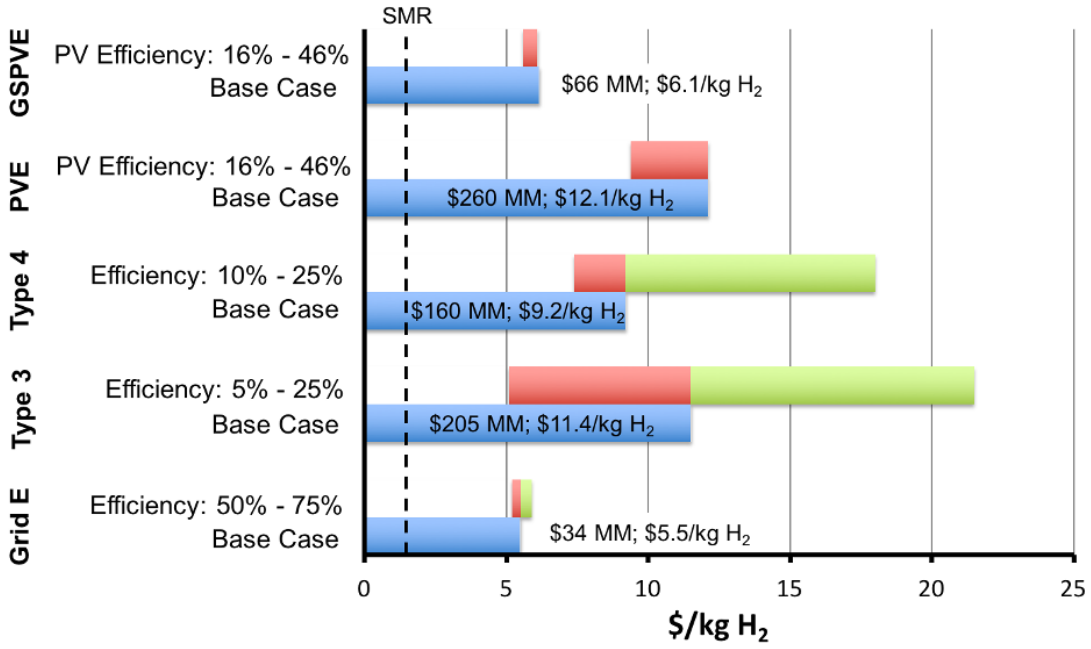

Figure 7.8: LCH summary of all systems analyzed A summary of the base-case scenario results with the current and future predicted market hydrogen value without a CO_2 tax indicated (dashed line, SMR current).

7.4.2 Solar H_2 vs Fossil Fuels

As compared to other, commercial, energy production and storage technologies, the solar-driven technologies analyzed herein are limited by an intrinsically diffuse solar power density of <1 kW m^{-2}, as well as by a low capacity factor, of under 25%, for fixed-tilt panels in the optimal locations in the U.S., and by a conversion efficiency of under 20%. These limitations, combined with relatively high capital expenses, result in estimated untaxed levelized hydrogen production costs that are far larger than the cost of hydrogen derived from steam methane reforming (SMR) or grid electrolysis using electricity derived from fossil fuel. Accordingly, in an unconstrained CO_2 energy market, solar electrolysis technologies based on the embodiments considered herein should not be expected to compete on a cost basis with fossil fuel-derived H_2 for hydrocarbon upgrading or ammonia production. A CO_2 tax of \$1000 (ton CO_2)$^{-1}$, \$800 (ton CO_2)$^{-1}$, \$1200 (ton CO_2)$^{-1}$and \$450 (ton CO_2)$^{-1}$ would be required to increase the price of SMR to parity with the base-case Type 3 and Type 4 PEC, PV-E, and GSPV-E (assuming CO_2-free electricity) technologies, respectively.

The difference between the grid electrolysis and solar hydrogen systems suggests that the effective price of solar electricity embedded within the PEC and PV-E systems is more than double the industrial average grid electricity price of \$0.07 kWh^{-1}. Similarly, at current electricity pricing, the use of solar electricity as only a fraction of the total electricity input, with the remainder of the input as grid electricity, while utilizing the electrolyzer unit at near its full capacity factor, resulted in a higher LCH than the sole use of grid electricity as the input. These findings thus both individually and collectively indicate that solar electricity has not reached grid parity, because the

generally quoted solar electricity production costs do not include the cost of the fossil fuel back-up capacity required to provide the reliability required from, and achieved by, utilities. In contrast, the solar fuel plants analyzed herein could, in principle, provide the required high capacity factor and attendant grid reliability by themselves. Succinctly, even at comparable LCOEs, the value of electricity produced from an intermittent source such as sunlight is less than the value of electricity that can be dispatched with high reliability to meet demand.

7.4.3 Grid Electrolysis vs Fossil Fuels

The LCH for both grid electrolysis and fossil fuel reforming is dominated by operating expenses in the form of fuel costs. Current natural gas prices of ~\$3 $(MM\ BTU)^{-1}$ result in a LCH of \$1.39 kg^{-1} or \$0.042 kWh^{-1} (33.3 kWh kg^{-1}), which is less than the average "fuel" (industrial electricity) price in the U.S., \$0.07 kWh^{-1}.[26] Natural gas prices would have to increase to \$8.2 $(MM\ BTU)^{-1}$ to reach parity with 100% efficient, zero capital cost grid electrolysis at the current average industrial electricity price. If the base-case grid electrolysis plant efficiency of 61% is assumed, the result is a natural gas parity point of \$13.4 $(MM\ BTU)^{-1}$. For comparison, liquefied natural gas (LNG) prices in Japan, where LNG prices have traditionally been highest worldwide, are currently < \$8 $(MM\ BTU)^{-1}$.[51] Thus, H_2 produced by grid electrolysis is more costly than H_2 produced by SMR, as is evidenced by the current market dominance of SMR for hydrogen production.

Grid electrolysis capital costs constitute 26% of the annual costs and are dominated by BoS costs, 59%, in comparison with 41% for the stack capital costs.[13] The active catalyst and membrane component costs constitute <25% of the stack capital costs, suggesting that research on lowering

these costs will provide small returns and thus the predominant efforts should be focused on cost-effective efficiency improvements.[26] Predicted advances suggest an 18% decrease in LCH for future grid electrolysis systems, based on increased efficiency and decreased capital costs, though such advances still result in LCH values far higher than that of H_2 produced by SMR.[13] Therfore, disruptive approaches to electrolysis that can provide high efficiencies at very low costs compared to the current approaches, including those related to the chlor-alkai process that has been practiced at scale for over a century, constitute an important avenue for sustained research and development efforts.

7.4.4 Solar H_2 vs low CO_2 or CO_2-Neutral Hydrogen Production

Hydrogen is an essential chemical feedstock in fertilizer production and fossil fuel upgrading, with demand expected to continue for fertilizer production and possibly biomass upgrading even in a CO_2-neutral economy. It is therefore important to assess different hydrogen production pathways and their economic competitiveness. Biomass reforming, CO_2-free grid electrolysis, and SMR with carbon capture and storage (CCS) are alternative routes to low CO_2 and CO_2-neutral hydrogen production. Technoeconomic studies of biomass reforming and gasification have yielded estimated hydrogen production costs of <\$3.0 kg^{-1} (adjusted to 2014 dollars).[52,53] However, the LCH is highly dependent on the feedstock type as well as on production and transportation costs. Biomass energy production, in general, is geographically constrained to areas not in competition with food production. Given this constraint, estimates for the US and California suggest that only a small portion of the projected liquid fuel demand could be met by biomass.[54,55] Dedicated use of biofuels for peaking capacity is possible, and given the enormous

installed storage capacity of gas pipelines, power production by combustion of carbon-neutral biogas may provide a low-cost solution for some peaking applications.

Nuclear fission reactors coupled with electrolyzers would produce hydrogen at \$7.4 kg^{-1} using estimated nuclear electricity production costs of \$0.1 kWh^{-1}.[56] This scenario of course explicitly assumes that the required nuclear fission power plants can overcome the financial and sociopolitical challenges such that sufficient numbers of plants are constructed and operated.

Natural gas- or coal-fired power plants with CCS constitute a low CO_2 electricity technology at pilot-plant scale. The added cost of CCS to fossil-fuel-derived electricity is a subject of current debate, with predicted n-th plant electricity costs for natural gas plants estimated to be ~ \$0.1 kWh^{-1}, yielding a LCH of \$7.4 kg^{-1} H_2 for systems that are designed to have an ~80% CO_2 capture efficiency.[56] However, this value assumes that the sequestration site exploration, and other currently large costs, as well as long-term technical and financial liability issues can be overcome.[57] Alternatively, CCS directly integrated with steam methane reforming is expected to increase the cost of SMR-derived H_2 by ~\$1 kg^{-1}, to ~\$2.5 $(kg\ H_2)^{-1}$, given estimated CCS costs of ~\$100 $(ton\ CO_2)^{-1}$ and a SMR CO_2 intensity of 10 ton CO_2 per ton H_2.

7.4.5 Solar H_2 vs Low CO_2 or CO_2-Neutral Energy Production and Storage Technologies

Two forms of energy consumption are considered here: electricity and transportation fuels. For low CO_2 or CO_2-neutral electricity production, nuclear fission and fossil fuels with CCS

technologies will compete with wind and solar systems that incorporate storage in the form of batteries, fuels (H_2), pumped hydro, compressed air, or other energy storage technologies. As discussed above, nuclear fission and fossil fuels plus CCS have a mutually similar predicted electricity production price of ~\$0.1 kWh^{-1} assuming the challenges, also discussed above, for each of these technologies can be surmounted.

Capital costs for fully installed battery systems are between \$500 to \$1000 kWh^{-1} or more per kWh of capacity.[58] The levelized cost of storage, excluding input electricity costs, ranges from \$0.25 kWh^{-1} to \$0.49 kWh^{-1} for a capital cost range of \$500 kWh^{-1} to \$1000 kWh^{-1} (assuming a 10 year lifetime, one cycle per day, a 10% discount rate, 92% round-trip efficiency, and a linear decay to 80% of capacity at the end of life). To provide reliability commensurate with current base-load utility generation systems, battery systems coupled to wind or solar systems would need to be significantly oversized to accommodate resource availability extremes (days with little or no sunshine or wind), which would increase the battery storage costs further due to lower utilization rates than those assumed herein. The needs for research and development to develop new battery chemistries that could provide cost-effective grid-scale energy storage are widely recognized.

Conversion of hydrogen into electricity requires storage and an energy conversion process. Little information is available on real-world compression efficiencies for hydrogen storage, but the existing data suggest that compression from 14 bar to 430 bar, roughly equivalent to high pressure storage conditions, is 75% efficient.[59] MW-scale fuel cell systems have efficiencies

ranging from 40-49%.[60-62] Including the efficiency losses only, with no inclusion of extra capital costs, the cost of electricity that results from hydrogen production costs of \$11.4 kg^{-1} and \$13.4 kg^{-1} H_2, respectively, in conjunction with the above compression and fuel-cell conversion efficiencies, are \$0.92 kWh^{-1} and \$1.09 kWh^{-1}, respectively. Because H_2 storage is relatively inexpensive, the cost associated with extra storage capacity for overcoming resource availability extremes is expected to be less than the cost to achieve the same functionality using battery storage.[59]

Pumped hydroelectric and compressed air storage in suitable geologic formations are less expensive than batteries and hydrogen for energy storage applications, but the geologically constrained capacity limits may require other technologies to make up the needed balance of storage capacity, which can be a majority in a low-CO_2 energy system that has a large amount of renewables in the generation mix.[63] The total capacity required for future energy storage will depend upon the ultimate mix of generation capacity and demand.

The above analysis suggests that solar or wind systems that utilize current battery or fuel storage to obtain reliability metrics similar to that of current base-load or dispatchable load power plants have costs that are one order of magnitude higher than current electricity prices and than the expected prices of nuclear or fossil fuel with CCS alternatives. Within storage technologies for intermittent energy sources, the high cost of both battery and fuel storage options suggests that neither is clearly advantaged. Consequently, dramatic cost reductions are required to achieve competitiveness with other electricity technologies that can provide electricity on demand,

providing a need for the development of disruptive technologies for cost-effective grid-scale energy storage.

A second possible market for solar hydrogen is transportation in the form of fuel cell vehicles, where H_2 is suited for use in light-duty vehicles as well as in some larger vehicles, such as buses. Hydrogen's relatively low volumetric energy density (4 MJ L^{-1} at 10,000 psi), as compared to conventional aviation and diesel fuels (35 MJ L^{-1}), provides at present a technical barrier to the use of high-pressure hydrogen fuel in these sectors.[64] Significant improvements in hydrogen's stored volumetric system energy density, through hydrogen storage research, can make hydrogen suitable for markets that have fewer and/or more expensive technology alternatives.

In currently suitable markets, hydrogen will compete primarily with batteries. Land requirements may constrain biofuels to a relatively low maximum penetration level, even if solar hydrogen is used for biofuel upgrading. As discussed above, the costs of storage in the form of batteries or hydrogen are similar yet high, and thus neither has a clear advantage; both electric and fuel cell vehicles are available to consumers although in limited quantities. The recharge times of batteries also are limited due to resistive heating losses, providing a refueling advantage to hydrogen.

7.4.6 Comparisons to Previous Work

The findings presented herein are consistent with previous life-cycle analysis (LCA) studies.[65] In particular, the energy-return on energy-invested (EROEI or EROI) for a large

photoelectrochemical hydrogen production facility has been shown to be positive, with a maximum EROI value, based on any single parameter sensitivity, of <3:1, and a base-case EROI of 1.66. The minimum EROI (petroleum based) necessary to sustain the minimum standards of life is reported to be 3:1, but to sustain present standards of life in first-world countries the minimum EROI is generally higher, upwards of 14:1, for many of the luxuries we currently enjoy (health care, athletics, art, etc.).[66] Current EROI values for petroleum are 20:1 – 30:1, and preferred new energy generation technologies would have similar EROI values, thereby allowing impoverished people to raise their standard of living to that of first-world countries.[66] Both the economic and EROI assessments for base case solar hydrogen systems are an order of magnitude lower than currently competitive values. The broad agreement with the analysis presented herein grounds our results, future outlook, and suggested research avenues for solar electrolysis technologies. Specifically, such applications provide an opportunity for foundational research to contribute to the development of disruptive approaches to solar fuels generation systems that can offer higher performance at much lower costs than current embodiments of solar fuels generators.

Additionally, previous technoeconomic analyses have been performed on different solar hydrogen technologies at different levels of depth. A 1998 report covering PEC and PV-E systems found LCH values similar to those calculated herein for their base-case systems.[67] However, their predicted advancements in both PEC and electrolysis performance and economics have not yet been realized. Thus current costs, as presented herein, remain aligned with the base-case values in the previous report. That report suggested that PEC technologies could be advantaged over PV-E systems if the performance and economic goals set therein were met, but no quantitative

argument was presented to determine the source of this advantage. In 2009, a comprehensive technoeconomic analysis focused solely on PEC systems.[26] Many of the PEC plant economic assumptions made herein were taken directly from that report. LCH values for panel-based PEC systems therein were similar to the LCH values for the PEC systems evaluated herein (Type 3 and 4 systems), though their systems did not explicitly include the costs for a membrane, as is done herein. However, two other particle-based systems were studied therein and found to possess the potential for significantly reduced LCH values due to reduced balance of system costs. Finally, a recent report that was focused on the PEC cell alone found that the catalyst cost contribution was negligible for even the most expensive electrocatalysts, Pt and Ir.[46] This finding is consistent with the full technoeconomic analysis of both the components and installed system presented herein.

7.4.7 Direct Solar CO_2 Reduction Potential

Recent efforts have refocused attention on the direct electrochemical reduction of CO_2, which has the possibility of making higher-value products that could potentially support a higher capital cost than can be supported by a hydrogen production process.

The direct use of CO_2 as an electrochemical reactant involves many chemical, engineering, and economic challenges due to the relatively low temperature and low electrode reaction rates, the absence of active and selective electrocatalysts, and the low concentration of CO_2 in the atmosphere, the ultimate source for a closed-cycle sustainable CO_2-based energy scenario. By necessity, a CO_2-reduction system needs an inexpensive source of CO_2 (as compared to the

product value) delivered to the catalyst surface at a rate greater than the current density provided by the photovoltaic component (24 mA cm^{-2} for an ideal tandem junction device[38] or equivalently $\frac{2.5 \times 10^{-3}}{\text{\# of electrons per product molecule}}$ mol CO_2 s^{-1} m^{-2}). The low concentration of CO_2 in air highly favors, and may require, capturing the atmospheric CO_2 from a much larger area than is subtended by the solar capture area. Capturing CO_2 from air is projected to cost more than \$600 (ton CO_2)$^{-1}$, which eliminates many CO_2 reduction products in an unconstrained energy market because their market prices, in \$-(ton CO_2)$^{-1}$ equivalence, are less than \$600 (ton CO_2)$^{-1}$ (Figure 7.9).[68,69] The products shown in Figure 7.9 are species that have been measured and quantified during the electrocatalytic reduction of CO_2 using copper electrodes.[70] Additional routes include a two-step procedure consisting of an initial electrocatalytic step followed by a thermochemical step to produce ethylene glycol from CO_2.[71] Delivering CO_2 in aqueous systems at a rate that is not limiting at 1 Sun solar fluxes requires a mass transport coefficient at least two orders of magnitude higher than is achievable for natural transport under optimistic conditions (high winds, limited by mass transport in the liquid phase) (see supplementary information for details).[72] The concentrated CO_2 sources and/or forced convection systems that are needed to overcome mass transport limitations will add cost to the overall system and product.

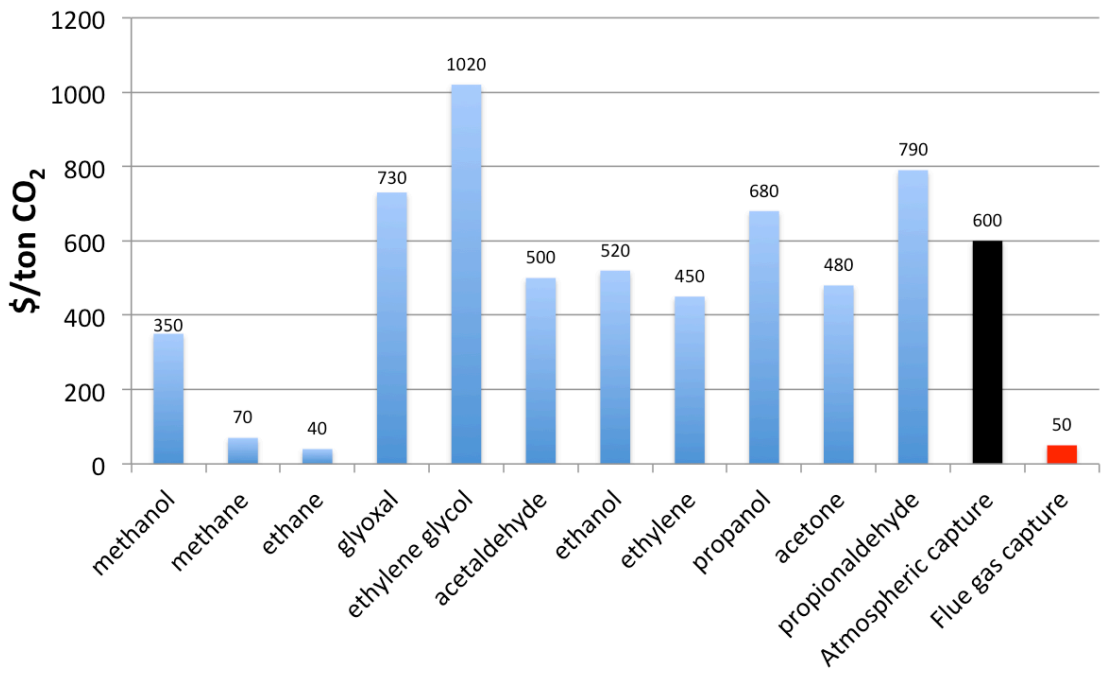

Figure 7.9: Breakeven cost of CO_2 for a variety of know Cu CO_2 reduction products The cost of CO_2 equivalence for a variety of known CO_2 electrochemical reduction products on Cu. The conversion calculation assumed 100% utilization of CO_2 and converted based on the mass of CO_2 retained in the product molecule. The CO_2 price of atmospheric capture (estimated) and state-of-the-art flue gas capture are shown for comparison.

One concentrated CO_2 source, shown in Figure 7.9, is carbon captured from flue gas, with current state-of-the-art CO_2 costs of \$50 (ton CO_2)$^{-1}$.[73] Product use in distributed applications would make the system a twice-thru carbon system that could serve to improve the efficiency of carbon utilization. The lower CO_2 cost expands the possible reduction products from an economic perspective. These value-added products are used today for their chemical attributes and not as fuel sources, and all current fuels are more costly to produce by CO_2 reduction than by current means even with CO_2 at \$50 (ton CO_2)$^{-1}$. Figure 7.9 also provides information on the most value-added target products for near-term CO_2 reduction approaches. Interestingly, an early-stage

company, Liquid Light, focused on electrochemical CO_2 reduction is targeting ethylene glycol production, likely in part due to the large spread at present between the reactant cost and the product value.[71]

Methanation of solar hydrogen with gas-phase CO_2 may circumvent the mass transport issue that is a barrier to sustainable CO_2 reduction in water. Other competing options for CO_2 reduction include known commercial thermochemical processes including Fischer-Tropsch and intermediate methanol synthesis using Cu-ZnO catalysts. Irrespective of the pathway chosen the challenge of a relatively expensive reactant (CO_2) remains. Further evaluation against the direct use of hydrogen is needed to understand these comparisons in more detail.

7.4.8 Guidance for Research

Solar hydrogen production systems, which are at a laboratory research scale, have been compared herein to more mature technologies, because such systems are ultimately what solar hydrogen will compete against in the commercial arena. The base-case scenarios herein are representative of the best-case currently available PEC systems based on laboratory demonstrations, and are representative of current PV and electrolyzer systems. Our conclusions are based on these comparisons and identify the largest opportunities for achieving cost-competitive solar hydrogen production technologies.

The results indicate that aggressive performance improvements and capital cost reductions are required simultaneously for solar hydrogen to achieve parity with fossil-fuel-derived hydrogen

costs. Specifically, achieving a maximum practical plant efficiency of 25% at the base-case PEC costs is not sufficient to attain this goal. Figure 7.10 illustrates this case and depicts the broader impact that changes in the total capital expense and plant efficiency can have on the LCH for generic PEC systems.

The maturity of the photovoltaic and electrolyzer industries, respectively, suggests that present balance of systems costs, combined with non-zero costs of the active components, will serve as barriers to constructing cost-effective solar hydrogen production facilities based on technologies that are cosmetically similar to current photovoltaic installations. Consequently, radically new plant-wide designs are needed, and the economics of such technologies should be validated through collaboration with chemical plant design engineers. For example, large-area installations of artificial turf, a relatively inexpensive robust outdoor material, cost ~\$110 m_S^{-2}.[74] For such an installation (\$110 m_S^{-2}) but composed of photoactive solar hydrogen generating materials operating at the maximum practical efficiency of 25% having a plant lifetime of 20 years and active component lifetime of 7 years, the LCH would be ~\$1.8 kg^{-1} H_2. This LCH is thus comparable to, but still somewhat higher than, current H_2 derived from fossil fuels.

These metrics of 25% plant-wide STH efficiency and 7 year active component lifetime are similar to the 25% efficiency, 10-year electrode lifetime that comprise DOE targets for PEC hydrogen production, but are significantly higher than the 10% efficiency, 5-year particle lifetime in DOE targets for PEC hydrogen production using Type 1 and 2 baggie systems. The analysis herein suggests that irrespective of the active component architecture and cost, very high efficiencies

are required, and thus all system efficiency targets should be ~25% with active component lifetimes of 7-10 years.

PEC technologies may be advantaged because they may facilitate the implementation of such new plant designs. For example, the Type 1 and 2 designs (particles in low cost polymeric bags) entail a completely different form factor that is predicted to produce hydrogen at costs much closer to current market prices.[14] Another potential design includes a flexible, membrane embedded device (using Si microwires for example) that could be rolled out like artificial turf with a hydrogen collection system similar to that used for landfill methane collection.[75,76] The practicality of such designs should be rigorously analyzed to understand the potential advantages of each approach and thus to guide research and development trajectories and milestones.

Assuming such radically new designs are possible, the performance and cost of the active components remain to be demonstrated simultaneously. A consistent theme throughout the solar hydrogen technoeconomic analysis is that membrane and semiconductor costs are dominant while the semiconductor efficiency and stability are the limiting performance components. Accordingly, one conclusion is that electrocatalysts contribute little to the overall capital cost, and the performance of known electrocatalysts is sufficient to reach the needed performance targets in several possible implementations of the technology.[46] The main area seen for potential impact is in acid- stable oxygen evolution catalysts, where iridium oxide is the only known material to exhibit satisfactory performance characteristics. [77] However, Ir is the least abundant element in the Earth's crust, and the scarcity of Ir would preclude scaling the

technology to terawatt levels of solar hydrogen capacity.[78] Thus, acid stable oxygen evolution electrocatalysts that have a performance similar to that of iridium oxide would be required to achieve very high penetration scenarios using this particular electrolysis technology implementation.

Additionally, the limiting semiconductor component is the wide bandgap material in a tandem stack. Few materials exist with the proper bandgap, and of those that do, all are unstable under solar fuels operating conditions and are much too expensive due to growth methods that require epitaxy to achieve high performance. This later point has been a continual challenge for the photovoltaic industry where tunnel junction formation and lattice matching constraints substantially restrict materials compatibility. Concepts such as spectral splitting or multi-terminal electronic architectures could relax some of the challenges involved with materials growth, but introduce their own challenges that have, to date, been less attractive than traditional epitaxial growth solutions. Another potential solution is nanowire growth, which can relax lattice mismatch growth defects more readily than planar architectures, and thus may broaden the range of materials compatibility.

Membrane development is another important area because the membranes used in electrolyzers are too expensive for implementation in base-case solar fuels systems achitectures and moreover have higher ionic conductivities than needed for PEC devices.[79] Thus, membranes designed specifically for PEC may enable lower costs due to different required performance targets in the associated technology implementation.

Device stability is critical to a cost-effective solar hydrogen technology. Protection of known high-efficiency semiconductors is likely the largest challenge. Improving recently developed protection and stabilization methods, and/or developing entirely new approaches that can protect square meters of semiconductor for years, while maintaining high efficiency, is needed to facilitate a viable, scalable solar hydrogen technology.[80-82] In addition, typical stability measurements are performed with no standard protocol and generally under constant illumination; hence protocols should be developed to facilitate the intercomparison of results, and measurements should be extended to include dark conditions as well as the stresses associated with diurnal cycling for extended periods of time.

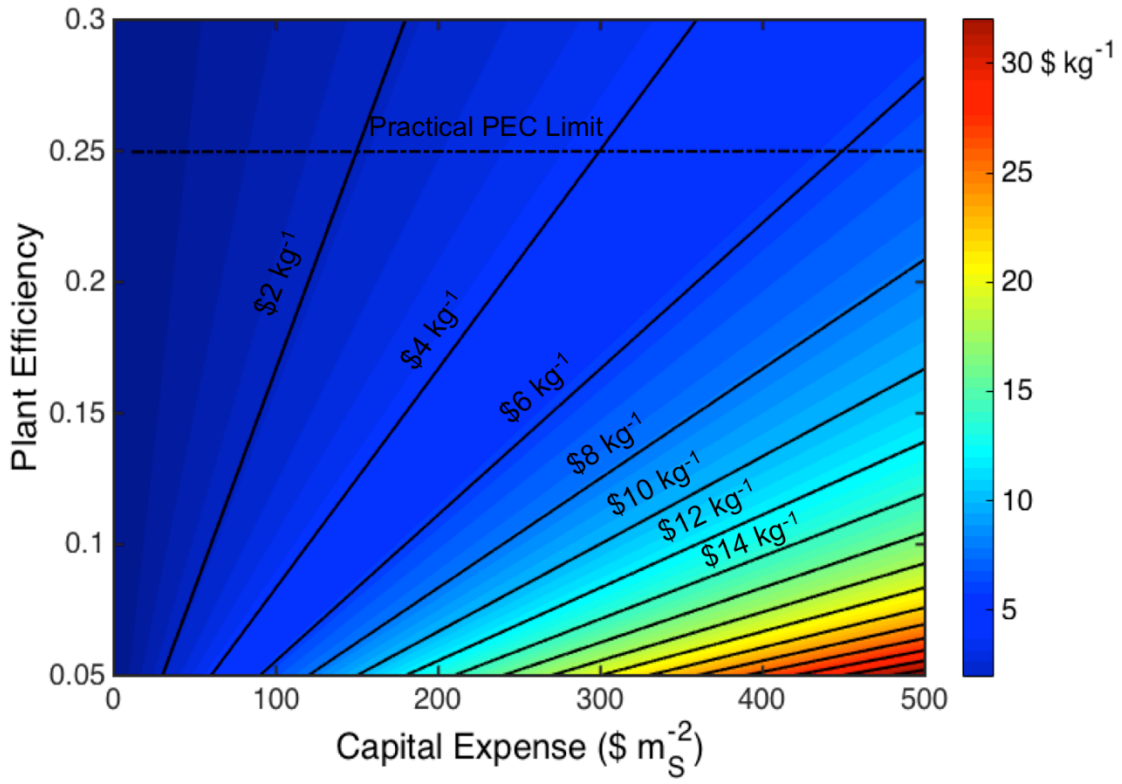

Figure 7.10: LCH contour plot of plant efficiency versus capital expense for a generic PEC system A contour plot of the LCH ($ kg^{-1}) for a generic PEC system as a function of the plant efficiency and capital expense ($ m_S^{-2}). This calculation includes identical assumptions to the specific PEC analyses above, except that the replacement costs at 7 and 14 years are assumed to be 15% of the total capital expense. Contours are labeled at \$2 kg^{-1} intervals and the practical efficiency limit for PEC systems is indicated assuming direct electrical connection between the semiconductor and catalyst components without additional power electronics.

7.5 Summary and Conclusions

Applied research based on firm scientific principles guided by realistic production and economic constraints is a foundation of societal progress. To have significant impact on the major problems of society, technological solutions must necessarily be competitive within the economic realities of the marketplace. Rigorous economic competitive analyses, applied after proof-of-concept

research and development, can provide critical guidance on a project's further resource allocation, priorities, and trajectory. This paradigm for applied research maintains unrestricted scientific imagination along with foundational research, while providing an economic rationale to calibrate the intensity of additional human and financial capital for applied research.

To this end, a comparative technoeconomic analysis of photoelectrochemical and photovoltaic-electrolytic solar hydrogen production systems was performed. The results indicate an estimated levelized cost of hydrogen (LCH) for base-case Type 3 and 4 photoelectrochemical systems of \$11.4 kg^{-1} and \$9.2 kg^{-1}, respectively. For comparison, the estimated LCH for base-case PV-E and GSPV-E systems were \$13.4 kg^{-1} and \$6.1 kg^{-1}, respectively. The base-case PEC systems are advantaged over the base-case PV-E systems because hydrogen transport from the panels to compression units is less expensive than electricity transport and conditioning from the PV panels to the electrolyzers.

Successful research and development, measured solely by achieving a system efficiency of greater than 20% within the current embodiments of solar H_2 generators, is not sufficient to produce systems with LCH values comparable to the LCH of fossil-fuel derived electricity. Panel mounting materials, labor, and other balance of systems costs, irrespective of the active materials, amount to LCH values in excess of current hydrogen and energy prices. For base-case PEC systems, a carbon tax of greater than \$800 $(ton\ CO_2)^{-1}$ would be required in an unconstrained CO_2 energy market for SMR to reach hydrogen price parity with these solar technologies.

Expected electricity prices from CO_2-neutral nuclear and low-CO_2 fossil fuel with CCS technologies are currently an order of magnitude lower than expected electricity prices from solar or wind systems with battery or fuel storage solutions that provide reliability similar to that of current base-load or dispatchable generation technologies. Given these low electricity prices, electrolytic hydrogen prices are also projected to be significantly lower than the solar hydrogen routes analyzed herein, requiring disruptive approaches to solar hydrogen generation relative to the present embodiments of the technology.

The capacity factor of presently known solar-based energy systems is their fundamental limitation; any capital item used only 20% or less of the day will be at a disadvantage to capital used more effectively. Efforts to increase the low capacity factor of terrestrial solar power, as well as re-designed solar installation schemes that significantly reduce the balance of system costs and increase the efficiency to near the Shockley-Queisser limit without increasing the capital cost, will have the largest impacts on the economic competitiveness of the resulting technology implementations. Radically new materials and system designs that achieve fully installed costs similar to simple material installations such as artificial grass are required to achieve the equally dramatic cost reductions needed for solar or wind power to compete with current generation technologies.

8 Conclusions

8.1 Thesis Summary

This thesis has focused on design, fabrication, and experimental characterization of Si microwire array based photoelectrodes for unassisted solar water splitting. Chapter 1 provided motivation, historical context, and a discussion of the relevant physical phenomena for this thesis work. Chapter 2 described a complete water splitting tandem junction Si microwire array device design and the general fabrication procedure for Si microwire array devices. Chapter 3 investigated the first of two Si microwire array tandem junction devices, this one consisting of a np^+-Si microwire homojunction array coated by tin-doped indium oxide (ITO) and tungsten oxide (WO_3), sequentially. This device showed proof-of-principle, but lacked the voltage necessary to perform unassisted water splitting under 1 sun illumination conditions.[31] A second tandem junction device was thus investigated in Chapter 4 to improve on the WO_3 device and consisted of the same np^+-Si microwire homojunction array, but now coated with the more stable fluorine-doped tin oxide (FTO) and titanium oxide (TiO_2). This device achieved unassisted water splitting under 1 sun illumination and improved stability over the ITO/WO_3 device. In sum, these two devices have laid the groundwork for one embodiment of a Si microwire array based device for solar water splitting that could be improved upon through incorporation of a narrower bandgap replacement for WO_3 and TiO_2 that produces similar or higher voltages than TiO_2 and simultaneously higher current densities due to the smaller bandgap.

Chapter 5 applied a recently developed amorphous, oxidatively-protective TiO_2 coating to np^+-Si microwire arrays and demonstrated >2200 hours of stability for oxygen evolution.[71] Chapter 6 investigated a Si microwire array based photocathode design aimed at decoupling light absorption and catalytic activity, two parameters that are traditionally anti-correlated in planar systems.[50]

The guiding theme throughout these experimental efforts has been that Si microwire arrays, or similar three-dimensionally structured materials, may provide performance and/or economic benefits for solar water splitting devices as compared to the planar designs that nearly all previous research has focused on (Chapter 2). To understand the validity of these claims and how solar fuels compares in the broader energy generation and storage sector a detailed technoeconomic analysis was performed (Chapter 7). The results confirm reality in that no commercial solar hydrogen facilities have been constructed to date because the economics are unfavorable. Projected hydrogen production costs, based on state-of-the-art laboratory-scale solar water splitting devices or photovoltaics connected to electrolyzers, are at least one order of magnitude more expensive than fossil fuel derived hydrogen. The analysis suggests that radically different plant-wide designs along with higher efficiencies, yet to be demonstrated, are needed to compete economically.

8.2 Technoeconomic Realities

Terrestrial solar power conversion is fundamentally constrained by a low power density (1 kW m^{-2}), low capacity factor (< 25% for non-tracking systems), and high resource variability as compared

to conventional fossil fuel and nuclear-based power production. These constraints combined with the high front loaded capital costs of solar power conversion facilities have made them economically unattractive to-date; it is only through large governmental subsidies that solar photovoltaics have seen recent high growth.

The maturity of the photovoltaic and electrolysis industries suggests that achieving the ten times cost reductions needed to enable solar fuels to compete economically should not be expected. Alternatively, Si microwire arrays enable flexible device architectures that could provide the foundation for the radically different facility wide changes needed. For example, a flexible device could be rolled out utilizing similar methods to landfill methane collection for hydrogen collection. However, such radically new designs still require the same technical attributes, such as high device efficiency and electrochemical and mechanical stability, that have not been demonstrated on any architecture, let alone Si microwire arrays, and need significant engineering scouting to verify that such optimistic ideas would actually enable the level of facility-wide cost reductions needed.

If Si microwire arrays are going to have a chance of making solar fuels at a scale that impacts the world, a host of technical challenges remain (most of these challenges remain for planar devices as well).

1. **Si microwire array efficiency:** The highest reported efficiency for single junction Si microwire arrays remains below that needed to achieve 20% STH efficiency in a tandem configuration, irrespective of the wide bandgap absorber.[37,40] Photovoltaic efficiencies should be doubled to >15% with significant improvement needed in the longer wavelength

spectral response as these are the photons that Si will see in a tandem device and is currently the worst performing region of the spectral response. Light scattering elements have been shown to improve the broadband absorption characteristics of Si microwire arrays, but translation into the high spectral response values needed at long wavelengths has not been demonstrated to the degree necessary.

2. **Wide bandgap semiconductor:** A high efficiency wide bandgap tandem partner for Si is required with a bandgap near 1.7 eV. Semiconductors with the proper bandgap exist, but integration with Si is difficult; the current growth methods employed (MO-CVD) are not economically scalable to-date and the efficiencies are low due to epitaxial growth challenges.[52] Discovery of a new material is a continual hope, but impossible to predict the timing of and, if history is repeated, requires significant research and development time before being commercially relevant.
3. **Tunnel junction:** A low resistance, transparent connection between Si and the wide bandgap semiconductor is required for high efficiency operation. This has been a major road block for integrating known materials on traditional surface orientations of Si through epitaxial growth.[139] Si microwire arrays have been even more difficult due to the multiple non-traditional crystallographic orientations present on the surface.[52] Alternative non-epitaxial methods may exist such as amorphous TiO_2 and transparent conductive oxides, but their ability to perform this task with high efficiency devices has yet to be demonstrated.
4. **Membrane embedment:** An ionically conductive, gas impermeable membrane should be able to be embedded in and provide mechanical support for the microwire array. This has been demonstrated for bare Si microwire arrays with Nafion®, a proton exchange membrane suitable in acidic media and that is too expensive at current prices, and QAPSF, an anion exchange membrane suitable in basic media and that remains at an academic research level.[59]

These have not been demonstrated in a tandem microwire array device and the operational mechanical stability of such a structure is unknown.

5. **Stability:** The complete device must be electrochemically and mechanically stable for many years. Many, if not all, of the known and relevant wide bandgap semiconductors are not stable under operation for either hydrogen or oxygen evolution and thus must be protected. Recent progress has been made using a variety of protective coatings, but these demonstrations are only possible on very small (<< 1 cm^2) areas and for limited times (<40 hours).[77] Stability of the many interfaces within the device also needs to be proven. Examples include catalyst/semiconductor, membrane/semiconductor, Si/tunnel junction/semiconductor, etc.
6. **Integration:** Many different materials must be present for efficient operation of such a device and their integration with one another must be compatible and optimized. For example, catalyst integration with semiconductors has proven to give non-intuitive results with the best semiconductors and best catalyst not necessarily producing the highest efficiency combination.[173]
7. **Dark conditions:** Nearly all experiments are performed under simulated solar illumination only. What happens in the dark? If a material is stable due to cathodic or anodic protection under operation, what happens at night? If 1 atm of H_2 and O_2 are present on their respective sides at night a chemical potential gradient exists across the device. The device would be under forward bias and short circuited in this configuration and thus is expected to run in reverse unless the H_2 and O_2 are actively pumped from the system every day. Can this be done economically? Do efficient enough hydrogen and oxygen evolution catalysts exist that simultaneously have sufficiently suppressed activity for the reverse reactions? Is there another technical solution?

The ultimate success of large-scale projects is largely determined by economics. Accordingly, the combination of technical and economic hurdles for solar fuels technologies, discussed above, must be acknowledged and addressed directly if we are to be successful. The active components that the research community works so hard on make up only a piece, and sometimes a small piece, of the cost of an energy generation facility. Using the bottom up, linear approach that focuses on individual components first and leaves integration and other higher level challenges until later, and has been the paradigm for the last 40+ years, may not be the most expedient route. Rather, a top down approach that allows for periodic evaluation of a solar fuel's technoeconomics would better direct subsequent funding allocation decisions and milestone goals. For instance, directed questions as to what parameters need to be meet for achieving commercial success and the presence or absence of thermodynamically and economically credible pathways able to meet those achievement metrics are crucial. These points of reference would better provide starting points to guide research efforts towards those areas that will have the most impact.

Inexpensive and abundant energy is the foundation of our highly efficient and productive civilization. Maintaining this favorable environment for future generations will require energy resources on the scale of and with an energy surplus similar to fossil fuels. This challenge is too large and important not to use all available tools, technical and economic, to focus our efforts on those technologies and their rate limiting challenges that can most effectively and sustainably provide for humanities advancement.

References

1 C. A. S. Hall and K. A. Klitgaard, *Energy and the Wealth of Nations*, Springer New York, New York, NY, 2012.

2 P. Tans and R. Keeling, *noaa.gov*.

3 D. Yergin, *The Prize*, 2008.

4 D. Yergin, *The Quest*, 2012.

5 D. J. C. MacKay, *Sustainable Energy--without the Hot Air*, Uit Cambridge Limited, 2009.

6 C. De Castro, M. Mediavilla, L. J. Miguel and F. Frechoso, *Energy Policy*, 2011.

7 A. C. Nielander, M. R. Shaner, K. M. Papadantonakis, S. A. Francis and N. S. Lewis, *Energy & Environmental Science*, 2014, **8**, 16–25.

8 S. M. Sze and K. K. Ng, *Physics of Semiconductor Devices*, John Wiley & Sons, 2006.

9 P. Würfel and U. Würfel, *Physics of Solar Cells*, John Wiley & Sons, 2009.

10 S. Fonash, *Solar Cell Device Physics*, Elsevier, 2012.

11 C. Kittel, *Introduction to solid state physics*, John Wiley & Sons, 2007.

12 N. W. Ashcroft and N. D. Mermin, *Solid State Physics*, 2011.

13 R. R. King, D. Bhusari, A. Boca, D. Larrabee, X. Q. Liu, W. Hong, C. M. Fetzer, D. C. Law and N. H. Karam, *Prog. Photovolt: Res. Appl.*, 2010, **19**, 797–812.

14 J. R. Bolton, S. J. Strickler and J. S. Connolly, *Nature*, 1985, **316**, 495–500.

15 S. Hu, C. Xiang, S. Haussener, A. D. Berger and N. S. Lewis, *Energy & Environmental Science*, 2013, **6**, 2984–2993.

16 S. Licht, B. Wang, S. Mukerji, T. Soga, M. Umeno and H. Tributsch, *Journal of Physical Chemistry B*, 2000, **104**, 8920–8924.

17 O. Khaselev and J. A. Turner, 1998, **280**, 425–427.

18 A. J. Bard and L. R. Faulkner, *Electrochemical Methods*, Wiley Global Education, 2000.

19 C. C. L. McCrory, S. Jung, I. M. Ferrer, S. M. Chatman, J. C. Peters and T. F. Jaramillo, *J. Am. Chem. Soc.*, 2015, **137**, 4347–4357.

20 M. R. Singh, K. Papadantonakis, C. Xiang and N. S. Lewis, *Energy & Environmental Science*, 2015, **8**, 2760–2767.

21 J. Jin, K. Walczak, M. R. Singh, C. Karp, N. S. Lewis and C. Xiang, *Energy & Environmental Science*, 2014, **7**, 3371–3380.

22 A. Berger, R. A. Segalman and J. Newman, *Energy & Environmental Science*, 2014, **7**, 1468–1476.

23 M. R. Shaner, K. T. Fountaine and H.-J. Lewerenz, *Appl. Phys. Lett.*, 2013, **103**, 143905.

24 R. H. Coridan, A. C. Nielander, S. A. Francis, M. T. McDowell, V. Dix, S. M. Chatman and N. S. Lewis, *Energy & Environmental Science*, 2015, **8**, 2886–2901.

25 A. Fujishima and K. Honda, *Nature*, 1972, **238**, 37–38.

26 O. Khaselev and J. A. Turner, *Science*, 1998, **280**, 425–427.

27 Y. Nakato, T. Ohnishi and H. Tsubomura, *Chem. Lett.*, 1975, 883–886.

28 J. A. Seabold and K.-S. Choi, *J. Am. Chem. Soc.*, 2012, **134**, 2186–2192.

29 F. F. Abdi, L. Han, A. Smets, M. Zeman and B. Dam, *Nature*, 2013.

30 C. Liu, J. Tang, H. M. Chen, B. Liu and P. Yang, *Nano Lett.*, 2013, **13**, 2989–2992.

31 M. R. Shaner, K. T. Fountaine, S. Ardo, R. H. Coridan, H. A. Atwater and N. S. Lewis, *Energy & Environmental Science*, 2014, **7**, 779–790.

32 J. W. Ager III, M. Shaner, K. Walczak, I. D. Sharp and S. Ardo, *Energy & Environmental Science*, 2015, 1–16.

33 O. Khaselev, A. Bansal and J. A. Turner, *International Journal of Hydrogen Energy*, 2001, **26**, 127–132.

34 G. Peharz, F. Dimroth and U. Wittstadt, *International Journal of Hydrogen Energy*, 2007, **32**, 3248–3252.

35 N. A. Kelly and T. L. Gibson, *International Journal of Hydrogen Energy*, 2006, **31**, 1658–1673.

36 R. E. Rocheleau, E. L. Miller and A. Misra, *Energy Fuels*, 1998, **12**, 3–10.

37 S. W. Boettcher, E. L. Warren, M. C. Putnam, E. A. Santori, D. Turner-Evans, M. D. Kelzenberg, M. G. Walter, J. R. McKone, B. S. Brunschwig, H. A. Atwater and N. S. Lewis, *J. Am. Chem. Soc.*, 2011, **133**, 1216–1219.

38 S. W. Boettcher, J. M. Spurgeon, M. C. Putnam, E. L. Warren, D. B. Turner-Evans,

M. D. Kelzenberg, J. R. Maiolo, H. A. Atwater and N. S. Lewis, 2010, **327**, 185–187.

39 M. D. Kelzenberg, S. W. Boettcher, J. A. Petykiewicz, D. B. Turner-Evans, M. C. Putnam, E. L. Warren, J. M. Spurgeon, R. M. Briggs, N. S. Lewis and H. A. Atwater, *Nature Materials*, 2010, **9**, 239–244.

40 M. C. Putnam, S. W. Boettcher, M. D. Kelzenberg, D. B. Turner-Evans, J. M. Spurgeon, E. L. Warren, R. M. Briggs, N. S. Lewis and H. A. Atwater, *Energy & Environmental Science*, 2010, **3**, 1037.

41 S. Haussener, C. Xiang, J. M. Spurgeon, S. Ardo, N. S. Lewis and A. Z. Weber, *Energy & Environmental Science*, 2012, **5**, 9922–9935.

42 J. M. Rubi and S. Kjelstrup, *Journal of Physical Chemistry B*, 2003, **107**, 13471–13477.

43 B. M. Kayes, H. A. Atwater and N. S. Lewis, *J. Appl. Phys.*, 2005, **97**, 114302.

44 C. Xiang, A. C. Meng and N. S. Lewis, *Proceedings of the National Academy of Sciences*, 2012, **109**, 15622–15627.

45 M. H. Lee, K. Takei, J. Zhang, R. Kapadia, M. Zheng, Y.-Z. Chen, J. Nah, T. S. Matthews, Y.-L. Chueh, J. W. Ager and A. Javey, *Angewandte Chemie International Edition*, 2012, **51**, 10760–10764.

46 J. R. Maiolo, B. M. Kayes, M. A. Filler, M. C. Putnam, M. D. Kelzenberg, H. A. Atwater and N. S. Lewis, *J. Am. Chem. Soc.*, 2007, **129**, 12346–12347.

47 H. J. Lewerenz, *Photoelectrochemical Materials and Energy Conversion Processes*,

Wiley-VCH Verlag GmbH & Co. KGaA, Weinheim, Germany, 2010, vol. 12.

48 M. D. Kelzenberg, D. B. Turner-Evans, M. C. Putnam, S. W. Boettcher, R. M. Briggs, J. Y. Baek, N. S. Lewis and H. A. Atwater, *Energy & Environmental Science*, 2011, **4**, 866.

49 E. L. Warren, J. R. McKone, H. A. Atwater, H. B. Gray and N. S. Lewis, *Energy & Environmental Science*, 2012, **5**, 9653.

50 M. R. Shaner, J. R. McKone, H. B. Gray and N. S. Lewis, *Energy & Environmental Science*, 2015, **8**, 2977–2984.

51 N. C. Strandwitz, D. B. Turner-Evans, A. C. Tamboli, C. T. Chen, H. A. Atwater and N. S. Lewis, *Adv. Energy Mater.*, 2012, **2**, 1109–1116.

52 C. C. Chen, D. B. Turner-Evans, H. Emmer, S. Aloni and H. A. Atwater, *39th IEEE Photovoltaic Specialists Conference*, 2013, 1–5.

53 A. C. Tamboli, M. Malhotra, G. M. Kimball, D. B. Turner-Evans and H. A. Atwater, *Appl. Phys. Lett.*, 2010, **97**, 221914–4.

54 Q. Mi, A. Zhanaidarova, B. S. Brunschwig, H. B. Gray and N. S. Lewis, *Energy & Environmental Science*, 2012, **5**, 5694–5700.

55 M. C. Putnam, D. B. Turner-Evans, M. D. Kelzenberg, S. W. Boettcher, N. S. Lewis and H. A. Atwater, *Appl. Phys. Lett.*, 2009, **95**, 163116.

56 M. Kelzenberg, California Institute of Technology, 2010.

57 J. M. Spurgeon, K. E. Plass, B. M. Kayes, B. S. Brunschwig, H. A. Atwater and N. S.

Lewis, *Appl. Phys. Lett.*, 2008, **93**, 032112.

58 A. G. Muñoz, C. Heine, M. Lublow, H. W. Klemm, N. Szabo, T. Hannappel and H. J. Lewerenz, *ECS Journal of Solid State Science and Technology*, 2013, **2**, Q51–Q58.

59 J. M. Spurgeon, M. G. Walter, J. Zhou, P. A. Kohl and N. S. Lewis, *Energy & Environmental Science*, 2011, **4**, 1772.

60 Y. Zhao, E. S. Smotkin and T. Mallouk, *Energy & …*, 2012.

61 Y. J. Hwang, A. Boukai and P. Yang, *Nano Lett.*, 2009, **9**, 410–415.

62 M. T. Mayer, C. Du and D. Wang, *J. Am. Chem. Soc.*, 2012, **134**, 12406–12409.

63 E. L. Warren, S. W. Boettcher, M. G. Walter, H. A. Atwater and N. S. Lewis, *J. Phys. Chem. C*, 2011, **115**, 594–598.

64 X. Liu, F. Wang and Q. Wang, *Phys Chem Chem Phys*, 2012, **14**, 7894.

65 R. H. Coridan, M. Shaner, C. Wiggenhorn, B. S. Brunschwig and N. S. Lewis, *J. Phys. Chem. C*, 2013, **117**, 6949–6957.

66 Z. Chen, T. F. Jaramillo, T. G. Deutsch, A. Kleiman-Shwarsctein, A. J. Forman, N. Gaillard, R. Garland, K. Takanabe, C. Heske, M. Sunkara, E. W. McFarland, K. Domen, E. L. Miller, J. A. Turner and H. N. Dinh, *Journal of Materials Research*, 2010, **25**, 3–16.

67 M. G. Walter, E. L. Warren, J. R. McKone, S. W. Boettcher, Q. Mi, E. A. Santori and N. S. Lewis, *Chem. Rev.*, 2010, **110**, 6446–6473.

68 S. P. Berglund, A. J. E. Rettie, S. Hoang and C. B. Mullins, *Phys Chem Chem Phys*,

2012, **14**, 7065–7075.

69 H. S. Park, K. E. Kweon, H. Ye, E. Paek, G. S. Hwang and A. J. Bard, *J. Phys. Chem. C*, 2011, **115**, 17870–17879.

70 B. Liu and E. S. Aydil, *J. Am. Chem. Soc.*, 2009, **131**, 3985–3990.

71 M. R. Shaner, S. Hu, K. Sun and N. S. Lewis, *Energy & Environmental Science*, 2014, **8**, 203–207.

72 J. H. Klootwijk and C. E. Timmering, *Merits and limitations of circular TLM structures for contact resistance determination for novel III-V HBTs*, IEEE, 2004, vol. 17.

73 J. R. McKone, N. S. Lewis and H. B. Gray, *Chem. Mater.*, 2014, **26**, 407–414.

74 Y. W. Chen, J. D. Prange, S. Dühnen, Y. Park, M. Gunji, C. E. Chidsey and P. C. McIntyre, *Nature Materials*, 2011, **10**, 539–544.

75 B. Mei, B. Seger, T. Pedersen, M. Malizia, O. Hansen, I. Chorkendorff and P. C. K. Vesborg, *J. Phys. Chem. Lett.*, 2014, **5**, 1948–1952.

76 M. T. McDowell, M. F. Lichterman, J. M. Spurgeon, S. Hu, I. D. Sharp, B. S. Brunschwig and N. S. Lewis, *J. Phys. Chem. C*, 2014, **118**, 19618–19624.

77 S. Hu, M. R. Shaner, J. A. Beardslee, M. Lichterman, B. S. Brunschwig and N. S. Lewis, 2014, **344**, 1005–1009.

78 S. Hu, C.-Y. Chi, K. T. Fountaine, M. Yao, H. A. Atwater, P. D. Dapkus, N. S. Lewis and C. Zhou, *Energy & Environmental Science*, 2013, **6**, 1879.

79 A. R. Madaria, M. Yao, C. Chi, N. Huang, C. Lin, R. Li, M. L. Povinelli, P. D. Dapkus

and C. Zhou, *Nano Lett.*, 2012, **12**, 2839–2845.

80 J. Zhu, Z. Yu, G. F. Burkhard, C.-M. Hsu, S. T. Connor, Y. Xu, Q. Wang, M. McGehee, S. Fan and Y. Cui, *Nano Lett.*, 2009, **9**, 279–282.

81 A. Chutinan and S. John, *Phys. Rev. A*, 2008, **78**, 023825.

82 T. Tayagaki, Y. Hoshi, Y. Kishimoto and N. Usami, *Opt. Express*, 2014, **22**, A225.

83 S. M. Sze and K. K. Ng, *Physics of Semiconductor Devices*, Wiley-Interscience, 3rd edn. 2006.

84 S. M. Eichfeld, H. Shen, C. M. Eichfeld, S. E. Mohney, E. C. Dickey and J. M. Redwing, *Journal of Materials Research*, 2011, **26**, 2207–2214.

85 E. L. Warren, H. A. Atwater and N. S. Lewis, *J. Phys. Chem. C*, 2014, **118**, 747–759.

86 J. R. McKone, S. C. Marinescu, B. S. Brunschwig, J. R. Winkler and H. B. Gray, *Chem. Sci.*, 2014, **5**, 865.

87 M. R. Shaner, H. A. Atwater and N. S. Lewis, 2012.

88 A. Heller, D. E. Aspnes, J. D. Porter, T. T. Sheng and R. G. Vadimsky, *J. Phys. Chem.*, 1985, **89**, 4444–4452.

89 J. R. McKone, B. F. Sadtler, C. A. Werlang, N. S. Lewis and H. B. Gray, *ACS Catal.*, 2013, **3**, 166–169.

90 E. J. Popczun, C. G. Read, C. W. Roske, N. S. Lewis and R. E. Schaak, *Angewandte Chemie International Edition*, 2014, **53**, 5427–5430.

91 E. J. Popczun, J. R. McKone, C. G. Read, A. J. Biacchi, A. M. Wiltrout, N. S. Lewis and

R. E. Schaak, *J. Am. Chem. Soc.*, 2013, **135**, 9267–9270.

92 L. Trotochaud, T. J. Mills and S. W. Boettcher, *J. Phys. Chem. Lett.*, 2013, **4**, 931–935.

93 Y. Chen, K. Sun, H. Audesirk, C. Xiang and N. S. Lewis, *Energy & Environmental Science*, 2015, **8**, 1736–1747.

94 A. P. Goodey, S. M. Eichfeld, K.-K. Lew, J. M. Redwing and T. E. Mallouk, *J. Am. Chem. Soc.*, 2007, **129**, 12344–12345.

95 G. Yuan, H. Zhao, X. Liu, Z. S. Hasanali, Y. Zou, A. Levine and D. Wang, *Angewandte Chemie International Edition*, 2009, **48**, 9680–9684.

96 T. F. Jaramillo, K. P. Jorgensen, J. Bonde, J. H. Nielsen, S. Horch and I. Chorkendorff, 2007, **317**, 100–102.

97 C. W. Roske, E. J. Popczun, B. Seger, C. G. Read, T. Pedersen, O. Hansen, P. C. K. Vesborg, B. S. Brunschwig, R. E. Schaak, I. Chorkendorff, H. B. Gray and N. S. Lewis, *J. Phys. Chem. Lett.*

98 R. H. Coridan, A. C. Nielander and S. A. Francis, *Energy & …*, 2015.

99 V. Mehta and J. S. Cooper, *Journal of Power Sources*, 2003, **114**, 32–53.

100 E. Aharon-Shalom and A. Heller, *J Electrochem Soc*, 1982, **129**, 2865–2866.

101 J. R. J. Davis, A. Rohatgi, R. H. Hopkins, P. D. Blais, P. Rai-Choudhury, J. R. McCormick and H. C. Mollenkopf, *Electron Devices, IEEE Transactions on*, 1980, **27**, 677–687.

102 S. Dillich, T. Ramsden and M. Melaina, *Hydrogen Production Cost Using Low-Cost*

Natural Gas, DOE Hydrogen and Fuel Cells Program, 2012.

103 V. Smil, *Scientific American*, 2014, 52–57.

104 G. Peharz, F. Dimroth and U. Wittstadt, *International Journal of Hydrogen Energy*, 2007, **32**, 3248–3252.

105 L. Arriaga, W. Martinez, U. Cano and H. Blud, *International Journal of Hydrogen Energy*, 2007, **32**, 2247–2252.

106 P. A. Lehman, C. E. Chamberlin, G. Pauletto and M. A. Rocheleau, *International Journal of Hydrogen Energy*, 1997, **22**, 465–470.

107 P. C. Ghosh, B. Emonts, H. Janssen, J. Mergel and D. Stolten, *Solar Energy*, 2003, **75**, 469–478.

108 M. Bolinger and S. Weaver, *Utility-Scale Solar 2013*, Lawrence Berkeley National Laboratory, 2014.

109 G. Barbose, S. Weaver and N. Darghouth, *Tracking the Sun VII*, Lawrence Berkeley National Laboratory, 2014.

110 W. G. Colella, B. D. James and J. M. Moton, *Hydrogen Pathways Analysis for Polymer Electrolyte Membrane (PEM) Electrolysis*, Strategic Analysis Inc., 2014.

111 B. D. James, G. N. Baum, J. Perez and K. N. Baum, *Technoeconomic Analysis of Photoelectrochemical (PEC) Hydrogen Production*, Directed Technologies Inc., 2009.

112 B. A. Pinaud, J. D. Benck, L. C. Seitz, A. J. Forman, Z. Chen, T. G. Deutsch, B. D. James,

K. N. Baum, G. N. Baum, S. Ardo, H. Wang, E. Miller and T. F. Jaramillo, *Energy & Environmental Science*, 2013, **6**, 1983–2002.

113 *Capacity Factors for Utility Scale Generators Not Primarily Using Fossil Fuels, January 2008-July 2014*, U.S. Energy Information Administration.

114 K. Walczak, Y. Chen, C. Karp, J. W. Beeman, M. Shaner, J. Spurgeon, I. D. Sharp, X. Amashukeli, W. West, J. Jin, N. S. Lewis and C. Xiang, *ChemSusChem*, 2015, **8**, 544–551.

115 *Renewable Power Generation Costs in 2014*, International Renewable Energy Agency, 2015.

116 J. Seel, G. Barbose and R. Wiser, *Why Are Residential PV Prices in Germany So Much Lower Than in the United States?* Lawrence Berkeley National Laboratory, 2013.

117 *PV Spot Price*, EnergyTrend, 2015.

118 D. Feldman, R. Margolis and D. Boff, *Q2/Q3 '14 Solar Industry Update*, U.S. Department of Energy: SunShot, 2014.

119 T. Kimbis, C. Honeyman, N. Litvak, S. Kann, M. J. Shiao, S. Mehta, J. Jones, J. Baca, S. Rumery and A. Holm, *Q2 2014 U.S. Solar Market Insight*, Greentech Media Inc. and Solar Energy Industries Association, 2014.

120 B. Paul and J. Andrews, *International Journal of Hydrogen Energy*, 2008.

121 M. Zhou and Y. Liu, *2013 International Conference on Materials for Renewable Energy and Environment*, 2014, 52–56.

122 *Electricity Data Browser*, U.S. Energy Information Administration.

123 B. D. James, W. G. Colella and J. M. Moton, *Techno-Economic Analysis of Hydrogen Production Pathways*, Strategic Analysis Inc., 2013.

124 K. Melkonyan, *Solar Glass Price Plunge to Cease as Trade Sanctions Take Effect*, IHS Technology, 2014.

125 *Platts Global Polypropylene (PP) Price Index*, Platts.

126 A. Goodrich, P. Hacke, Q. Wang, B. Sopori, R. Margolis, T. L. James and M. Woodhouse, *Solar Energy Materials and Solar Cells*, 2013, **114**, 110–135.

127 C. Houchins, G. Kleen, J. Spendelow, J. Kopasz, D. Peterson, N. Garland, D. Ho, J. Marcinkoski, K. Martin, R. Tyler and D. Papageorgopoulos, *Membranes*, 2012, **2**, 855–878.

128 C. R. Cox, J. Z. Lee, D. G. Nocera and T. Buonassisi, *Proceedings of the National Academy of Sciences*, 2014, **111**, 14057–14061.

129 T. J. Jacobsson, V. Fjallstrom, M. Sahlberg, M. Edoff and T. Edvinsson, *Energy & Environmental Science*, 2013, **6**, 3676.

130 M. Carmo, D. L. Fritz, J. Mergel and D. Stolten, *International Journal of Hydrogen Energy*, 2013, **38**, 4901–4934.

131 *Injection Molded Plastics Market (Polypropylene, ABS, HDPE, Polystyrene) Analysis By Application (Packaging, Consumables and Electronics, Automotive, Building and Construction) And Segment Forecasts To 2020*, Grand View Research, 2014.

132 R. R. Barth, K. L. Simmons and C. S. Marchi, *Polymers for Hydrogen Infrastructureand Vehicle Fuel Systems*, Sandia National Laboratories, 2013.

133 USDA, *Plant Hardiness Zone Map*, 2015.

134 M. Woodhouse and A. Goodrich, *A Manufacturing Cost Analysis Relevant to Single- and Dual-Junction Photovoltaic Cells Fabricated with III-Vs and III-Vs Grown on*, National Renewable Energy Laboratory, 2014.

135 S. Kann, M. J. Shiao, C. Honeyman, N. Litvak, J. Jones, L. Cooper, T. Kimbis, J. Baca, S. Rumery and A. Holm, *U.S. Solar Market Insight*, Greentech Media Inc. and Solar Energy Industries Association, 2015.

136 C. Turchi, *Parabolic Trough Reference Plant for Cost Modeling with the Solar Advisor Model (SAM)*, National Renewable Energy Laboratory, 2010.

137 NREL, *Best Research-Cell Efficiencies*, 2015.

138 T. G. Deutsch and J. A. Turner, *Semiconductor Materials for Photoelectrolysis*, 2014.

139 T. J. Grassman, J. Carlin, C. Ratcliff, D. J. Chmielewski and S. A. Ringel, *Photovoltaic Specialists Conference (PVSC)*, 2013, 149–153.

140 C. A. Rodriguez, M. A. Modestino, D. Psaltis and C. Moser, *Energy & Environmental Science*, 2014, **7**, 3828–3835.

141 R. Pletka, J. Khangura, A. Rawlins, E. Waldren and D. Wilson, *Capital Costs for Transmission and Substations*, Western Electricity Coordinating Council, 2014.

142 Edison Electric Institute, *Transmission Projects: At A Glance*, 2013.

143 W. Leighty, J. Holloway, R. Merer, B. Somerday, C. San Marchi, G. Keith and D. White, *Compressorless hydrogen transmission pipelines deliver large-scale stranded renewable energy at competitive cost*, Lyon, 2006.

144 S. Baufumé, F. Grüger, T. Grube, D. Krieg, J. Linssen, M. Weber, J.-F. Hake and D. Stolten, *International Journal of Hydrogen Energy*, 2013, **38**, 3813–3829.

145 *Trend of the price of spot-LNG*, Japanese Ministry of Economy, Trade and Industry, 2015.

146 P. Spath, A. Aden, T. Eggeman, M. Ringer, B. Wallace and J. Jechura, *Biomass to Hydrogen Production Detailed Design and Economics Utilizing the Battelle Columbus Laboratory Indirectly- Heated Gasifier*, National Renewable Energy Laboratory, 2005.

147 C. E. G. Padro and V. Putsche, *Survey of the Economics of Hydrogen Technologies*, National Renewable Energy Laboratory, 1999.

148 J. C. S. Long, *California's Energy Future: The View to 2050*, California Council on Science and Technology, 2011.

149 J. Reilly and S. Paltsev, *MIT Joint Program on the Science and Policy of Global Change*, MIT Joint Program on the Science and Policy of Global Change, 2007.

150 *Levelized Cost and Levelized Avoided Cost of New Generation Resources in the Annual Energy Outlook 2014*, U.S. Energy Information Administration, 2014.

151 A. J. Garnet, C. R. Greig and M. Oettinger, *ZeroGen IGCC with CCS*, The University

of Queensland, 2014.

152 D. M. Rastler, *Electricity Energy Storage Technology Options*, Electric Power Research Institute, 2011.

153 G. Parks, R. Boyd, J. Cornish and R. Remick, *Hydrogen Station Compression, Storage, and Dispensing Technical Status and Costs: Systems Integration*, NREL, 2014.

154 FuelCell Energy, *1.4 Megawatts DCF1500 Specifications Sheet*, FuelCell Energy, 2013.

155 Ballard, *CLEARgen Specifications Sheet*, Ballard, 2014.

156 Hydrogenics, *Fuel Cell Megawatt Power Generation Platform*, Hydrogenics, 2014.

157 D. Steward, G. Saur, M. Penev and T. Ramsden, *Lifecycle Cost Analysis of Hydrogen Versus Other Technologies for Electrical Energy Storage*, National Renewable Energy Laboratory, 2009.

158 C. Yang, J. Ogden, D. Sperling and R. Hwang, *California's Energy Future: Transportation Energy Use in California*, California Council on Science and Technology, 2011.

159 R. Sathre, C. D. Scown, W. R. Morrow, J. C. Stevens, I. D. Sharp, J. W. Ager, K. Walczak, F. A. Houle and J. B. Greenblatt, *Energy & Environmental Science*, 2014, **7**, 3264–3278.

160 C. A. S. Hall, S. Balogh and D. J. R. Murphy, *Energies*, 2009, **2**, 25–47.

161 M. K. Mann, P. L. Spath and W. A. Amos, *Technoeconomic Analysis of Different*

Options for the Production of Hydrogen from Sunlight, Wind and Biomass, 1999.

162 R. Socolow, M. Desmond, R. Aines, J. Blackstock, O. Bolland, T. Kaarsberg, N. S. Lewis, M. Mazzotti, A. Pfeffer, K. Sawyer, J. Siiola, B. Smit and J. Wilcox, *Direct Air Capture of CO2 with Chemicals*, American Physical Society, 2011.

163 K. Z. House, A. C. Baclig, M. Ranjan, E. A. van Nierop, J. Wilcox and H. J. Herzog, *Proceedings of the National Academy of Sciences*, 2011, **108**, 20428–20433.

164 K. P. Kuhl, E. R. Cave, D. N. Abram and T. F. Jaramillo, *Energy & Environmental Science*, 2012, **5**, 7050.

165 M. S. Reisch, *Chemical Engineering News*, 2015, **93**, 15.

166 H. Herzog, *Assessing the Feasibility of Capturing CO2 from the Air*, MIT Laboratory for Energy and the Environment, 2003.

167 J. Davison, *Energy*, 2007, **32**, 1163–1176.

168 *Cost Analysis*, http://www.fieldturf.com/en/fieldturf-difference/cost-analysis.

169 J. M. Spurgeon, S. W. Boettcher, M. D. Kelzenberg, B. S. Brunschwig, H. A. Atwater and N. S. Lewis, *Adv. Mater.*, 2010, **22**, 3277–3281.

170 Y. Chen, K. Sun, H. Audesirk, C. Xiang and N. S. Lewis, *Energy & Environmental Science*, 2015, **8**, 1736–1747.

171 S. Hu, M. R. Shaner, J. A. Beardslee, M. Lichterman, B. S. Brunschwig and N. S. Lewis, *Science*, 2014, **344**, 1005–1009.

172 B. Seger, T. Pedersen, A. B. Laursen, P. C. K. Vesborg, O. Hansen and I. Chorkendorff,

J. Am. Chem. Soc., 2013, **135**, 1057–1064.

173 H. Ye, H. S. Park and A. J. Bard, *J. Phys. Chem. C*, 2011, **115**, 12464–12470.

174 A. Subrahmanyam and A. Karuppasamy, *Solar Energy Materials and Solar Cells*, 2007, **91**, 266–274.

175 J. M. Berak and M. J. Sienko, *Journal of Solid State Chemistry*, 1970, **2**, 109–133.

176 H. Jin, J. Zhu, J. Hu, Y. Li, Y. Zhang, X. Huang, K. Ding and W. Chen, *Theor Chem Acc*, 2011, **130**, 103–114.

177 J. M. Spurgeon, H. A. Atwater and N. S. Lewis, *J. Phys. Chem. C*, 2008, **112**, 6186–6193.

178 A. Rohatgi, Z. Chen, P. Doshi, T. Pham and D. Ruby, *Appl. Phys. Lett.*, 1994, **65**, 2087.

A Detailed Fabrication Processes for Si Microwire Devices

A.1 Chapter 3: Si/WO_3 Tandem Device Methods

A.1.1 Si Microwire Array Growth

Phosphorous-doped (N_D =3 x 10^{17} cm^{-3}) and boron-doped (N_A = 1 x 10^{17} cm^{-3}) Si microwire arrays were grown via a Cu-catalyzed vapor-liquid-solid (VLS) process on As-doped n^+-Si or on B-doped p^+-Si <111> wafers (<0.005 Ω-cm, Addison).[38,46,48] The n^+-Si and p^+-Si <111> growth wafers were received with a 400 nm thick thermal oxide (SiO_2) that had been photolithographically patterned to produce 3 μm diameter holes filled with Cu in a square lattice (7 μm x 7 μm). The growth of Si microwire arrays was performed in a chemical-vapor deposition (CVD) furnace at atmospheric pressure using $SiCl_4$ (Strem, 99.9999+%) at 25 sccm flow rate, H_2 (Matheson, research grade) at 500 sccm flow rate, and BCl_3 (Matheson, 0.25% in H_2) at 1 sccm flow rate for 20 min or PH_3 (Matheson, 100ppm in H_2) at 0.3 sccm flow rate for 9 min. Following growth, the samples were cooled to ~ 200 °C under a 500 sccm flow of He.

A.1.2 Microwire Array Processing

Microwire arrays were cleaned using a 6:1:1 (by volume) H_2O:HCl(fuming, aqueous):H_2O_2(30% in H_2O) metal etch (RCA 2) for 20 min at 60 °C. The samples were then subjected to a 15 s etch in buffered HF(aq) (BHF) etch, an H_2O rinse, an organic

(piranha) etch in 3:1 H_2SO_4(99.6%, aqueous):H_2O_2(30% in H_2O) for 10 min at room temperature, and an H_2O rinse. Following a 30 s etch in 10% BHF and a rinse with H_2O, a 150 nm thick SiO_2 layer was grown via dry thermal oxidation in a tube furnace at 1050 °C under an O_2 atmosphere for 2.5 h. A 15 µm thick PDMS layer was deposited at the base of the wires by spin coating a solution, consisting of 1.1 g of polydimethylsiloxane (PDMS, Sylgard 185, Dow Corning) and 0.1 g of PDMS curing agent dissolved in 5 mL of toluene, on the sample at 3000 rpm for 30 s, followed by a 30 min cure in vacuum oven at 150 °C. These PDMS-infilled arrays were submerged in BHF for 5 min, to remove the SiO_2 on the exposed microwire surfaces. The PDMS was removed by a 30 min soak in 3:1 N-methyl-2-pyrrolidone(NMP):tetrabutylammonium fluoride(TBAF, aq 75 wt%), followed by a 30 s rinse with H_2O. The samples were then dried under a stream of N_2(g). Residual organics were then removed by a 10 min etch in a piranha solution.

A.1.3 Si Homo-junction Formation

A boron-doped p^+-Si radial emitter was formed on the n-Si microwire arrays and on planar <111> n-Si wafers (Silicon Inc., 0.7Ω-cm) by exposure of the samples in a CVD furnace to a 20:400 sccm flow of BCl_3 (Matheson, 0.25% in H_2):H_2(Matheson, research grade) at 950 °C for 30 min, immediately following a 30 sec etch in10% BHF. The samples were then rinsed with H_2O and dried under a stream of N_2(g).

A.1.4 ITO Deposition

Immediately following a 15 sec etch in 10% BHF, a rinse in H_2O and drying under a stream of N_2(g), 400 nm of In-doped tin oxide was sputtered (48 W, 3 mTorr, 20:0.75 sccm Ar:10% O_2 in Ar) onto n-p^+-Si microwire arrays and p-Si microwire arrays, by DC magnetron sputtering under 10 W of substrate bias (to facilitate conformal deposition on the microwire sidewalls). The thickness of the ITO was determined by spectroscopic ellipsometry measurements on a planar Si sample.

A.1.5 WO_3 Deposition

n-WO_3 was electrodeposited from a tungstic peroxy-acid solution, as described previously[54]. Briefly, 4.6 g of tungsten powder (0.6-1μm, 99.99%, Sigma Aldrich) was dissolved in molar excess (60 mL) of H_2O_2 (30% in H_2O). Excess H_2O_2 was dissolved by addition of a trace amount of Pt black (99.9%, Sigma Aldrich) for 24 h. The H_2O_2 concentration was monitored by peroxide test strips (EM Quant) unitl final peroxide concentration was < 30 ppm. A concentrated stock solution was made by addition of 80 mL of H_2O and 60 mL of isopropyl alcohol (IPA) to the as made solution. To increase its lifetime, the stock solution was protected from light and stored at 2°C in a refrigerator. A 3:7 IPA:H_2O mixture was used to dilute the stock solution (3:2 IPA/H_2O mix:stock solution) to generate the deposition solution. Stock solutions were used for one week before and thereafter were freshly prepared. All ITO-coated samples were used as prepared for

deposition of WO_3, and were contacted directly to the ITO layer using a flat alligator clip. Deposition of WO_3 on n-p^+-Si and p-Si microwire arrays was performed potentiostatically at -0.5 V vs Ag/AgCl for 60 min. After deposition, all samples were annealed in air at 400 °C for 2 h. This process formed monoclinic WO_3, as confirmed by X-ray diffraction data.

A.1.6 Product Analysis

Oxidation products (peroxydisulfate ($S_2O_8^{2-}$)) generated at the WO_3/1.0M H_2SO_4 interface were detected using a UV-visable spectrophotometer (Agilent 8453, 1-cm quartz cuvette) as reported previously.[54] Working curves were determined using potassium peroxydisulfate ($K_2S_2O_8$).

Reduction products (H_2(g)) generated at the Pt disc/1.0M H_2SO_4 interface were detected using a mass spectrometer (Hiden Analytical HPR-20 QIC). Current was passed through the Pt disc electrode for 40 min under identical conditions (identical electrochemical cell, current (-6.5 μA), solution (trace metal grade 1.0M H_2SO_4) and Ar(g) purge) as used in the two-electrode experiment described above. The experiment was started only after obtaining a steady baseline.

A.1.7 Light Absorption Simulation

1D and 2D light absorption was simulated in Lumerical FDTD, a commercially available Maxwell's equation solver that uses the FDTD method. The experimentally fabricated microwire structures were reproduced in the Lumerical workspace in 2D. Bloch boundary conditions were used to model an infinite planar structure and an infinite 2D microwire array. Each structure was illuminated with single-wavelength plane waves with the electric field polarized in the 2D structured plane, at wavelengths ranging from 350 to 1100 nm in 50 nm intervals. Partial spectral averaging was used to remove simulation artifacts that were caused by the use of single-wavelength simulations. The structure was meshed with 20 mesh boxes per wavelength. The spatially resolved electric field, *E*, and complex refractive index (ϵ) were recorded and then used to calculate the spatially resolved carrier generation rate, C_{gen} (Equation A.1.1):

$$C_{gen} = \frac{\pi|\square|^2 imag(\epsilon)}{h} \qquad \text{A.1.1}$$

where h is Planck's constant. The spatially resolved carrier generation rate was used as the optical input for the electronic simulations. The power absorbed in each material was calculated by integrating the spatially resolved absorbed power, P_{abs} (Equation A.1.2).

$$P_{abs} = -0.5\omega|E|^2 imag(\epsilon) \qquad \text{A.1.2}$$

The absorbed photon flux in each material as a function of wavelength was weighted with the AM1.5G spectrum, integrated over wavelength, and multiplied by Faraday's constant

to obtain a short-circuit current density assuming unity internal quantum yield (IQY). The concentrated illumination modeling was performed at 11 Suns using the AM1.5G spectrum to match the experimental photon flux of 12x of AM1.5D.

A.1.8 Electronic Simulations

Electronic device simulations were performed in Synopsys Sentaurus, a commercially developed software package that solves the drift-diffusion equation for charge carriers using a finite-element method. For simplicity, a single n-p^+-Si homo-junction and an n-WO_3/(O_2/H_2O) liquid junction were modeled separately.

A.1.8.1 n-p^+-Si junction

The built-in materials parameter file for Si was used with modified time constants (τ_n(N_A=10^{20} cm^{-3}) = 3x10^{-6} s; $\tau_{p\text{-}}$(N_D=10^{17} cm^{-3}) = 1x10^{-3} s). The silicon p^+-n junction was constructed with a 100 µm thick n-region with N_D=10^{17} cm^{-3} and a 0.2 µm thick p^+-region with N_A=10^{20} cm^{-3}. In the quasi-neutral bulk of the n-Si, a standard mesh size of 500 nm and 5 µm was used transverse and parallel to the junction, respectively. Near the ohmic contact with n-Si, the mesh was refined to 500 nm and 100 nm, and near the junction, the mesh was refined to 500 nm and 20 nm, to accurately model band-bending in these regions. The *J-E* (current density vs. potential) characteristics of this structure were obtained by first solving for the *V* = 0 case in the dark. Subsequently, the voltage was

stepped at 0.010 V intervals in both the positive and negative directions, to obtain the dark *J-E* behaviour. The carrier generation rate from Lumerical was then applied to extract the *J-E* characteristics in the presence of illumination. Similarly, the $V = 0$ case in the light was solved first, and then the voltage was stepped at 0.010 V intervals, to obtain the light *J-E* performance. Shockley–Read–Hall recombination was used for all simulations.

A.1.8.2 WO_3-liquid junction

The built-in "oxide as semiconductor" materials parameter file was used to model WO_3, with the following parameters and their values in parentheses: modified band-gap (E_g = 2.6 eV), work function (χ = 4.4 eV), relative permittivity (ε_r = 5.76), conduction- and valence-band density of states ($N_C = 1.8 \times 10^{19}$ cm^{-3}, $N_V = 7.1 \times 10^{19}$ cm^{-3}), recombination time constant ($\tau_n = \tau_p = 1 \times 10^{-8}$ s) and mobility ($\mu_n = \mu_p = 40$ cm^2 V^{-1} s^{-1}). The band-gap was experimentally measured from absorption measurements using an integrating sphere and a Tauc plot. The relative permittivity was calculated from ellipsometric measurements of the complex refractive index. The work function was chosen based on reports found in the literature.[174] The density of states can be calculated from *m**, the effective mass of holes in the valence band and of electrons in the conduction band (Equation A.1.3):

$$N_c = 2\left(\frac{2\pi m_e^* k_B T}{h^2}\right)^{\frac{3}{2}} \quad \text{A.1.3}$$

Effective masses in the conduction band have been reported to be ~ 0.8 $m_{0,}$[175] where m_0 is the mass of a free electron. Density functional theory calculations of the band structure of WO_3 indicate that the valence band has less curvature than the conduction band, indicating heavier holes and leading to an estimate of 2 m_0 for the hole effective mass.[176] The mobility values were also taken from the literature.[175] Preliminary experimental measurements indicated a diffusion length of 1 μm, thereby determining the time constant.

The WO_3/liquid junction was modeled as a Schottky junction, with the metal work function equal to the water oxidation redox potential, χ = 5.68 eV, which was in contact with a 1 μm thick slab of WO_3. A value of $N_D = 10^{15}$ cm^{-3} was chosen to match the experimentally observed short-circuit current density and open-circuit voltage. Mesh sizes of 10 nm and 250 nm were used perpendicular and parallel to the junction, respectively. The method to obtain the dark and light *J-E* behaviour was identical to that used for modeling the Si junction. Shockley-Reed-Hall recombination and thermionic emission physics were used for these simulations.

A.1.8.3 Hydrogen Evolution Catalysis Modeling

Butler–Volmer kinetics in the absence of mass transport limitations were used with α = 1 and $j_0 = 10^{-3}$ A-cm^{-2}, to simulate the cathodic overpotential (Equation A.1.4) of platinum (Pt) for hydrogen evolution in 1.0 M H_2SO_4.

$$\eta = -\frac{RT}{F} ln\left(\frac{j}{j_0} + 1\right) \qquad \text{A.1.4}$$

The overpotential was added to the n-p$^+$-Si homo-junction *J-E* data at the same current density to yield a simulated hydrogen generation device curve in the absence of mass transport.

A.2 Chapter 4: Si/TiO_2 Tandem Device Methods

A.2.1 Chemicals

All chemicals were used as received unless noted otherwise. Water was filtered using a MilliPore system and had a resistivity > 18 MΩ-cm.

A.2.2 Si Microwire Fabrication

Phosphorous-doped (N_D =3 x 10^{17} cm^{-3}) n-type Si (n-Si) and highly boron-doped p$^+$-type Si (p$^+$-Si) microwire arrays were grown via a Cu-catalyzed vapor-liquid-solid (VLS) process on As-doped n$^+$-Si <111> or B-doped p$^+$-Si <111> wafers (<0.005 Ω-cm, Addison).[38,46,48] The growth wafers were received as 3” wafers with a 500 nm thick thermal oxide (SiO_2) and

were photolithographically patterned to form an array of 3 μm diameter holes filled with Cu in a 7 μm x 7 μm square lattice. The photolithography process began with the application of a positive photoresist layer (Shipley S1813) to the SiO_2 surface. Next, the photoresist was exposed to UV illumination through a mask that contained the growth pattern (3 μm diameter holes in a 7 μm x 7 μm square lattice), and the exposed and cured photoresist was removed with a developer (Microposit MF-319). This process left 3 μm diameter holes in the photoresist through which the underlying SiO_2 was etched with buffered HF(aq) (BHF) (Transene Inc.), to reveal the underlying Si. 500nm of high-purity Cu (EPSI 6N) was then thermally evaporated onto the sample. All of the Cu, except for that in the 3 μm diameter holes, was removed in a lift-off process that utilized acetone to remove the remaining photoresist. This entire process produced 3" growth wafers that were diced to fit into the microwire array growth tube furnace.

Growth of Si microwire arrays was performed in a chemical-vapor deposition (CVD) tube furnace at atmospheric pressure using $SiCl_4$ (Strem, 99.9999+%) at 25 sccm flow rate, H_2 (Matheson, research grade) at 500 sccm flow rate, and either BCl_3 (Matheson, 0.25% in H_2) at 1 sccm flow rate for 20 min (p^+-Si) or PH_3 (Matheson, 100ppm in H_2) at 0.3 sccm flow rate for 9 min (n-Si). Following growth, the samples were cooled to ~ 200 °C under a 500 sccm flow of He.

A.2.2.1 Microwire Array Processing

Microwire arrays were cleaned using a 6:1:1 (by volume) H_2O:HCl(fuming, aqueous):H_2O_2(30% in H_2O) metal etch (RCA 2) for 20 min at 60 °C. The samples were then subjected sequentially to a 15 s BHF etch, a H_2O rinse, a 10 min organic (piranha) etch in 3:1 H_2SO_4(99.6%, aqueous):H_2O_2(30% in H_2O) at room temperature, and a H_2O rinse. Following a 30 s etch in 10% BHF and H_2O rinse, a 150 nm thick SiO_2 layer was grown via dry thermal oxidation in a tube furnace for 2.5 h at 1050 °C under an O_2 atmosphere. A 15 μm thick PDMS layer was deposited at the base of the wires by spin coating a solution, consisting of 1.1 g of polydimethylsiloxane (PDMS, Sylgard 185, Dow Corning) and 0.1 g of PDMS curing agent dissolved in 5 mL of toluene, onto the sample at 3000 rpm for 30 s, followed by a 30 min cure in a vacuum oven at 150°C. These PDMS-infilled arrays were submerged in BHF for 3 min, to remove the SiO_2 on the exposed microwire surfaces. The PDMS was removed by a 30 min soak in 3:1 N-methyl-2-pyrrolidone(NMP):tetrabutylammonium fluoride(TBAF, aq 75 wt%), followed by a 30 s H_2O rinse. The samples were then dried under a stream of N_2(g) and residual organics were removed by a 10 min piranha etch.

A.2.2.2 p^+ Emitter Formation

A boron-doped p^+-Si radial emitter was formed on the processed n-Si microwire arrays by exposure of the samples in a CVD furnace to a 20:400 sccm flow of BCl_3 (Matheson, 0.25%

in H_2):H_2(Matheson, research grade) at 950 °C for 30 min, immediately following a 30 s etch in 10% BHF. The samples were then rinsed with H_2O and dried under a stream of N_2(g).

A.2.2.3 FTO Deposition

np^+-Si and p^+-Si microwire arrays were etched in BHF for 15 s and placed on a hotplate that had been preheated to 500 °C in a chemical hood. The microwire sample was secured to the hotplate by placing ceramic weights onto the corners of the chip. Fluorine-doped tin oxide (FTO) was deposited using an airbrush gun (Aztek A220 Broad Stroke) using air that was pressurized at 60 psi. The precursor solution consisted of 0.015 M ammonium fluoride (KMG, 40% Cleanroom® MB) and 0.49 M butyltin trichloride (Strem, 95% min) in an ethanol/water solution. This solution was made by mixing a 97% by volume solution of 0.5 M butyltin trichloride in 200 proof ethanol (Sigma Aldrich, HPLC/spectrophotometric grade) with a 3% by volume solution of 0.5 M ammonium fluoride in H_2O. A single FTO deposition cycle consisted of a 2-3 s spray followed by a 12-13 s pause, to reestablish a stable substrate temperature following the spray. 30 total cycles were used to obtain the FTO layers used throughout this study. The sample was not rotated during the deposition, however conformal coverage was obtained with no directionality observable in SEM images of the resulting device. Samples were removed

from the hotplate following the last deposition cycle and were cooled in air to room temperature.

A.2.2.4 TiO_2 Deposition

A conformal nano-structured TiO_2 layer was deposited on FTO coated microwire arrays from an aqueous solution of 0.05M titanium n-butoxide and 6M HCl.[70] 10 mL of this solution was placed into an ~15 mL Teflon cell made for hydrothermal processing. FTO coated Si microwire arrays were then placed into this solution and rested vertically with support from the Teflon cell sidewalls. The hydrothermal bomb was placed in a muffle furnace that was subsequently heated to 150˚C and remained there for 6 hours. The furnace was allowed to cool to room temperature and the sample was removed from the Teflon cell. Next the TiO_2 coated microwire array was annealed at 450˚C for 30 minutes in air.

A.2.3 Electrode Fabrication

Electrodes were fabricated from diced pieces of processed microwire growth arrays that had undergone the appropriate fabrication process. To make ohmic contact to the samples, In-Ga (99.99%, Alfa-Aesar) eutectic was scratched into the back-side of the growth wafer with a diamond-tipped scribe. Exposed In-Ga (Si electrodes) was affixed to a coiled Cu-Sn wire with Ag paint (SPI 05001-AB). The active area was defined with epoxy

(Loctite Hysol 9460) and the entire electrode was sealed with epoxy to the bottom of a glass tube (6mm O.D.). The electrode orientation, down- or side-facing, was determined by the orientation of the coiled wire that protruded from the glass tube. Geometric areas were measured by scanning the active area, and using software (ImageJ) to calculate the area.

A.2.4 Photoelectrochemical Measurements in Aqueous Solutions

Side-facing electrodes were used in both 1.0 M KOH and 1.0 M H_2SO_4 solutions. Three-electrode cyclic voltammetry (CV) measurements were conducted using a Biologic (SP-200) potentiostat in conjunction with a borosilicate single-compartment cell that had a flat quartz glass window mounted on the side of the cell. A saturated calomel reference electrode (SCE) (CH Instruments, CHI 150) reference electrode and a fritted Pt counter electrode were used for measurements in 1.0 M KOH and 1.0 M H_2SO_4. Illumination was provided by a Xe lamp (Oriel 67005, Newport Corporation) with an AM1.5G filter (Newport Instruments 81094) that was calibrated to 1 Sun by a calibrated Si photodiode. Calibration was performed such that the highest light intensity anywhere in the cell was at the cited light intensity, and the position of the photodiode at this light intensity was marked to assure sample positioning was at the same point. All of the measurements were referenced to the potential of the RHE ($E(H^+/H_2)$), obtained empirically using a Pt disc electrode under 1 atm of H_2(g), -0.255 V vs. SCE.

A.2.5 Photoelectrochemical Characterization in Non-Aqueous Solvents

Bottom-facing electrodes that contained np^+-Si microwire arrays were etched for 10 s in BHF immediately prior to introducing the samples into a N_2-filled glove box. Solutions for photoelectrochemical measurements consisted of CH_3CN (anhydrous, 99.8%, Sigma Aldrich) dried through Al_2O_3 sieves in a solvent column system and stored over 3Å dry molecular sieves, 1M $LiClO_4$ (battery grade, 99.99%, Sigma Aldrich), and 25 mM bis(cyclopentadienyl) iron(II) (ferrocene, $FeCp_2^0$, Sigma Aldrich) and 3 mM bis(cyclopentadienyl) iron(III) tetrafluoroborate (ferrocenium, $FeCp_2^+ \cdot BF_4^-$, Sigma Aldrich). Ferrocene was purified by vacuum sublimation at room temperature, and ferrocenium was recrystallized prior to use. An ELH-type W–halogen lamp with a dichroic rear reflector was used for illumination, and was set to produce the same current density on a calibrated Si photodiode as was obtained from 100 mW cm^{-2} of 1 Sun AM1.5 G illumination. Three-electrode photoelectrochemical data were obtained in a single-compartment boroscilicate glass cell with a flat bottom window by use of a Biologic potentiostat (SP-200), with a Pt counter electrode and a Pt quasi-reference electrode at scan rates of 20 mV-s^{-1}.

A.2.6 Circular Transmission Line Measurements (cTLM)

cTLM measurements were made on photolithographically patterned FTO architectures on p^+-Si (0.003 ohm-cm) wafers. The processing scheme to achieve the samples began with a standard FTO deposition on a planar p^+-Si wafer as described above. Next, the FTO coated wafer was subjected to an identical Shipley S1813 photolithographic patterning procedure as for the microwire growth substrates with the exception of the mask. The mask was printed on a transparency slide and was affixed to a glass plate for mounting purposes in the mask aligner. The mask consisted of 18 test sites with a constant inner pad diameter of 180 μm and a varying space between the outer pad from 30 μm to 120 μm.

The FTO etch procedure implemented was adopted from US patent 7115212 B2. An aqueous etch solution of 0.5 M HCl, 0.4 M $FeSO_4 \bullet H_2O$ and 0.1 M $FeCl_3$ was poured ~ 5 mm high in a ~2" diameter glass petri dish. The FTO coated Si wafer covered in patterned photoresist was submersed in the solution and 3.5 g Zn powder (<10 microns) was poured slowly into the solution while manually shaking the petri dish for agitation. Vigorous reaction occurred and after ~2 min the solution became clear and the reaction ceased. Following this, the sample was soaked for 30 s in an aqueous solution of 1.0 M HCl and 0.5 $FeCl_3$ to remove any residual metal left from previous etch. No visible reaction occurred on the surface. The photoresist was removed with a ~30 s soak in acetone.

These samples were tested using two and four point probe solid-state measurements, though both provided nearly identical data. Analysis was performed for a current range that corresponded to current densities expected for solar fluxes <100 mA cm^{-2}, based on the inner pad area. A previously published method for determining the contact resistance was used herein.[72]

A.2.7 X-Ray Diffraction (XRD) Measurements

XRD measurements were made on a Bruker D2 Phaser desktop instrument. Peak positions were identified using the ICSD database (https://icsd.fiz-karlsruhe.de/search/basic.xhtml).

A.2.8 Imaging

All scanning-electron micrograph (SEMs) were taken on an FEI Nova NanoSEM 450.

A.3 Chapter 5: Si Photoanodic Protection Methods

A.3.1 Chemicals

All chemicals were used as received unless noted otherwise. Water was filtered using a MilliPore system and had a resistivity > 18 MΩ-cm.

A.3.2 Si Microwire Fabrication

Phosphorous-doped (N_D =3 x 10^{17} cm^{-3}) Si microwire arrays were grown via a Cu-catalyzed vapor-liquid-solid (VLS) process on As-doped n^+-Si <111> wafers (<0.005 Ω-cm, Addison)[38,46,48]. The n^+-Si <111> growth wafers were received as 3" wafers with a 500 nm thick thermal oxide (SiO_2) and were photolithographically patterned to form an array of 3 μm diameter holes filled with Cu in a 7 μm x 7 μm square lattice. The photolithography process began with the application of a positive photoresist layer (Shipley S1813) to the SiO_2 surface. Next, the photoresist was exposed to UV illumination through a mask that contained the growth pattern (3 μm diameter holes in a 7 μm x 7 μm square lattice), and the exposed and cured photoresist was removed with a developer (Microposit MF-319). This process left 3 μm diameter holes in the photoresist through which the underlying SiO_2 was etched with buffered HF(aq) (BHF) (Transene Inc.), to reveal the underlying Si. 500nm of high-purity Cu (EPSI 6N) was then thermally evaporated onto the sample. Through a lift-off process, all of the Cu, except for that in the 3 μm diameter holes, was removed. This entire process produced 3" growth wafers that were diced to fit into the tube furnace.

Growth of Si microwire arrays was performed in a chemical-vapor deposition (CVD) tube furnace at atmospheric pressure using $SiCl_4$ (Strem, 99.9999+%) at 25 sccm flow rate, H_2

(Matheson, research grade) at 500 sccm flow rate, and PH_3 (Matheson, 100ppm in H_2) at 0.3 sccm flow rate for 9 min. Following growth, the samples were cooled to ~ 200 °C under a 500 sccm flow of He.

A.3.3 Microwire Array Processing

Microwire arrays were cleaned using a 6:1:1 (by volume) H_2O:HCl(fuming, aqueous):H_2O_2(30% in H_2O) metal etch (RCA 2) for 20 min at 60 °C. The samples were then subjected sequentially to a 15 s BHF etch, a H_2O rinse, a 10 min organic (piranha) etch in 3:1 H_2SO_4(99.6%, aqueous):H_2O_2(30% in H_2O) at room temperature, and a H_2O rinse. Following a 30 s etch in 10% BHF and H_2O rinse, a 150 nm thick SiO_2 layer was grown via dry thermal oxidation in a tube furnace for 2.5 h at 1050 °C under an O_2 atmosphere. A 15 μm thick PDMS layer was deposited at the base of the wires by spin coating a solution, consisting of 1.1 g of polydimethylsiloxane (PDMS, Sylgard 185, Dow Corning) and 0.1 g of PDMS curing agent dissolved in 5 mL of toluene, onto the sample at 3000 rpm for 30 s, followed by a 30 min cure in a vacuum oven at 150 °C. These PDMS-infilled arrays were submerged in BHF for 3 min, to remove the SiO_2 on the exposed microwire surfaces. The PDMS was removed by a 30 min soak in 3:1 N-methyl-2-pyrrolidone(NMP):tetrabutylammonium fluoride(TBAF, aq 75 wt%), followed by a 30 s H_2O rinse. The samples were then dried under a stream of N_2(g) and residual organics were removed by a 10 min piranha etch.

A.3.3.1 p^+ Emitter Formation

A boron-doped p^+-Si radial emitter was formed on the processed n-Si microwire arrays by exposure of the samples in a CVD furnace to a 20:400 sccm flow of BCl_3 (Matheson, 0.25% in H_2):H_2(Matheson, research grade) at 950 °C for 30 min, immediately following a 30 s etch in 10% BHF. The samples were then rinsed with H_2O and dried under a stream of N_2(g).

A.3.4 TiO_2 Deposition

TiO_2 was deposited by atomic-layer deposition (ALD) on np^+-Si microwires at 150 °C using tetrakis(dimethylamino)titanium (TDMAT) as the Ti source heated to 75 °C and H_2O as the O source. 2000 cycles were performed with pulse and purge times of 0.1 s and 15 s for the TDMAT, respectively and 0.015 s and 15 s for the H_2O respectively, with the H_2O pulse beginning each new cycle. Prior to ALD deposition, the samples were etched for 15 s in 10% HF(aq), cleaned using a RCA SC-2 procedure, and dried with N_2(g). In the RCA SC-2 procedure, the samples were immersed in a 5:1:1 (by volume) solution of H_2O, concentrated hydrochloric acid (11.1 M), and hydrogen peroxide (conc.~ 1 M) for 10 min at 75 °C.

A.3.5 $NiCrO_x$ Deposition

$NiCrO_x$ was deposited on np^+-Si/TiO_2 microwire arrays by reactive RF magnetron sputtering (AJA) with separate Ni and Cr targets at 150 W and 90 W, respectively. The deposition chamber was at a pressure of 5 mTorr, fed by 20 sccm N_2(g) and 1 sccm of O_2(g). The deposition time was 20 min, which resulted in a thickness of ~ 40 nm planar equivalent.

A.3.6 Electrode Fabrication

Electrodes were fabricated from diced pieces of each processed microwire growth array. To make ohmic contact to the samples, In-Ga (99.99%, Alfa-Aesar) eutectic was scratched into the back-side of the growth wafer with a diamond-tipped scribe. Exposed In-Ga (Si electrodes) was affixed to a coiled Cu-Sn wire with Ag paint (SPI 05001-AB). The active area was defined with epoxy (Loctite Hysol 9460) and the entire electrode was sealed with epoxy to the bottom of a glass tube (6mm O.D.). The electrode orientation, down- or side-facing, was determined by the orientation of the coiled wire that protruded from the glass tube. Geometric areas were measured by scanning the active area, and using software (ImageJ) to calculate the area.

A.3.7 Photoelectrochemical Measurements in Aqueous Solutions

Bottom-facing electrodes were used in both 1 M KOH and aqueous ferri-/ferro-cyanide solutions. Four np^+-Si/TiO_2/$NiCrO_x$ and two n-Si/TiO_2/$NiCrO_x$ microwire array electrodes were made and tested, with the reported results being representative of all electrodes in each specified class. Three-electrode cyclic voltammetry (CV) measurements were conducted using a Biologic (SP-200) potentiostat in conjunction with a borosilicate single-compartment cell that had a flat-bottom glass window. A mercurous/mercury oxide (Hg/HgO, 1.0 M KOH filling solution) (CH Instruments) reference electrode and a fritted carbon counterelectrode were used for measurements in 1 M KOH, whereas a Luggin-capillary Pt reference electrode placed as close to the working electrode surface as possible and a Pt mesh counterelectrode were used for measurements in ferri-/ferrocyanide solutions. The ferri-/ferrocyanide data were plotted versus the solution potential at the reference electrode, while the potential axis for the 1 M KOH data was shifted to the reversible hydrogen electrode (RHE) scale based on the value provided by CH Instruments, 0.14 V vs RHE. For these experiments, illumination was provided by a Xe lamp (Oriel 67005, Newport Corporation) with an AM1.5G filter (Newport Instruments 81094) that was calibrated to 1 Sun by a calibrated Si photodiode. A mirror (10Q20BB.HR broadband dielectric mirror, Newport Corporation) was used to direct the horizontally projected illumination from the lamp in the vertical direction, to produce normal incidence light for the bottom-facing electrodes. Calibration was performed such that the

highest light intensity anywhere in the cell was at the cited light intensity, and the position of the photodiode at this light intensity was marked to assure sample positioning was at the same point. Varying illumination intensities were achieved through the use of neutral density filters (ND 0.3) (Newport FSQ-OD30). This approach allowed determination of the diode quality factor by a linear line fit to a plot of the open-circuit potential vs. $\ln(J_{ph})$.

A.3.8 Photoelectrochemical Characterization in Non-Aqueous Solvents

Bottom-facing electrodes that contained n-p^+-Si microwire arrays were etched for 10 s in BHF immediately prior to introducing the samples into a glove box. Solutions for photoelectrochemical measurements consisted of CH_3CN (anhydrous, 99.8%, Sigma Aldrich) dried through Al_2O_3 sieves in a solvent column system and stored over 3Å dry molecular sieves, 1M $LiClO_4$ (battery grade, 99.99%, Sigma Aldrich), and 25 mM bis(cyclopentadienyl) iron(II) (ferrocene, $FeCp_2^0$, Sigma Aldrich) and 3 mM bis(cyclopentadienyl) iron(III) tetrafluoroborate (ferrocenium, $FeCp_2^+ \cdot BF_4^-$, Sigma Aldrich). Ferrocene was purified by vacuum sublimation at room temperature, and ferrocenium was recrystallized prior to use. An ELH-type W–halogen lamp with a dichroic rear reflector was used for illumination, and was set to produce the same current density on a calibrated Si photodiode as was obtained from 100 mW cm^{-2} of 1 Sun AM1.5 G illumination. Three-electrode photoelectrochemical data were obtained in a single-

compartment cell by use of a Biologic potentiostat (SP-200), with a Pt counter electrode and a Pt quasi-reference electrode at scan rates of 20 mV-s^{-1}.

A.3.9 Spectral Response

Spectral response measurements were obtained to determine the external quantum efficiency (Φ_{ext}) as a function of wavelength. Monochromatic light with a bandwidth of 10 nm was produced using an Oriel monochromator and an Oriel Xe lamp. The beam was chopped at 20 Hz and was focused to a spot size that under-filled the sample. A mirror (10Q20BB.HR broadband dielectric mirror, Newport Corporation) was used to direct the horizontal beam vertically for the bottom-facing electrodes. The electrodes were tested in the same photoelectrochemcial cell as described above for the 1 M KOH measurements. Each electrode was held potentiostatically at 1.63 V vs RHE with a Biologic potentiostat (SP200) that was connected to a lock-in amplifier (SRS 830). A second lock-in amplifier was connected to a second photodiode that continuously monitored the light intensity provided by a quartz beam-split portion of the incident beam. Calibration of the light incident on the electrodes was performed using a bottom-facing calibrated photodiode (Newport FDS100-CAL) that was placed in the same location as the electrodes.

A.3.10 Oxygen-Evolution Faradaic Efficiency

The Faradaic efficiency for oxygen evolution of a single np^+-Si/TiO_2/$NiCrO_x$ microwire array electrode was measured in the same cell as for the 1 M KOH measurements described above. Both the oxygen concentration and the charge passed were simultaneously monitored over a 40 min photoelectrochemical measurement, After a 10-min waiting period at open circuit, the microwire electrode was held potentiostatically at 1.63 V vs RHE with a Biologic potentiostat (SP200) for 30 min, and the oxygen concentration in solution was measured over the entire 40 min period with an Ocean Optics fluorescent probe (NeoFox HIOXY). Illumination was provided by a Xe lamp (Oriel 67005, Newport Corporation) with a AM 1.5G filter and was calibrated to 1-Sun intensity with a Si photodiode. Prior to measurement, the solution (approximately 48 mL in volume) was purged with N_2(g) for ~ 20 min to obtain a near oxygen-free environment

The10-min measurement at open circuit without oxygen production provided a measurement of the oxygen leak rate of the cell. These leak rates were interpolated during the 40 min photoelectrochemical measurement and were subtracted from the overall oxygen detection to yield an oxygen evolution rate for the electrode itself. The corrected oxygen concentration data were then converted to micrograms of O_2, using the amount of O_2 dissolved in water at room temperature under 1 atm (7700 $\mu g \cdot L^{-1}$), the solution volumne (~48 mL), and the concentration of O_2 in air under 1 atm at 25°C (20.9%). 100% Faradaic efficiency was assumed as 4 electrons are used to generate 1 O_2 molecule,

i.e. 0.33 mA h of charge passed to generate 100 μg of O_2. All the data were processed using a Matlab script.

A.3.11 Imaging

All scanning-electron micrograph (SEMs) were taken on an FEI Nova NanoSEM 450.

A.4 Chapter 6: Si/Ni-Mo Photocathode Methods

A.4.1 Modeling

A zero-dimensional model was constructed to predict the maximum performance expected from the MEA-type photocathode device, based on a previously derived analytical expression for a buried junction in series with a catalyst and an additional resistor.[23] The expression was modified to produce Equation A.4.1, where the γ factor (calculation shown in Equation A.4.2) accounts for the additional junction area compared to the geometric (projected) area of illumination for a microwire array.[43,177] Here n_d is the diode quality factor, k is Boltzmann's constant, T is the temperature in K, q is the unsigned charge on a single electron, J_L is the light- limited current density, $J_{0,PV}$ is the diode dark-current density, α is the catalytic charge-transfer coefficient (assumed to be equal for both forward and reverse directions), n_e is the number of electrons transferred, $J_{0,cat}$ is the catalyst exchange-current density, and R_s is the series resistance.

$$V(J) = \frac{n_d kT}{q} \ln\left(\frac{J_L - J}{\gamma J_{0,PV}} + 1\right) + \frac{kT}{\alpha n_e q} \sinh^{-1}\left(\frac{J}{2J_{0,cat}}\right) + JR_s \quad \text{A.4.1}$$

$$\gamma \equiv \frac{actual\ junction\ surface\ area}{projected\ surface\ area} = \frac{\pi \times 1.9\mu m \times 70\mu m}{7\mu m \times 7\mu m} \quad \text{A.4.2}$$

$$= 8.5$$

Eqn A.4.3

Table A. 1: Values used for the zero-dimensional model

Variable	Value
n_d	1.75
k	1.38 x 10^{-23} m^2 kg s^{-2} K^{-1}
T	298 K
q	1.6 x 10^{-19} C
J_L	25 mA – cm^{-2}
γ	8
$J_{0,PV}$	10^{-7} A cm^{-2}
α	0.5
n_e	2 electrons
$J_{0,cat}$	1.3 mA cm^{-2}
R_s	2.6 x 10^{-6} Ohm cm^2

Table A. **1** shows the values used for the parameters in the model. The light-limited current density, J_{ph}, was determined through two-dimensional full-wave simulations using a Maxwell's equations solver (Lumerical) employing finite-difference time-domain algorithms.[87] Each simulation consisted of a 60 μm tall and 2 μm diameter Si microwire loaded at the base by a layer of 200 nm diameter Ni-Mo particles at a mass loading of ~1 mg cm^{-2}, covered by a layer of 200 nm diameter TiO_2 particles (~1 mg cm^{-2}). A two-dimensional, 7 μm wide, unit cell was used with Bloch boundary conditions on the sides, to simulate an infinite array as well as to yield transmissive top and bottom boundary conditions. Light was incident at an angle of 30 degrees. Single-wavelength simulations at 50 nm intervals from 350 nm – 1050 nm were performed and integrated using the AM 1.5G spectrum that had been binned to match the intervals at which the simulation data were computed. A 100 nm thick n^+-Si emitter layer on the outer edge of the Si microwire was assumed to recombine all photoexcited carriers, and thus make no contribution to the J_{ph} value. The maximum J_{ph} value was calculated by summing all of the calculated photocurrent densities over the range of excitation wavelengths considered in the simulation.

The roughness factor, γ, was calculated for an array of 1.9 μm diameter and 70 μm tall microwires. The dark saturation-current density for the p-Si microwires with radial n^+ emitters, $J_{0,PV}$, grown by the vapor-liquid-solid growth method, was taken from the

literature.[48] The exchange-current density for the Ni-Mo catalyst, $J_{0,cat}$, was determined by modeling experimental data using the Butler-Volmer equation and by evaluation of the series resistance as determined by impedance measurements (Figure 3 in main text). The series resistance, R_s, was a general lumped circuit-element term that accounted for any additional resistances in the system. The sole contribution to R_s considered for this model was electron transport down the n^+-Si emitter to reach the Ni-Mo catalyst deposited at the base of each microwire. The value of R_s was determined by assuming that all of the current flowed down the entire 70 μm length of the microwire, through a 200 nm thick emitter with a carrier concentration of 1019 cm-3 on a 1.9 μm diameter Si microwire.

A.4.2 Fabrication of Electrodes

Boron-doped ($N_A = 1 \times 10^{17}$ cm^{-3}) Si microwire arrays were grown via a Cu-catalyzed vapor-liquid-solid (VLS) process on B-doped (111)-oriented p-Si wafers (0.1–1 Ω-cm resistivity, Silicon Inc.).[38] Three-inch diameter p-Si(111) growth wafers were received with a 500 nm thick thermal oxide (SiO_2) and were patterned photolithographically (MCC Primer and Shipley 1813 Microchem photoresist) using a mask with square pattern of 3 μm diameter holes on a 7 μm pitch. The exposed holes were etched through to the underlying Si by use of buffered hydrofluoric acid (BHF, Transene Inc.) for 5 min. 500 nm of Cu (EPSI 6N) was then thermally evaporated onto the wafer and the Cu was removed from everywhere

but the 3 μm holes by lift-off in acetone. The wafer was diced to pieces that fit a 1" (OD) home-built chemical-vapor deposition (CVD) tube furnace, for microwire growth.

Si microwires were grown at atmospheric pressure using $SiCl_4$ (Strem, 99.9999+%) at 25 sccm flow rate, H_2 (Matheson, research grade) at 500 sccm flow rate, and BCl_3 (Matheson, 0.25% in H_2) at 1 sccm flow rate for 15 min. Following growth, the samples were cooled to ~ 200 °C under a 500 sccm flow of He. Microwire arrays were cleaned using a 6:1:1 (by volume) H_2O:HCl (12 M, aqueous):H_2O_2 (9.8 M, 30 wt%) metal etch (RCA 2) for 20 min at 70 °C. The samples were then subjected to a 15 s etch in BHF etch, a H_2O rinse, a 45 s etch with 5.4 M (30 wt%) KOH (semiconductor grade, Aldrich), and a H_2O rinse. A 100 nm thick SiO_2 layer was then grown via dry thermal oxidation for 100 min under an O_2 atmosphere in a tube furnace at 1050 °C. The samples were then etched for 3 min in BHF to remove the oxide. This oxidation step is thought to getter Cu and other impurities from the core of the Si microwire, and etching of the oxide layer removes 50–100 nm of the metal-rich Si surface layer.[38]

Photoactive devices were made by forming phosphorus-doped n^+-Si radial emitters and aluminum-doped p^+-Si back surface fields on the p-Si microwire arrays and on planar, single-side-polished (111)-oriented p-Si wafers (Silicon Inc., 0.7 Ω-cm). The substrates were first etched in BHF for 15 s, then rinsed with H_2O, and cleaned using a 5:1:1 (by

volume) H_2O:NH_4OH(aqueous):H_2O_2(30% in H_2O) organic etch (RCA 1) for 20 min at 70 °C. The samples were then etched in BHF for 15 s, rinsed with H_2O and cleaned using the RCA 2 metal etch for 20 min at 70 °C. The samples were then etched in BHF for 15 s, rinsed in H_2O, dried in a stream of N_2(g), and the unpolished side of the sample was coated with 100 nm of aluminum by electron-beam evaporation. These samples were coated with a spin-on dopant (P509 Filmtronics) by spin coating at 2000 rpm for 30 s. The spin-on dopant was cured for 15 min at 200 °C on a hotplate in air. The samples were then annealed in a rapid thermal annealing (RTA) furnace under a 15 L min^{-1} flow of N_2(g) with the following process: a 20 s ramp to 880 °C, a 30 s soak at 880 °C, a 180 s linear cool to 820 °C, and a cool to ~200 °C in a flow of N_2(g).[178] In the RTA furnace, a 3" or 4" diameter Si wafer that had been coated once with spin-on dopant and cured was used as a holder for the samples. The planar and microwire samples were placed with the spin-on-dopant side facing downwards on the spin-on-dopant face of the Si holder wafer. This configuration allowed for gas-phase access of phosphorus dopants to any uncoated parts of the Si microwires from the Si holder wafer during the doping process. After cooling, the samples were etched in BHF for 3 min, rinsed with H_2O, and dried in a stream of N_2(g). A porous underlayer (resulting from the spin-on dopant) that was not susceptible to etching in BHF remained near the microwire bases. To remove this residual material, an oxidation that consisted of a 10 min dry oxidation (3 L min^{-1} O_2) at 800 °C, a 40 min wet oxidation at 800 °C with Ar bubbling through 95 °C water, and an additional 10 min dry

oxidation at 800 °C, was performed. The warm up and cool down were performed under a 3 L min^{-1} flow of Ar. A final 3 min etch in BHF removed the residual defects, resulting in clean microwire and planar samples that were washed with H_2O and dried under a stream of N_2(g). Immediately prior to deposition of the catalyst/scattering layer, the samples were etched for 15 s in BHF, washed in H_2O, and dried in a stream of N_2(g).

After the processing had been completed, ohmic contact was made to the Si substrates using an In-Ga (99.99%, Alfa-Aesar) eutectic that was scratched into the rear surface of the samples. Both Si and Ti foil substrates were affixed to a coiled Cu-Sn wire with Ag paint (SPI 05001-AB), with the Ag paint contacting the In-Ga on the Si substrates. The active area of the electrode was defined with epoxy (Loctite Hysol 9460), and the entire electrode was sealed with epoxy to the opening of a glass tube (6 mm outer diameter). The electrode orientation was determined by the orientation of the coiled wire that protruded from the glass tube. Geometric areas were measured by imaging the active area using a calibrated flat-bed scanner, and using software (ImageJ) to calculate the electrode area.

A.4.3 Synthesis and Deposition of Electrocatalysts

For synthesis and preparation of catalysts and photoelectrodes, all chemicals were used as received unless noted otherwise. Water was filtered using a MilliPore system and had a resistivity > 18 MΩ-cm.

Ni–Mo nanopowder was synthesized following a previously reported procedure.[89] Briefly, an ammoniacal solution of nickel nitrate hexahydrate and ammonium molybdate containing a 3:2 ratio of Ni to Mo was mixed with diethylene glycol and heated rapidly to precipitate a mixed Ni-Mo oxide. The oxide was recovered and purified by consecutive washing and centrifugation first with water, then with acetone, and then with methanol, and was then dried in air. The resulting pale green powder was reduced under forming gas (5% H_2(g) in N_2(g)) at 400-500 °C for > 60 min to yield a black, pyrophoric Ni-Mo nanopowder. This powder was carefully suspended in isopropanol and the resulting colloid was used to generate catalyst inks.

The synthesis was slightly modified to produce Ni–Mo/C nanopowder, whereby the oxide was mixed with 20% by mass of carbon black (Vulcan XC72) and the mixture was thoroughly ground with a mortar and pestle. The subsequent reduction step was carried out as with the standard Ni–Mo nanopowder. The resulting carbon-composite powder

was ~50% carbon content by mass and was significantly less pyrophoric than the pure Ni–Mo nanopowder.

Ni–Mo nanopowder was deposited on Ti foil electrodes and on Si photoelectrodes (both planar and microwire arrays) by centrifugal flocculation from the nanoparticle inks. The inks consisted of 1–2 mg mL^{-1} of Ni-Mo nanopowder suspended in isopropanol with the addition of ~ 2% (by weight, relative to Ni-Mo) polytetrafluoroethylene (PTFE) particles from a water/alcohol suspension (Aldrich). The PTFE was added to increase the adherence of the nanoparticles to planar substrates. For deposition, the substrate was placed on a flat surface of polydimethysiloxane (PDMS) in a centrifugation vial, and the appropriate amount of ink was added to achieve mass loadings of ~1 mg cm^{-2}. Prior to deposition, the ink was sonicated using a bath sonicator (Branson) for at least 30 min. The Ni-Mo/PTFE films were then flocculated by centrifugation at 3000 rpm for at least 5 min, after which the films were carefully removed and either air dried (planar samples) or manually dried by placing the films face-down on a paper tissue (Kimtech Kimwipe).

The PDMS/centrifugation-vial construct described above was produced by centrifuging the PDMS mixture overnight at 3000 rpm, which had the beneficial effects of removing air bubbles and producing a flat PDMS surface. Following deposition, the Si/Ni-Mo

samples were annealed in forming gas for 30 min at 450 °C, but samples that contained Ni-Mo/C catalyst did not require this anneal.

TiO_2 nanoparticle suspensions were generated from hydrophobized TiO_2 pigment particles (DuPont TiPure R-105) suspended in isopropanol at a concentration of 100 mg mL^{-1} of TiO_2 mass loading with 2% Nafion (by weight, relative to TiO_2; Aldrich). Deposition was performed in the same centrifugation vials as for Ni-Mo deposition, and consisted of drop-casting 15 µL of the TiO_2 ink and immediately centrifuging the electrode at 3000 rpm for several min. The Nafion was then cured by an anneal at 150 °C for 15 min in air. Initial experiments were performed with both hydrophobic and hydrophilic TiO_2 particles, with the hydrophobic particles showing superior performance.

Platinum particles were deposited electrolessly on Si substrates by use of a solution that consisted of 1 mM Pt and 2% HF in H_2O. Each electrode was etched for 15 s in buffered HF(aq) solution, washed, dried under a stream of N_2(g), and submerged for 1 min in the electroless Pt deposition bath. The electrode was then washed with H_2O, dried with a stream of N_2(g) and immediately tested to determine the photoelectrochemical behavior of the sample.

A.4.4 Characterization of Electrodes

Structural characterization of the various electrocatalyst deposits on Si electrodes was performed using a FEI Nova NanoSEM scanning-electron microscope. The current density vs potential behavior of the catalytic electrodes and photoelectrodes was measured using either a Gamry Reference 600 or a Biologic SP-200 potentiostat.

Electrochemical measurements were performed using either 0.5 M or 1.0 M trace-metal grade H_2SO_4 aqueous solutions (Fischer) as the electrolyte. Electrochemical experiments were performed in a two-compartment Pyrex cell that was equipped with a flat Pyrex window and with a Ag/AgCl reference electrode that was located in the same compartment as the working electrode. A Pt mesh or Ir/Ru/Ti oxide counter electrode was contained in a separate compartment that was isolated from the main cell compartment by a fine-porosity frit or by a Nafion membrane. All of the electrochemical data were collected with rapid stirring of the solution, to minimize mass-transport effects and to rapidly remove nucleated bubbles from the electrode surface.

The electrolyte was constantly bubbled with research grade H_2(g) (Air Liquide) to maintain a constant reversible hydrogen electrode (RHE) potential, as determined by measurement of the open-circuit potential of a platinized Pt wire. The electrochemical potentials were adjusted to the RHE scale after data collection.

Electrodes were tested using cyclic voltammetry (CV) or linear-sweep voltammetry (LSV), at scan rates ranging from 5–20 mV s-1, which were sufficiently slow to produce quasi steady-state behavior (validated by independent potentiostatic measurements). The current- density versus potential (*J*–*E*) data were not corrected for uncompensated resistance losses or for concentration overpotentials. Forward and reverse CV sweeps generally showed minimal hysteresis. When hysteresis was observed, the data collected while sweeping from negative toward positive potentials (reverse sweep) corresponded better to the steady-state polarization measurements, and thus were used for final analysis. LSV measurements generally were initiated at potentials that were several hundred mV negative of E_{RHE}, and were terminated at potentials just positive of where the electrode began to pass anodic current. This protocol effectively prevented the Si surface from oxidizing and minimized anodic stripping of the non-noble catalyst particles from the electrode surface.

The characteristics of the photoelectrodes were evaluated under simulated sunlight that was provided by a custom-built ELH-type tungsten-halogen light source or by a Xe lamp (Oriel 67005, Newport Instruments) equipped with an AM 1.5G filter (Newport Instruments 81094). The light source was placed at a distance from the electrochemical cell sufficient to generate an incoming photon flux above the Si indirect band gap (1.1 eV)

equivalent to 1 Sun illumination, as measured by a Si photodiode (Thorlabs) that was calibrated relative to a NIST-traceable standard (Solarex).

The ideal regenerative cell efficiency (η_{IRC}) was adopted as the figure-of-merit for device performance.[98] The value of η_{IRC} corresponds to the system efficiency of a two-electrode cell operating such that no net chemical reactions occur, in which the second, dark electrode is an ideally non-polarizable electrode performing the same reaction as the photoelectrode, but in the reverse direction. Equation A.4.4 describes calculation of η_{IRC}, which is identical to the calculation of the efficiency of a photovoltaic cell. Here V_{mp} and J_{mp} are the voltage and photocurrent density at the maximum power point and P_s is the input solar power density; equivalently, V_{oc} is the open-circuit voltage, J_{sc} is the short-circuit current density and *ff* is the fill factor of the device.

$$\eta_{IRC} = \frac{V_{mp} \cdot J_{mp}}{P_s} = \frac{V_{oc} \cdot J_{sc} \cdot ff}{P_s} \qquad \text{A.4.4}$$